Carrier Synchronization in High Bit-Rate Optical Transmission Systems

Kittipong Piyawanno
Der Fakultät für Elektrotechnik und Informationstechnik

der Universität der Bundeswehr München
zur Erlangung des akademischen Grades eines

Doktor-Ingenieur
(Dr.-Ing.)

vorgelegte Dissertation.
Neubiberg, 18. Juli 2012

Dissertation

Carrier Synchronization
in
High Bit-Rate Optical Transmission Systems

Kittipong Piyawanno

Erstprüfer
Prof. Dr.-Ing. Berthold Lankl
Zweitprüfer
Prof. Dr.-Ing. Henning Bülow
Drittprüfer
Prof. Dr.-Ing. Gerhard Bauch

Universität der Bundeswehr München
Fakultät für Elektrotechnik und Informationstechnik
Institut für Informationstechnik
Professur für Informationstechnische Systeme
Prof. Dr.-Ing. Berthold Lankl

Universität Erlangen-Nürnberg
Lehrstuhl für Informationsübertragung
Prof. Dr.-Ing. Henning Bülow

Universität der Bundeswehr München
Fakultät für Elektrotechnik und Informationstechnik
Institut für Informationstechnik
Professur für Informationsverarbeitung
Prof. Dr.-Ing. Gerhard Bauch

18. Juli 2012

Acknowledgements

This dissertation and conferral of a doctorate at the Institute for Communications Engineering at the University of the Bundeswehr in Munich is an assignment of the Royal Thai Navy and can be seen as the continuation of the cooperation between German Bundeswehr and Royal Thai Armed Forces. It cannot be possible without supports from many people.

First of all, I would like to thank my adviser Prof. Dr.-Ing. Berthold Lankl from the Institute for Communications Engineering at the University of the Bundeswehr in Munich for the opportunity for conferral of a doctorate, supports, inspiration, valuable advices and guidances. Sometimes, problems in our researches seemed to be unsolvable for us. Because of his wide knowledge in communication technology and literatures, with his suggestions for problem analysis and apposite literatures, we can propose resultant researches from apparently unsolvable problems.

I also would like to thank Prof. Dr.-Ing. Henning Bülow from the Institute for Information Transmission of Friedrich-Alexander-University Erlangen-Nuremberg as the second reviewer of this dissertation. Moreover, his works and presentations in conferences are also an inspiration for our research team. I feel honored that Prof. Dr.-Ing. Henning Bülow is the second reviewer for this dissertation. For the chairman and dissertation committee, I would like to thank Prof. Dr.-Ing. Gerhard Bauch from the Institute for Information Processing at the University of the Bundeswehr in Munich.

The person, who recommended me to make a PhD in optical communication systems and gives me many supports and advices on life and researches especially at the beginning of the PhD, is my colleague and friend Fabian Hauske. Without him, my doctoral study can be much more complicated. Likewise, Maxim Kuschnerov is an important colleague and friend of mine. Many ideas in our researches have been evolved from our discussions. Moreover, he gave me his statements, which improve my works in many aspects. With him, conferences for optical transmission systems were much more interesting and colorful for me.

A special thank for another colleague, who gave me experimental measured data for our researches, is M.Eng Mohammad Alfiad. During the doctoral study, I had monthly meeting with researchers from Nokia Siemens Networks like Bernhard Spinnler, Ernst-Dieter Schmidt and Stefano Calabrò. They gave me the direction of researches. I also thank my colleagues Danial Schmidt, Stephan Ludwig, Nora Tax, Vito Dantona and Leoni for the teamwork at our institute. Furthermore, I would like to thank Karl Heinrich Besthorn like Bernhard Börner, Dagmar Frendl, Karl-Heinz Schlücker, Johannes Schmidt, Angelika Bauer and Hannelore Heidrich for thier helpfulness. For advices about the technique of academical writing, and grammatical improvement of this dissertation, I would like to thank Chalat Santivarangkna.

Last but not least, I would like to thank my girlfriend Sawatree Suksri for her understanding, patience and love, my parent and sisters for unconditional supports and love.

Munich, December 2010

Contents

1. Introduction

1.1. Internet and Optical Transmission Systems

In the information age like nowadays, internet becomes a part of daily routine for millions or even billions people around the world. The internet simplifies many tasks of their users. For many companies, it is actually unthinkable without internet e.g. Google, Yahoo!, Facebook and so on. The creativity of internet applications cannot be stopped anymore. The internet applications like social network, mobile internet application, on-line gaming, cloud computing attract more and more interest and users. However, what is the internet without connections. More internet means more connections and more bandwidth requirements.

Since invention of the internet and its applications, bandwidth requirements for transmission systems have exponentially grown as illustrated in Figure 1.1 [1]. With conventional copper cables and the wireless transmission systems, bandwidth and data-rate requirements for many application domains especially for *long-haul* connections cannot be fulfilled. Due to the high data-rate, a high channel capacity, a low attenuation and many other advantages, the transmission systems with optical fibers are the promising choice for the data transmissions in the future.

In many years of the development for the optical transmission systems, *direct detection techniques* are the dominant technology concerning the limitation of laser accuracy and the speed

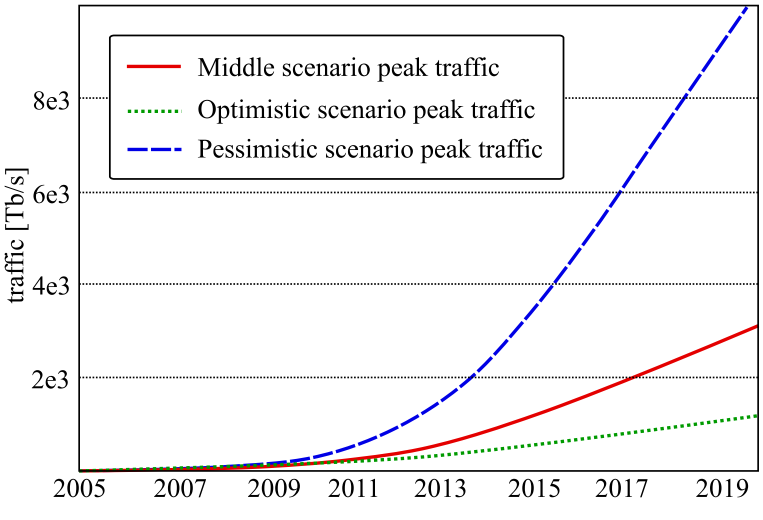

Figure 1.1.: World internet traffic and the prediction

of digital circuits for *digital signal processing.* With direct detection, the data information can be recovered without digital signal processing, and the costs for the receiver implementation can be reduced. However, the channel capacity of the optical fibers cannot be fully utilized. Moreover, the high priced *in-line compensation* must be optimized and deployed.

With the the accuracy improvement of the laser and the drastic development of the digital circuits, *coherent detection* can be realized in the optical transmission systems. Coherent detection establishes a new era of the optical transmission systems. With coherent detection and digital signal processing, data can be transmitted over a long distance without in-line compensation, advanced modulation formats can be realized, and the channel capacity of the optical fibers can be better utilized. Digital signal processing has to be a part of coherent detection and coherent detection without the digital signal processing can be deployed only with high limitations. One of the key components for coherent detection is the *carrier synchronization.*

1.2. Carrier Synchronization

In coherent detection schemes, *carrier signal* at the transmitter and receiver sides must be synchronized. Although the new generation lasers provide a reliable and accurate carrier signal, the synchronization of the carrier signal cannot be obtained without an additional carrier synchronization. We can classify carrier synchronization in two types namely the optoelectronic synchronization with the *controlled local oscillator* [2] and the digital synchronization with the *free running local oscillator* [3]. Due to the simpler implementation, in this dissertation, only digital synchronization schemes with the free running local oscillator are described and analyzed.

Moreover, many impairments in the optical transmission systems can be mitigated with a powerful and suitable carrier synchronization. Hence, in this dissertation, various algorithms for carrier synchronization for various applications are proposed.

1.3. Outline of the Dissertation

Although in the last years, many algorithms for carrier synchronization in high bit-rate optical transmission systems have been proposed. Not all of them are practicable or can fulfill the requirements in optical transmission systems. In this dissertation, we firstly describe the channel model and the structure of transceivers for the optical transmission systems to determine the requirements of its carrier synchronization. Afterwards, basics of the carrier synchronization are introduced. And finally, the algorithms for carrier synchronization sorted by their structures and their applications are depicted and evaluated. It should be emphasized that only the relevant results for the optical transmission systems are evaluated. Moreover, the implementation of the algorithms is always considered to guarantee that the algorithms proposed in the dissertation are practicable for optical transmission systems.

In Chapter 2, the channel models of optical fibers are described to show the characteristics and the features of optical transmission systems. Moreover, the phase noise caused by the channel nonlinearities are key impairments for optical transmission systems and can be compensated with a suitable carrier synchronization. This means that the channel nonlinearities, which are key challenges for carrier synchronization, are defined in this chapter.

In Chapter 3, we concentrate on the optical transmitter and receiver or a so-called optical transceiver in order to define and understand the role of the carrier synchronization in the optical transmission systems. Furthermore, the components of the optical transmitters and receivers with direct detection as well as coherent detection techniques are introduced.

In Chapter 4, the algorithms for the carrier synchronization are classified to give an overview of estimation methods. Moreover, the chapter is dedicated to the basic principles and the estimation theory for carrier synchronization, which is used for the derivation of carrier synchronization algorithms in this dissertation.

From Chapter 5 to Chapter 8, the algorithms for the carrier synchronization sorted by their structures and application cases are briefly described. The performance of the algorithms is investigated in many aspects, which are related to optical transmission systems.

In Chapter 9, conclusions of the dissertation and future outlooks for carrier synchronization in optical transmission systems are given.

2. Channel Characteristics of Optical Fiber Transmission

In most communication systems, channel distortions are usually a minor aspect of the carrier synchronization due to the assumption of a perfect equalization. In the high bit-rate optical transmission, however, phase noise can be induced by nonlinear distortions like self phase modulation (SPM) and cross phase modulation (XPM), which interact with the linear distortions like chromatic dispersion (CD) and polarization mode dispersion (PMD). Hence, the channel distortions should be considered in the design of a carrier synchronization. Moreover, it has been shown in [4] that a carrier phase estimation can mitigate the channel nonlinear impairment. In this chapter, the channel distortions and the other channel characteristics of optical transmission like fiber losses will be described.

2.1. Fiber Losses

Fiber losses are important limitations of the transmission performance and distance in the optical transmission system. If P_0 is the power launched at the input of a fiber of length L_f, the received power P_s is given by [6]

$$P_s = P_0 \cdot \exp\left(-\frac{\alpha \cdot L_f}{4.343}\right) \tag{2.1}$$

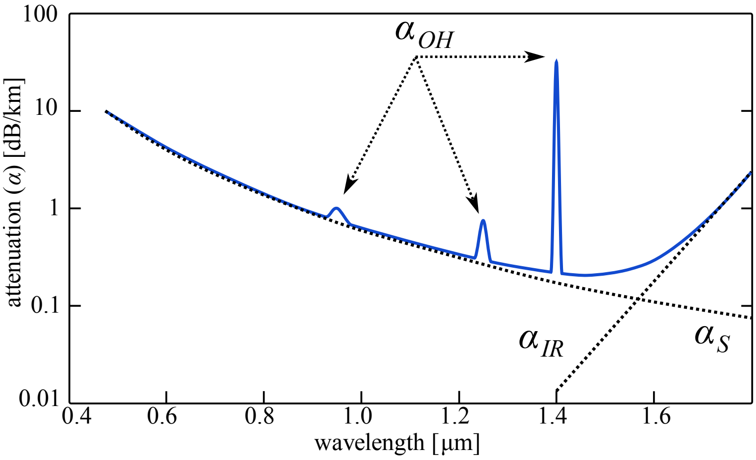

Figure 2.1.: Attenuation coefficient of a SSMF [5]

where the attenuation coefficient α is a measure of the total fiber losses from all sources and depends on the wavelength λ. Figure. 2.1 shows α of a standard single mode fiber (SSMF). It can be seen that α is influenced by Rayleigh-scattering attenuation (α_S), infrared-absorption attenuation (α_{IR}) and OH-absorption attenuation (α_{OH}). Modern fibers exhibit a loss of ≈0.2dB/km near the wavelength $\lambda = 1.55\mu$m, which is the reference wavelength for most long haul optical transmission systems [6].

2.2. Chromatic Dispersion

Chromatic Dispersion (CD) is a deterministic linear effect in fiber optics. CD is induced by the frequency dependence of the refractive index $n(\omega)$. The origin of chromatic dispersion can be observed as a relation to the characteristic resonance frequencies at which the medium absorbs the electromagnetic radiation through oscillations of bound electrons. For the resonances of the medium, the refractive index can be approximated by the Sellmeier equation [7]

$$n^2(\omega) = 1 + \sum_{j=1}^{m} \frac{B_j \omega_j}{\omega_j^2 - \omega^2} \tag{2.2}$$

where ω_j is the resonance frequency and B_j is the strength of jth resonance. The sum in Eq.(2.2) extends over all material resonances which contribute to the frequency of interest [6].

The effects of the dispersion in fiber optics are accounted by expanding the mode-propagation constant $\beta(\omega)$ in a Taylor series about the frequency ω_0 at which the transmitted pulse spectrum is centered:

$$\beta(\omega) = n(\omega)\frac{\omega}{c} = \beta_0 + \sum_{m=1}^{\infty} \frac{1}{m!} \cdot \beta_m \cdot (\omega - \omega_0)^m, \tag{2.3}$$

where c is the speed of light in vacuum and

$$\beta_m = \frac{d^m \beta(\omega)}{d\omega^m}, \qquad \text{with } m \in \mathbb{N}^+. \tag{2.4}$$

The parameters β_1 and β_2 are related to the refractive index $n(\omega)$ and can be derived as following

$$\beta_1(\omega) = \frac{1}{v_g} = \frac{n_g(\omega)}{c} = \frac{1}{c}\left(n(\omega) + \omega \frac{dn(\omega)}{d\omega}\right) \tag{2.5}$$

$$\beta_2(\omega) = \frac{1}{c}\left(2\frac{dn(\omega)}{d\omega} + \omega \frac{d^2 n(\omega)}{d\omega^2}\right) \tag{2.6}$$

where v_g is group velocity and n_g is the group index. In physical observation, the envelope of an optical pulse moves at the group velocity, while the parameter β_2 represents the dispersion of the group velocity and induces the pulse broadening. This phenomenon can be described as the group-velocity dispersion (GVD). For the convenience in practice, the dispersion parameter D, defined as $d\beta_1/d\lambda$, is also used. It is related to β_2 and n and can be given by

$$D(\omega) = \frac{d\beta_1(\omega)}{d\lambda} = -\frac{2\pi c}{\lambda^2}\beta_2(\omega) = -\frac{\lambda}{c} \cdot \frac{d^2 n(\omega)}{d\lambda^2}. \tag{2.7}$$

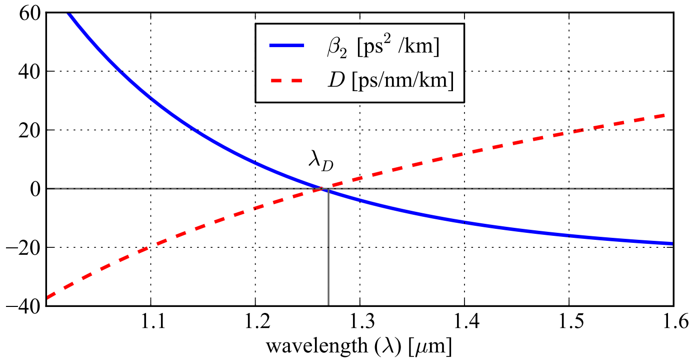

Figure 2.2.: Variation of β_2 and D with wavelength for SSMF. Both β_2 and D vanish at the zero-dispersion wavelength (λ_D) occurring near 1.27μm.

With changing fiber-design parameter such as core-cladding index difference and core radius, D can be adjusted for the application of the fiber optics. For the reduction of CD in optical communication systems, we can use this feature to shift the zero dispersion wavelength (λ_D) to 1.55μm where the fiber loss is minimum. These fibers are known as dispersion shifted fibers [8]. The so-called dispersion-compensation fiber (DCF) is a fiber with the shifting of GVD to the wavelength region beyond 1.6μm exhibiting a large positive value of β_2. It should be emphasized that DCF in combination with SSMF are widely used in transmission systems with dispersion-managed links (DM).

2.3. Polarization Mode Dispersion

We can apply two orthogonal polarization states in a single mode fiber to increase the channel capacity for the signal transmission. Assuming perfect cylinder symmetry and a stress-free fiber or rather ideal conditions, the light wave propagations are not coupled in each polarization states. In a real fiber, however, these conditions cannot be achieved. and the two polarization states can be mixed. Due to the random variations in the core shape along the fiber length and the stress-induced anisotropy, the mode degeneracy can be broken. Hence, for two polarization states, the $\beta(\omega)$ becomes slightly different. These characteristics of the light wave propagations are known as dimensionless modal birefringence B_m [9, 6] and can be given by

$$B_m = \frac{|\beta_x - \beta_y|}{k_0} = |n_x - n_y|\,, \tag{2.8}$$

where n_x and n_y are the modal refractive indices for x- and y-polarization. For a given value of B_m, the two modes exchange periodically their power with the period of the *beat length* L_B, which can be written as

$$L_B = \frac{2\pi}{|\beta_x - \beta_y|} = \frac{\lambda}{B_m}. \tag{2.9}$$

Note that the indices in both axes are different. The axis with the larger index is called *slow axis* and with the smaller index *fast axis*.

Due to fluctuations in the core shape and anisotropic stress, B_m changes randomly along the fiber. Hence, the light wave launched into the fiber changes randomly the polarization. For optical transmission systems with polarization-multiplex (PolMux) and transmission short pulses, signals in both polarizations propagate with different speed due to the different group velocities. At the output, pulse becomes broader due to the fact that group velocities change randomly in response to random changes in fiber birefringence. This phenomenon is known as PMD. Due to its importance for optical long haul transmission systems, PMD and its compensation [10, 11] have been studied extensively [12, 13, 14, 15, 16].

In [6], it has been shown that the extend of pulse broadening induced by PMD can be estimated from the time delay ΔT occurring between the two polarizations. For a fiber of a constant birefringence B_m and the length L_f, ΔT can be written as

$$\Delta T = \left| \frac{L_f}{v_{gx}} - \frac{L_f}{v_{gy}} \right| = L_f \left| \beta_{1x} - \beta_{1y} \right| = L_f \Delta\beta_1, \tag{2.10}$$

where $\Delta\beta_1$ is the group-velocity mismatch. For the PMD estimation, ΔT cannot be directly used due to the random changes of birefringence. An important parameter for the description of the characterization of PMD is the variance of ΔT, which can be given by

$$\sigma_T^2 = \mathrm{Var}\left\{\Delta T\right\} = 2\left(\Delta\beta_1 l_c\right)^2 \left[\exp\left(\frac{L_f}{l_c}\right) + \frac{-L_f}{l_c} - 1\right], \tag{2.11}$$

where $\Delta\beta_1 = \Delta\tau / L_f$. $\Delta\tau$ represents the differential group delay (DGD) along the principle states of polarization, and the correlation length l_c is defined as the length over which two polarization states remain correlated. Assuming that $l_c \ll L_f$, then

$$\sigma_T \approx \Delta\beta_1 \sqrt{2 l_c L_f} \equiv D_p \sqrt{L_f}, \tag{2.12}$$

where D_p is the PMD parameter. It should be noted that values of D_p are in the range of 0.1 to 1 ps/$\sqrt{\text{km}}$ for most fibers.

2.4. Nonlinear Impairments

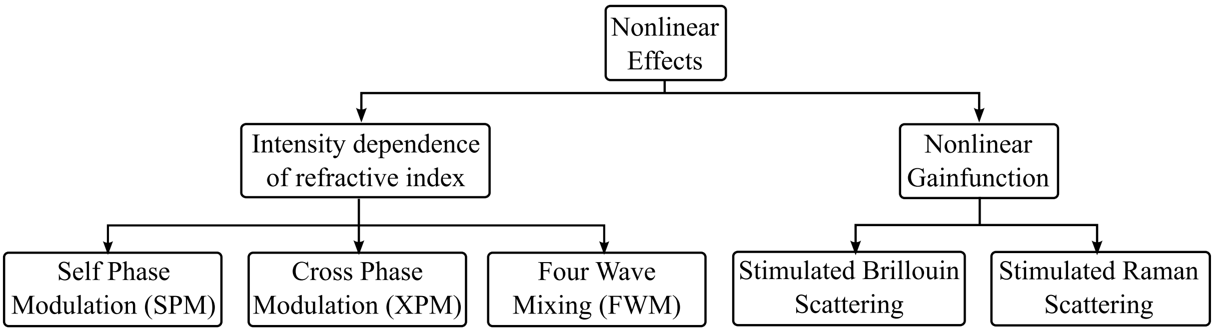

Figure 2.3.: Classification of nonlinear effects in standard single mode fibers

On the one hand, nonlinearity in fiber optics can be used for CD compensation, optical signal amplifiers, pulse compression and optical signal processing. On the other hand, nonlinear effects induce significant impairments in fiber optics. Figure. 2.3 shows the physical classification of the nonlinear effects in a SSMF. In the first group, SPM, XPM and four wave mixing (FWM) belong to the nonlinear effects, which are caused by intensity dependence of refractive index. In the other group, stimulated Raman and Brillouin scattering are parts of the nonlinearity induced gain-function. For the carrier synchronization, however, only the nonlinear effects in the first group are important due to thier impacts on the phase of the light wave signal.

2.4.1. Self Phase Modulation

It has been shown in [15] that with the intensity dependent refractive index, the light wave signal is phase modulated by the instantaneous intensity of the pulse itself resulting in the spectrum broadening. The effect is defined as *self phase modulation* (SPM) and induces a phase rotation φ_{SPM}, which is given by

$$\varphi_{SPM}(L_f, t) = -\gamma \cdot P(t) \cdot L_{eff}, \tag{2.13}$$

with

$$L_{eff} = \frac{1 - \exp\left(-\alpha L_f\right)}{\alpha}, \tag{2.14}$$

where γ represents the fiber specified nonlinear propagation coefficient, $P(t)$ the instantaneous power of the pulse, L_{eff} the effective fiber length, L_f the fiber length and α the attenuation coefficient. Moreover, the carrier instantaneous frequency is deviated due to the SPM. The SPM frequency deviation Δf_{SPM} can be given by

$$\Delta f_{SPM} = \frac{1}{2\pi} \cdot \gamma L_{eff} \cdot \frac{dP(t)}{dt}. \tag{2.15}$$

From Eq.(2.15), we can see that with the rising edge of the impulse, the carrier frequency is slided to the lower frequency. Similarly with falling edge to the higher frequency, the SPM frequency range ΔB_{SPM} is generated, which can be given by

$$\Delta B_{SPM} \approx \pm\frac{1}{2\pi} \cdot \gamma \cdot L_{eff} \cdot \frac{P_{max}}{a \cdot T_s}, \tag{2.16}$$

where P_{max} represents the maximal impulse power, $a \cdot T_s$ rising time, a the ratio of impulse rising time and T_s the symbol interval. From Eq.(2.15) and (2.16), we can see that the effect of SPM is increased with the data-rate.

2.4.2. Cross Phase Modulation

Cross phase modulation (XPM) describes the phase modulation of the optical light wave which induced by the intensity dependent refractive index and the cross talk between optical wave lengths. The XPM phase rotation φ_{XPM} can be given by [15]

$$\varphi_{XPM}(L_f, t) = -\gamma \cdot \xi \cdot P_{cp}(t) \cdot L_{eff}, \tag{2.17}$$

where ξ is the XPM weighting factor and $P_{cp}(t)$ the instantaneous co-propagate power. Table 2.1 shows the value of ξ, which depends on the polarization state and the carrier wavelength of the impulse.

Table 2.1.: XPM weighting factor

carrier wavelength	polarization state	weighting factor ξ
$f_1 = f_2$	$\parallel$	1
$f_1 \neq f_2$	$\parallel$	2
arbitrary	$\perp$	2/3

The impact of XPM can be split into two steps. Firstly, the optical signal is phase modulated by the other co-propagating signal as shown in Eq.(2.17). Afterwards, CD converts the phase modulation into the power deviation and induces walk-off between the wavelength channels. Hence, the XPM effect is reduced with the increasing CD. Like SPM as shown in Eq.(2.16), the XPM frequency range of ΔB_{XPM} can be defined by [15]

$$\Delta B_{XPM} = \pm \frac{1}{\pi} \cdot \gamma \cdot L_{eff,XPM} \cdot \frac{P_{cp}(t)}{a \cdot T_s}, \tag{2.18}$$

where

$$L_{eff,XPM} = \frac{a \cdot T_s}{D \cdot \Delta\lambda} \tag{2.19}$$

represents walk-off fiber length, D dispersion parameter and $\Delta\lambda$ the wavelength difference between co-propagate impulses.

2.4.3. Four Wave Mixing

Four wave mixing (FWM) describes the generation of new waves at other frequencies by raising the total electrical field of a wavelenght division multiplexing (WDM) signal to the third power. When considering the interaction of three waves at the frequencies f_i, f_j and f_k to compose a forth wave at

$$f_{ijk} = f_i + f_j - f_k, \tag{2.20}$$

a total number of the new generated mixing products N_{FWM} can be defined as

$$N_{FWM} = \frac{N_{WDM}^3 - N_{WDM}^2}{2}, \tag{2.21}$$

where N_{WDM} is the number of WDM channels. In standard WDM systems with equidistantly arranged channel spacings, the mixing products fall directly into the spectral bands of WDM channels. Like XPM, the efficiency of FWM is reduced with the increasing CD. Nevertheless, FWM can be a limiting effect using fibers with low dispersion and for narrow channel spacings [17].

3. Optical Transceivers

The carrier synchronization impairments in optical transmission systems are mainly caused by imperfect signal generating on the transmitter side and imperfect signal down-mixing in the receiver side. This chapter gives an overview of optical transmitter and receiver or a so-called optical transceiver to define and understand the role of the carrier synchronization in optical transmission systems. Firstly the components of the optical transmitters and receivers are described in Section 3.1 and 3.2 respectively. Afterwards, the design of the optical transmitter for the light wave signal generation is shown in Section 3.3. Since the optical signal can be detected with the direct and coherent detection techniques, the description of both detection techniques can be found in Section 3.4 and 3.5 respectively. In Section 3.6, the loop experiment, which consists of optical transceivers and optical links, is depicted.

3.1. Transmitter Components

In this section, the key components of optical transmitters are briefly described. Lasers can be applied for the carrier signal generation, which is depicted in 3.1.1. Due to performance degradations by direct data signal modulation, one or more external optical modulators like optical phase modulators (PM) (3.1.2), Mach-Zehnder modulators (MZM) (3.1.3) and/or optical IQ modulators (IQM) (3.1.4) can be composed to modulate the transmitted signal with higher-order modulation formats.

3.1.1. Lasers

In optical transmission systems, the laser is a key component for a generation of the carrier light wave. Hence, the quality of a carrier light wave as well as of detection highly depends on the quality of the lasers. A carrier signal with constant amplitude, frequency and phase can be assumed as an ideal for optical transmission systems. Unfortunately, the perfect carrier cannot be generated in practice. At the beginning of the development of optical transmission systems, light emitting diodes (LED) with very broad spectral widths and low input powers were applied to generate the carrier signal. Nowadays, with the modern technologies like single-mode distributed feedback lasers (DFB) and external cavity lasers (ECL), we can generate carrier signal with linewidths in the sub-MHz range [17]. Thus the feasibility of the optical transmission systems can be increased.

The simplest method for signal generation is the direct modulation of the data signal with the carrier signal. However, the method is limited by carrier laser chirping, which is caused by the incidental frequency modulation of the laser under amplitude modulation. An alternative to the direct modulation is the external modulation, which can avoid the above limitation. Therefore, the laser can be referred as a continuous wave (CW) light source. For the description of the signal generation from the lasers, the *normalized electrical vector* of an ideal optical carrier $\vec{E}_{CW}(t)$ can be given by [17]

$$\vec{E}_{CW}(t) = \sqrt{P_s} \cdot \exp\left(j\left(2\pi f_s t + \varphi_s\right)\right) \vec{e}_s, \tag{3.1}$$

where f_s is the frequency, P_s the power, φ_s phase and $\vec{e}_s$ the polarization of optical carrier.

Noting that spontaneous emission of photons induces light wave intensity fluctuations $\delta P(t)$ and phase fluctuations in $\vec{E}_{CW}(t)$, which can be represented by the signal laser phase noise $\varphi_{n_s}(t)$. At transmitter side, the normalized electrical vector of noisy carrier signal $\vec{E}_{CWn}(t)$ can thereby be defined as

$$\vec{E}_{CWn}(t) = \sqrt{P_s + \delta P(t)} \cdot \exp\left(j\left(2\pi f_s t + \varphi_s + \varphi_{n_s}(t)\right)\right) \vec{e}_s, \tag{3.2}$$

The laser phase noise $\varphi_{n_s}(t)$ is caused by spontaneous emission photons, not generated in phase with the stimulated emission photons but with random phase [18]. The evolution of the actual phase can be characterized as a random walk in the time domain.

The phase exhibits a random phase change of

$$\Delta\varphi_{n_s}(t) = \varphi_{n_s}(t) - \varphi_{n_s}(t-\tau), \tag{3.3}$$

in a time interval τ. Due to the fact that the phase changes $\Delta\varphi_{n_s}(t)$ are caused by a high number of independent random process, $\Delta\varphi_{n_s}(t)$ can be modeled as Gaussian distribution. Furthermore,

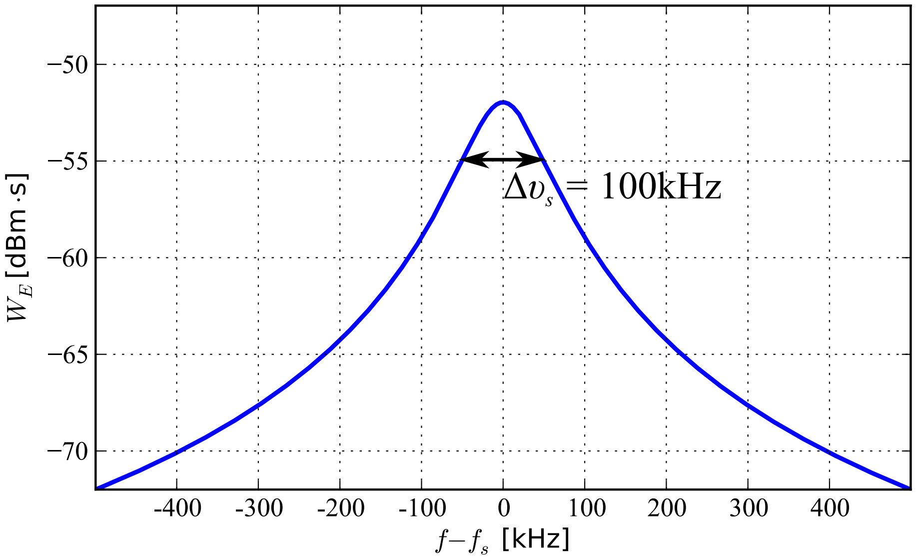

Figure 3.1.: Power spectral density of the carrier signal $W_E(f)$ with P_s=0dBm, $\Delta\nu_s$=100kHz and $f_s = c/1550$nm

the model is approximately realistic with the assumption of a white power spectral density of frequency noise $\dot{\varphi}_{n_s}(t)$. In [19, 20], it is shown that the variance of $\Delta\varphi_{n_s}(t)$ can be given by

$$\text{Var}\left\{\Delta\varphi_{n_s}(t)\right\} = 2\pi\Delta\nu_s|\tau|, \tag{3.4}$$

where $\Delta\nu_s$ is laser linewidth of the signal laser.

Assuming that the intensity noise can be neglected, the power spectral density of the optical field $W_E(f)$ can be described as a spectrum with the shape of Lorentzian function (see A.1)

$$W_E(f) = \frac{2t_c P_s}{1 + \left[2\pi(f - f_s)t_c\right]^2}, \tag{3.5}$$

Figure 3.1 illustrates $W_E(f)$ with P_s=0dBm, $\Delta\nu_s$=100kHz and $f_s = c/1550\text{nm}$.

From Eq.(3.4) we can see that the phase uncertainly increases with the laser linewidth and the observed time interval. More detailed analysis is described in [20]. It should be emphasized that the laser phase noise is one of the main limitations for the performance of carrier synchronization and the whole transmission system. However, the impairment of the laser phase noise can be reduced with a suitable design of the carrier recovery.

Since the laser is one of the components in the optical transmission system, the performance of the whole transmission system can be limited by the instability of the laser caused by mechanical disturbance. Following, the frequency variations and the stability of an ECL in the presence of mechanical disturbances is experimentally investigated by the author in [21, 22].

For separating frequency variations from residual effects, the experiment as shown in Fig. 3.2 is evaluated. The CW signal from the transmitter laser (TxLO) is directly demodulated with the laser signal from the receiver laser (RxLO) with a frequency offset of 1.5GHz. Due to the high speed transient effect, the frequency variations cannot be directly detected with conventional measurement instruments. Hence, the frequency discriminator and the power detector circuit are applied to transform the frequency variations into signal power variations, which can be simply detected and stored for further investigation with a digital storage oscilloscope of a

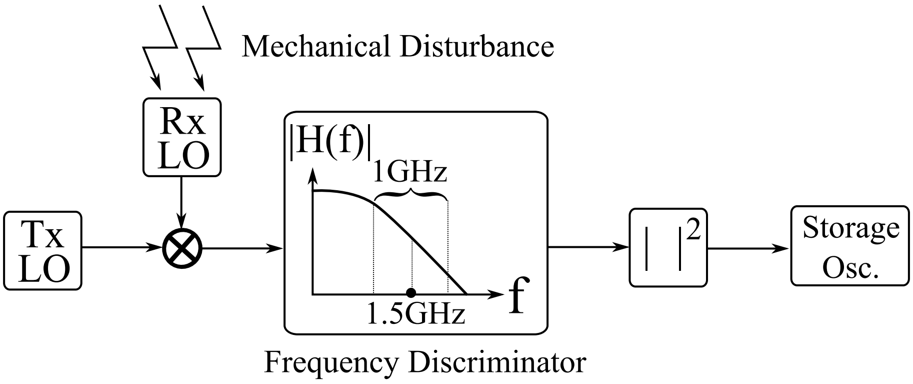

Figure 3.2.: Block diagram of experimental setup for investigation of laser stability

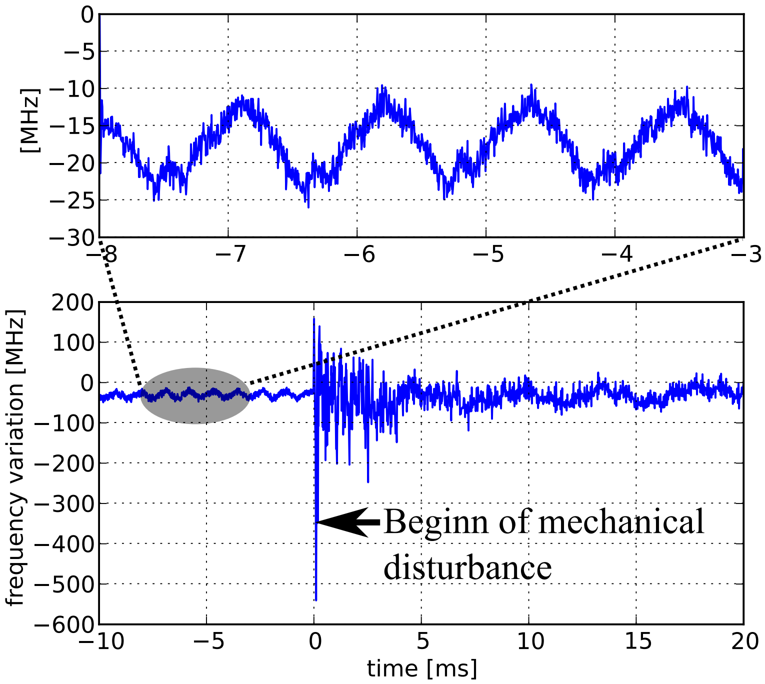

Figure 3.3.: Frequency variation by tapping a metallic tool on the laser

sampling rate of 10MHz. The frequency discriminator is a wideband lowpass filter with an approximate linear slope of 1GHz around the frequency of 1.5GHz, which is matched to the frequency offset between TxLO and RxLO.

As in microwave telecommunications, several components can cause phase noise degradation in presence of mechanical vibrations [23]. Due to the fact that the laser contains the components with high sensitivity against mechanical disturbances, we focus in this experiment on the laser only. The output signal of the laser with mechanical disturbances $f_{md}(t)$ can be approximately written as

$$f_{md}(t) = \sin\left(2\pi t\left(f_s + \frac{A_{pp}}{2}\cdot f_n(t)\right) + \varphi_{n_s}(t)\right), \tag{3.6}$$

where f_s is the carrier frequency, A_{pp} the maximum peak-to-peak of frequency variations, $f_n(t)$ general function of frequency variations over the time and $\varphi_{n_s}(t)$ is the phase noise from Eq.(3.2).

Table 3.1.: Measured maximum peak-to-peak of frequency variations A_{PP} for different mechanical disturbances

Disturbance	A_{pp}
Metallic tool tap on the laser	500MHz
Metallic tool tap on the receiver case	350MHz
Wooden brush tap on the laser	370MHz
Hand tap on the laser	250MHz
Hand hit on the table	120MHz

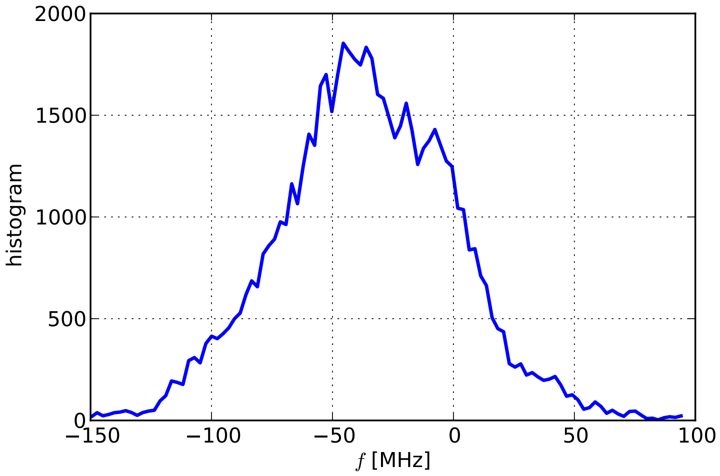

Figure 3.4.: Histogram of frequency variations induced by mechanical disturbance for 65536 measurement samples

It can be seen from Figure 3.3 that in the steady state, the laser is stabilized and $f_n(t)$ can be given by

$$f_n(t) = \sin(2 \cdot \pi \cdot f_m \cdot t), \tag{3.7}$$

where f_m is modulation frequency for laser stabilization. In the experiment, f_m is roughly 1kHz with $A_{pp} < 40$MHz. If mechanical disturbances occur, $f_n(t)$ becomes noisy and can be described as a random variable. As an example, Figure 3.4 shows histogram of frequency variations induced by mechanical disturbance for 65536 measurement samples. Moreover, A_{pp} increases rapidly at the moment of mechanical disturbances and is damped over time. Table 3.1 shows measured A_{pp} for for different mechanical disturbances.

For the convenience, mechanical disturbances in the investigation of carrier synchronizations are modeled as a stabilized laser with $f_n(t)$ as shown in Eq.(3.7).

3.1.2. Optical Phase Modulator

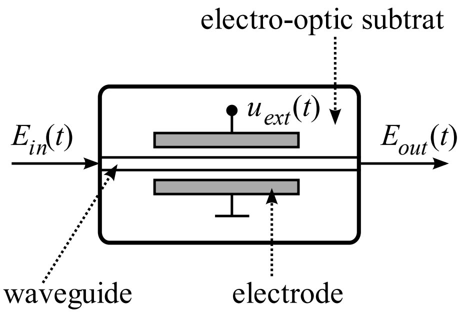

Figure 3.5.: Integrated optical phase modulator

Figure 3.5 shows the physical structure of a PM, which can be implemented embedding an optical waveguide in an electro-optical substrate e.g. $LiNbO_3$ [17]. The structure allows that the effective refractive index $n_{eff}(t)$ of the waveguide can be changed by applying an external voltage through a coated electrode.

The electrical field of the incoming light wave carrier can be modulated in phase [24] and the phase modulation $\varphi_{PM}(t)$ can be written as

$$\varphi_{PM}(t) = \frac{2\pi}{\lambda} \Delta n_{eff}(t) \cdot l_{PM}, \tag{3.8}$$

where λ is the wavelength, l_{PM} the length of the electrode and $\Delta n_{eff}(t)$ the effective refractive index. Considering the Pockels effect [24], $\Delta n_{eff}(t)$ can be assumed as a linear proportion to the applied external voltage $u_{ext}(t)$. The relation between the incoming optical carrier $E_{in}(t)$ and the outgoing phase modulated optical field $E_{out}(t)$ can be expressed as

$$E_{out}(t) = E_{in}(t) \cdot \exp\left(j\varphi_{PM}(t)\right) = E_{in}(t) \cdot \exp\left(j\pi \frac{u_{ext}(t)}{V_\pi}\right), \tag{3.9}$$

where V_π is the driving voltage for achieving a phase shift of π.

3.1.3. Mach-Zehnder Modulator

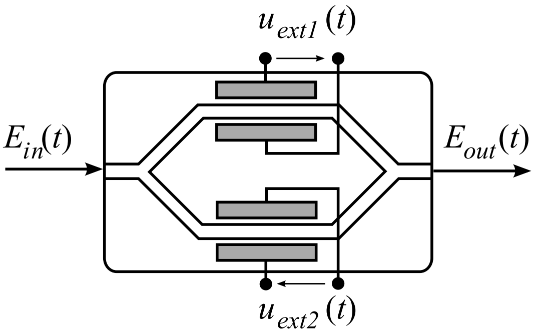

Figure 3.6.: Integrated optical Mach-Zehnder modulator

Figure 3.6 illustrates a dual-drive *Mach-Zehnder modulator*. Assumming that the insertion loss can be neglected, the transfer function of such an MZM can be given by [17]

$$\frac{E_{out}(t)}{E_{in}(t)} = \frac{1}{2} \cdot \left(\exp\left(j\pi \frac{u_{ext1}(t)}{V_{\pi 1}}\right) + \exp\left(j\pi \frac{u_{ext2}(t)}{V_{\pi 2}}\right)\right), \tag{3.10}$$

where $V_{\pi 1}$ and $V_{\pi 2}$ represent specified driving voltage to obtain a phase shift of π in the upper and lower arms respectively. On the one hand, by operating the MZM in the push-push mode, $u_{ext1}(t)$ and $u_{ext2}(t)$ are identical, and a pure phase modulation as shown in Eq.(3.9) can be achieved. On the other hand, for $u_{ext1}(t) = -u_{ext2}(t) = 0.5 \cdot u_{ext}(t)$, the MZM is operated in push-pull mode. In this case, chirp-free amplitude modulation can be obtained. And $E_{out}(t)$ can be expressed as

$$E_{out}(t) = E_{in}(t) \cdot \cos\left(\frac{\varphi_1(t) - \varphi_2(t)}{2}\right) = E_{in}(t) \cdot \cos\left(\frac{u_{ext}(t)}{2V_\pi}\pi\right), \tag{3.11}$$

with $V_{\pi 1} = V_{\pi 2 = V_\pi}$. By squaring Eq.(3.11), the power transfer function of the MZM can be obtained :

$$\frac{P_{out}(t)}{P_{in}(t)} = \frac{1}{2} + \frac{1}{2} \cdot \cos\left(\varphi_1(t) - \varphi_2(t)\right) = \frac{1}{2} + \frac{1}{2} \cdot \cos\left(\frac{u_{ext}(t)}{V_\pi}\pi\right) \tag{3.12}$$

3.1.4. Optical IQ Modulator

The optical IQM can be composed of a PM and two MZMs, which is commercially available in an integrated form [25]. As we can see from Figure 3.7, the incoming light is equally split into two arms namely the in-phase (I) and the quadrature (Q) arm. A field amplitude modulation can be performed by operating the MZM in the push-pull mode in both arms. Furthermore, a relative phase shift of $\pi/2$ is adapted in one arm, for instance by an additional PM. With this method any constellation point can be reached in the complex IQ-plane. Within the IQM, the induced phase differences of the MZMs in the upper and lower paths can be given by

$$\Delta\varphi_I(t) = \frac{u_I(t)}{V_\pi}\pi, \tag{3.13}$$

$$\Delta\varphi_Q(t) = \frac{u_Q(t)}{V_\pi}\pi. \tag{3.14}$$

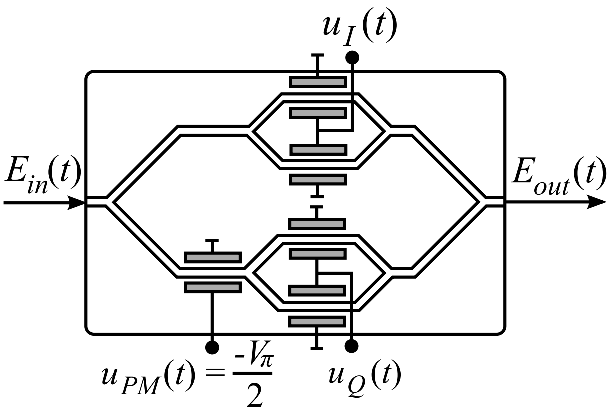

Figure 3.7.: Integrated optical IQ modulator

When any insertion loss is neglected and the driving voltage of the PM is set to $u_{PM}(t) = -V_\pi/2$, the field transfer function of the IQM can be written as [17]

$$\frac{E_{out(t)}}{E_{in}(t)} = \frac{1}{2}\cos\left(\frac{\Delta\varphi_I(t)}{2}\right) + j\frac{1}{2}\cos\left(\frac{\Delta\varphi_Q(t)}{2}\right) \tag{3.15}$$

Applying Eq.(3.13), Eq.(3.14) and Eq.(3.15), the amplitude modulation $a_{IQM}(t)$ and phase modulation $\varphi_{IQM}(t)$, performed by the $\varphi_{IQM}(t)$, can be given by [17]

$$a_{IQM}(t) = \left|\frac{E_{out(t)}}{E_{in}(t)}\right| = \frac{1}{2}\sqrt{\cos^2\left(\frac{u_I(t)}{2V_\pi}\pi\right) + j\cos^2\left(\frac{u_Q(t)}{2V_\pi}\pi\right)}, \tag{3.16}$$

$$\varphi_{IQM}(t) = \arg\left\{\cos\left(\frac{u_I(t)}{2V_\pi}\pi\right), \cos\left(\frac{u_Q(t)}{2V_\pi}\pi\right)\right\}. \tag{3.17}$$

Noting that the $\arg\{\}$ operation denotes the calculation of the angle of a complex value from the real and imaginary parts in the range $[-\pi;\pi]$.

3.1.5. Pulse Carvers and Impulse Shapers

The overall performance of optical transmission systems strongly depends on the shape of the transmitted optical pulses. For the commercial available systems, non-return to zero (NRZ) can be considered as a standard pulse shape. Thereby, a pulse filling the entire bit slot is transmitted for all symbols with non-zero power, and the power does not always go to zero when passing one symbol to another.

By contrast, in the case of return to zero (RZ) pulses, the optical power goes to zero within each symbol period. Hence, the power is smaller during the symbol transitions. Moreover, the undesired frequency modulation arising during the phase transitions cannot take effect or is at least reduced, depending on the optical pulse width and the rise time of the electrical driving signals. Optical signal with RZ pulse shape can be realized in the optical domain by applying an extra optical pulse carver. For generating RZ pulses with a duty cycle of 50%, the field transfer function of the *optical RZ pulse carver* can be given by [17]

$$\frac{E_{out}(t)}{E_{in}(t)} = cos\left[\frac{\pi}{4}\cdot\sin\left(2\pi\frac{t}{T_s}-\frac{\pi}{2}\right)-\frac{\pi}{4}\right]. \tag{3.18}$$

Even though the pulse shape with realized with the pulse carver in the optical domain, the optical pulse form depends also on the shape of the electrical driving signals, which can be formed by electrical impulse shapers (IS) before feeding into the modulator driving electrodes. For the electrical pulse generation without overshoots and with a specified rise, a rectangular input time function must be filtered by a non-causal linear time invariant filter with Gaussian shaped impulse response.

$$h(t) = \frac{2}{\sqrt{\pi}T_s}\cdot\exp\left(-\left(\frac{2t}{T_e}\right)^2\right). \tag{3.19}$$

The convolution of the rectangular signal with the impulse response $h(t)$ results in the output pulse of the IS and can be given by [17]

$$p(t) = \frac{1}{2}\left[\operatorname{erfc}\left(\frac{2(t-Ts)}{T_e}\right)-\operatorname{erfc}\left(\frac{2t}{T_e}\right)\right]. \tag{3.20}$$

As we can see from Eq.(3.19) and Eq.(3.20), T_e is the filter time constant, which can be approximately related to the electrical rise time Δt as [17]

$$\Delta t \approx \frac{3}{4}T_e, \tag{3.21}$$

assuming that the symbol time T_s is much longer than T_e.

3.2. Receiver Components

In this section, the key components like optical and electrical filters (3.2.1) and 2 x 4 90° hybrid (3.2.2) are briefly described. For coherent receivers, lasers (see 3.1.1) are also required.

3.2.1. Optical and Electrical Filter

Like in other transmission systems, filters are crucial and multi-purpose components for optical transmission systems, especially at the receiver side. The noise bandwidth can be limited with optical band-pass filters for improving receiver sensitivity. Furthermore, the optical band-pass filters can separate optical channels in WDM. In the electrical domain, low-pass filters can be performed to achieve a further noise reduction.

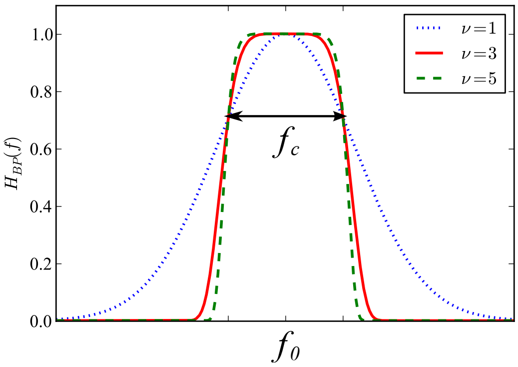

Figure 3.8.: Transfer function of Gaussian band-pass filter for various ν

On the one hand, for ideal filters, all frequencies inside the pass-band can be transmitted without any distortion and frequencies inside the stop-band must be completely rejected [26]. On the other hand, assuming the ideal filter as a matched filter the output signal to noise ratio can be maximized [27].

For the simulation of optical transmission systems, optical band-pass filter are often modeled as non-causal Gaussian filters with Gaussian amplitude and real-valued transfer function. The transfer function of a Gaussian optical band-pass filter $H_{BP}(f)$ can be given by

$$H_{BP}(f) = \cdot\exp\left(-\frac{\ln(2)\cdot 2^{2\nu}}{2(2\pi f_c)^{2\nu}}(2\pi(f-f_0))^{2\nu}\right), \tag{3.22}$$

where ν is the filter order, f_0 the center frequency and f_c the 3dB bandwidth.

Since Bessel filters can be physically implemented and can exhibit a linear phase response and excellent step response with minimal overshoot and ringing, electrical filters are often modeled as Bessel filters. The normalized transfer function of an Bessel low-pass filter can be given by

$$H_{TP}(S) = \frac{B_\nu(S=0)}{B_\nu(S)}, \tag{3.23}$$

$$S = j2\pi f\tau_{gr0} \tag{3.24}$$

where τ_{gr0} is group delay for $f = 0$. The polynomials $B_\nu(S)$ can be written as [28]

$$B_1(S) = 1 + S \tag{3.25}$$

$$B_2(S) = 3 + 3S + S^2 \tag{3.26}$$

$$B_\nu(S) = (2\nu - 1) \cdot B_{\nu-1}(S) + S^2 \cdot B_{\nu-2}(S). \tag{3.27}$$

The 3dB bandwidth f_c of the electrical Bessel low-pass filter is related to the group delay τ_{gr0} and can be given by

$$f_c = \frac{1.3616}{2\pi\tau_{gr0}}. \tag{3.28}$$

For a higher filter order, f_c can be approximately calculated as

$$f_c \approx \frac{\sqrt{(2\nu - 1) \cdot \ln 2}}{\tau_{gr0}}, \nu \geq 3. \tag{3.29}$$

3.2.2. 2 x 4 90° Hybrid

Since photodiodes can only detect the power of light signal, an additional component is necessary for the detection of phase information. With the 2 x 4 90° hybrid, the detection of the in-phase and quadrature components of the optical signal is enabled. It is used for coherent receivers to demodulate the signal light with the LO light and for direct detection receivers to convert the phase difference information into intensity information. Two incoming optical signals of a 2 x 4 90° hybrid can be defined as

$$E_{in_1}(t) = |E_{in_1}(t)| \cdot \exp\left(j\phi_1(t)\right), \tag{3.30}$$

$$E_{in2}(t) = |E_{in2}(t)| \cdot \exp\left(j\phi_2(t)\right). \tag{3.31}$$

At the four hybrid outputs ($n = 0, 1, 2, 3$), the following output powers can be achieved [17]:

$$\begin{aligned} P_{out_n}(t) &= E_{out_n}(t) \cdot E^*_{out_n}(t) \\ &= \frac{1}{4}\left|E_{in_1}(t)\right|^2 + \frac{1}{4}\left|E_{in2}(t)\right|^2 + \\ &\quad \frac{1}{2}\left|E_{in_1}(t)\right| \cdot \left|E_{in2}(t)\right| \cdot \cos\left(\phi_1(t) - \phi_2(t) - n \cdot 90^\circ + \psi\right), \end{aligned} \tag{3.32}$$

to enable the detection of the in-phase and quadrature components. Since the initial phase of the input signals are arbitrary, the phase shift ψ in Eq.(3.32) is allowed to be arbitrary.

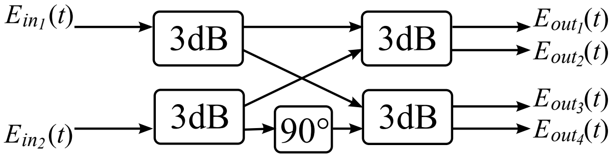

Figure 3.9.: Example for implementation of 2 x 4 90° hybrid

The quadrature property can be exploited to detect the in-phase and quadrature components of high-order modulation signals. Moreover, it can be performed for the implementation of the special coherent receivers such as the phase diversity receiver [29], the image-rejection receiver [30] and receivers with optical phase locked loop [31, 32].

Assuming a lossless device with ideal uniformity, with the transfer function of 2 x 4 90° hybrid, the output power from Eq.(3.32) can be given by

$$\begin{bmatrix} E_{out_1}(t) \\ E_{out_2}(t) \\ E_{out_3}(t) \\ E_{out_4}(t) \end{bmatrix} = \frac{1}{2} \cdot \begin{bmatrix} e^{j\psi_{11}} & e^{j\psi_{12}} \\ e^{j\psi_{21}} & j \cdot e^{j\psi_{22}} \\ e^{j\psi_{31}} & -e^{j\psi_{32}} \\ e^{j\psi_{41}} & -je^{j\psi_{42}} \end{bmatrix} \cdot \begin{bmatrix} E_{in_1}(t) \\ E_{in_2}(t) \end{bmatrix} \tag{3.33}$$

where the following conditions must be satisfied :

$$\psi_{11} - \psi_{12} = \psi_{21} - \psi_{22} = \psi_{31} - \psi_{32} = \psi_{41} - \psi_{42} = \psi. \tag{3.34}$$

Due to the fact that the difference of the relative phase shifts of added input fields at the four outputs is n time 90°, this component is denoted as a 90° hybrid.

In [33], different implementation of 2 x 4 90° hybrid and its practical feasibility are in-depth discussed. Figure 3.9 illustrates an option for the implementation of the hybrid. The implementation is a composition of four 3dB couplers and an additional phase shifter in one branch. When setting the phase shift in the lower branch to 90° and using the inputs and outputs as defined in Figure 3.9, the transfer function is equal to Eq.(3.33) with $\psi = 0$ [33]. The configuration should be implemented in an integrated form to achieve sufficient IQ balance. A version on $LiNbO_3$ is analyzed and discussed in [34]. The device is commercially available [25].

3.2.3. Delay Line Interferometer

A delay line interferometer (DLI) is the key component for the phase information detection for an optical direct detection. Figure 3.10 shows the structure of DLI. Firstly, the incoming light wave is split into two branches by a 3dB coupler. In one branch, the optical signal is delayed by T_s. In another branch, a phase shift of φ_{DPI} is applied. Afterwards, the optical signal is recombined with a second 3dB coupler. The output signals from the first 3dB coupler can be given by [17]

$$\begin{bmatrix} \tilde{E}_{out_1}(t) \\ \tilde{E}_{out_2}(t) \end{bmatrix} = \frac{1}{2} \begin{bmatrix} 1 & j \\ j & 1 \end{bmatrix} \cdot \begin{bmatrix} E_{in_1}(t) \\ E_{in_2}(t) \end{bmatrix} \tag{3.35}$$

From Eq.(3.35), it can be seen that the relative phase rotation of 90° is applied on the output signal for the upper branch of 3dB coupler and the phase rotation of −90° for lower branch.

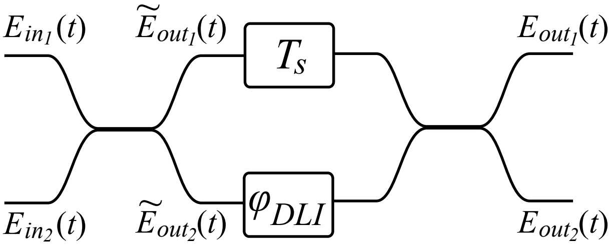

Figure 3.10.: Structure of delay line interferometer

Hence, the 3dB coupler is often denoted as 180° hybrid. With neglecting the phase shift within the interferometer, the output signals from DLI are

$$E_{out_1}(t) = \frac{1}{2} \cdot E_{in_1}(t - T_s) - \frac{1}{2} E_{in_1}(t) \cdot \exp\left(j\varphi_{DLI}\right), \tag{3.36}$$

$$E_{out_2}(t) = j\frac{1}{2} \cdot E_{in_1}(t - T_s) + j\frac{1}{2} E_{in_1}(t) \cdot \exp\left(j\varphi_{DLI}\right). \tag{3.37}$$

3.3. Transmitter Design

Generally, the transmitter design depends on the modulation formats. Although the number of the feasible modulation formats is immense, in this dissertation we focus on the three most promising modulation formats for optical transmission systems. They are phase shift keying (PSK) [35], amplitude-phase shift keying (ASK-PSK) [36] and quadrature amplitude modulation (QAM) [37].

3.3.1. Multi-Level Signaling

Denoting that $\{b_{1_k}, b_{2_k}, ..., b_{m_k}\}$ are data bits for the signal with higher order modulation format. For the signal generation, the data bits must be collected and mapped to the complex symbol b_k. Each symbol b_k can be interpreted as a complex number with the given phase and can be depicted in the in-phase b_k^i and quadrature b_k^q components with

$$b_k = b_k^i + jb_k^q. \tag{3.38}$$

The alternative description of b_k can be given as the amplitude and phase state with

$$a_{b_k} = \sqrt{{b_k^i}^2 + {b_k^q}^2}, \tag{3.39}$$

$$\varphi_{b_k} = \arg\left\{b_k^i, b_k^q\right\}. \tag{3.40}$$

Denote that the integer k in range of 1 to ∞. One of the $M = 2^m$ symbols is assigned to each symbol interval of the length $T_s = m \cdot T_b$, where $r_b = 1/T_b$ is the data rate, and T_b is bit duration. The assignment of respective combinations of m bits to symbols with particular amplitude and phase states is defined as a so-called *constellation diagram*. Bit mapping should be arranged for the optimal optical signal to noise ratio (OSNR) performance so that only one bit per symbol differs from a neighboring symbol (Gray coding). The symbols are transmitted on the symbol rate $r_S = 1/T_s = r_b/m$.

3.3.2. Differential Encoding

For the carrier synchronization especially carrier phase estimation, phase ambiguity and cycle-slip [38] problems cannot be completely avoided. With differential encoding/decoding and phase unwrapping (see Section 6.6 and 6.7), the problems can be simply solved with a minimal implementation complexity. Unfortunately, the differential encoding/decoding induces a performance penalty, which depends on the modulation format. The penalty is inversely proportional to the order of the modulation format m [39]. This part briefly describes the differential encoding for higher-order modulation formats in optical transmitters. For the data recovery from the differential encoded bit-sequence, a differential decoder at the receiver side is required. This can be simply realized by reverse function of the according differential encoder.

For the simplification of the description, we define A_k as integer representation of a complex symbol b_k. Table 3.2 shows the mapping between the integer representation A_k and the data bits b_{1_k}, b_{2_k} for $m = 2$ and Table 3.3 for $m = 3$.

Table 3.2.: Mapping between integer representation A_k and data bits b_{1_k}, b_{2_k} for $m = 2$

A_k	b_{1_k}	b_{2_k}
0	0	0
1	0	1
2	1	1
3	1	0

Table 3.3.: Mapping between integer representation A_k and data bits b_{1_k}, b_{2_k} and b_{3_k} for $m = 3$

A_k	b_{1_k}	b_{2_k}	b_{3_k}
0	0	0	0
1	0	0	1
2	0	1	1
3	0	1	0
4	1	1	0
5	1	1	1
6	1	0	1
7	1	0	0

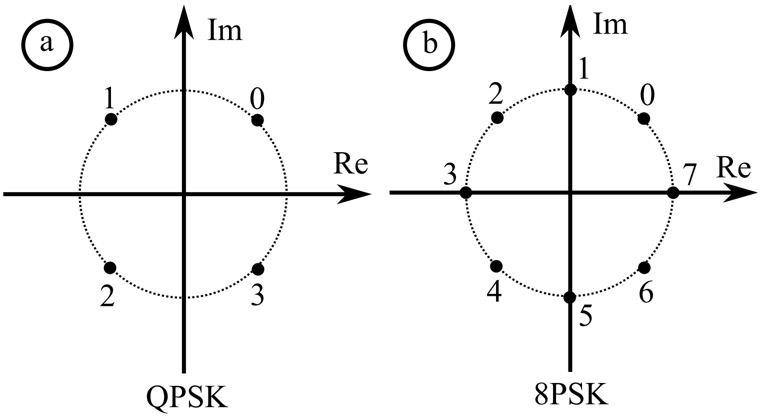

Figure 3.11.: Constellation diagram of M-PSK signal with integer representation A_k on complex coordination a) for $m = 2$ (QPSK) b) for $m = 3$ (8-PSK)

For M-PSK modulation formats, Figure 3.11 depicts the relation between the integer representation A_k and the data symbol b_k on the complex constellation diagram. The relation can be mathematically expressed as

$$b_k = \sqrt{P_s} \cdot \exp\left(j\left(\frac{2\pi A_k}{M} + \frac{\pi}{4}\right)\right). \tag{3.41}$$

The differential integer representation A_{d_k} at the transmitter side can be calculated by

$$A_{d_k} = \left(A_{d_{k-1}} + A_k\right) \ \mathrm{mod}\ M, \tag{3.42}$$

where mod is the modulus operation. At the receiver side, the differential decoding can be given by

$$A_k = \left(A_{d_k} + A_{d_{k-1}} + M\right) \ \mathrm{mod}\ M. \tag{3.43}$$

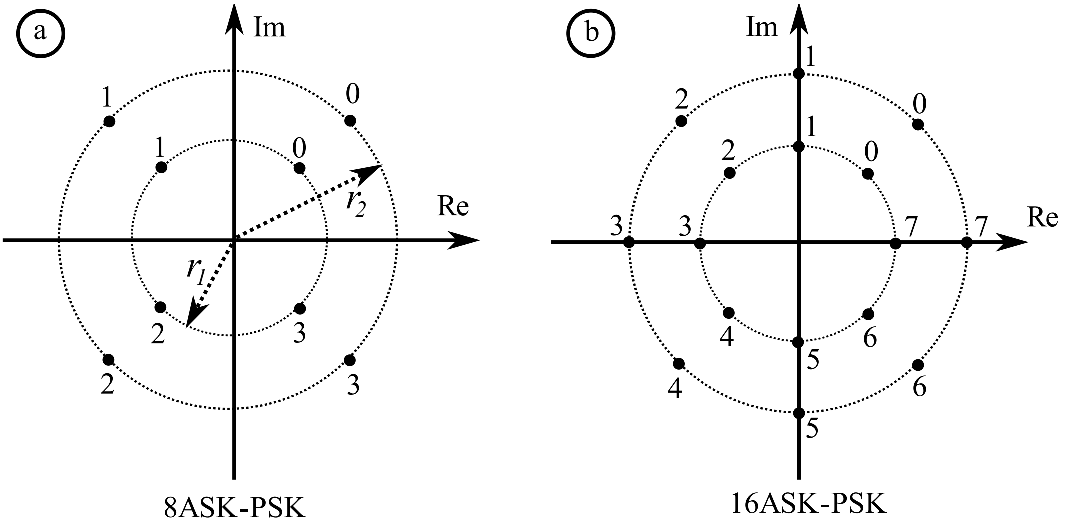

Figure 3.12.: Constellation diagram of ASK-PSK signal with integer representation A_{PSK_k} on complex coordination a) for $m = 3, m_{ASK} = 1, m_{PSK} = 2$ (8-ASK-PSK) b) for $m = 4, m_{ASK} = 1, m_{PSK} = 3$ (16-ASK-PSK)

For the initial value, $A_{d_{k=0}}$ can take an arbitrary value from the interval $[0; M-1]$. Afterwards, A_{d_k} can be mapped to the differential data bit d_{1_k} and d_{2_k} using Table 3.2 for $m = 2$ and Table 3.3 for $m = 3$. The described method for differential encoding can be scaled up for arbitrary M-PSK modulation formats using the according mapping tables between A_k and b_{n_k} or A_{d_k} and d_{n_k} respectively, with $n \in \{1, 2, ..., m\}$.

For M-ASK-PSK modulation formats, the information can be represented by the amplitude and the phase of the carrier signal as shown in Figure 3.12. However, for the differential encoding against phase ambiguity, it is sufficient to differentially encode only the phase information. For the approach, the data bits must be separated into the amplitude shift keying (ASK) bits and the PSK bits.

We define the number of the ASK bits as m_{ASK} and the PSK bits as m_{PSK} with $m = m_{ASK} + m_{PSK}$. The number of the ASK symbols and PSK symbols can be expressed as

$$M_{ASK} = 2^{m_{ASK}}, M_{PSK} = 2^{m_{PSK}}, M = M_{ASK} \cdot M_{PSK} \tag{3.44}$$

Moreover, we can separate the integer representation A_k into an ASK integer representation A_{ASK_k} and PSK integer representation A_{PSK_k}. The relation between b_k, A_{ASK_k} and A_{PSK_k} can be defined as

$$b_k = a_{b_k} \cdot \exp\left(j\left(\frac{2\pi A_{PSK_k}}{M_{PSK}} + \frac{\pi}{4}\right)\right), \tag{3.45}$$

where $a_{b_k} \in \{r_1, r_2, ..., r_{M_{ASK}}\}$ is amplitude of the symbol b_k as shown in Eq.(3.39). With the separation, the differential integer representation for the PSK signal can firstly be calculated by

$$A_{PSK,d_k} = \left(A_{PSK,d_{k-1}} + A_{PSK_k}\right) \bmod M_{PSK}. \tag{3.46}$$

The initial value $A_{PSK,d_{k=0}}$ can take the arbitrary value from interval $[0; M_{PSK}-1]$. Afterwards, the differential integer representation for ASK-PSK is given by

$$A_{d_k} = A_{ASK_k} \cdot M_{PSK} + A_{PSK,d_k}, \tag{3.47}$$

with $A_{ASK_k} \in [0; M_{ASK} - 1]$. Like differential encoding for M-PSK, the mapping between A_{d_k} and d_{n_k} can be realized by the mapping tables. Furthermore, the order of the modulation format can be scaled up using the according mapping tables.

For M-QAM modulation formats, the information is modulated into the in-phase and quadrature amplitude. Hence, the phase difference of the neighbor symbols is not constant like PSK. And ASK-PSK and the described differential encoding/decoding, which is designed for PSK based modulation formats, cannot be directly applied. However, we can separate the constellation diagram of M-QAM into two sub-constellations for the differential encoding against the phase ambiguity [40]. The first sub-constellation represents the quadrant of the signal, and we define the integer representation in this sub-constellation as A_{1_k}. In the second sub-constellation, the integer representation is defined as A_{2_k}, and the mapping of the symbol to the integer representation must be robust against the phase ambiguity. Hence, the second sub-constellation always has the phase shift of 90° to the neighbor sub-constellation as shown in Figure 3.13. With the separation of the constellation, we can apply the differential encoding

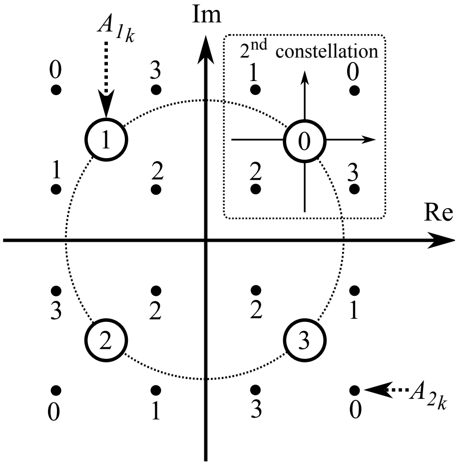

Figure 3.13.: Constellation diagram of 16QAM signal with integer representation A_{1_k} for quadrant constellation and A_{2_k} for second constellation on complex coordination

on the quadrant constellation by

$$A_{d1_k} = \left(A_{d1_{k-1}} + A_{1_k}\right) \mod 4, \tag{3.48}$$

where the initial value $A_{d1_{k=0}}$ can take the value from $\{0, 1, 2, 3\}$. And the differential encoding for M-QAM at the transmitter side can be calculated by

$$A_{d_k} = A_{d1_k} \cdot \frac{M}{4} + A_{2_k}. \tag{3.49}$$

At the receiver side, the differential decoding can be given by

$$A_k = \left(A_{d1_k} - A_{d1_{k-1}} + 4\right) \mod 4, +A_{2_k}. \tag{3.50}$$

Afterwards, A_{d_k} is mapped to the Gray-coding bit-sequence. The method can be scaled up to the arbitrary M-ary QAM modulation formats using an appendent mapping for A_{2_k}.

3.3.3. Higher Modulation Transmitter

There are various possible configurations and designs for the signal generation at the transmitter side. In this section, we describe only a widely used configuration example for the particular modulation format. More detailed transmitter configurations can be found in [17].

Figure 3.14 illustrates an alternative for generating PSK signals with binary electrical driving signals using m consecutive PMs as shown in [17]. A binary phase shift keying (BPSK) signal can be obtained from the first PM. Afterwards, quadrature phase shift keying (QPSK) signal can be obtained from the second PM, and so on.

The data signal is first parallelized with a $1 : m$ demultiplexer in the electrical part of the transmitter. After the data signal demultiplexing, the data bits are fed into a differential

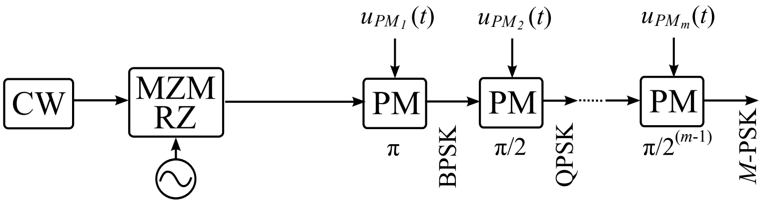

Figure 3.14.: PSK transmitter

encoder. As illustrated in Figure 3.14, the differential encoded data bits $\{d_{1_k}, d_{2_k}, d_{3_k}, ..., d_{m_k}\}$ are obtained and passed to IS and subsequently to the optical modulator. The optical output signal is given by [17]

$$\begin{aligned} E(t) \quad = \quad & \sqrt{P_s} \cdot \exp\left(j\left(2\pi f_s t + \varphi_s\right)\right) \cdot \exp\left(j\pi \frac{u_{PM_1}(t)}{V_\pi}\right) \\ & \cdot \exp\left(j\pi \frac{u_{PM_2}(t)}{V_\pi}\right) \cdot ... \cdot \exp\left(j\pi \frac{u_{PM_m}(t)}{V_\pi}\right). \end{aligned} \tag{3.51}$$

In Eq.(3.51), the binary electrical driving voltages $u_{PM_n}(t)$ can be given by

$$u_{PM_n}(t) = \frac{V_\pi}{2^{n-1}} \cdot \sum_k \left(d_{n_k} \cdot p(t - kT_s)\right), \tag{3.52}$$

where $p(t - kT_s)$ is output signal from IS as shown in Eq.(3.20) and $n \in \{1, 2, 3, ..., m\}$ the nth differentially encoded of a bit consisting of m bits in the kth symbol interval.

As shown in Figure 3.15, the transmitter configuration or ASK-PSK can be simply implemented, extending a PSK transmitter with an ASK component. For the ASK component, the data bits are directly passed to IS without the differential encoding. In contrast to the ASK bits, the PSK bits are differentially encoded and modulated like in the PSK transmitter. After the differential encoding, the signal is modulated in the optical domain with the MZM modulator. The output signal of the ASK-PSK transmitter can be written as

$$\begin{aligned} E(t) \quad = \quad & \sqrt{P_s} \cdot \exp\left(j\left(2\pi f_s t + \varphi_s\right)\right) \cdot \exp\left(j\pi \frac{u_{PM_1}(t)}{V_\pi}\right) \\ & \cdot \exp\left(j\pi \frac{u_{PM_2}(t)}{V_\pi}\right) \cdot ... \cdot \exp\left(j\pi \frac{u_{PM_{m-1}}(t)}{V_\pi}\right) \cdot \cos\left(\frac{u_{IM(t)}}{2V_\pi}\pi\right). \end{aligned} \tag{3.53}$$

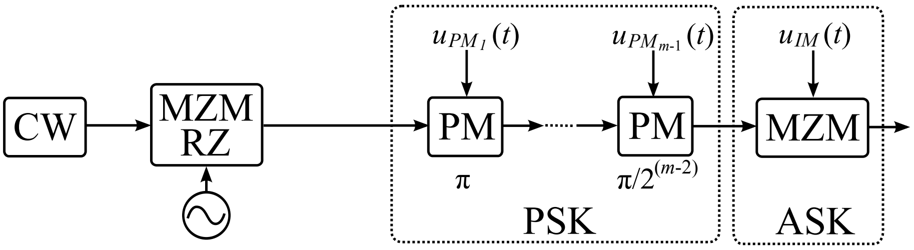

Figure 3.15.: ASK-PSK transmitter

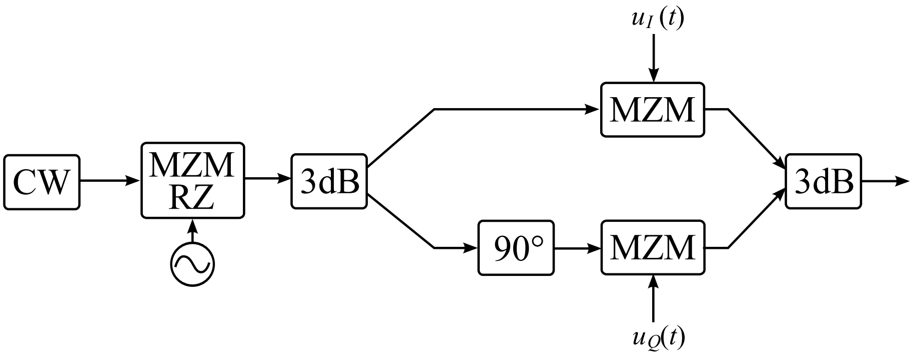

Figure 3.16.: QAM transmitter

For intensity modulation, the electrical driving signal can be given by

$$u_{IM}(t) = -\frac{2\arccos\left(\frac{r_1}{r_2}\right)}{\pi}V_\pi + \frac{2\arccos\left(\frac{r_1}{r_2}\right)}{\pi}V_\pi \cdot \sum_k \left(d_{m_k} \cdot p(t-kT_s)\right) \tag{3.54}$$

As shown in Figure 3.16, multi-level electrical driving signals are required for the signal generation for M-QAM modulation formats. Noting that the number of levels of the electrical driving signals is equal to the number of projections of the symbol that points to the I-axis and the Q-axis. The optical output signal for M-QAM modulation format can be given by

$$E(t) = \sqrt{P_s} \cdot \exp\left(j\left(2\pi f_s t + \varphi_s\right)\right) a_{IQM}(t) \cdot \exp\left(j\varphi_{IQM}(t)\right), \tag{3.55}$$

where a_{IQM} and φ_{IQM} are amplitude and phase modulation of IQM respectively (see 3.1.4). The in-phase and quadrature driving signals are multi-level and can be written as

$$u_I(t) = V_\pi + \frac{2V_\pi}{\pi} \cdot \sum_k \left[\arcsin(i_k) \cdot p(t-kT_s)\right], \tag{3.56}$$

$$u_Q(t) = V_\pi + \frac{2V_\pi}{\pi} \cdot \sum_k \left[\arcsin(q_k) \cdot p(t-kT_s)\right]. \tag{3.57}$$

The arcsin-function should be applied to the whole sum in both equations [41] for the ideal driving case.

3.4. Optical Direct Detection for Phase Modulated Signal

With DLI, it is possible to detect the phase information of the optical signal with the direct detection technique. However, the resulting signal is limited to M-ary differential phase shift keying (DPSK) modulation formats. The receiver with DLI can be extended with a photodiode to detect M-ary amplitude shift keying with differential phase shift keying (ASK-DPSK) modulation formats [17]. Thereby, the phase information can be detected with the DLI and the

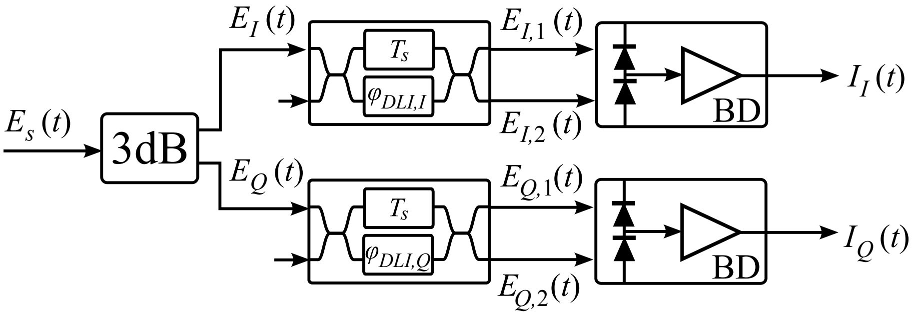

Figure 3.17.: Direct detection IQ receiver for M-DPSK modulation formats

amplitude information with the photodiode. Due to the nonlinear nature of the optical direct detection, the linear digital signal processing like linear equalization cannot be applied to the signal. Figure 3.17 illustrates the receiver with the direct detection technique for M-DPSK.

Firstly, the received signal $E(t)$ is split by a coupler for detection of the in-phase and quadrature components. Assuming 3dB couplers and taking the phase shifts of the couplers, two field components with a phase difference of 90° namely $E_I(t)$ and $E_Q(t)$ are obtained at the upper and the lower output of the coupler :

$$\begin{aligned} E_I(t) &= \frac{1}{2} \cdot a(t) \cdot \sqrt{P_s} \cdot \exp\left(j\left(2\pi f_s t + \varphi_s + \varphi(t) + \varphi_{n_s}(t) + 90^\circ\right)\right), && (3.58) \\ E_Q(t) &= \frac{1}{2} \cdot a(t) \cdot \sqrt{P_s} \cdot \exp\left(j\left(2\pi f_s t + \varphi_s + \varphi(t) + \varphi_{n_s}(t) + 180^\circ\right)\right). && (3.59) \end{aligned}$$

From Eq.(3.36) and (3.37), the electrical fields from the in-phase branch can be given by

$$\begin{aligned} E_{I,1}(t) &= \frac{1}{2} \cdot E_I(t - T_s) - \frac{1}{2} E_I(t) \cdot \exp\left(j\varphi_{DLI,I}\right), && (3.60) \\ E_{I,2}(t) &= j\frac{1}{2} \cdot E_I(t - T_s) + j\frac{1}{2} E_I(t) \cdot \exp\left(j\varphi_{DLI,I}\right). && (3.61) \end{aligned}$$

where $\varphi_{DLI,I}$ represents the phase shift of the DLI in the in-phase branch. Due to the detecting the fields as shown in Eq.(3.60) and Eq.(3.61), the two photocurrents within the balanced detectors (BD) can be written as

$$\begin{aligned} I_{I,1} &= R \cdot E_{I,1}(t) \cdot E^*_{I,1}(t) && (3.62) \\ I_{I,2} &= R \cdot E_{I,2}(t) \cdot E^*_{I,2}(t). && (3.63) \end{aligned}$$

In Eq.(3.62) and (3.63), the response of the photodiodes R is given by

$$R = \eta \frac{2\pi \cdot e}{h 2\pi f_s}, \tag{3.64}$$

with the Planck constant h= $6.63 \cdot 10^{-34}$J·s, the charge per electron e= $1.6 \cdot 10^{-19}$C, and η represents the quantum efficiency of the photodiode. After balanced detection, the photocurrent becomes

$$I_I(t) = I_{I,2}(t) - I_{I,1}(1). \tag{3.65}$$

Substituting the variables from Eq.(3.58), (3.59), (3.60), (3.61), (3.62) and (3.63) into Eq.(3.65), the photocurrent from the in-phase branch can be obtained as

$$I_I(t) = \frac{R}{4} \cdot P_s \cdot a(t) \cdot a(t - T_s) \cdot cos\left(\Delta\varphi(t) + \Delta\varphi_{n_s}(t) + \varphi_{DLI,I}\right). \tag{3.66}$$

The difference of the modulation phase of two consecutive symbols $\Delta\varphi(t)$, and the phase change due to laser phase noise at the DLI output $\Delta\varphi_{n_s}(t)$ are defined as

$$\Delta\varphi(t) = \varphi(t) - \varphi(t - T_s), \tag{3.67}$$

$$\Delta\varphi_{n_s}(t) = \varphi_{n_s}(t) - \varphi_{n_s}(t - T_s). \tag{3.68}$$

It should be noted that $\Delta\varphi_{n_s}(t)$ in Eq.(3.3) and (3.68) are the same variables with $\tau = T_s$. In the same manner, when performing the same calculations for the quadrature branch, the quadrature photocurrent can be written as

$$I_Q(t) = \frac{R}{4} \cdot P_s \cdot a(t) \cdot a(t - T_s) \cdot cos\left(\Delta\varphi(t) + \Delta\varphi_{n_s}(t) + \varphi_{DLI,Q}\right). \tag{3.69}$$

In Eq.(3.69), $\varphi_{DLI,Q}$ is the phase shift of DLI in the quadrature branch. Basically, choosing the phase shift of the DLI as $\varphi_{DLI,I} = 0°$ and $\varphi_{DLI,Q} = 90°$, the in-phase and quadrature components of arbitrary DPSK constellation can be obtained. Assuming that the laser phase noise can be neglected, the in-phase and quadrature photocurrents are

$$I_I(t) = \frac{R}{4} \cdot P_s \cdot a(t) \cdot a(t - T_s) \cdot \cos\left(\Delta\varphi(t)\right), \tag{3.70}$$

$$I_Q(t) = \frac{R}{4} \cdot P_s \cdot a(t) \cdot a(t - T_s) \cdot \sin\left(\Delta\varphi(t)\right). \tag{3.71}$$

3.5. Optical Coherent Detection

In the coherent receivers, all the information of the optical signal such as amplitude, frequency, phase and polarization can be transfered into the electrical domain. Hence, the demodulation can be performed completely in the electrical domain and the complexity for the optical components can be reduced. The further advantages of coherent receivers are possibilities for electronic compensation of transmission impairments and flexible tunable WDM receivers, with highly selective channel separation. Although the coherent receivers provide desired field parameters in the electrical domain, they require a controlled state of the remaining field parameters to evaluate the information on demand.

3.5.1. Coherent Detection Principle

Neglecting PolMux, the description of the coherent receiver for an in-phase component is illustrated in Figure 3.18. With this structure the received light wave signal can be transformed into the electrical domain.

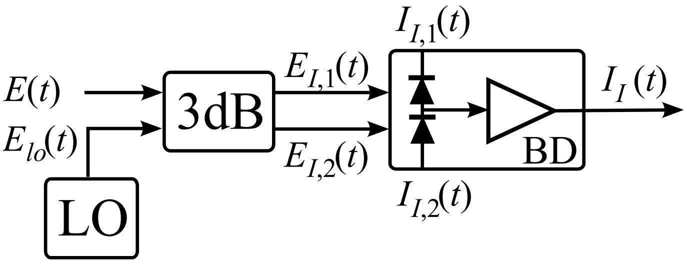

Figure 3.18.: Principle of coherent detection

Firstly, the optical information signal is interfered with the light of local oscillator (LO) laser before photo-detection, e.g. in a 3dB coupler. Afterwards, with the normalized electrical field of the received optical information, the signal can be written as

$$E(t) = \sqrt{P_s} \cdot \exp\left(j\left(2\pi f_s t + \varphi_s\right)\right) \cdot a(t) \cdot \exp\left(j\varphi(t)\right) \cdot \exp\left(j\varphi_{n_s}(t)\right) \tag{3.72}$$

and the CW light of the LO can be given by

$$E_{lo}(t) = \sqrt{P_{lo}} \cdot \exp\left(j\left(2\pi f_{lo} t + \varphi_{lo}\right)\right) \cdot \exp\left(j\varphi_{n_{lo}}(t)\right). \tag{3.73}$$

The variables in Eq.(3.72) and Eq.(3.73) are

- P_s, P_{lo} : CW power,
- f_s, f_{lo} : frequencies,
- φ_s, φ_{lo} : initial phases,
- $\varphi_{n_s}(t)$, $\varphi_{n_{lo}}(t)$: laser phase noise.

The resulting photocurrents within the balanced detector are [17]

$$\begin{aligned} I_{I,1}(t) &= \frac{1}{2}R \cdot (E_s + jE_{lo}) \cdot (E_s + jE_{lo})^* + i_{sh_1} \\ &= \frac{1}{2}R \cdot P_s \cdot a^2(t) + \frac{1}{2}R \cdot P_{lo} + i_{sh_1} + \\ &\quad R \cdot \sqrt{P_s P_{lo}} \cdot a(t) \cdot \sin\left(2\pi\Delta f t + \varphi_n(t) + \varphi_0 + \varphi(t)\right) \qquad (3.74) \\ I_{I,2}(t) &= \frac{1}{2}R \cdot (jE_s + E_{lo}) \cdot (jE_s + E_{lo})^* + i_{sh_2} \\ &= \frac{1}{2}R \cdot P_s \cdot a^2(t) + \frac{1}{2}R \cdot P_{lo} + i_{sh_2} - \\ &\quad R \cdot \sqrt{P_s P_{lo}} \cdot a(t) \cdot \sin\left(2\pi\Delta f t + \varphi_n(t) + \varphi_0 + \varphi(t)\right) \qquad (3.75) \end{aligned}$$

where i_{sh_1} and i_{sh_2} are the shot-noise photocurrents of the two photodiodes. The frequency offset Δf can be defined as

$$\Delta f = f_s - f_{lo}. \tag{3.76}$$

The overall laser phase noise $\varphi_n(t)$ and the initial phase offset φ_0 can be given by

$$\varphi_n(t) = \varphi_{n_s}(t) - \varphi_{n_{lo}}(t) \tag{3.77}$$

$$\varphi_0 = \varphi_s - \varphi_{lo}. \tag{3.78}$$

The overall laser phase noise $\Delta\varphi_n(t)$ within a time interval τ [42] can be written as

$$\Delta\varphi_n(t) = \varphi_n(t) - \varphi_n(t-\tau). \tag{3.79}$$

The variance of $\Delta\varphi_n(t)$ can be calculated as

$$\mathrm{Var}\left\{\Delta\varphi_n(t)\right\} = 2\pi\Delta\nu_{eff}|\tau|, \tag{3.80}$$

where $\Delta\nu_{eff}$ is the beat-linewidth and given by

$$\Delta\nu_{eff} = \Delta\nu_s + \Delta\nu_{lo}. \tag{3.81}$$

Since $P_s \ll P_{lo}$ and the first and second terms in Eq.(3.74) and Eq.(3.75) are equal, the output signal of the balanced photodiodes $I_I(t)$ can be given by

$$\begin{aligned} I_I(t) &= I_{I_1}(t) - I_{I_2}(t) && (3.82)\\ &= 2R\sqrt{P_sP_{lo}}\cdot a(t)\cdot \sin\left(2\pi\Delta f t + \varphi_n(t) + \varphi_0 + \varphi(t)\right) + i_{sh}. && (3.83) \end{aligned}$$

In Eq.(3.82), i_{sh} is overall shot-noise photocurrent after balanced detection and can be written as

$$i_{sh} = i_{sh_1} - i_{sh_2}. \tag{3.84}$$

The variance of i_{sh} can be given by

$$\mathrm{Var}\left\{i_{sh}\right\} = \mathrm{Var}\left\{i_{sh_1}\right\} + \mathrm{Var}\left\{i_{sh_2}\right\}, \tag{3.85}$$

assuming uncorrelated noise events of the two photodiodes.

3.5.2. Optical Quadrature Frontend

An optical quadrature frontend can be performed for the detection of in-phase and quadrature components. In the quadrature frontend, we can mix down the received signal with the LO light with a 2 x 4 90° hybrid (see Section 3.2.2). Afterwards, the balanced photodiodes can be applied to transfer the signal from the optical domain into the electrical domain as shown in Figure 3.19

From Eq.(3.33) and Eq.(3.34) with setting ψ to zero and neglecting phase shifts in both input fields, the output fields are

$$\begin{bmatrix} E_{out_1}(t) \\ E_{out_2}(t) \\ E_{out_3}(t) \\ E_{out_4}(t) \end{bmatrix} = \frac{1}{2}\cdot\begin{bmatrix} E_s(t) + E_{lo}(t) \\ E_s(t) + jE_{lo}(t) \\ E_s(t) - E_{lo}(t) \\ E_s(t) - jE_{lo}(t) \end{bmatrix}. \tag{3.86}$$

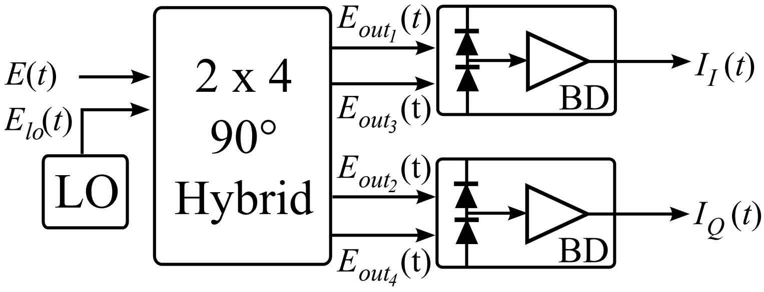

Figure 3.19.: Optical quadrature frontend for coherent detection

After detecting the output fields $E_{out_1}(t)$ and $E_{out_3}(t)$, and $E_{out_2}(t)$ and $E_{out_4}(t)$ with the upper and the lower balanced detector, the in-phase and quadrature photocurrents are obtained as

$$\begin{aligned} I_I(t) &= R \cdot E_{out_1}(t) \cdot E^*_{out_1}(t) - R \cdot E_{out_3}(t) \cdot E^*_{out_3}(t) \\ &= R\sqrt{P_s P_{lo}} \cdot a(t) \cdot e_s \cdot e_{lo} \cdot \cos\left(2\pi\delta f + \varphi_n(t) + \varphi_0 + \varphi(t)\right) + i_{sh_I} \qquad (3.87) \\ I_Q(t) &= R \cdot E_{out_2}(t) \cdot E^*_{out_2}(t) - R \cdot E_{out_4}(t) \cdot E^*_{out_4}(t) \\ &= R\sqrt{P_s P_{lo}} \cdot a(t) \cdot e_s \cdot e_{lo} \cdot \sin\left(2\pi\delta f + \varphi_n(t) + \varphi_0 + \varphi(t)\right) + i_{sh_Q}, \qquad (3.88) \end{aligned}$$

where i_{sh_i} and i_{sh_q} are the overall shot-noise photocurrents in the in-phase and quadrature arms, respectively.

3.5.3. Digital Signal Processing

For receivers with coherent detection, digital signal processing (DSP) is required to recover the data information. Due to the coherent technique, the polarization information of the signal can also be transferred into the electrical domain and PolMux can be utilized. Figure 3.20 illustrates the PolMux coherent receiver with DSP. With polarization beam splitters (PBS) and doubling of the optical quadrature frontend, polarization diversity can be implemented. The optical information signals are allowed to exhibit an arbitrary polarization state and are split proportionately to the power corresponding to the PBS reference directions. The LO must be polarized at 45° with respect to the PBS reference direction for even LO power splitting.

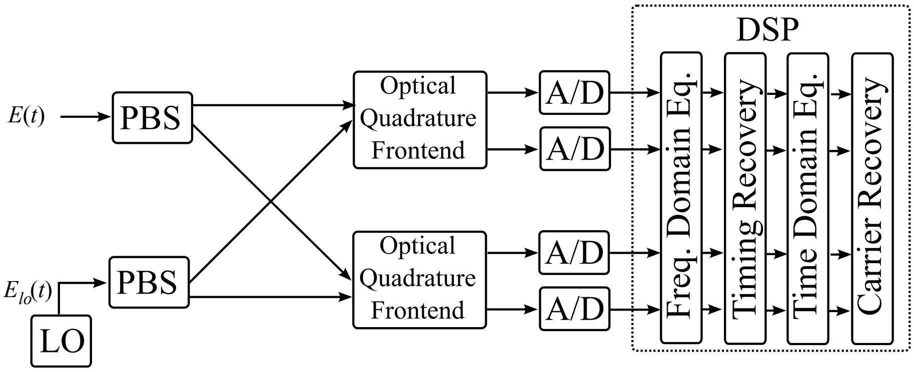

Figure 3.20.: Polarization multiplexed coherent receiver with DSP

Signal light then interferes with the LO light in both quadrature frontends with defined parallel polarization. The electrical signal from the quadrature frontends is digitized with analog digital converters (A/D) and fed into the DSP unit.

In the DSP, a frequency domain equalization can be applied for CD compensation and complexity reduction for the time domain equalization [43, 44, 45, 46]. Afterwards, the sample rate synchronization and the optimal sample time estimation can be performed with a timing recovery e.g., Gardner timing recovery [47], square timing recovery [48], Meuller & Mueller timing recovery [49], and histogram based timing recovery [50, 51]. The PMD and residual CD can be compensated with an adaptive time domain equalization, which is usually implemented with a finite impulse response (FIR) butterfly structure. The non-data-aided adaptation of the coefficients of the FIR filter can be implemented with the constant modulus algorithm (CMA) [52] or the decision directed least mean square (LMS) [53] algorithm. For the data-aided adaptation, CMA, LMS and minimum mean square error (MMSE) [54] are suitable algorithms. It is assumed that the frequency domain equalization the timing recovery and the time domain equalization can perfectly work, and the optimal sampled signal without channel linear distortion from the time domain equalization can be achieved.

Although many timing recovery algorithms can tolerate channel distortions like CD and PMD, we can relax the timing recovery by applying the frequency domain equalization before it. Moreover, the frequency domain equalization can operate without timing synchronization. In contrast for the time domain equalization, timing synchronization is required for channel estimation and filter coefficients adaptation. Since adaptation algorithms for time domain equalization like CMA, LMS can tolerate phase and frequency variations, and the most algorithms for carrier synchronization cannot operate in presence of the channel distortions, we apply the carrier recovery after the time domain equalization. As a consequence, the DSP is configured with the structure as shown in Figure 3.20. Due to the fact that many algorithms for the phase recovery are robust against the frequency offset with some limitations and the LO frequency offset in transmission systems with high qualitative lasers is small enough.

3.6. Loop Experiment

Due to the fact that, in the simulation, the particular effects in the transmission systems can be separated, most evaluations in this dissertation are based on Monte-Carlo simulation method [55] with the split-step Fourier method [56] for optical channel simulation. However, not all effects and impairments, which occur in the real world, can be simulated. Hence, in addition, experimental measurements were performed. Since the measurements in deployed systems are nearly impossible, loop experiments in the laboratory are necessary.

Figure 3.21 shows the setup for the loop experiment of dispersion managed links, which consist of the optical transmitter, the optical receiver and the fiber optic links. Due to the fact that the bandwidth of the electrical and optical components is limited, WDM [57] or optical time-division multiplexing (OTDM) [58] technique is applied to increase the transmission bandwidth.

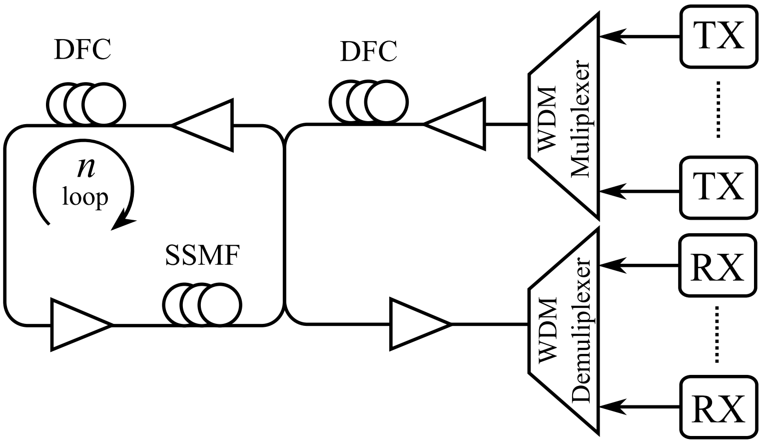

Figure 3.21.: Overview of loop experiment setup

Since in high bit-rate optical transmission systems, WDM has been so far preferred, the loop experiments in this dissertation are also based on the WDM technique. At the transmitter side, the light wave signal is firstly generated with the optical transmitter as described in Section 3.1 and 3.3. Afterwards, the signal is multiplexed into different optical wavelengths with the WDM-multiplexer. As an example, Figure 3.22 shows the power spectral density of the WDM 11x112GB/s PolMux QPSK with a channel spacing of 50GHz.

After the signal generating and multiplexing, the light wave signal is firstly amplified and then CD is pre-compensated with a DCF. In the loop, the signal will be amplified before feeding into the DCF or SSMF. Since the CD compensation for modulation formats based on direct detection like DPSK and on off keying (OOK) is limited and/or very complex [59, 60, 61], dispersion managed links have been so far preferred. For the in-line CD compensation, the CD management must be accurately designed in order to reduce the channel nonlinearities like SPM and XPM as shown in [62, 63]. Figure 3.23 shows an example for the CD management, which is mostly used for the simulation and the loop experiment in this dissertation.

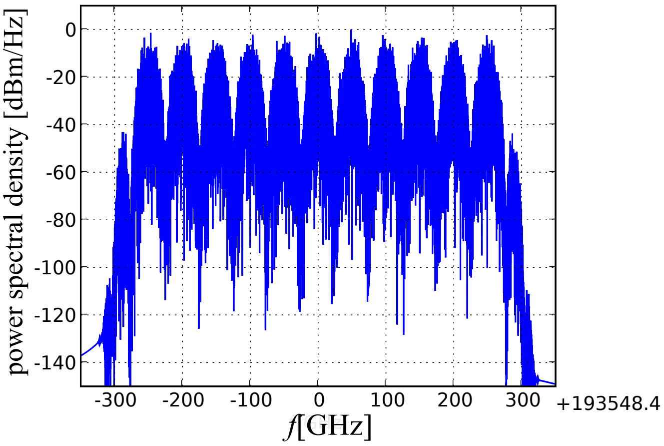

Figure 3.22.: Power spectral density of the WDM 11x112GB/s PolMux QPSK with a channel spacing of 50GHz

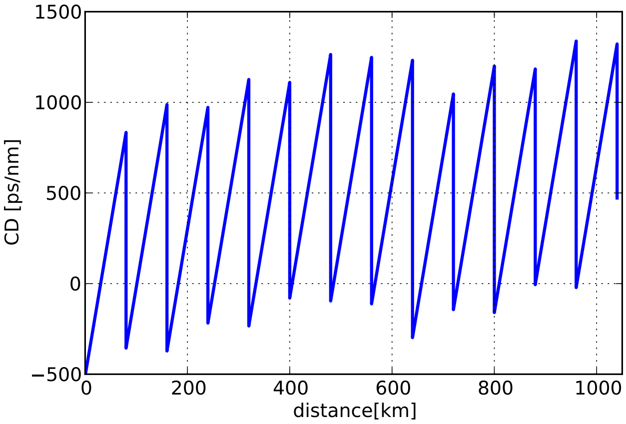

Figure 3.23.: An example for the design of the in-line chromatic dispersion management

In contrast to direct detection, in case of coherent detection, the channel linear distortions like CD and PMD can be simply compensated by DSP. Therefore, the importance of the in-line CD compensation can be decreased by applying coherent detection. Furthermore, it is shown in [64] that with none dispersion managed links (NDM), the channel nonlinearities can be reduced and hence the transmission performance can be improved. Since higher modulation formats induce more channel nonlinearity due to the higher peak-to-average power ratio (PAPR), the nonlinearity reduction applying NDM attracts more and more attention. However, most deployed transmission systems are based on the dispersion managed concept.

At the receiver side, the received wave-length multiplexed signal is firstly demultiplexed with an WDM- demultiplexer. Then the light wave signal is transformed into an electrical signal with the detection techniques as described in Section 3.4 or 3.5.

4. Basics for Carrier Synchronization

The estimation structures and principles for carrier synchronization are briefly described in this chapter. In Section 4.1, algorithms for carrier synchronization are classified. Since DSP can be implemented only with the parallelization of commercially available integrated circuits, the architecture for the parallelization is shown in Section 4.2. Although a perfect synchronization and estimation is usually desired, it is impossible to obtain such an estimation, and phase errors always occur. Section 4.3 shows performance degradations caused by phase error. In Section 4.4, a bit repetition estimation theory, which is the foundation of all algorithms for carrier synchronization, are derived and briefly described. For the derivation of the estimation algorithms, the probability density function (PDF) is important. However, the computation of the PDF can be very complex. Hence, the likelihood function is derived in Section 4.5 for convenience. In Section 4.6, the modified Cramér-Rao-Bounds (MCRB), a lower bound for the performance limit of the carrier phase and frequency estimation are derived. MCRB can be used as a reference for the performance evaluation of the estimator.

4.1. Classification of Synchronization Algorithms

Carrier synchronization algorithms can be classified by the criteria as shown in Figure 4.1. Each class of these carrier synchronization algorithms has benefits and drawbacks. To achieve the optimal performance, a suitable class of the carrier synchronization with respect to the application case should be selected.

4.1.1. Classification by Structure

Carrier synchronization algorithms can be grouped into feed-forward (FF) and feedback (FB) solutions structure by the structure criterion as shown in Figure 4.2. The characteristics of a carrier synchronization depend highly on its structure.

For the FF carrier synchronization, the estimation of the carrier phase is realized by FIR filter structure to avoid the feedback of the phase information. In contrast to conventional linear FIR filters, an additional nonlinear operation will be applied to extract the phase information from the modulated input signal. With the FF structure, the carrier synchronization can be simply parallelized with conventional parallelization architectures without any performance degradation. Hence, the FF structure is preferred for high-speed hardware implementation. In

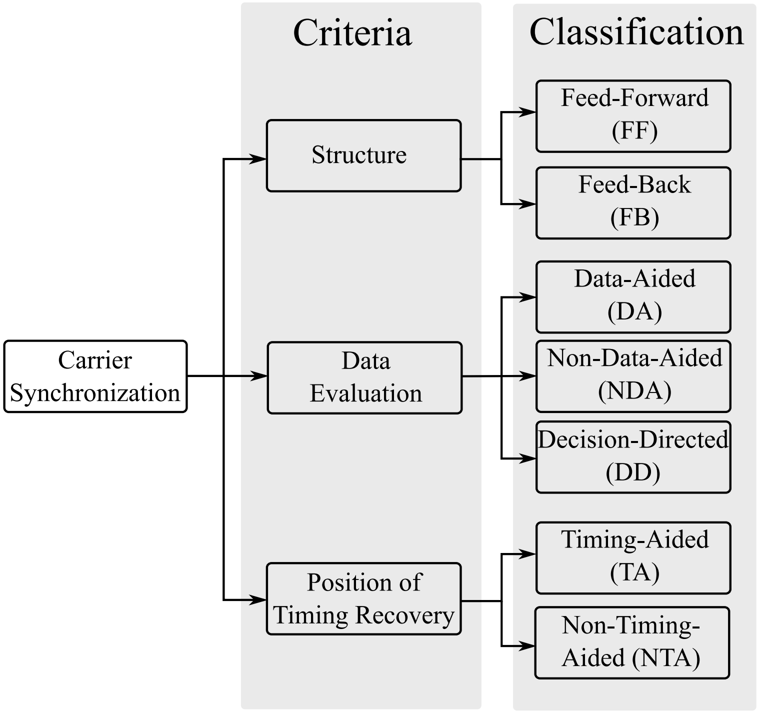

Figure 4.1.: Criteria and classification of carrier synchronization

feed forward estimation algorithms, input signals are generally segmented into blocks and the estimation is processed block by block. Without the corresponding between blocks, values of estimates are limited to a basic interval [65]. As a consequence, feed forward algorithms cannot follow the dynamics of the synchronization parameters and the phase ambiguity can occur. Therefore, a phase unwrapping is usually required for the carrier synchronization with an FF structure to suppress the cycle-slip probability and avoid the phase ambiguity.

In the carrier synchronization with the FB structure, an *error signal generator* will be applied to obtain direction of phase error, which can be defined as phase difference between the estimated phase and the actual phase. After generating the error signal, it will be fed back to the input of the phase estimation to improve the estimation in the next iteration. The most well-known carrier synchronization with the FB structure is the phase locked loop (PLL). The FB structure is comparable to the infinite impulse response (IIR) filter structure. However, the memory length of the carrier synchronization with the FB structure is much shorter than the conventional linear IIR filter due to the stability of the estimation [66]. The FB structure

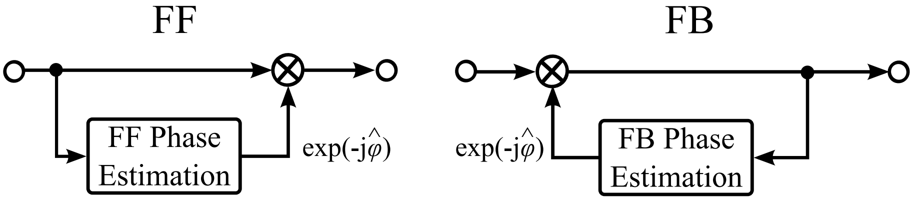

Figure 4.2.: Carrier synchronization classification by feed-forward (FF) and feed-back (FB) structures

provides typically an efficient estimation with a low implementation complexity in comparison to the FF structure. Furthermore, in FB algorithms, the probability for the cycle-slip is relative low without any additional signal processing like a phase unwrapping in FF algorithms. However, with the conventional hardware parallelization, the performance of the phase estimation with FB structure will be significantly degraded.

In high bit-rate optical transmission systems, the FF structure is preferred due to the necessary high-speed hardware implementation.

4.1.2. Classification by Data Evaluation

With the classification by data evaluation, the carrier synchronization can be grouped into decision-directed (DD), non-data-aided (NDA) and data-aided (DA). The DA carrier synchronization is an ideal method for the phase estimation. However, with the DA method, an additional framing synchronization [67] is required and the implementation complexity is increased. Moreover, the DA method in the FF structure has only limited advantages in comparison to DD and NDA for the suppression of the phase noise caused by laser linewidth, which is a random walk process as shown in section 3.1.1.

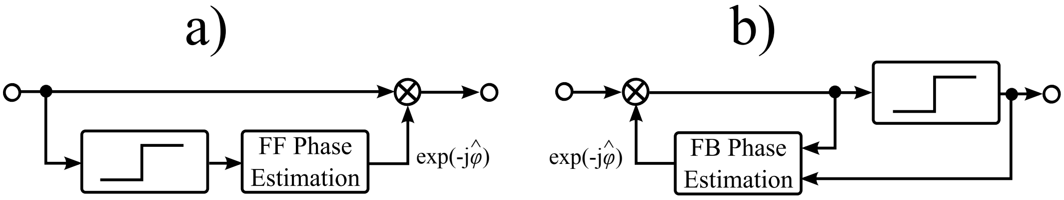

Figure 4.3.: Carrier synchronization with decision directed (DD) a) in feed-forward (FF) structure b) in feed-back (FB) structure

In transmission systems without training symbols, the data information can be estimated by a data symbol detector which can also be applied for the data recovery. We can use the data information from the symbol detector to improve estimation performance. The method with the data symbol detector is called *decision-directed* DD. Figure 4.3 shows the block diagram of carrier synchronization with DD for FF and FB structures. Due to the fact that the estimation accuracy of DD depends on the detector accuracy, the performance of the estimation with DD is limited in transmission systems with low signal to noise ratio (SNR). Since the FF structure with DD method can be simply implemented with a relative high performance, the widely-used algorithms in high-speed optical transmission systems for carrier synchronization are mostly based on this combination.

The worst case for the estimation is that no data information is available. The algorithms, which operate in this situation, are called the NDA estimators. The NDA estimators are applied in the transmission systems with low SNR, high distortion, or high disturbance.

It should be emphasized that carrier synchronization algorithms with the DD and NDA methods encounter the phase ambiguity problem in the FF and FB structures.

4.1.3. Classification by Position of Timing Recovery

With the position of the timing recovery, we can classify the carrier synchronization into timing-aided (TA) and none-timing-aided (NTA). Due to the implementation complexity and the performance, the carrier synchronization is usually performed after the timing recovery (TA). The incorrect timing synchronization can induce a noise enhancement for the carrier phase estimation and the SNR sensitivity can be thereby degraded or unstable. Furthermore, in the optical transmission system, the timing recovery should be applied before or together with the equalization due to the estimation performance. In [68], a joint timing synchronization and equalization with a significant performance improvement has been propose. Most carrier synchronization algorithms cannot be applied without the equalization from the channel distortions. Hence, the structure of DSP as shown in Section 3.5.3 is the standard configuration for the optical transmission systems. However, the timing synchronization and the carrier synchronization can be jointly applied as shown in [69, 70, 71, 72]. It should be noted that, in optical transmission systems, the joint timing and carrier synchronization are not widely used.

4.2. Parallelization Architecture

Since transmission rates in optical transmission systems are much higher than the clocking rates of commercially available integrated circuits, DSP can only be implemented using hardware parallelization. In Section 4.2.1, the interleaving hardware parallelization architecture is briefly described, which is a well-known architecture for the DSP in optical transmission systems. Due to the fact that the performance of carrier synchronization with feedback structure is strongly impaired using the interleaving architecture, carrier synchronization with feed forward structure have been preferred so far. However, the interleaving architecture is not mandatory for the hardware implementation. An alternative to the interleaving architecture is the Superscalar architecture as described in Section 4.2.2. In [73], the application of the Superscalar architecture for carrier synchronization in high bit-rate optical transmission systems is demonstrated by the

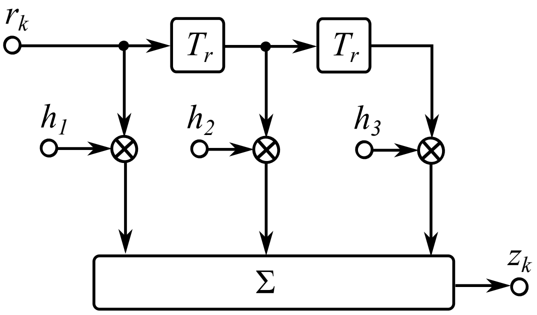

Figure 4.4.: Block diagram of FIR filter

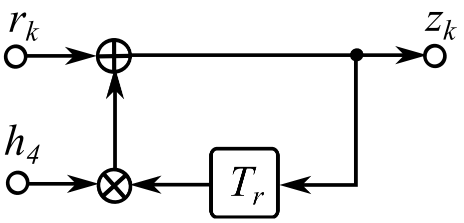

Figure 4.5.: Block diagram of IIR filter

author for the first time. In contrast to the interleaving architecture, carrier synchronization with feedback can be parallelized without performance loss using the Superscalar architecture.

As examples for DSP in parallelized hardware implementation, an FIR with three filter coefficients and an IIR filter with one filter coefficient as shown in Figure 4.4 and 4.5 respectively are given. The output signal from the given FIR filter can be written as

$$z_k = h_1 \cdot r_k + h_2 \cdot r_{k-1} + h_3 \cdot r_{k-2} \tag{4.1}$$

and from the given IIR filter

$$z_k = r_k + h_4 \cdot z_{k-1}. \tag{4.2}$$

It should be emphasized that the functionality of IIR filter in parallelized hardware implementation is usually limited. The limitations of IIR filter depends on the parallelization architecture and will be described in Section 4.2.1 and 4.2.2.

4.2.1. Interleaving Parallelization Architecture

In the interleaving parallelization architecture, the digitized input signal r_k is firstly demultiplexed in P parallelization paths with a serial to parallel converter (S/P). Afterwards, the demultiplexed signal is concurrently processed with the DSP and the out put signal from the DSP is fed into a parallel to serial converter (P/S) in order to multiplex the signal in the serial data flow. For further description of the parallelization architecture, we define the parallelization index p, and the processing iteration i, which can be given by

$$i = \lfloor k/P \rfloor, \tag{4.3}$$

where $\lfloor x \rfloor$ is the so called *floor function* and can be defined as

$$\lfloor x \rfloor = \max \{ n \in \mathbb{Z} | n \leq x \} . \tag{4.4}$$

According to Eq.(4.3), the signal sample index k can be calculated as

$$k = i \cdot P + p \tag{4.5}$$

In the first example, the FIR filter as shown in Figure 4.4 and described in Eq.(4.1) is parallelized. Figure 4.6 shows block diagram of the parallelized FIR filter with $P = 4$. As we can

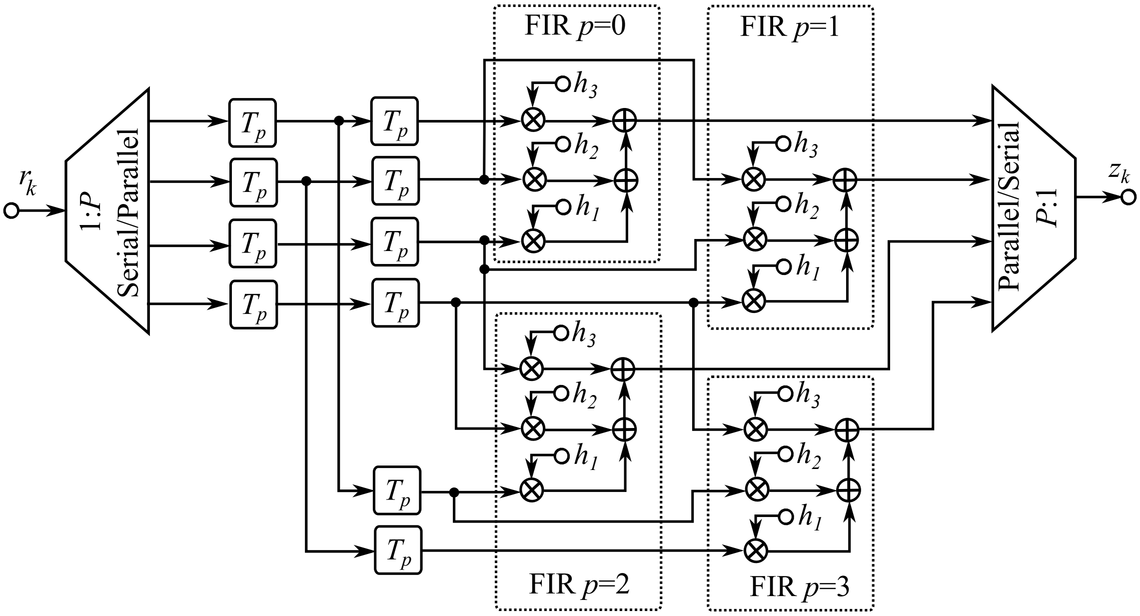

Figure 4.6.: Block diagram of FIR filter in interleaving parallelization

see from Figure 4.6 that 10 additional buffer units between S/P and FIR filter are required to cover memory length L_m= 3 of the FIR filter. It should be noted that the buffer units in Figure 4.6 entail a time delay of processing time in a processing iteration T_p instead of simpling time duration T_r as shown in Figure 4.4, where T_p can be calculated as

$$T_p = P \cdot T_r. \tag{4.6}$$

Although, the parallelization of a feed forward algorithm like a FIR filter from the example in Figure 4.6 is simple and straightforward, the parallelization of a feedback algorithm is complicated as mentioned in the following. For the parallelization of a feedback algorithm with

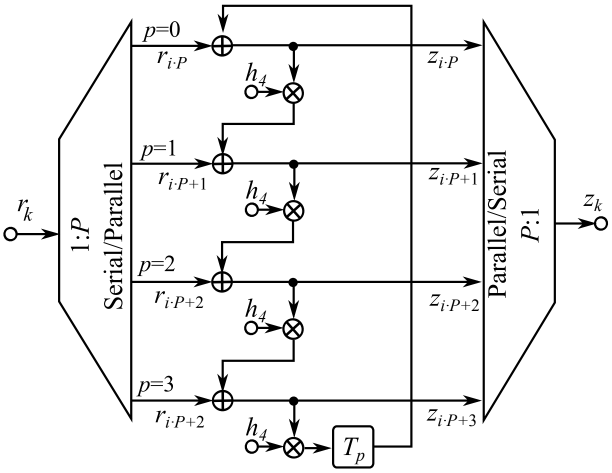

Figure 4.7.: Block diagram of IIR filter in interleaving parallelization *with* connection between parallelization paths regardless of processing time

interleaving architecture, two approaches can be applied.

Figure 4.7 shows block diagram of the first approach of interleaving parallelization with $P = 4$ for the IIR filter as shown in Figure 4.5 and described in Eq.(4.2). In this approach, output signal from each parallelization path is connected with the followed parallelization path. In the first processing iteration $i = 0$, the output signal can be calculated as followed

$$z_{k=0} = r_{k=0} \tag{4.7}$$

$$z_{k=1} = r_{k=1} + h_4 \cdot z_{k=0} \tag{4.8}$$

$$z_{k=2} = r_{k=2} + h_4 \cdot z_{k=1} \tag{4.9}$$

$$z_{k=3} = r_{k=3} + h_4 \cdot z_{k=2}. \tag{4.10}$$

Note that for the calculation of the initial output signal $z_{k=0}$ for IIR filter, $z_{k=-1}$ is not available and we have $z_{k=0} = r_{k=0}$. We define t_{mul} as processing time for multiplication and t_{add} as processing time for addition. For the calculation of $z_{k=4}$ in the next processing iteration $i = 1$, $z_{k=3}$ must be available. Since the calculation from $r_{k=0}$ to $z_{k=3}$ requires P multiplications and P additions, $z_{k=3}$ can be available in $i = 1$ only if

$$T_p \geq P \cdot (t_{mul} + t_{add}) \,. \tag{4.11}$$

Due to the fact that in commercially available hardware

$$t_{mul} \gg t_{add}, \tag{4.12}$$

Eq.(4.11) can be reduced to

$$T_p \geq P \cdot t_{mul} \tag{4.13}$$

Although, T_p in commercially available hardware can be adjusted, multiplication is an complex operation and roughly requires the maximum processing rate or minimum possible processing time $T_{p,min}$:

$$t_{mul} \approx T_{p,min} \tag{4.14}$$

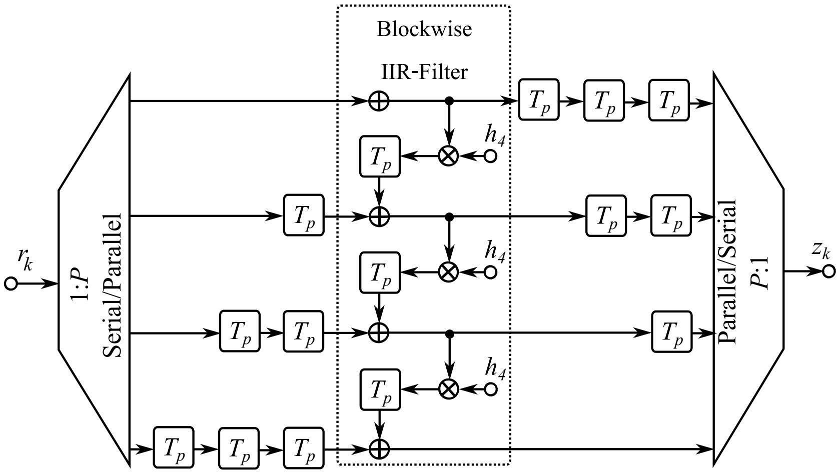

Figure 4.8.: Block diagram of blockwise IIR filter in interleaving parallelization *with* connection between parallelization paths

Assume that T_p is increased, for the given constant T_r, P must be also increased due to Eq.(4.6). According to Eq.(4.13) and Eq.(4.14), $z_{k=3}$ can be achieved after $4 \cdot t_{mul} \approx 4 \cdot T_{p,min}$. Hence, $z_{k=3}$ from $p = 3$ cannot be fed back into $p = 0$ for $z_{k=4}$ within T_p under the assumption of Eq.(4.14). Hence, the feedback between parallelization paths must be omitted and the IIR filter in Eq.(4.2) must be reduced to *a blockwise IIR filter*, whose impulse response can be given by

$$z_k = r_k + h_4 \cdot z_{k-1} \text{ with } k \in [0; P-1]. \tag{4.15}$$

Figure 4.8 shows the block diagram of blockwise IIR filter in interleaving parallelization with connection between parallelization paths. Buffer units prior to addition is designed in order to wait for the output signal from the previous parallelization path. Moreover, buffer units between the blockwise IIR filter and P/S are also required to avoid signal block mismatching by signal multiplexing. Consequently the number of required buffer units N_{buff} for this approach can be given by

$$N_{buff} = P^2 - P, \tag{4.16}$$

in addition to the buffer units in IIR filter.

Note that from 4.15, the memory length of the blockwise IIR filters is

$$L_m = P. \tag{4.17}$$

In order to increase L_m, P and the number of additions and multiplications must also be increased. This means that the implementation complexity is proportional to L_m. Hence, this approach is not suitable for the interleaved parallelization of feedback algorithms with large memory length. Moreover, signal overlaps between each signal blocks can be applied to prevent the undesirable initial value of the signal output in each block. It should be noted that in the further chapter, feedback algorithms with small memory length are parallelized with this approach. For convenience, buffer units between S/P and DSP and P/S are not illustrated in the block diagram of those algorithms.

In contrast to the first approach, feedback algorithms with infinite memory length can be implemented with the second approach of interleaving parallelization. However, it should be emphasized that the functionality of the feedback algorithm must be modified using this approach. For an IIR filter like in Figure 4.5, this approach is unqualified due to the modified transfer function of the given filter. For carrier synchronization, on the other hand, the modified functionality of the algorithms is acceptable in many cases.

The key difference of this approach in comparison to the first approach is that in each parallelization path, the given algorithm is separately performed without the data connection between the paths. As example, Figure 4.9 shows the block diagram of a feedback carrier phase estimation in interleaving parallelization with this approach. Feedback data is allowed and the memory length L_m becomes infinite for each parallelization path. However, available data in each path is limited to data indices $i \cdot P + p$, since the connection between parallelization paths is omitted.

In our example, the estimated phase $\hat{\varphi}_k$ is fed back to the input for the estimation in the next processing iteration. Basically, $\hat{\varphi}_{k-1}$ from the feedback and r_k are required. Due to

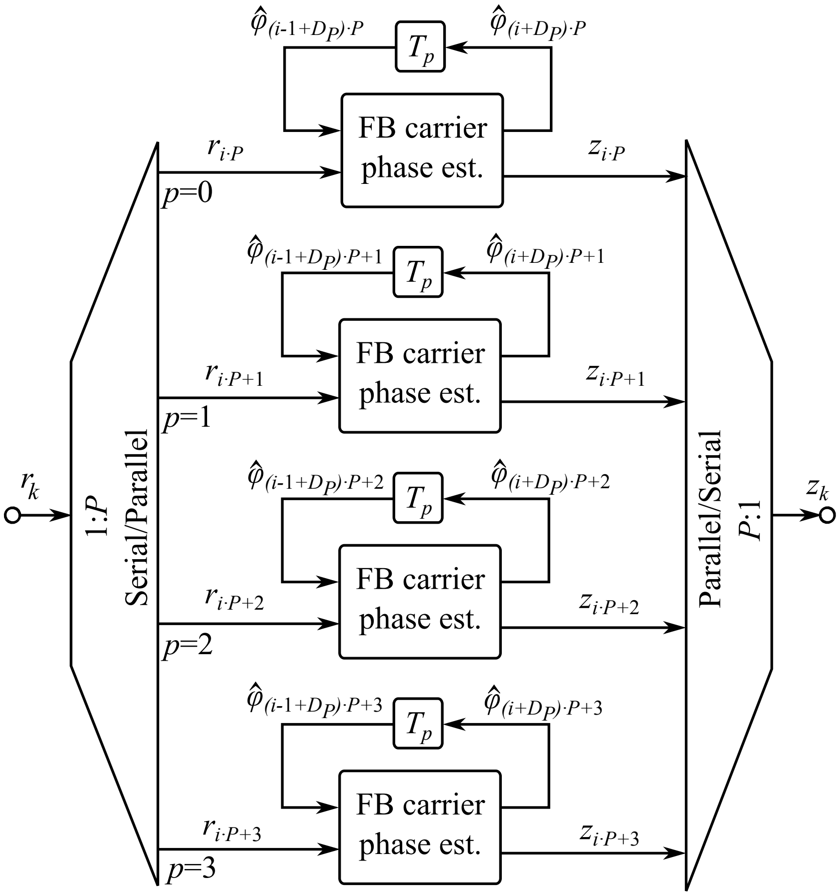

Figure 4.9.: Block diagram of feedback carrier phase estimation in interleaving parallelization *without* connection between parallelization paths

the limitation of the parallelization structure, $\hat{\varphi}_{(i-1-D_P)\cdot P+p}$ is available for the feedback data instead of $\hat{\varphi}_{k-1}$, where D_P is processing delay of the implemented algorithm. In this condition, feedback algorithms for carrier synchronization like the maximum likelihood loop and Costas loop described in Chapter 7 are operable. However, the bandwidth of the loop filter is increased and tracking performance is degraded.

According to Eq.(4.14), we can see that one multiplication requires usually one processing iteration. In feedback algorithms with multiple multiplications per closed loop, $D_P = n{\cdot}T_p,\ n > 1$ must be generally considered. In order to describe D_P, Figure 4.10 illustrates feedback algorithms with one multiplication per closed loop ($D_P = T_p$) in comparison to multiplications per closed loop ($D_P = n \cdot T_p,\ n > 1$). For feedback algorithms with one multiplication per closed loop ($D_P = T_p$), number of closed loops can be larger than 1, e.g. IIR filter with multiple feedback coefficients.

Considering D_P, the entire feedback delay D_{FB} in this approach as shown in Figure 4.9 can be given by

$$D_{FB} = ((i-1+D_P)\cdot P + p) - (i\cdot P + p) = D_P\cdot P - P. \tag{4.18}$$

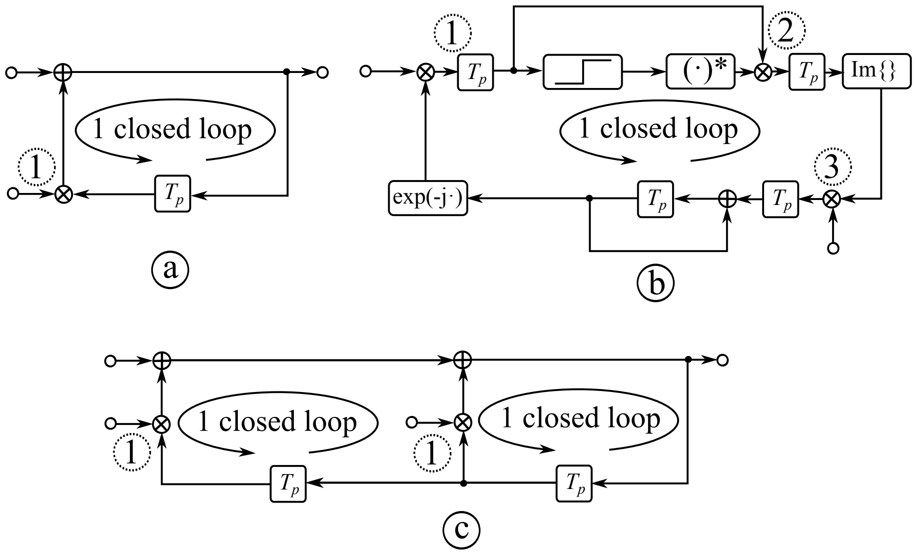

Figure 4.10.: Number of multiplication in feedback loop a) feedback algorithm with 1 multiplication per closed loop ($D_P = T_p$) b) feedback algorithm with 3 multiplication per closed loop ($D_P = 4 \cdot T_p$) c) feedback algorithm with multiple closed loops and 1 multiplication per closed loop ($D_P = T_p$)

For high bit-rate optical transmission systems, where $T_p \gg T_r$, P and, hence, D_{FB} can be very large. As an example, in 10Gbaud optical transmission systems ($T_r = 1/10\text{GHz}$ for 1 sampling per symbol signal processing),where hardware for DSP can operate with a processing rate of 500MHz ($T_p = 1/500\text{MHz}$), number of parallelization paths must be $P \geq 20$ regarding to Eq.(4.6). Consequently, the characteristics and the performance of feedback algorithms are strongly impaired due to large D_{FB} [74].

In comparison to the first approach, the memory length L_m is allowed to be infinite. Moreover, the complexity can be reduced, since L_m does not depend on P. However, not all feedback algorithms can be implemented with this approach and for implementable algorithms, the characteristics and the performance are strongly impaired.

4.2.2. Superscalar Parallelization Architecture

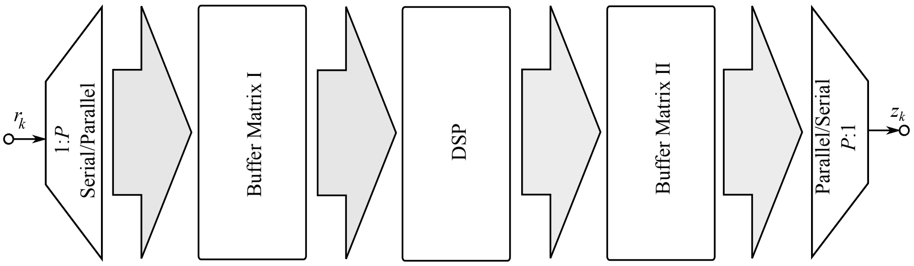

Figure 4.11.: Overview of Superscalar parallelization

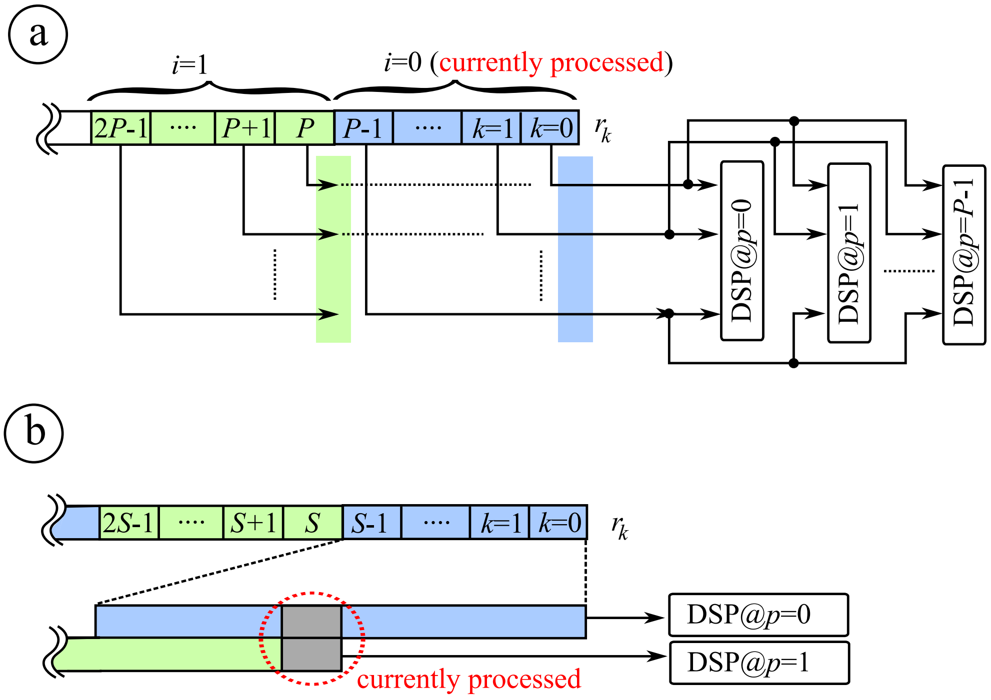

Figure 4.12.: Data flow of a) interleaving parallelization b) Superscalar parallelization

Superscalar parallelization was designed for the use with microprocessors [75]. However, we can apply Superscalar parallelization for the DSP in optical transmission systems to reduce implementation complexity or feedback delay due to parallelization. Figure 4.11 illustrates overview of Superscalar parallelization. Input signal r_k is firstly demultiplexed with a S/P like in interleaving architecture. Afterwards, the demultiplexed signal is fed into the buffer matrix I in order to transfer the signal from conventional S/P into a feasible form for Superscalar processing. After the signal processing with the DSP, the processed signal is inversely transfered into the feasible form for conventional P/S with the buffer matrix II. Finally the output signal is multiplexed with P/S. Since the signal processing with feed forward and feedback algorithms in Superscalar architecture is identical, only the feedback algorithm like IIR filter as shown in Figure 4.5 is described.

Figure 4.12 shows the data flow of the Superscalar parallelization in comparison to the interleaving parallelization, where the difference between both architectures can be pointed out. In the interleaving, consecutive signal samplings in the interval $[i \cdot P; (i+1) \cdot P - 1]$ are demultiplexed and fed into different parallelization paths. In the Superscalar architecure, on the other hand, consecutive signal samplings in the interval $[i \cdot S; (i+1) \cdot S - 1]$ are fed into the same parallelization path, where S is the sample block length for each parallelization path in the Superscalar parallelization architecture.

In order to illustrate the functionality of the Superscalar parallelization architecture, an example is depicted in Figure 4.13. In this example, we have $P = 4$ and $S = 4$. After signal demultiplexing with S/P, the digitized signal samples $r_{k=0}, r_{k=1}, r_{k=2}, r_{k=3}$ is stored in the first processing iteration $i = 0$ into the buffer column $p = 0$ of *Buffer Matrix I*. In the next process-

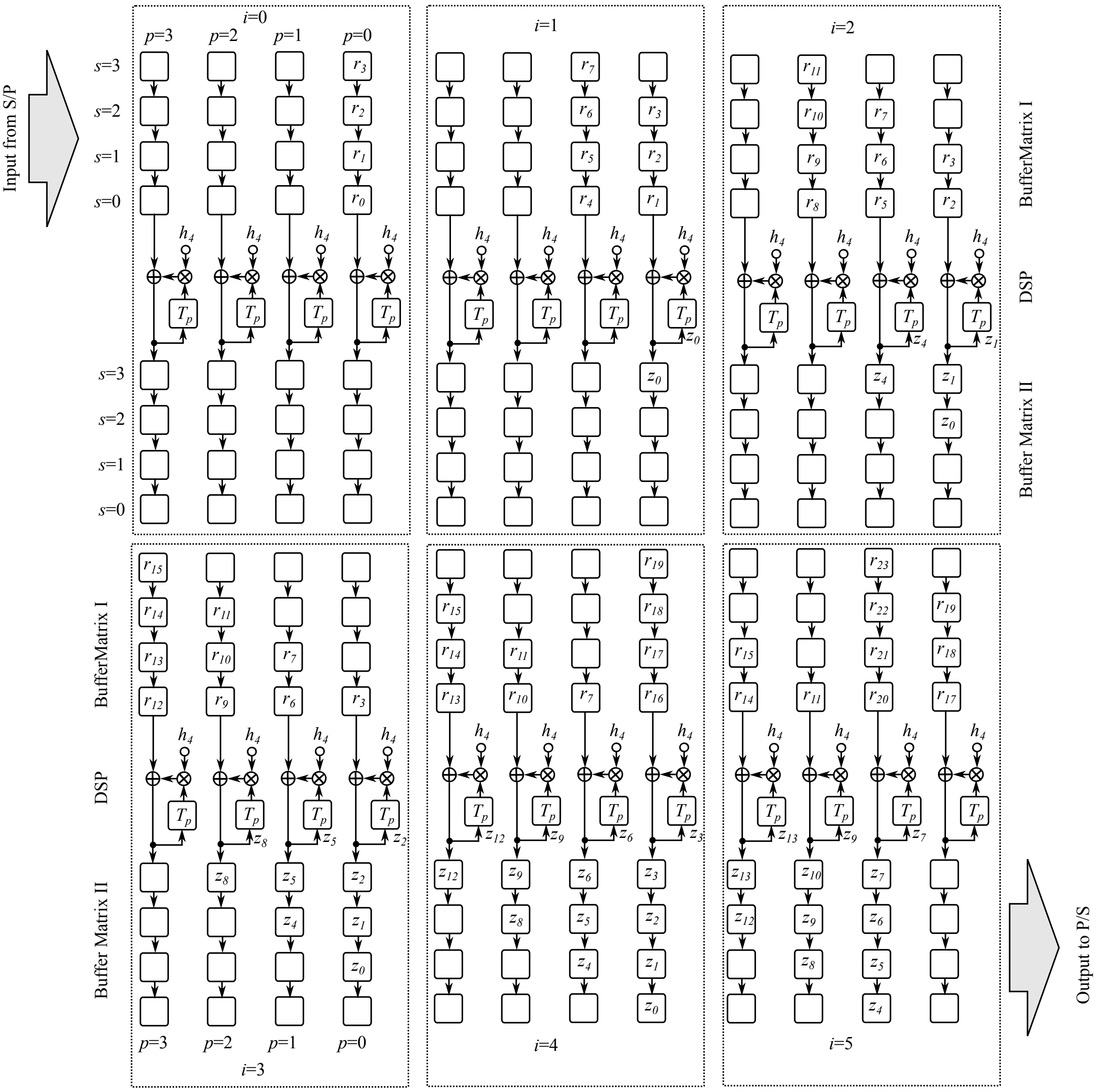

Figure 4.13.: Example for signal processing with the Superscalar parallelization architecture $(P = 4, S = 4)$

ing iteration $i = 1$, the second block of $r_{k=4}, r_{k=5}, r_{k=6}, r_{k=7}$ are stored into the buffer column $p = 1$ of Buffer Matrix I and $r_{k=0}$ is fed into the IIR filter in the parallelization path $p = 0$. Afterwards, the output signal $z_{k=0}$ is calculated and stored into the *Buffer Matrix II* with $p = 0, s = 3$, where s is the row index of the buffer matrix I and II. Moreover, $z_k k = 0$ is fed back into the IIR filter for the calculation of the next output signal $z_{k=1}$. It should be noted that $r_{k=0}$ is the initial value of the IIR filter and no feedback signal is available. Hence, we have $z_{k=0} = r_{k=0}$. For $i = 2$, $r_{k=8}, r_{k=9}, r_{k=10}, r_{k=11}$ are stored into buffer column $p = 2$ of Buffer Matrix I, $r_{k=1}$ and $r_{k=4}$ are fed into the IIR filter.

In summary, the following procedures are performed until the buffer row $s = 0$ in the Buffer Matrix I is fully occupied :

1. Storing of the input signal r_k into the Buffer Matrix I.
2. Signal processing with DSP.
3. Storing of the output signal z_k into the Buffer Matrix II. For feedback algorithms, z_k is also fed back into the input of algorithm.

In our example, the buffer row $s = 0$ is is fully occupied in the processing iteration $i = 3$. Afterwards, the buffer column $p = 0$ is free again and the input signal $r_{k=16}, r_{k=17}, r_{k=18}, r_{k=19}$ can be stored in the buffer column $p = 0$ in the iteration $i = 4$.

In the processing iteration $i = 5$, the buffer column $p = 0$ in the Buffer Matrix II is fully occupied and we can feed the output signal $z_{k=0}, z_{k=1}, z_{k=2}, z_{k=3}$ into the P/S for the output signal demultiplexing. After feeding signal into P/S, the buffer column $p = 0$ is free again and is ready to store the next output signal.

In the next iteration $i = 6$, the output signal $z_{k=16}$ can be calculated as

$$z_{k=16} = r_{k=16} + h_4 \cdot z_{k=3}. \tag{4.19}$$

This means that $z_{k=16}$ is calculated from two different signal blocks, which do not belong together. For some feedback algorithms, this characteristic is not desirable. Hence, the feedback value in each parallelization path must be reset after every $S \cdot T_p$. Consequently the impulse response of the given IIR filter can be given by

$$z_k = r_k + h_4 \cdot z_{k-1} \text{ with } k \in [0; S-1]. \tag{4.20}$$

Note that in order to prevent the undesirable initial value of the signal output in each block signal overlaps between each signal blocks can be applied.

From this example, we can see that in each parallelization path p the input signal in the interval $[i \cdot p \cdot S; i \cdot (p+1) \cdot S - 1]$ can be continuously fed into the DSP. Considering the processing delay D_P, the entire feedback delay D_{FB} in the Superscalar parallelization becomes

$$D_{FB} = D_P - 1. \tag{4.21}$$

In comparison to the interleaving architecture with the second approach for feedback algorithms, D_{FB} is strongly reduced. Furthermore, the required buffer units N_{buff} in the Superscalar can be given by

$$N_{buff} = 2 \cdot S \cdot P, \tag{4.22}$$

regardless of buffer units in the DSP.

In contrast to the first approach of interleaving parallelization for feedback algorithms, where the memory length of the blockwise IIR filter $L_m = P$, in the Superscalar architecture

$$L_m = S. \tag{4.23}$$

This means that L_m can be increased without increasing P and the number of addition and multiplication. In other words, the implementation complexity for feedback algorithms with large L_m can be reduced with the Superscalar architecture. Moreover, from Eq.(4.16), Eq.(4.17), Eq.(4.22) and Eq.(4.23), we can see that for large L_m, the number of required buffer units can also be reduced with the Superscalar architecture in comparison to the first approach of the interleaving for feedback algorithms.

Hence, the Superscalar architecture with $S > P$ is described in the next example. Figure 4.14 depicts an example with $P = 4, S = 8$. In the first processing iteration $i = 0$, $r_{k=0}, r_{k=1}, r_{k=2}, r_{k=3}$ are stored into the Buffer Matrix I in the column $p = 0$ and $s = 0, s = 1, s = 2, s = 3$ like in the previous example. In the iteration $i = 1$, $r_{k=4}, r_{k=5}, r_{k=6}, r_{k=7}$ are stored into the column $p = 0$ and $s = 3, s = 4, s = 5, s = 6$ and the signal $r_{k=0}$ is fed into the DSP in the parallelization path $p = 0$. The buffer column $p = 1$ is firstly used, if number of the residual free buffer in buffer column $p = 0$ is less than P. In this example, the buffer column $p = 1$ is firstly used by $i = 2$.

In the last example, we demonstrate the Superscalar architecture with $P > S$. This is useful for transmission systems, where the processing rate of DSP is much lower than symbol rate and required L_m is small. Figure 4.15 illustrates an example with $P = 4, S = 2$. The key procedure for this configuration is that multiple buffer columns are concurrently used for the storage of the input signal samples. As we can see from Figure 4.15, in the first processing iteration $i = 0$, $r_{k=0}, r_{k=1}, r_{k=2}, r_{k=3}$ are stored into the buffer columns $p = 0$ and $p = 1$ of Buffer Matrix I. Afterwards, the signal samples are processed like in the previous examples.

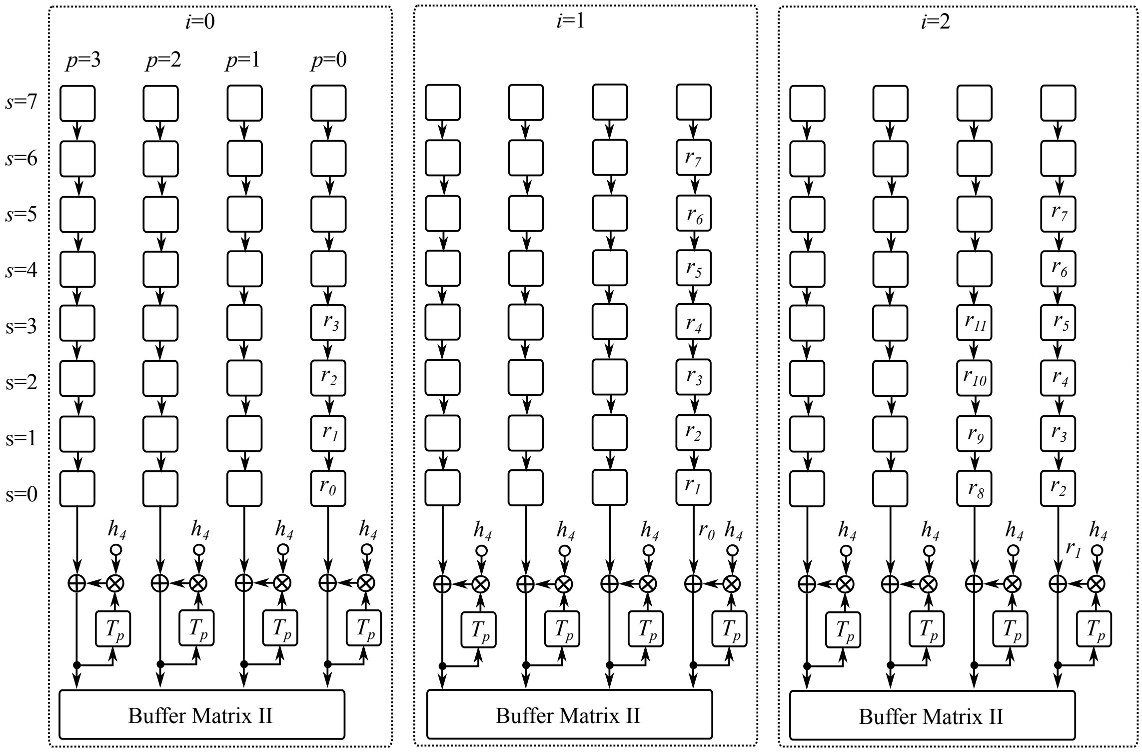

Figure 4.14.: Example for signal processing with the Superscalar parallelization architecture ($P = 4, S = 8$)

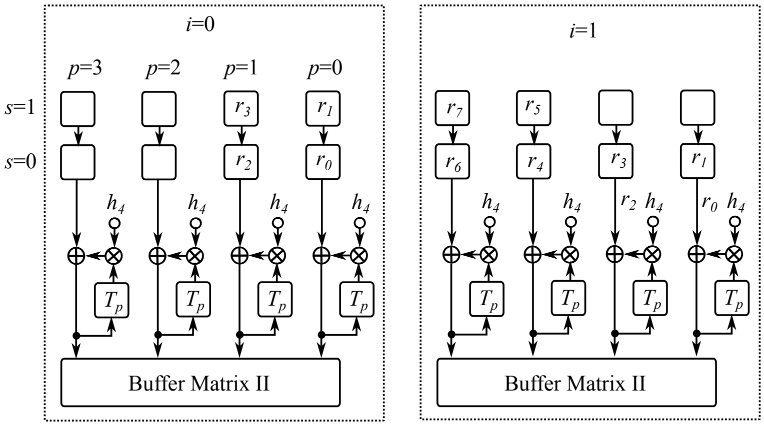

Figure 4.15.: Example for signal processing with the Superscalar parallelization architecture ($P = 4, S = 2$)

4.3. Degradations due to Phase Errors

Since carrier phases and frequencies cannot perfectly estimated, performance degradations due to phase errors can occur. In this Section, the performance degradations due to phase errors is shown. For simplicity, a perfect equalization and timing estimation are assumed. We firstly define the phase error $\tilde{\boldsymbol{\varphi}}$:

$$\tilde{\boldsymbol{\varphi}} = \boldsymbol{\varphi} - \hat{\boldsymbol{\varphi}} \tag{4.24}$$

as a random variable with some probability density function $f_{\tilde{\boldsymbol{\varphi}}}(\tilde{\varphi})$, where $\boldsymbol{\varphi}$ is a random variable for actual phase and $\hat{\boldsymbol{\varphi}}$ for estimated phase. If the phase errors are not too large, $f_{\tilde{\boldsymbol{\varphi}}}(\tilde{\varphi})$ can be assumed as Gaussian probability density function, which can be given by

$$f_{\tilde{\boldsymbol{\varphi}}}(\tilde{\varphi}) = \mathcal{N}\left(\mu_{\tilde{\varphi}}, \sigma_{\tilde{\varphi}}^2\right) = \frac{1}{\sigma_{\tilde{\varphi}}\sqrt{2\pi}} \exp\left(\frac{-\left(\tilde{\varphi} - \mu_{\tilde{\varphi}}\right)^2}{2\sigma_{\tilde{\varphi}}^2}\right), \tag{4.25}$$

where $\mu_{\tilde{\varphi}}$ is the mean value and $\sigma_{\tilde{\varphi}}^2$ the variance.

Due to the scope of this dissertation, we concentrate on three modulation formats namely, QPSK, 16-ASK-PSK and 16-QAM. Figure 4.16 shows the performance degradations due to phase errors, with Gaussian probability density function as shown in Eq.(4.24) and Eq.(4.25) for each modulation format. The derivation for numerical evaluations in Figure 4.16 can be found in Section A.2, A.3 and A.4 for QPSK, 16-ASK-PSK and 16-QAM respectively. It should be noted that symbol error probability depends on SNR and $\sigma_{\tilde{\boldsymbol{\varphi}}}$ is mathematically not resolvable. Hence, the performance degradations are numerically evaluated. To verify the derivations and the numerical evaluations, the simulations are also performed and its results are depicted in Figure 4.16 for comparison. As we can see, the numerical evaluations and the simulation results are identical.

For all modulation formats, the evaluations show that the random phase error can induce a symbol error floor even though $\sigma_{\tilde{\boldsymbol{\varphi}}}$ is relative small. Consequently, if the algorithms carrier synchronizations are not well designed and such random phase error occurs, the performance of the entire system is strongly impaired. For higher modulation formats like 16-ASK-PSK and 16-QAM, the degradation due to phase errors is naturally larger than for QPSK. Furthermore, the evaluations show that while 16-QAM is robuster against the additive white noise in comparison to 16ASK-PSK, 16-ASK-PSK has a lower performance degradation due to phase errors.

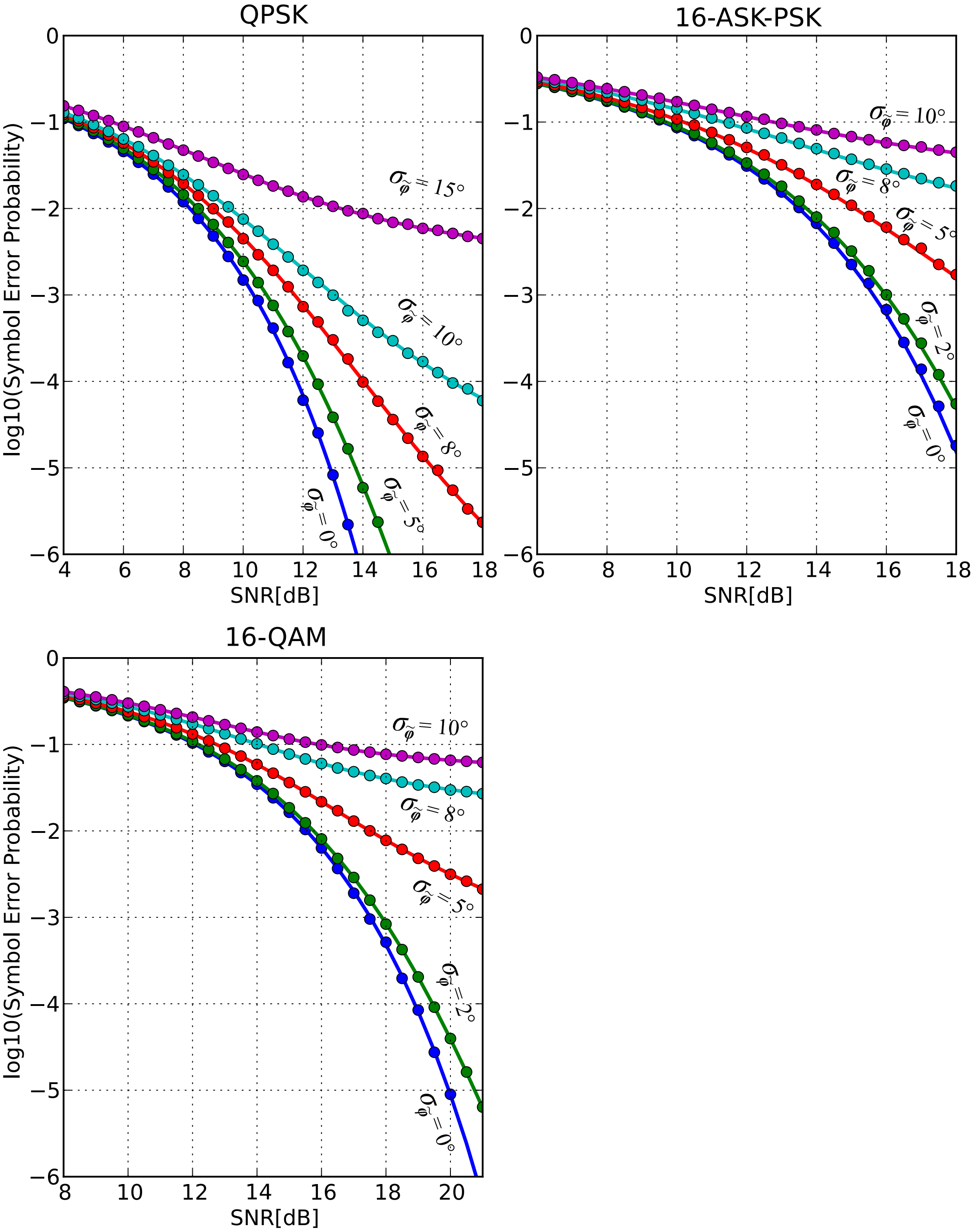

Figure 4.16.: Symbbol error probability degradation due to phase errors (continuous lines for numerical evaluations, maked points for simulation results)

4.4. Estimation Theory

In this section the basics of estimation theory are briefly described.

4.4.1. Optimal Estimation

Noting that a signal $s(t)$ is a continuous real-valued function over the time t. And $r(t)$ is another real-valued signal that is generated from $s(t)$. Mathematically, we can express the relation between $r(t)$ and $s(t)$ as

$$r(t) = g_{sn}(s(t), n(t), t), \tag{4.26}$$

where $n(t)$ is a noise and g_{sn} a function, which represents the degradation of $r(t)$ from $s(t)$. We can observe $r(t)$ as a *measurement* of the signal $s(t)$. It should be noted that the function g generally depend on time t. The determination of $s(t)$ from $r(t)$ is a type of estimation or filtering problem, and a device which produces an estimate $\hat{s}(t)$ of $s(t)$ is called *estimator* [76]. Generally, the estimate Υ of $\hat{s}(t)$ depends on $r(\tau)$ for some range of values of the variable τ and can be given by [76]

$$\hat{s}(t) = \Upsilon\left(\{r(\tau) : -\infty < \tau \leq t\}, t\right) \tag{4.27}$$

For the evaluation of an estimator, properties for behavior of the estimator should be investigated. The first intuitive property of the estimator is the expectation value of $\hat{s}(t)$, which should equal to the true expectation value of $s(t)$. The property of the expectation value of $\hat{s}(t)$ can be written as

$$\mathrm{E}\left\{\hat{s}(t)\right\} = \mathrm{E}\left\{s(t)\right\}. \tag{4.28}$$

Defining the estimation error $\tilde{s}(t)$ as

$$\tilde{s}(t) = s(t) - \hat{s}(t), \tag{4.29}$$

the property of the expectation value becomes [76]

$$\mathrm{E}\left\{\tilde{s}(t)\right\} = 0. \tag{4.30}$$

It means that the expected value of the estimation error should be zero. An estimator that satisfies Eq.(4.28) or Eq.(4.30) can be defined as *unbiased estimator* and the estimate of $\hat{s}(t)$ is so-called *unbiased estimate*.

For an estimation over a period of time, we can define an estimate as an *asymptotically unbiased* estimate if

$$\lim_{t\to\infty} \mathrm{E}\left\{\hat{s}(t)\right\} = \mathrm{E}\left\{s(t)\right\}. \tag{4.31}$$

Eq.(4.31) means that the estimate becomes unbiased in the limit. It should be emphasized that the asymptotically unbiased characteristic is a weaker property than the simply unbiased.

For the next property of the estimator, we define the mean square error (MSE) as

$$MSE = \mathrm{E}\left\{\tilde{s}^2(t)\right\}. \tag{4.32}$$

Satisfying MSE, consequently we have

$$\lim_{t\to\infty} \mathrm{E}\left\{\tilde{s}^2(t)\right\} = 0. \tag{4.33}$$

An estimator that satisfies Eq.(4.33), can be defined as a *consistent estimator* [76].

For the estimator with simply or asymptotically unbiased and consistent properties, an error-free estimate of the signal $s(t)$ can be achieved for $t \to \infty$. Therefore, the estimator with such properties can be defined as a *perfect estimator* [76].

4.4.2. Estimation Based on Discrete Measurements

For the convenience, the estimate can be formulated in the form of the estimation based on the discrete time measurements. The values of $r(t)$, $s(t)$ and $n(t)$ at $t = k \cdot T$ will be denoted by r_k, s_k and n_k, respectively, where T is defined as sampling interval. Hence, the discrete measurement can be given by

$$r_k = g_{sn}(s_k, n_k, k). \tag{4.34}$$

In causal case, the general form of the estimate $\hat{s}_k$ is

$$\hat{s}_k = \Upsilon\left(\{r_i : -\infty < \tau \leq k\}, k\right), \tag{4.35}$$

where α is a function of time index k. If the estimator is causal and linear, the estimate is given by

$$\hat{s}_k = \sum_{i=-\infty}^{k} h_{k,i} \cdot r_k, \tag{4.36}$$

where $h_{k,i}$ is the time variant impulse response of the estimator at sampling time i. For the causal, linear and time invariant estimator, the impulse response is constant with the time and the estimate is given by

$$\hat{s}_k = \sum_{i=-\infty}^{k} h_{k-i} \cdot r_k = h_k * r_k, \tag{4.37}$$

where $h_k * r_k$ is the convolution of h_k and r_k. It should be noted that we can evaluate the unbiased and consistent properties as shown in section 4.4.1 for the continuous time as well as the discrete time signal estimation.

4.4.3. Maximum Likelihood Estimation

For a random variable $\boldsymbol{x}$ with an unimodal PDF [1] $f_{\boldsymbol{x}}(x)$, the most-likely value of $\boldsymbol{x}$ relates to the peak of $f_{\boldsymbol{x}}(x)$. Hence, the estimate of $\boldsymbol{x}$ can be expressed as [76]

---

[1] An unimodal PDF is a PDF, which has a unique maximum.

$$\text{most-likely value of } \boldsymbol{x} = \text{value of } x \text{ that maximizes } f_{\boldsymbol{x}}(x).$$

Supposing that we have a single measurement r, a simple realization from $\boldsymbol{r} = g(\boldsymbol{s}, \boldsymbol{n})$, where $\boldsymbol{r}$, $\boldsymbol{s}$ and $\boldsymbol{n}$ are random variables with the realization of r, s and n respectively. It is intuitive to estimate $\boldsymbol{s}$ finding the value of s that is most likely to have produced r. For convenience, the conditional density $f_{\boldsymbol{r}}(r|\boldsymbol{s} = s)$ should be treated as a function of s and called the *likelihood function*. The value of s that maximizes the likelihood function, is the estimate of s. The described estimation method is known as maximum likelihood (ML). The ML estimate $\hat{s}_{\text{ML}}$ can be expressed as

$$\hat{s}_{\text{ML}} = \text{value of } \ s \ \text{ that maximizes } \ f_{\boldsymbol{r}}(r|\boldsymbol{s} = s). \tag{4.38}$$

Assume that the likelihood function is differentiable with a unique maximum in the interior of its domain, consequently

$$\hat{s}_{\text{ML}} = \text{value of } \ s \ \text{ for which } \ \left.\frac{\partial f_{\boldsymbol{r}}(r|\boldsymbol{s} = s)}{\partial s}\right|_{s=\hat{s}_{\text{ML}}} = 0. \tag{4.39}$$

Since the natural logarithm is a monotonically increasing function, we can equivalently maximize $\ln\left(f_{\boldsymbol{r}}(r|\boldsymbol{s} = s)\right)$, which is called the log-likelihood function. With maximizing the log-likelihood function, we have [76]

$$\hat{s}_{\text{ML}} = \text{value of } \ s \ \text{ for which } \ \left.\frac{\partial \ln\left(f_{\boldsymbol{r}}(r|\boldsymbol{s} = s)\right)}{\partial s}\right|_{s=\hat{s}_{\text{ML}}} = 0. \tag{4.40}$$

4.4.4. Maximum a Posteriori Estimation

An alternative optimality criterion for the estimation is the maximum a posteriori (MAP) estimation. Assume that a realization r from a random variable $\boldsymbol{r}$ can be measured. The most probable value of $\boldsymbol{s}$, which has occurred, is the value of s that maximizes the conditional density $f_{\boldsymbol{s}}(s|\boldsymbol{r} = r)$. Since the density after the measurement r has become available, this density is known as *a posteriori* density. The estimate $\hat{s}_{\text{MAP}}$based on this MAP criterion can be expressed as [76]

$$\hat{\boldsymbol{s}}_{\text{MAP}} = \text{value of } \ s \ \text{ that maximizes } \ f_{\boldsymbol{s}}(s|\boldsymbol{r} = r). \tag{4.41}$$

Assuming that $f_{\boldsymbol{s}}(s|\boldsymbol{r} = r)$ is differentiable and is unimodal in the interior of its domain. Eq.(4.41) can be rewritten as

$$\hat{\boldsymbol{s}}_{\text{MAP}} = \text{value of } \ s \ \text{ for which } \ \left.\frac{\partial f_{\boldsymbol{s}}(s|\boldsymbol{r} = r)}{\partial s}\right|_{s=\hat{s}_{\text{MAP}}} = 0. \tag{4.42}$$

With the Bayesian probability formula, we have

$$f_{\boldsymbol{s}}(s|\boldsymbol{r} = r) = \frac{f_{\boldsymbol{r}}(r|\boldsymbol{s} = s)}{f_{\boldsymbol{r}}(r)} \cdot f_{\boldsymbol{s}}(s) \tag{4.43}$$

Since r is given, $f_{\boldsymbol{r}}(r)$ is constant and hence independent of s, denominator can be neglected, and $\hat{s}_{\text{MAP}}$ can be given by

$$\hat{\boldsymbol{s}}_{\text{MAP}} = \text{value of } \ s \ \text{ that maximizes } \ f_{\boldsymbol{r}}(r|\boldsymbol{s}=s)\cdot f_{\boldsymbol{s}}(s). \tag{4.44}$$

Note that in contrast to the ML estimate, the density $f_{\boldsymbol{s}}(s)$ of $\boldsymbol{s}$ must be known in this case. Due to the use of the Bayesian probability formula, MAP can be classified as a form of *Bayesian estimation*.

4.4.5. Minimum Mean-Square Error Estimation

Considering the single-measurement case, another criterion for the estimation optimality can be used. In the first step, we define the estimate error $\tilde{\boldsymbol{s}}$ as the difference between the signal $\boldsymbol{s}$ and the estimate $\hat{\boldsymbol{s}}$, which can be given by

$$\tilde{\boldsymbol{s}} = \boldsymbol{s} - \hat{\boldsymbol{s}}. \tag{4.45}$$

In the next step, the MSE can be defined as [76]

$$\text{MSE} = \text{E}_{\boldsymbol{s}}\left\{\text{E}_{\boldsymbol{r}}\left\{\tilde{\boldsymbol{s}}^2|\boldsymbol{r}\right\}\right\} = \text{E}_{\boldsymbol{s}}\left\{\text{E}_{\boldsymbol{r}}\left\{(\boldsymbol{s}-\hat{\boldsymbol{s}})^2|\boldsymbol{r}\right\}\right\} = \text{E}_{\boldsymbol{s}}\left\{(\boldsymbol{s}-\hat{\boldsymbol{s}})^2\right\}. \tag{4.46}$$

From Eq.(4.46), the MSE can be presented as the average power of error. We can now minimize the average error power as shown in Eq.(4.46) to achieve the MMSE estimate $\hat{s}_{\text{MMSE}}$ of $\boldsymbol{s}$. Hence, $\hat{s}_{\text{MMSE}}$ of $\boldsymbol{s}$ is the conditional expectation for a given measurement random variable $\boldsymbol{r}$ and can be given by [76]

$$\hat{\boldsymbol{s}}_{\text{MMSE}} = \text{E}\{\boldsymbol{s}|r\}. \tag{4.47}$$

Within the scope of this dissertation, the derivation of Eq.(4.47) is omitted. From Eq.(4.43) and Eq.(4.47), it should be noted that MMSE requires also information about $\boldsymbol{s}$ like the MAP approach. Hence, MMSE estimation is another type of *Bayesian estimation*. From Eq.(4.45) and Eq.(4.47), the expectation of $\hat{s}_{\text{MMSE}}$ can be given by

$$\begin{aligned}
\text{E}\{\tilde{\boldsymbol{s}}_{\text{MMSE}}\} &= \text{E}\{\boldsymbol{s}-\hat{\boldsymbol{s}}_{\text{MMSE}}\}\\
&= \text{E}\{\boldsymbol{s}-\text{E}\{\boldsymbol{s}|\boldsymbol{r}\}\}\\
&= \text{E}\{\boldsymbol{s}\}-\text{E}\{\text{E}\{\boldsymbol{s}|\boldsymbol{r}\}\}\\
&= \text{E}\{\boldsymbol{s}\}-\text{E}\{\boldsymbol{s}\}\\
&= 0.
\end{aligned} \tag{4.48}$$

With Eq.(4.48), the unbiased property of MMSE estimation is proven [76].

4.5. Likelihood Function

It can be seen from Section 4.4 that the PDF of signals is an important part for the estimation. However, PDF is not always available or mostly very complex and not convenient for the estimation derivations and calculations. Therefore, a *likelihood function* is defined for the simplification of the estimation problems. A likelihood function must be proportional to its PDF. In other words, a likelihood function is a normalized function with a constant factor of a PDF. In this section, the likelihood functions for the carrier frequency and carrier phase estimation are derived. They will be extensively used in the further chapters.

Assume that the signal component $s(t)$ is linear digital modulated and a completely known function of time except of a set of parameters. For carrier synchronization problems, we limit the set of parameters to the frequency offset Δf and the phase error $\tilde{\varphi}$. Hence, $s(t)$ can be given by

$$s(t) = \exp\left(j \cdot (2\pi t \Delta f + \tilde{\varphi})\right) \cdot \sum_k b_k \cdot g(t - kT_s), \tag{4.49}$$

with $g(t)$ signaling pulse and T_s symbol duration. It should be noted that the data symbols b_k in Eq.(4.49) are also unknown parameters in case of a non-data-aided estimation. For simplification of derivations, however, b_k are always assumed to be known parameters for this section. To stress the signal dependence on Δf and $\tilde{\varphi}$, we temporarily adopt the notation $s(t, \Delta f, \tilde{\varphi})$ in place of $s(t)$. And the measured based band signal can be written as

$$r(t) = s(t, \Delta f, \tilde{\varphi}) + n(t), \tag{4.50}$$

where $n(t)$ is an complex zero mean additive white noise with spectral density $2N_0$ (N_0 in each in-phase and quadrature component), and the discrete form of Eq.(4.50) can be written as

$$r_k = s_k(\Delta f, \tilde{\varphi}) + n_k. \tag{4.51}$$

In the next step, we define $\vec{\boldsymbol{r}}$ as a vector of random variable $\boldsymbol{r}$ with the length of L and r_k is a realization of $\boldsymbol{r}$. The conditioned PDF $f_{\vec{\boldsymbol{r}}}(\vec{r}|\Delta f, \tilde{\varphi})$ can be given by [77]

$$\begin{aligned} f_{\vec{\boldsymbol{r}}}(\vec{r}|\Delta f, \tilde{\varphi}) &= \prod_{l=1}^{L} f_{\boldsymbol{r}}(r|\Delta f, \tilde{\varphi}) \\ &= \prod_{k=1}^{L} \frac{1}{2\pi N_0} \cdot \exp\left(-\frac{|r_k - s_k(\Delta f, \tilde{\varphi})|^2}{2N_0}\right) \\ &= \frac{1}{(2\pi N_0)^L} \cdot \exp\left(-\frac{\sum_{k=1}^{L} |r_k - s_k(\Delta f, \tilde{\varphi})|^2}{2N_0}\right). \end{aligned} \tag{4.52}$$

We replace the PDF from Eq.(4.52) with a likelihood function Λ:

$$\Lambda(\vec{r}|\Delta f, \tilde{\varphi}) = (2\pi N_0)^L \cdot \exp\left(\frac{1}{2N_0} \sum_{k=1}^{L} |r_k|^2\right) \cdot f_{\vec{\boldsymbol{r}}}(\vec{r}|\Delta f, \tilde{\varphi}), \tag{4.53}$$

and consider

$$|r_k - s_k(\Delta f, \tilde{\varphi})|^2 = |r_k|^2 + |s_k(\Delta f, \tilde{\varphi})|^2 - 2\mathrm{Re}\left\{r_k \cdot s_k^*(\Delta f, \tilde{\varphi})\right\}. \tag{4.54}$$

The Eq.(4.53) can be rewritten as

$$\Lambda(\vec{r}|\Delta f, \tilde{\varphi}) = \exp\left(\frac{1}{N_0}\sum_{k=1}^{L} \mathrm{Re}\left\{r_k \cdot s_k^*(\Delta f, \tilde{\varphi})\right\} - \frac{1}{2N_0}\sum_{k=1}^{L} |s_k(\Delta f, \tilde{\varphi})|^2\right). \tag{4.55}$$

From Eq.(4.55), it should be emphasized that the argument of exponential convergence as L tends to infinity [78].

For maximum likelihood estimation, parameters that maximize the likelihood function in Eq.(4.55), should be found. Due to the fact that the parameters maximizing the likelihood function in Eq.(4.55) are equal to the parameters maximizing the natural logarithm of the likelihood function, a *log-likelihood function* Λ^{log} is also an important function for the estimation and can be given by

$$\begin{aligned} \Lambda^{log}(\vec{\boldsymbol{r}}|\Delta f, \tilde{\varphi}) &= \ln(\Lambda(\vec{\boldsymbol{r}}|\Delta f, \tilde{\varphi})) \\ &= \frac{1}{N_0}\sum_{k=1}^{L} \mathrm{Re}\left\{r_k \cdot s_k^*(\Delta f, \tilde{\varphi})\right\} - \frac{1}{2N_0}\sum_{k=1}^{L} |s_k(\Delta f, \tilde{\varphi})|^2. \end{aligned} \tag{4.56}$$

4.6. Performance Limits in Carrier Synchronization

The goal of an estimation design is an *unbiased* accurate estimator. For the performance evaluations, the accuracy of an estimator is compared to the theoretical limit that gives the lower bounds of the estimation variance. A well-known and widely used theoretical limit in the estimation theory is the so called Cramér-Rao-Bounds (CRB) [79, 80, 81, 78]. The further approaches for the theoretical limit proposed in [82, 83, 84, 85] are infrequently used. Due to some difficulties of the application of CRB in the carrier synchronization [86, 87, 88, 89], an simplified derivative of CRB called MCRB can also be used. In this section, a brief overview of CRB and MCRB is present. Moreover, the derivation of MCRB in carrier synchronization is depicted.

4.6.1. Cramér-Rao-Bound and Modified Cramér-Rao-Bound

The expectation value of the estimation error should be zero for an unbiased estimator as shown in Eq.(4.30). However, it is only valid for the signal estimation. For the parameter estimation, Eq.(4.30) can be rewritten as

$$\int\limits_{-\infty}^{\infty} (\hat{\boldsymbol{\varepsilon}} - \boldsymbol{\varepsilon})\, f_{\boldsymbol{r}}(\vec{r}|\varepsilon) dr = 0, \tag{4.57}$$

where $\boldsymbol{\varepsilon}$ is a random variable for the parameter with a realization of ε and $\hat{\boldsymbol{\varepsilon}}$ a random variable for the estimated parameter. By differentiating Eq.(4.57) with respect to ε, we have

$$\int\limits_{-\infty}^{\infty} (\hat{\boldsymbol{\varepsilon}} - \boldsymbol{\varepsilon})\, \frac{\partial f_{\boldsymbol{r}}(\vec{r}|\varepsilon)}{\partial \varepsilon} ds - \int\limits_{-\infty}^{\infty} f_{\boldsymbol{r}}(\vec{r}|\varepsilon) dr = 0. \tag{4.58}$$

Since the total area under the PDF is always one and

$$\frac{\partial f_{\boldsymbol{r}}(\vec{r}|\varepsilon)}{\partial \varepsilon} = \frac{\partial \ln f_{\boldsymbol{r}}(\vec{r}|\varepsilon)}{\partial \varepsilon} \cdot f_{\boldsymbol{r}}(\vec{r}|\varepsilon), \tag{4.59}$$

we have

$$\int\limits_{-\infty}^{\infty} (\hat{\boldsymbol{\varepsilon}} - \boldsymbol{\varepsilon}) \frac{\partial \ln f_{\boldsymbol{r}}(\vec{r}|\varepsilon)}{\partial \varepsilon} \cdot f_{\boldsymbol{r}}(\vec{r}|\varepsilon) ds = 1. \tag{4.60}$$

Applying *Cauchy–Schwarz inequality* [90]:

$$\int\limits_{-\infty}^{\infty} |f(x)|^2 dx \cdot \int\limits_{-\infty}^{\infty} |g(x)|^2 dx \geq \left| \int\limits_{-\infty}^{\infty} f(x) \cdot g(x) dx \right|^2, \tag{4.61}$$

and squaring on Eq.(4.60) yields

$$\int\limits_{-\infty}^{\infty} (\hat{\boldsymbol{\varepsilon}} - \boldsymbol{\varepsilon})^2 \cdot f_{\boldsymbol{r}}(\vec{r}|\varepsilon) ds \cdot \int\limits_{-\infty}^{\infty} \left(\frac{\partial \ln f_{\boldsymbol{r}}(\vec{r}|\varepsilon)}{\partial \varepsilon} \cdot f_{\boldsymbol{r}}(\vec{r}|\varepsilon) \right)^2 f_{\boldsymbol{r}}(\vec{r}|\varepsilon) ds \geq 1. \tag{4.62}$$

Assuming that the estimator is unbiased, the first term of the left side of Eq.(4.62) is equal to the variance of the estimation error. Hence, the bound for the variance of the estimation error can be given by [91]

$$CRB(\varepsilon) = \frac{1}{\mathrm{E}\left\{ \left(\frac{\partial \ln f_{\boldsymbol{r}}(\vec{r}|\varepsilon)}{\partial \varepsilon} \right)^2 \right\}} = -\frac{1}{\mathrm{E}\left\{ \left(\frac{\partial^2 \ln f_{\boldsymbol{r}}(\vec{r}|\varepsilon)}{\partial \varepsilon^2} \right) \right\}} \tag{4.63}$$

Due to the computing of $f_{\boldsymbol{r}}(\vec{r}|\varepsilon)$, the application of CRB in carrier synchronizations is not practicable. Hence, we average out the unwanted parameters $\vec{\tilde{\varepsilon}}$ [77]

$$f_{\boldsymbol{r}}(\vec{r}|\varepsilon) = \int\limits_{-\infty}^{\infty} f_{\boldsymbol{r}}(\vec{r}|\varepsilon, \vec{\tilde{\varepsilon}}) \cdot f_{\tilde{\boldsymbol{\varepsilon}}}(\vec{\tilde{\varepsilon}}) d\tilde{\varepsilon} = \mathrm{E}_{\tilde{\boldsymbol{\varepsilon}}} \left\{ f_{\boldsymbol{r}}(\boldsymbol{r}|\varepsilon, \vec{\tilde{\varepsilon}}) \right\}. \tag{4.64}$$

Since the the integration in Eq.(4.64) cannot be performed analytically or the expectation in Eq.(4.63) cannot be solved, the computation of CRB is considered as impracticable.

For any unbiased estimation, we can apply MCRB to simplify the computation of the theoretical limit for carrier synchronization [92]. Substituing Eq.(4.64) into Eq.(4.63) yields

$$CRB(\varepsilon) = \frac{-1}{\mathrm{E}\left\{ \left(\frac{\partial^2 \ln \mathrm{E}_{\tilde{\boldsymbol{\varepsilon}}}\{f_{\boldsymbol{r}}(\boldsymbol{r}|\varepsilon, \tilde{\boldsymbol{\varepsilon}})\}}{\partial \varepsilon^2} \right) \right\}}. \tag{4.65}$$

Applying *Jensen's inequality* [93]:

$$\mathrm{E}\{f(x)\} \geq f(\mathrm{E}\{x\}) \tag{4.66}$$

on Eq(4.65), the MCRB can be given by [77]

$$MCRB(\varepsilon) = \frac{-1}{\mathrm{E}_{\boldsymbol{r},\tilde{\boldsymbol{\varepsilon}}}\left\{\left(\frac{\partial^2 \ln f_{\boldsymbol{r}}(\boldsymbol{r}|\varepsilon,\tilde{\boldsymbol{\varepsilon}})}{\partial\varepsilon^2}\right)\right\}} \leq CRB(\varepsilon) \tag{4.67}$$

From Eq.(4.67), it can be seen that the $MCRB(\varepsilon)$ can be calculated without knowledge about unwanted parameter $\tilde{\boldsymbol{\varepsilon}}$. Hence, the calculation of $MCRB(\varepsilon)$ is relatively simple in comparison to $CRB(\varepsilon)$. It should be noted that $MCRB(\varepsilon)$ and $CRB(\varepsilon)$ can be equal in two special cases : when $\tilde{\boldsymbol{\varepsilon}}$ are perfectly known or empty. The latter case means that there are no unwanted parameters.

It is shown in [92] that for carrier synchronization problems, $MCRB(\varepsilon)$ can be simplified as

$$MCRB(\varepsilon) = \frac{N_0}{\mathrm{E}_{\tilde{\boldsymbol{\varepsilon}}}\left\{\int_0^{T_0}\left|\frac{\partial s(t)}{\partial\varepsilon}\right|^2 dt\right\}} \tag{4.68}$$

for band pass signals and

$$MCRB(\varepsilon) = \frac{N_0/2}{\mathrm{E}_{\tilde{\boldsymbol{\varepsilon}}}\left\{\int_0^{T_0}\left|\frac{\partial s(t)}{\partial\varepsilon}\right|^2 dt\right\}} \tag{4.69}$$

for base band signals, where T_0 is the observation or estimation time and N_0 the noise power spectral density. Due to Eq.(4.67), the $MCRB(\varepsilon)$ can cause a pessimistic misunderstanding for a good estimator that has an error variance closed to $CRB(\varepsilon)$.

4.6.2. MCRB for Carrier Frequency Estimation

The starting point is Eq.(4.69) with $\varepsilon = \Delta f$ and the signal component from Eq.(4.49). We firstly substitute Eq.(4.49) into Eq.(4.69) and modify the denominator of Eq.(4.69) :

$$\begin{aligned}
\mathrm{E}_{\tilde{\boldsymbol{\varepsilon}}}\left\{\int_0^{T_0}\left|\frac{\partial s(t)}{\partial\varepsilon}\right|^2 dt\right\} &= \mathrm{E}_{\tilde{\boldsymbol{\varepsilon}}}\left\{\int_0^{T_0}\left|\frac{\partial \exp\left(j\cdot(2\pi t\Delta f+\tilde{\varphi})\right)\cdot\sum\limits_k b_k\cdot g(t-kT)}{\partial\Delta f}\right|^2 dt\right\}\\
&= \mathrm{E}_{\tilde{\boldsymbol{\varepsilon}}}\left\{\int_0^{T_0}\left|2\pi t\left(-\sin(2\pi t\Delta f+\tilde{\varphi})+j\cdot\cos(2\pi t\Delta f+\tilde{\varphi})\right)\cdot m(t)\right|^2 dt\right\}\\
&= (2\pi)^2\int_0^{T_0} t^2\mathrm{E}\left\{|m(t)|^2\right\} dt,
\end{aligned} \tag{4.70}$$

with

$$m(t) = \sum_k b_k\cdot g(t-kT_s). \tag{4.71}$$

For the base band signal, the expectation value in Eq.(4.70) can be expressed as the averaged value of signal power P_s :

$$\mathrm{E}\left\{|m(t)|^2\right\} = P_s = \frac{E_s}{T_s}, \tag{4.72}$$

where E_s is energy per symbol and T_s symbol duration. Substituting Eq.(4.72) into Eq.(4.70) yields

$$\begin{aligned} \mathrm{E}_{\tilde{\varepsilon}}\left\{\int_0^{T_0}\left|\frac{\partial s(t)}{\partial \varepsilon}\right|^2 dt\right\} &= (2\pi)^2\int_0^{T_0} t^2\frac{E_s}{T_s}dt && (4.73)\\ &= \frac{4\pi^2 E_s T_0^3}{3T_s}. && (4.74)\end{aligned}$$

4.6.3. MCRB for Carrier Phase Estimation

The assumption for the carrier phase estimation is that it equals to the carrier frequency estimation. Hence, Eq.(4.49) is also valid for the derivation of $MCRB(\tilde{\varphi})$. Substituting Eq.(4.49) into Eq.(4.69) with $\varepsilon = \tilde{\varphi}$, the dominator of Eq.(4.49) can be given by

$$\begin{aligned} \mathrm{E}_{\tilde{\varepsilon}}\left\{\int_0^{T_0}\left|\frac{\partial s(t)}{\partial \varepsilon}\right|^2 dt\right\} &= \mathrm{E}_{\tilde{\varepsilon}}\left\{\int_0^{T_0}\left|\frac{\partial \exp\left(j\cdot(2\pi t\Delta f+\tilde{\varphi})\right)\cdot m(t)}{\partial \Delta\tilde{\varphi}}\right|^2 dt\right\}\\ &= \int_0^{T_0}\mathrm{E}\left\{|m(t)|^2\right\}dt\\ &= E_s\cdot L. && (4.75)\end{aligned}$$

Inserting into Eq.(4.69) yields

$$MCRB(\tilde{\varphi}) = \frac{1}{2L}\cdot\frac{1}{E_s/N_0}. \tag{4.76}$$

As with frequency estimation, the $MCRB(\tilde{\varphi})$ is inversely proportional to the SNR. In contrast to the $MCRB(\Delta f)$, the parameter L in the domination is now raised to the first power, not the third. As a result, phase errors are less sensitive to the observation length than frequency errors.

5. Phase Estimation for Differential Phase Detection

Optical differential phase detection based on DLI as shown in Section 3.4 is a widely-used technique in optical transmission systems. It has improved sensitivity with comparable implementation complexity in comparison to the technique based on power detection like OOK. However, with the differential detection, the noise power is increased due to the phase differentiation of two consecutive symbols. With suitable DSP, the impact of the differential technique can be reduced. In this chapter, DSPs for optical differential phase detection are presented. This DSPs are based on phase estimation over multiple symbols.

5.1. Multiple Symbol Differential Detection

The first approach for the performance improvement for phase differential detection is multiple symbol differential detection (MSDD) [94, 95]. MSDD is based on the maximum likelihood approach and can be performed without any additional coding of the input information.

5.1.1. Derivation of a Decision Rule

Assume that $s(t)$ is the transmitted signal over the additive white Gaussian noise (AWGN) channel with

$$s(t) = a(t) \cdot \exp(j \cdot \varphi(t)), \tag{5.1}$$

where $a(t)$ is the amplitude and $\varphi(t)$ the phase of signal. At the receiver side, the sampled received signal r_k can be given by

$$r_k = s_k \cdot \exp(j \cdot \theta_k) + n_k, \tag{5.2}$$

where n_k is a sample of zero-mean normal distributed complex noise with the variance of σ_n^2 and θ_k is an arbitrary phase introduced by the channel in the absence of any side information and is assumed to be uniformly distributed in the interval $(-\pi; \pi)$.

Furthermore, we assume that θ_k is independent of k over the length of this sequence, i.e., $\theta_k = \theta$. We define $\vec{r}_k$ and $\vec{s}_k$ as a vector form of the received sequence and transmitted signal respectively with the length L, where

$$\vec{r}_k = \begin{pmatrix} r_{k-L-1} \\ r_{k-L-2} \\ \vdots \\ r_{k-1} \\ r_k \end{pmatrix} \tag{5.3}$$

and

$$\vec{s}_k = \begin{pmatrix} s_{k-L-1} \\ s_{k-L-2} \\ \vdots \\ s_{k-1} \\ s_k \end{pmatrix}. \tag{5.4}$$

Analogous to Eq.(5.2) the received sequence $\vec{r}$ can be written in a vector form as

$$\vec{r}_k = \vec{s}_k \cdot \exp(j \cdot \theta) + \vec{n}. \tag{5.5}$$

With the assumption of the AWGN channel, the a posteriori probability of $\vec{r}$ given $\vec{s}$ can be written as [94]

$$f_{\boldsymbol{r}}(\vec{r}|\vec{s},\theta) = \frac{1}{(2\pi\sigma_n^2)^L} \cdot \exp\left(-\frac{\|\vec{r} - \vec{s} \cdot \exp(j \cdot \theta)\|^2}{2\sigma_n^2}\right), \tag{5.6}$$

with

$$\|\vec{r} - \vec{s} \cdot \exp(j \cdot \theta)\|^2 = \sum_{i=0}^{L-1} |r_{k-i} - s_{k-i} \cdot \exp(\theta)|^2 \tag{5.7}$$

$$= \sum_{i=0}^{L-1} \left(|r_{k-i}|^2 + |s_{k-i}|^2\right) - 2\left|\sum_{i=0}^{L-1} r_{k-i} \cdot s_{k-i}^*\right| \cdot \cos(\theta - \theta_{rs}) \tag{5.8}$$

and

$$\theta_{rs} = \arg\left\{\sum_{i=0}^{L-1} r_{k-i} \cdot s_{k-i}^*\right\}. \tag{5.9}$$

Due to the assumed uniform distribution of θ, it has been shown in [94] that a posteriori probability of $\vec{r}$ given $\vec{s}$ can be given by

$$\begin{aligned} f_{\boldsymbol{r}}(\vec{r}|\vec{s}) &= \int_{-\pi}^{+\pi} f_{\boldsymbol{r}}(\vec{r}|\vec{s},\theta) \cdot f_{\boldsymbol{\theta}}(\theta)\, d\theta \\ &= \frac{1}{(2\pi\sigma_n^2)^L} \cdot \exp\left(-\frac{1}{2\sigma_n^2} \sum_{i=0}^{L-1} \left(|r_{k-i}|^2 + |s_{k-i}|^2\right)\right) \cdot \\ &\quad I_0\left(\frac{1}{\sigma_n^2} \cdot \left|\sum_{i=0}^{L-1} r_{k-i} \cdot s_{k-i}^*\right|\right), \end{aligned} \tag{5.10}$$

where $I_0(x)$ is the zeroth order modified Bessel function of the first kind. It should be noted that for M-PSK, $|s_k|^2$ is constant for all phases. Since $I_0(x)$ is a monotonically increasing function, maximizing $f_{\boldsymbol{r}}(\vec{r}|\vec{s})$ over $\vec{s}$ is equivalent to find

$$\max_i \left| \sum_{i=0}^{L-1} r_{k-i} \cdot s_{k-i}^* \right|^2 . \tag{5.11}$$

We can now use Eq.(5.1) in the decision rule

$$\vec{\hat{\varphi}} = \text{value of } \vec{\hat{\varphi}} \text{ that maximizes } \left| \sum_{i=0}^{L-1} r_{k-i} \cdot \exp(-j\vec{\hat{\varphi}}_{k-i}) \right|^2 , \tag{5.12}$$

where $\vec{\hat{\varphi}}_k$ is defined as

$$\vec{\hat{\varphi}}_k = \begin{pmatrix} \hat{\varphi}_{k-L-1} \\ \hat{\varphi}_{k-L-2} \\ \vdots \\ \hat{\varphi}_{k-1} \\ \hat{\varphi}_k \end{pmatrix} \tag{5.13}$$

and $\hat{\varphi} \in \{0, \pi/M, 2\pi/M, 3\pi/M, ..., (M-1)\pi/M\}$.

Since the addition of an arbitrary fixed phase to all L estimated phases results in the same decision for $\vec{\hat{\varphi}}$, the decision rule in Eq.(5.12) has a phase ambiguity associated with it. The decision rule in Eq.(5.12) can be alternatively calculated as choosing the sequence $\vec{\hat{\varphi}}$ that maximizes the following metric η_D [94]

$$\eta_D = \left| \sum_{i=0}^{L-1} r_{k-i} \cdot \exp\left(-j(\varphi_{k-i} - \varphi_{k-L+1})\right) \right|^2 . \tag{5.14}$$

The differential encoding/decoding as shown in Section 3.3.2 can be applied to solve the above phase ambiguity. We define now $\varphi_{d,k}$ as the differentially encoded version of φ_k and the metric η_D for the decision becomes

$$\eta_D = \left| r_{k-L+1} + \sum_{i=0}^{L-2} r_{k-i} \cdot \exp\left(-j \cdot \sum_{m=0}^{L-2} \varphi_{d,k-i-m}\right) \right|^2 \tag{5.15}$$

For the calculation of the metric η_D, we have to observe the received signal over L symbols. Hence, this observation makes a simultaneous decision on $L-1$ data phases.

Some special cases of Eq.(5.15) are analyzed here. Firstly, we focus on the case of $L = 1$, where the received signal is observed over one symbol interval. Now we can simplify Eq.(5.15) to

$$\eta_D = |r_k|^2 . \tag{5.16}$$

Note that η_D in Eq.(5.16) is completely independent of the input data phases and thus cannot be used for making decisions on differentially encoded M-PSK modulation.

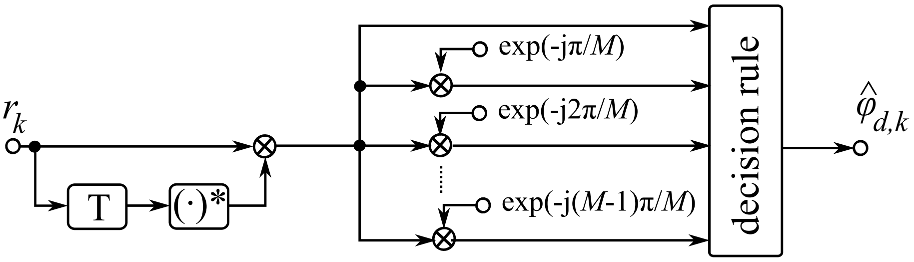

Figure 5.1.: Conventional differential detector of M-PSK

In the next case, we set $L = 2$ and Eq.(5.15) becomes

$$\begin{aligned} \eta_D &= \left| r_{k-1} + r_k \cdot \exp(-j\varphi_{d,k}) \right| && (5.17) \\ &= |r_{k-1}|^2 + |r_k|^2 + 2\mathrm{Re}\left\{ r_k \cdot r_{k-1}^* \cdot \exp(-j\varphi_{d,k}) \right\}. && (5.18) \end{aligned}$$

Since $\varphi_{d,k}$ is independent of $|r_{k-1}|^2 + |r_k|^2$, the decision rule based on Eq.(5.17) can be written as

$$\hat{\varphi}_k = \text{value of } \hat{\varphi}_k \text{ that maximizes Re}\left\{ r_k \cdot r_{k-1}^* \cdot \exp(-j\hat{\varphi}_{d,k}) \right\}, \qquad (5.19)$$

which is implemented in complex form as shown Figure 5.1. This result is the well-known decision rule for conventional M-DPSK. From Eq.(5.17), we can see that the conventional differential detection of M-PSK is the optimum receiver in the sense of minimizing the symbol error probability based on Eq.(5.11).

We focus now on the case of $L = 3$. With the consideration of Eq.(5.15), the metric η_D for the

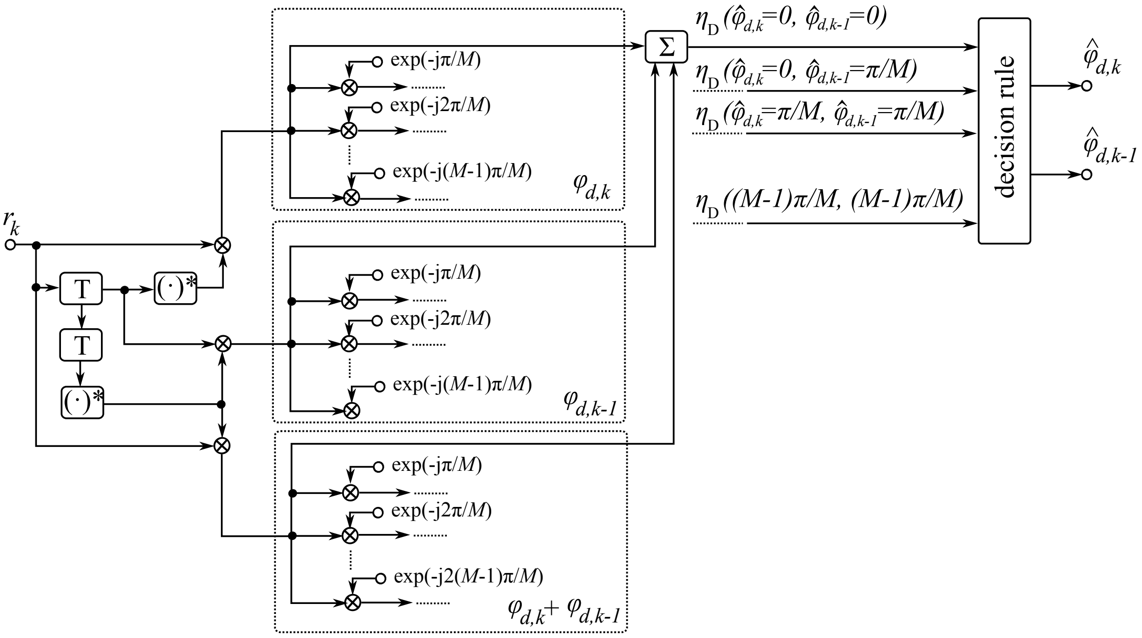

Figure 5.2.: Parallel implementation of multiple symbol differential detection for $L = 3$

decision rule can be given by [94]

$$\begin{aligned}\eta_D &= |r_{k-2} + r_k \cdot \exp(-j(\varphi_{d,k} + \varphi_{d,k-1})) + r_{k-1} \cdot \exp(-j\varphi_{d,k})| && (5.20)\\ &= |r_{k-2}|^2 + |r_{k-1}|^2 + |r_k|^2 + 2\mathrm{Re}\left\{r_k \cdot r_{k-2}^* \cdot \exp(-j(\varphi_{d,k} + \varphi_{d,k-1}))\right\} + \\ &\quad 2\mathrm{Re}\left\{r_{k-1} \cdot r_{k-2}^* \cdot \exp(-j\varphi_{d,k-1})\right\} + 2\mathrm{Re}\left\{r_k \cdot r_{k-1}^* \cdot \exp(-j\varphi_{d,k})\right\}. && (5.21)\end{aligned}$$

Finally, the decision rule can be written as

$$\begin{aligned}\hat{\varphi}_k \text{ and } \hat{\varphi}_{k-1} &= \text{values of } \hat{\varphi}_k \text{ and } \hat{\varphi}_{k-1} \text{ that maximize}\\ &\quad 2\mathrm{Re}\left\{r_k \cdot r_{k-2}^* \cdot \exp(-j(\varphi_{d,k} + \varphi_{d,k-1}))\right\} + \\ &\quad 2\mathrm{Re}\left\{r_{k-1} \cdot r_{k-2}^* \cdot \exp(-j\varphi_{d,k-1})\right\} + \\ &\quad 2\mathrm{Re}\left\{r_k \cdot r_{k-1}^* \cdot \exp(-j\varphi_{d,k})\right\}. && (5.22)\end{aligned}$$

It should be noted that the second and third terms of the metric used in the decision rule of Eq.(5.22) are identical to $\varphi_{d,k}$ and $\varphi_{d,k-1}$ in conventional M-DPSK. The additional information to the conventional M-DPSK decision is in the first term, whereas the combination of the last two are required to make an optimum joint decision on $\varphi_{d,k}$ and $\varphi_{d,k-1}$. The block diagram of the decision rule with $L = 3$ is shown in Figure 5.2.

Due to the joint decision, a receiver implemented on the basis of Eq.(5.22) clearly outperforms conventional M-DPSK. Before demonstrating the performance improvement as a function of the number of phases M, we firstly discuss the implementation of the optimum $L = 3$ receiver.

5.1.2. Implementation in Optical Receivers

For optical receivers, we can obtain $r_k \cdot r_{k-1}^*$ by applying the optical direct detection IQ receiver as shown in section 3.4. However, for $r_k \cdot r_{k-2}^*$ and other differential products, additional

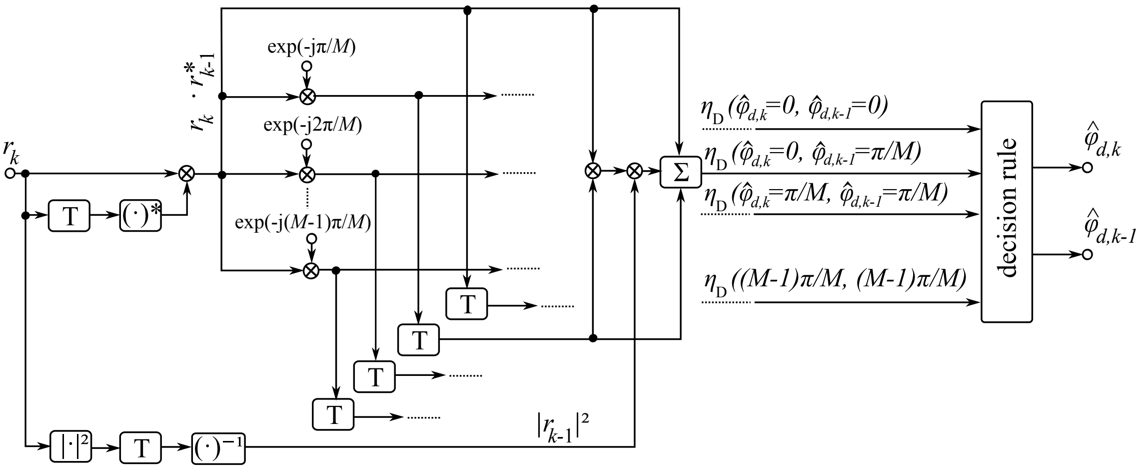

Figure 5.3.: Serial implementation of multiple symbol differential detection for $L = 3$

receivers are required, and are not commercially available. Hence, the parallel implementation of MSDD [94] e.g. as shown in Figure 5.2 is not suitable for the optical receiver. In contrast, for the serial implementation of MSDD e.g., as shown in Figure 5.3, only $r_k \cdot r_{k-1}^*$ and $|r_{k-1}|^2$ are necessary. Thus, the serial implementation should be preferred for the optical receivers with the differential phase direct detection technique.

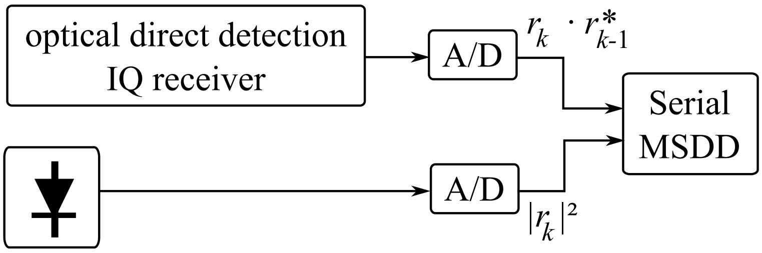

Figure 5.4.: Optical frontend for serial MSDD

Figure 5.4 shows the optical front end for serial MSDD. In additional to the optical direct detection IQ receiver, a photo diode is also required to detect the power of the received optical signal. After converting the light wave signal into the electrical signal, two A/D must be applied to digitize the signal for the DSP.

5.1.3. Detection Performance

For performance evaluations, the back-to-back optical signal is simulated. The coherent detection is also simulated for comparison. Due to the phase ambiguity problem, the differential encoding/decoding must be applied in the coherent transceivers.

Due to the fact that in optical transmission systems, the noise bandwidth is much wider than the signal bandwidth, bit error rate (BER) is usually evaluated as a function of OSNR instead of SNR. The derivation and the description of OSNR are shown in Section A.5.

The detection performance for 25Gb/s DBPSK, 50Gb/s DQPSK and 75Gb/s 8-DPSK is depicted in Figure 5.5. It can be clearly seen that the detection performance is significantly improved by increasing the observation length L. Assuming that the coherent detection with differential encoding/decoding is the theoretical limit for the performance improvement for MSDD, with $L = 5$ and DBPSK as modulation format, a detection performance close to this limit can be obtained. At this point, we have a performance gain of 0.5dB for BER=10^{-3}. Furthermore, the implementation complexity for the MSDD for BPSK with $L = 5$ is acceptable where the number of the estimated phases is $2^{L-1} = 16$.

On the one hand, for higher order modulation formats like DQPSK and 8-DPSK, the performance difference between coherent detection and the differential phase detection is increased. On the other hand, the performance impacts caused by the differential encoding/decoding is decreased. Although we have more performance improvement for DQPSK and 8-DPSK with MSDD, the difference between MSDD and the coherent detection with differential encoding/decoding is increased. Furthermore, the implementation complexity of MSDD grows exponentially with L and M. For DQPSK with $L > 5$ and 8-DPSK with $L > 3$, the implementation of MSDD is not practicable for high bit-rate optical transmission systems.

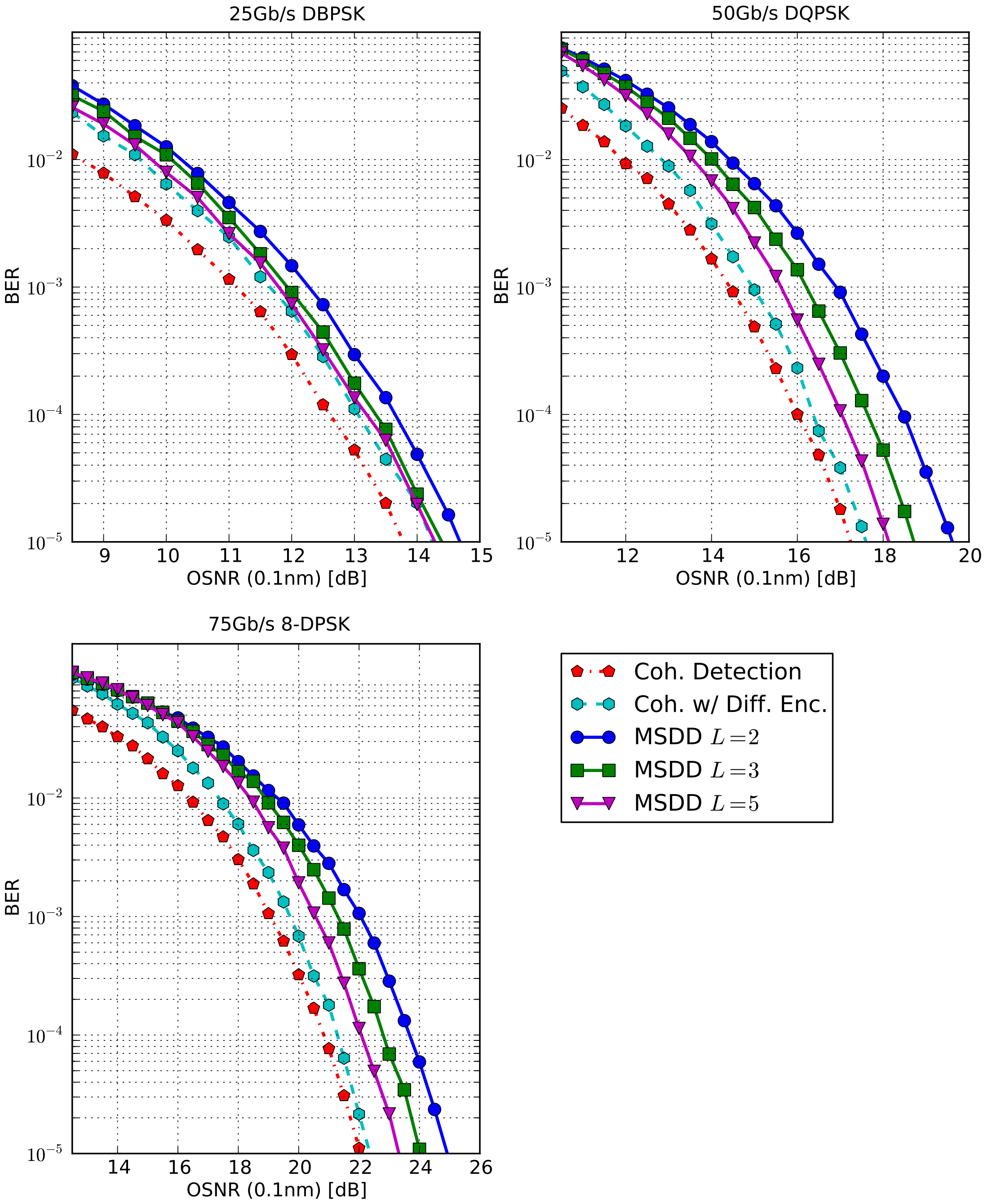

Figure 5.5.: Simulation results for MSDD detection performance in comparison to coherent detection and coherent detection with differential encoding/decoding for 25Gb/s DBPSK, 50Gb/s DQPSK and 75Gb/s 8-DPSK

5.2. Multiple Symbol Phase Estimation

In Section 5.1, it is shown that with MSDD, the phase estimation can be significantly improved by increasing the observation length L. It should be, however, emphasized that the implementation complexity of MSDD increases exponentially with L. An efficient alternative to MSDD is the recursive form of MSDD as shown in [96, 97]. In optical transmission systems, the recursive form of MSDD is known as multiple symbol phase estimation (MSPE), which is successfully applied in combination with the optical direct detection receivers as shown in [98, 99, 100, 101, 102]. In this section, MSPE is derived. Furthermore, the application of MSPE in optical transmission systems and its performance is outlined.

5.2.1. Derivation and Structure

For the implementation complexity reduction, the MSDD must be transformed into a feedback structure. It is shown in [96] that the calculation of η_d in Eq.(5.15) can be written in the recursion form, and the signal for the decision can be written as

$$q_k = r_k + w \cdot q_{k-1} \cdot \exp(j \cdot \hat{\varphi}_{d,k-1}), \tag{5.23}$$

where q_k is the new phase reference for M-DPSK and w a forgetting factor with $0 \leq w \leq 1$. The observation length L in MSDD can be adjusted with w in the recursive form e.g. for $w = 0$, we have the conventional coherent detection and for $w = 1$, we have MSDD with an endless memory. From q_k, the improved complex decision variable z_k can be obtained and given by

$$z_k = r_k \cdot q_{k-1}^* \tag{5.24}$$

With the optical coherent detection as shown in Section 3.5, r_k can be simply obtained and Eq.(5.23) and Eq.(5.24) can also be simply calculated. In contrast to the coherent detection, r_k cannot be directly accessed with the optical direct detection. Hence, it is desirable to express the improved decision variable in Eq.(5.24) in terms of the measurable signal u_k for the direct detection with the differential phase technique namely

$$u_k = r_k \cdot r_{k-1}^*. \tag{5.25}$$

Substituting Eq.(5.25) and Eq.(5.24) into Eq.(5.23) yields

$$\begin{aligned} z_k &= r_k \cdot [r_{k-1} + w \cdot q_{k-2} \cdot \exp(j \cdot \hat{\varphi}_{d,k-1})]^* \\ &= u_k + r_k \cdot \frac{r_{k-1}^*}{r_{k-1}^*} w \cdot q_{k-2}^* \cdot \exp(-j \cdot \hat{\varphi}_{d,k-1}) \\ &= u_k + w \cdot u_k \cdot \frac{1}{r_{k-1}^*} q_{k-2}^* \cdot \exp(-j \cdot \hat{\varphi}_{d,k-1}). \end{aligned} \tag{5.26}$$

When the signal performance is limited by phase noise rather than the amplitude noise, we can approximate that

$$r_k \approx \exp(j \cdot \varphi_k), \tag{5.27}$$

which is usually applicable to the optical M-DPSK. From Eq.(5.27), it follows that

$$\frac{1}{r^*_{k-1}} \approx r_{k-1}. \tag{5.28}$$

Substituting Eq.(5.28) into Eq.(5.26) and applying Eq.(5.24) yields [98, 100]

$$\begin{aligned} z_k &\approx u_k + w \cdot u_k \cdot r_{k-1} q^*_{k-2} \cdot \exp(-j \cdot \hat{\varphi}_{d,k-1}) \\ &= u_k + w \cdot u_k \cdot z_{k-1} \cdot \exp(-j \cdot \hat{\varphi}_{d,k-1}). \end{aligned} \tag{5.29}$$

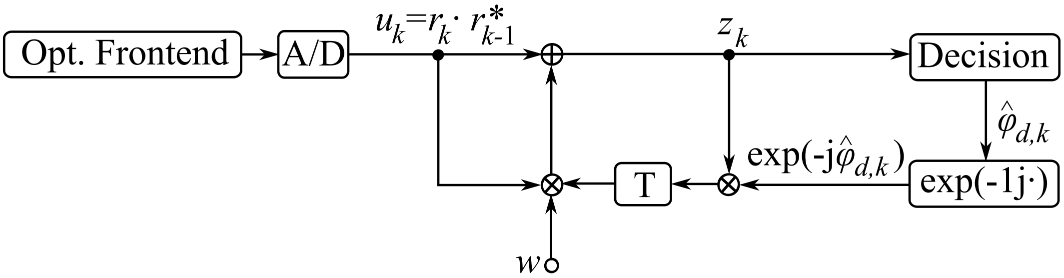

Figure 5.6.: MSPE implementation with optical frontend

We can now apply Eq.(5.24) on the digitized signal from the optical frontend as shown in Figure 5.6. Like in Eq.(5.23) the memory length in Figure 5.6 can be set by the forgetting factor w. The decision part in Figure 5.6 is a conventional phase decision for respective modulation formats as illustrated in Figure 5.7. Hence, 5.6 can be performed for arbitrary M-DPSK modulation formats without additional signal processing. In comparison to the MSDD, the implementation of MSPE is much more efficient due to the recursive form of the algorithm.

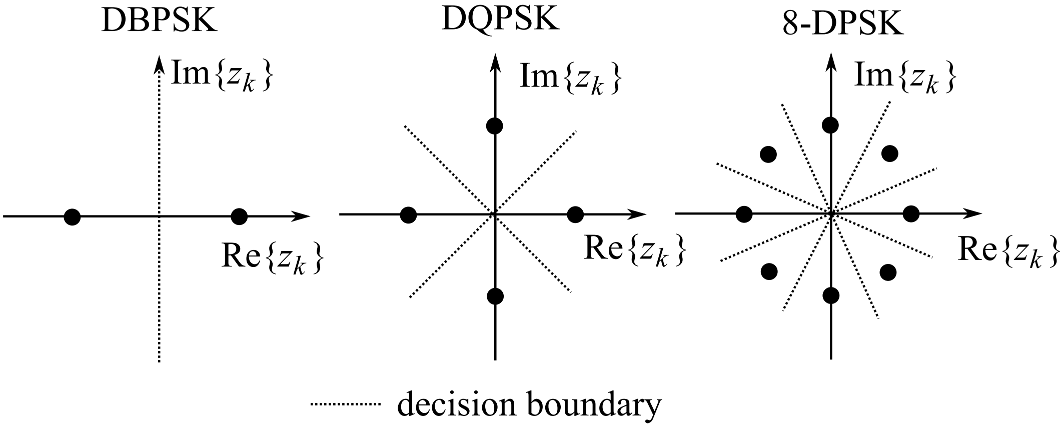

Figure 5.7.: Decision scheme for BDSPK, DQPSK and 8-DPSK modulation format

5.2.2. Estimation Performance

Like the performance evaluations for MSDD as shown in Section 5.1.3, the optical back-to-back transmission without PolMux is simulated. In Figure 5.8, the BER performance of MSPE depends on OSNR and the forgetting factor w for 25Gb/s DBPSK is depicted. The estimation performance of MSPE is directly compared with the performance of the coherent detection and the coherent detection with differential encoding/decoding. Since the memory length of the estimation is proportional to the forgetting factor w, the performance is also improved increasing w. This characteristic is similar to MSDD by increasing the observation length L. It should be noted that with $w = 0$, the MSPE part of the detection as shown in Figure 5.6

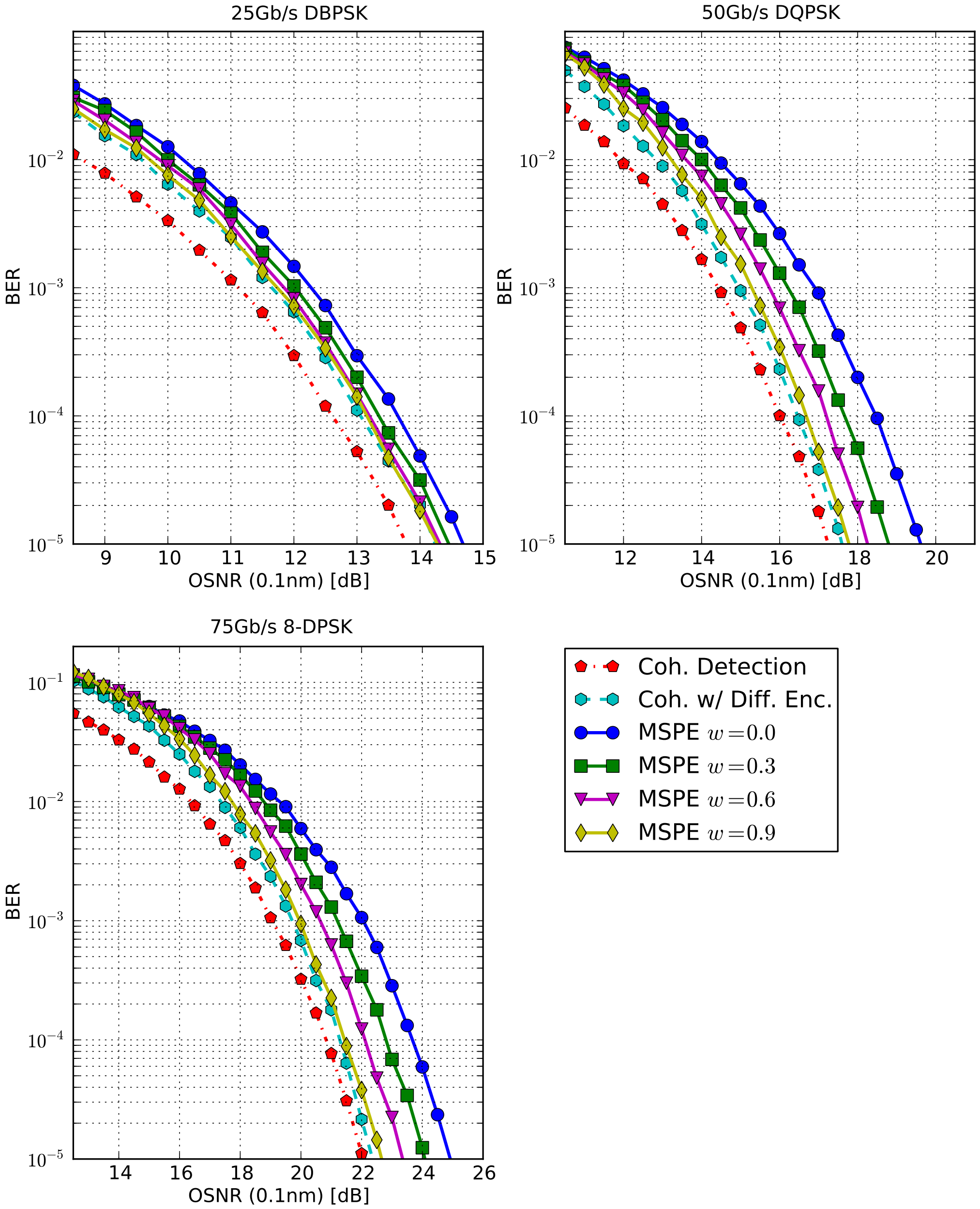

Figure 5.8.: Simulation results for MSPE estimation performance in comparison to coherent detection and coherent detection with differential encoding/decoding for 25Gb/s DBPSK, 50Gb/s DQPSK and 75Gb/s 8-DPSK

has no influence on the detection, and we have the same performance as the differential phase detection without MSPE. As we can see from Figure 5.8, with $w \geq 0.9$, the performance of MSPE is close to the coherent detection with differential encoding/decoding, which can be seen as the performance limit of the differential phase detection.

Unlike MSDD, for higher order modulation formats like DQPSK and 8-DPSK, MSPE can improve the performance of the differential phase detection close to the coherent detection with differential encoding/decoding. It can be seen that at BER= 10^{-3}, we have the OSNR sensitivity improvement of 1.1dB for DBPSK, 1.8dB for DQPSK and 2.0dB for 8-DPSK.

Since equalizing based on DSP is usually not performed in the receivers with direct detection technique, the CD compensation is applied using only DCF. The static CD compensation with DCF cannot ensure that the complete CD can be compensated and residual CD must be assumed for detection. Moreover, the signal is usually transmitted without PolMux and PMD can be neglected. Therefore, CD is the dominant impairment for the optical receivers with direct detection. Figure 5.9 shows that the MSPE estimation performance dependent on the residual chromatic dispersion for 50Gb/s DQPSK. It can be seen that the performance gain of MSPE is decreased by increasing CD because MSPE is based on the decision-directed approach, which can be impaired by distortions like CD.

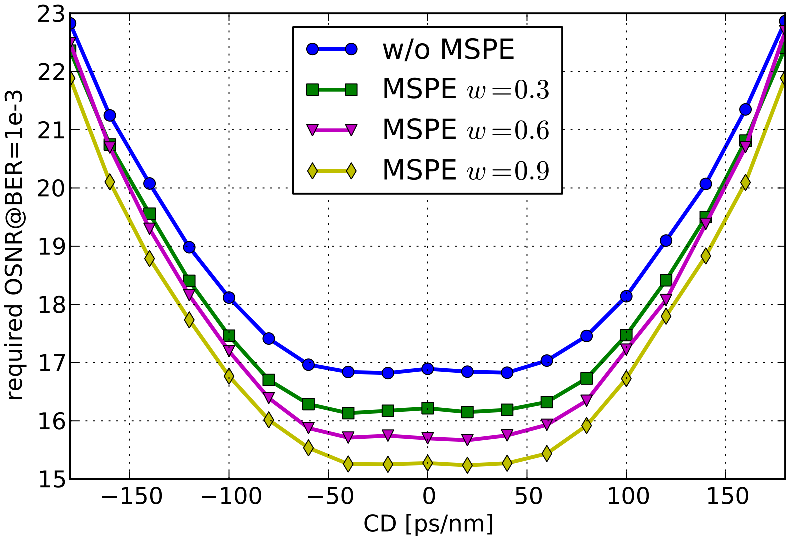

Figure 5.9.: Simulation results for MSPE estimation performance vs. residual chromatic dispersion for 50Gb/s DQPSK

The channel simulation with in-line CD compensation and a signal launch power of 2dBm for 50Gb/s DQPSK transmitted over 1040km of SSMF (13 spans of 80km SSMF) as described in Section 3.6 are performed. The residual CD is compensated by applying DCF for all simulation points. It can be assumed that the whole CD is compensated, and PMD is neglected. Hence, the performance loss depicted in Figure 5.10 is caused by the channel nonlinearities. It can be seen from Figure 5.10. that with MSPE, we have more tolerance against the channel nonlinearities. However, the performance gain from MSPE is decreased by increasing the channel nonlinearities. Due to the fact that MSPE is a decision based algorithm, the channel impairment with the impact to the decision and data recovery like CD and the nonlinearities can degrade the performance of MSPE.

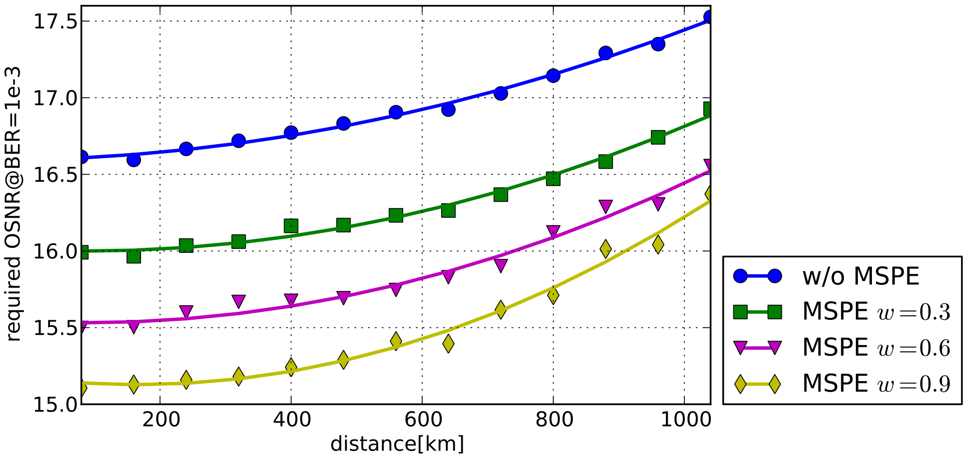

Figure 5.10.: MSPE estimation performance vs. transmission distance for 50Gb/s DQPSK

5.3. Iterative Multiple Symbol Phase Estimation

Although the implementation complexity of MSPE is clearly lower than MSDD, in the receivers with DSP that applies interleaving architecture for the hardware parallelization (see Section 4.2.1), it is not suitable to perform algorithm with feedback structure like MSPE. Therefore, an iterative form of MSPE does not contain any feedback structure and can be simply adapted in the DSP with interleaving parallelization. This iterative form of MSPE is proposed by the author in [103]. In comparison to MSDD, which also does not contain any feedback structure, the iterative MSPE has lower implementation complexity and better performance.

5.3.1. Derivation and Structure

The phase estimation of MSPE from Eq.(5.29) can be rewritten in sum and product form as

$$z_k = u_k + \sum_{i=1}^{k} \left(w^i \cdot u_k \cdot \prod_{ii=1}^{i-1} \left[u_{k-ii} \cdot \exp(-j \cdot \hat{\varphi}_{d,k-ii}) . \right] \right) . \tag{5.30}$$

The construction of MSPE as shown in Eq.(5.30) can be directly implemented with the data-aided approach as shown in [102]. However, from Eq.(5.30) the length of summation can be indefinitely increased for very large k. In order to limit the implementation complexity,

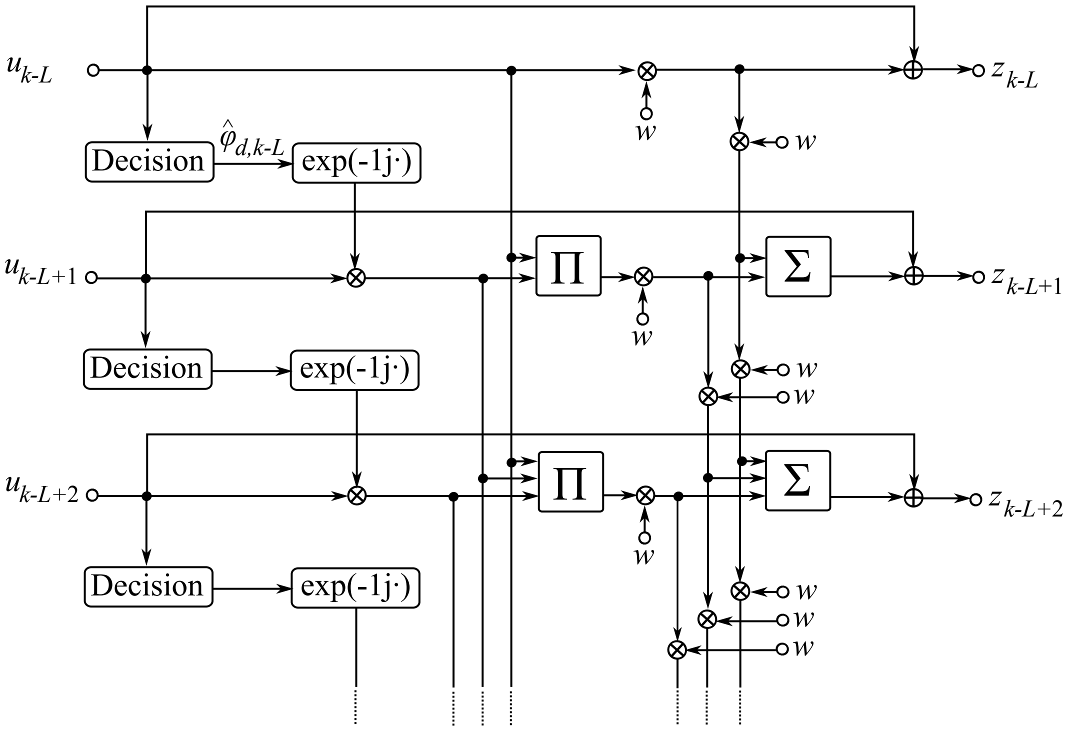

Figure 5.11.: Feed forward MSPE with a decision directed approach applying the interleaving parallelization architecture

Eq.(5.30) can be rewritten as

$$z_k = u_k + \sum_{i=k-L}^{k} \left(w^i \cdot u_k \cdot \prod_{ii=1}^{i-1} \left[u_{k-ii} \cdot \exp(-j \cdot \hat{\varphi}_{d,k-ii}) . \right] \right), \tag{5.31}$$

where L is the estimation length of MSPE. It should be emphasized that the implementation complexity is linearly increased with L. In comparison to MSDD, where the implementation complexity is exponentially increased with L, the construction of MSPE as shown in Eq.(5.31) has much lower implementation complexity.

An alternative approach to the data-aided is the decision-directed approach, where the data information can be obtained by performing a decision rule e.g., as shown in Figure 5.7. The decision-directed approach with interleaving parallelization is shown in Figure 5.11.

The main difference between the feed forward structure as shown in Figure 5.11 and the feedback in Figure 5.6 is that the estimated phase $\hat{\varphi}_{d,k}$ in the feedback structure has already the improved decision rule from the previous symbols. In contrast, in the feed forward structure, $\hat{\varphi}_{d,k}$ is directly estimated from u_k without any decision improvement. Hence, iterative multiple symbol phase estimation (IMSPE) is proposed by the author in [103]. The key idea of IMSPE is applying MSPE with the feed forward structure in multiple iterations and thus the decision of $\hat{\varphi}_{d,k}$ can be improved for each iteration.

However, the calculation of z_k without the decision improvement of $\hat{\varphi}_{d,k}$ induces error propagation in each iteration, which has the characteristic of burst errors. To avoid the error

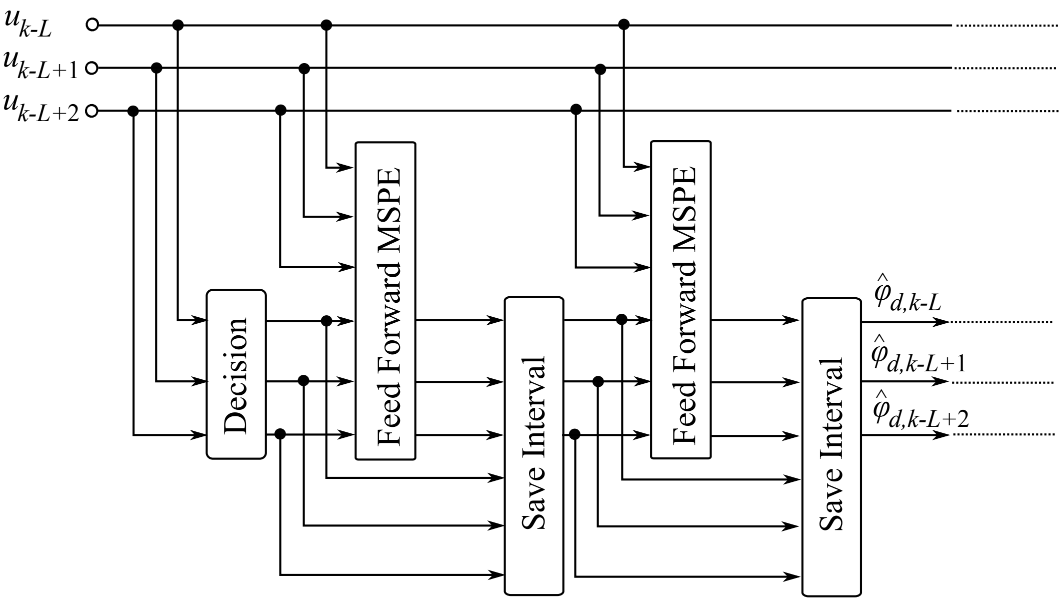

Figure 5.12.: Iterative MSPE with save interval for observation length of L, and iteration number of $N = 2$

propagation a save interval (SI) is applied between the iterations. Thereby, SI compares the estimated phase $\hat{\varphi}_{d,k}$ of the current iteration to the previous iteration. Note that $\varphi_{d,k,c}$ is defined as estimated phase from feed forward MSPE in the current iteration and $\varphi_{d,k,c}$ in the previous iteration. In order to detect burst error, the burst error length $l_{b,k}$ can be calculated using comparison of output signal from two feed forward MSPE as

$$l_{b,k} = \begin{cases} 0 & \text{, for } \varphi_{d,k,c} = \varphi_{d,k,p} \text{ or } l_{b,k-1} = L \\ l_{b,k-1} + 1 & \text{, else.} \end{cases} \tag{5.32}$$

Due to the fact that the feed forward MSPE has a memory length of L, the maximum burst error length induced by the feed forward MSPE is also L. In this case, $l_{b,k}$ will be reset and assigned to 0. With the calculation of $l_{b,k}$, the output estimated phase of SI $\varphi_{SI,k}$ can be given by

$$\varphi_{SI,k} = \begin{cases} \varphi_{d,k,p} & \text{, for } l_{b,k} > 0 \\ \varphi_{d,k,c} & \text{, else.} \end{cases} \tag{5.33}$$

In other words, if the burst errors occur ($l_{b,k} > 0$), the output signal from the feed forward MSPE in the current iteration contains error and SI uses the output signal from the previous iteration $\varphi_{d,k,p}$ as its output signal. On the other hand, if $\varphi_{d,k,p} \neq \varphi_{d,k,c}$ and $l_{b,k} = 0$, the difference between two iterations can be caused by the improvement of the feed forward MSPE and $\varphi_{d,k,c}$ is selected as the output signal.

Although with SI, the burst errors can be reduced, the decision improvement of consecutive phases is thereby avoided. In order to correct the consecutive phases, multiple iterations of feed forward MSPE with SI between iterations are applied and we call this structure IMSPE, which is illustrated in Figure 5.12.

5.3.2. Estimation Performance

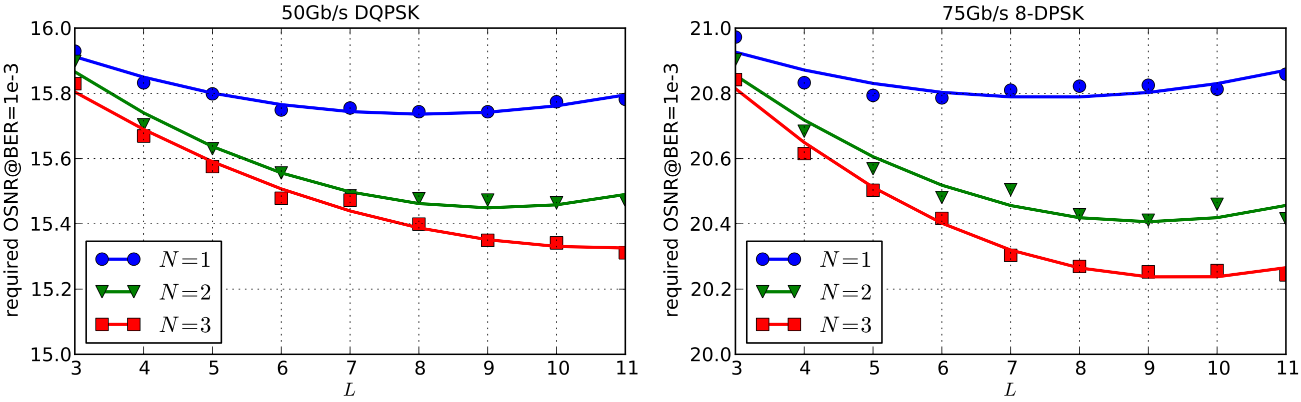

Figure 5.13.: Simulation results for OSNR performance vs. observation length L and number of iteration N for 50Gb/s DQPSK and 75Gb/s 8-DPSK with IMSPE

Like the performance evaluations for MSDD and MSPE as shown in Section 5.1.3 and 5.2.2, the optical back-to-back transmission without PolMux is simulated. Although IMSPE is a derivation of MSPE, the performance of IMSPE does not strongly depend on the forgetting factor w like MSPE, since burst errors are reduced by SI. In stead of w, the performance of IMSPE depends more on the observation length L and the number of iteration N.

Figure 5.13 shows that the OSNR performance of IMSPE depends on the observation length L and the number of iteration N for 50Gb/s DQPSK and 75Gb/s 8-DPSK. Since the performance improvement for DBPSK applying MSPE and also IMSPE is marginal, the performance difference varying L and N is not observable and is not shown here. From Figure 5.13, it can be seen that the optimal performance can be obtained with $L \geq 8$ for DQPSK and 8-DPSK. Hence, we use $L = 8$ for the further performance evaluations. For the iteration number N, the simulation results show that the performance for DQPSK and 8-DPSK can be improved by increasing N up to $N = 3$.

Figure 5.14 depicts the BER performance of IMSPE in comparison to the coherent detection, the coherent detection with differential encoding/decoding and MSPE for DBPSK, DQPSK and 8-DPSK respectively. The simulation results for DBPSK show that, with $N = 1$, where the implementation complexity is minimal, there is no performance difference between the recursive MSPE and IMSPE. In contrast, the performance of IMSPE with $N \geq 3$ is close to recursive MSPE for higher modulation formats like DQPSK and 8-DPSK. However, the performance difference between the recursive MSPE and IMSPE is increased with higer modulation formats e.g. the difference is 0.1dB for DQPSK and 0.2dB for 8-DPSK.

The tolerance of the IMSPE against CD for 50Gb/s DQPSK in comparison to the recursive MSPE is shown in Figure 5.15. Like the recursive MSPE, the performance gain of the IMSPE

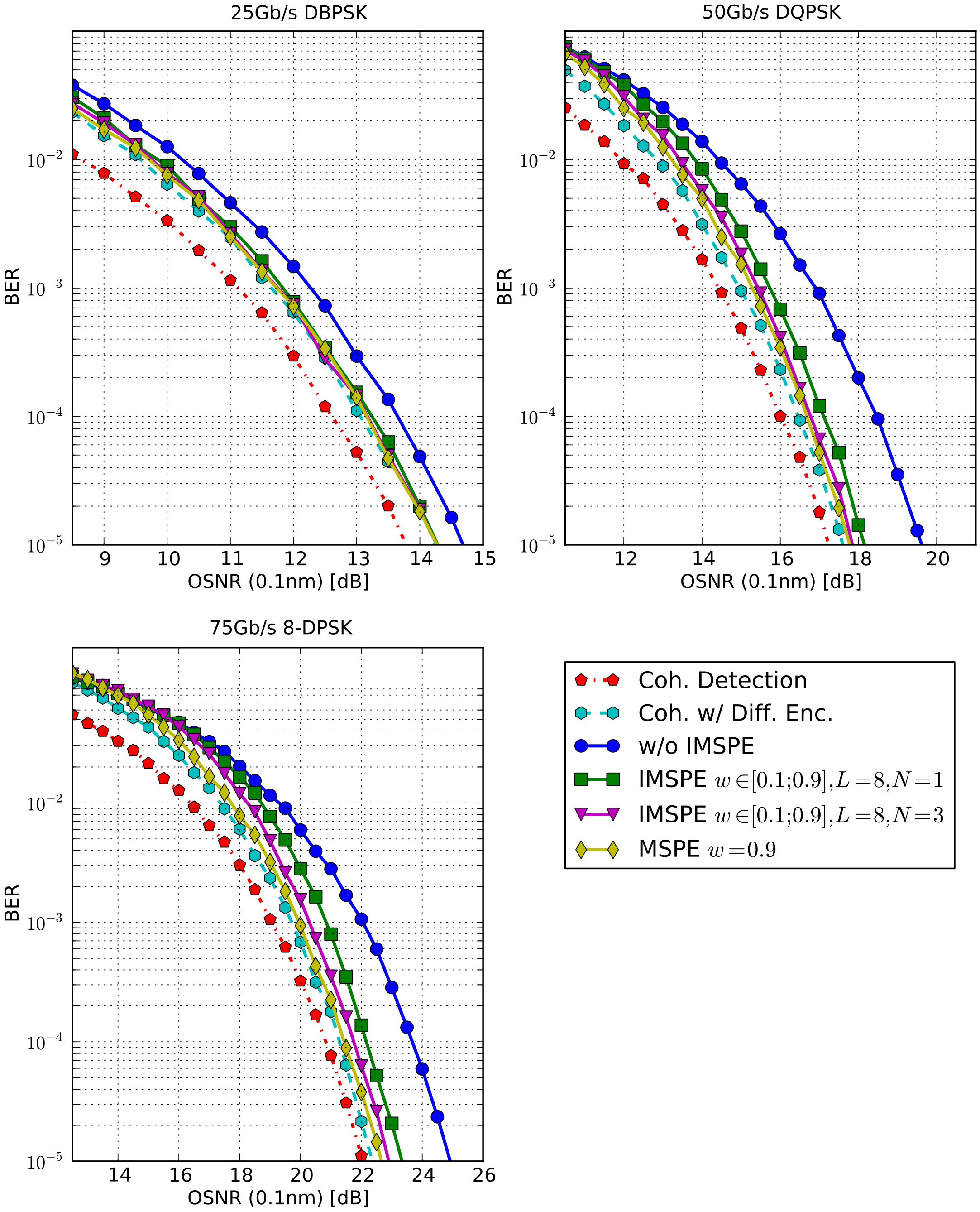

Figure 5.14.: IMSPE estimation performance in comparison to coherent detection and coherent detection with differential encoding/decoding for 25Gb/s DBPSK, 50Gb/s DQPSK and 75Gb/s 8-DPSK

is decreased by increasing CD. For the residual CD in interval [-100ps/nm;100ps/nm], the performance gain of the recursive MSPE and the IMSPE with $N = 3$ is roughly the same. For higher CD, however, the performance gain of the IMSPE is rapidly decreased and the difference between the recursive MSPE and the IMSPE is significant.

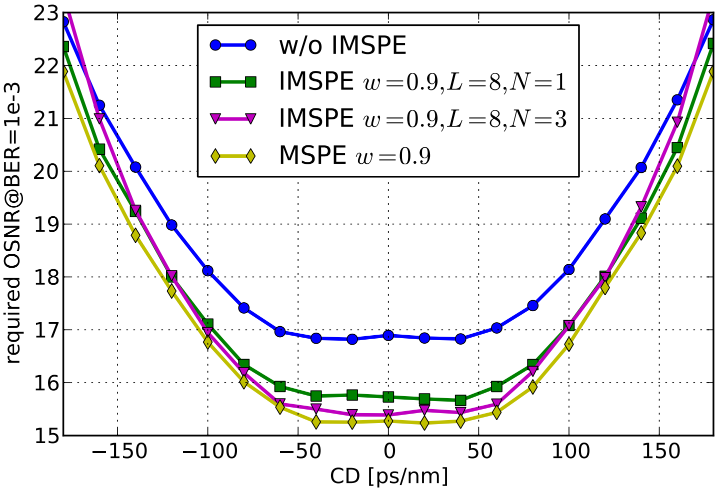

Figure 5.15.: IMSPE estimation performance vs. residual chromatic dispersion for 50Gb/s DQPSK

The other similarity of IMSPE to MSPE is the tolerance against the channel nonlinearities. For the evaluation, 50Gb/s QPSK is transmitted over the simulated optical channel with in-line compensation as described in Section 3.6 and the signal launch power of 2dBm. It can be assumed that the whole CD is compensated and PMD is neglected, hence, the performance loss depicted in Figure 5.16 is caused by the channel nonlinearities. Like MSPE, the performance improvement of IMSPE is decreased by increasing transmission distance and hence the channel nonlinearities due to the impact to the decision and data recovery.

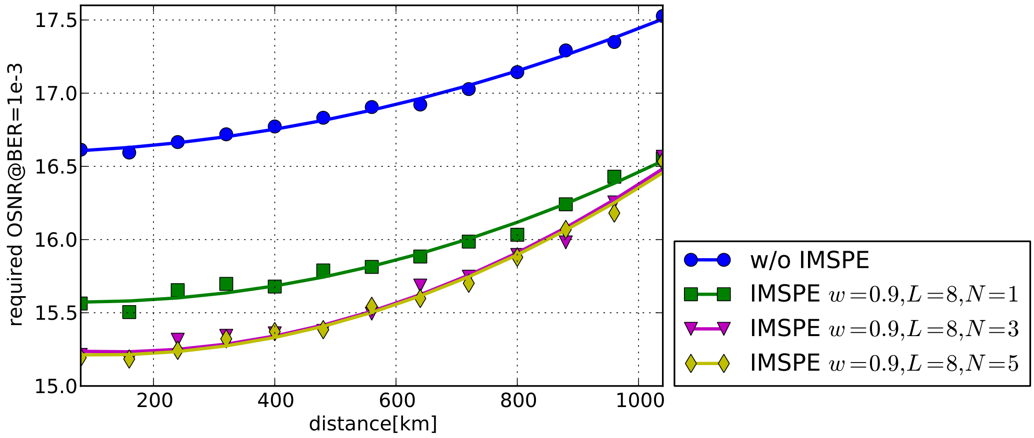

Figure 5.16.: IMSPE estimation performance vs. transmission distance for 50Gb/s DQPSK

5.4. Conclusions

In this chapter, the DSP based on the data and phase estimation over multiple symbols for the optical differential phase detection has been described. The significant performance improvement can be achieved from all algorithms namely MSDD, MSPE and IMSPE. Not only the performance improvement but also the implementation complexity must be considered for choosing suitable algorithms. Although MSDD has a feed forward structure, due to the exponential growth with M and L, its implementation is only suitable for lower order modulation format like DBPSK ($M = 2$) or with limited estimation block length L.

An recursive alternative of MSDD is MSPE. In comparison to MSDD, with MSPE the implementation complexity is strongly reduced and the performance can be further improved. With optimal forgetting factor w, the performance of MSPE is close to the performance of the coherent detection with the differential encoding/decoding. Since the last previous decided symbol is always required for the signal processing, MSPE is not a suitable DSP for the high speed transmission system with hardware parallelization for DSP. Also with Superscalar parallelization architecture as shown in Section 4.2, the processing delay can be reduced but not completely avoided. Hence, the implementation of MSPE can be complicated in high bit-rate optical transmission systems.

To resolve the implementation problem of MSPE, IMSPE is proposed. The IMSPE has a feed forward structure and can be simply parallelized. Although, IMSPE has a higher implementation complexity in comparison to MSPE, the implementation complexity of IMSPE is proportional to L, unlike MSDD, where the implementation complexity grows exponentially with L. The performance of IMSPE is approximately equal to MSPE and also close to the coherent detection with the differential encoding/decoding. Due to the feed forward structure, the implementation complexity and the performance improvement, IMSPE proposed from the author is the most suitable algorithm for high bit-rate optical transmission system with differential phase detection technique, from three algorithms described in this chapter.

6. Feed Forward Carrier Recovery

Due to cost efficiency, DSP in the optical transmission system can be implemented with application-specific integrated circuits (ASIC) or field-programmable gate arrays (FPGA). However, the optical transmission rate is much faster than the processing rate of ASICs or FPGAs. Therefore, DSP included carrier synchronization must be parallelized for the hardware implementation. In optical transmission systems, the well-known and widely used parallelization architecture is the interleaving. For the interleaving parallelization, the feed forward carrier estimation enables efficient hardware implementation for DSP without performance degradations. Hence, feed forward carrier estimation is a attractive and preferred approach for the carrier synchronization in optical transmission systems with coherent receiver. In this chapter, various algorithms for the feed forward carrier estimation will be described and reviewed with performance evaluations.

6.1. M-Power Carrier Phase Estimation

M-power carrier phase estimation is the most well-known algorithm for carrier phase estimation in optical transmission systems, due to a low implementation complexity and a high tolerance against phase variations. The estimation is classified as a clock-aided but non-data-aided carrier phase recovery for M-PSK modulation formats. Due to the fact that the phase detection of M-ASK-PSK modulation formats is based on M-PSK, the estimation can be also applied for M-ASK-PSK.

6.1.1. Likelihood Function and Derivation

For a non-data-aided carrier phase recovery, not only the phase error $\tilde{\varphi}$ but also the data symbol b_k should be estimated. Based on Section 4.5, the likelihood function for the estimation can be given by

$$\Lambda(\vec{\boldsymbol{r}}|\tilde{\varphi}, b_k) = \exp\left(\frac{1}{N_0}\sum_{k=1}^{L}\mathrm{Re}\left\{r_k\hat{s}_k^*\right\} - \frac{1}{2N_0}\sum_{k=1}^{L}|\hat{s}_k|^2,\right). \tag{6.1}$$

In the next step of derivation, we define $v(t)$ as matched filter output of $r(t)$

$$v(t) = (r(t)\cdot\exp(2\pi t\Delta f)) * g(-t). \tag{6.2}$$

For the signal processing in digital domain, we define v_k as the sampled signal of $v(t)$ at $k \cdot T_s$. From Eq.(4.49), the first term in the exponential function of Eq.(6.1) can be approximately given by

$$\sum_{k=1}^{L} \mathrm{Re}\left\{r_k \hat{s}_k^*\right\} \approx \sum_{k=1}^{L} \mathrm{Re}\left\{v_k b_k^* \cdot \exp(-j\tilde{\varphi})\right\} \tag{6.3}$$

and the second term

$$\sum_{k=1}^{L} |\hat{s}_k|^2 \approx \sum_{k=1}^{L} |b_k|^2. \tag{6.4}$$

Substituting Eq.(6.3) and Eq.(6.4) into Eq.(6.1) yields [77]

$$\Lambda(\vec{\boldsymbol{r}}|\tilde{\varphi}, b_k) = \exp\left(\frac{1}{N_0}\sum_{k=1}^{L} \mathrm{Re}\left\{v_k b_k^* \cdot \exp(-j\tilde{\varphi})\right\} - \frac{1}{2N_0}\sum_{k=1}^{L} |b_k|^2\right). \tag{6.5}$$

For mathematical convenience, we multiply the right-hand side of Eq.(6.5) by any positive constant C_{MP}, which should be independent of $\tilde{\varphi}$ and b_k to avoid the consequences for our purpose. In particular, we take

$$C_{MP} = \exp\left(\frac{1}{2N_0}\sum_{k=1}^{L} |\hat{v}_k|^2\right) \tag{6.6}$$

and rearranging yields [77]

$$\begin{aligned}\Lambda(\vec{\boldsymbol{r}}|\tilde{\varphi}, b_k) &= \exp\left(-\frac{1}{2N_0}\sum_{k=1}^{L} \left|v_k \cdot \exp(-j\tilde{\varphi}) - b_k\right|^2\right) \\ &= \prod_{k=1}^{L} \exp\left(-\frac{1}{2N_0}\left|v_k \cdot \exp(-j\tilde{\varphi}) - b_k\right|^2\right). \end{aligned} \tag{6.7}$$

In the next step, the data symbol b_k in Eq.(6.7) should be averaged out to make the likelihood function independent of b_k. For the purpose, we denote P_m of the constellation points of the given M-PSK modulation format with $m \in 1, 2, 3, ..., M$. With the assumption of independent symbols, the expectation of the likelihood function can be calculated by a factor-by-factor basis and can be rewritten as [77]

$$\Lambda(\vec{\boldsymbol{r}}|\tilde{\varphi}) = \prod_{k=1}^{L}\left(\frac{1}{M}\sum_{m=1}^{M} \exp\left(-\frac{1}{2N_0}\left|v_k \cdot \exp(-j\tilde{\varphi}) - P_m\right|^2\right)\right). \tag{6.8}$$

According to Eq.(4.4.3), the ML estimate can be achieved by choosing $\tilde{\varphi}$ that maximizes $\Lambda(\vec{\boldsymbol{r}}|\tilde{\varphi})$. Unfortunately, the likelihood function cannot be directly calculated. However, we can apply the approximate methods with the assumption of either high or low SNR.

For the M-PSK modulation format, the constellation points can be written as

$$P_m = \exp\left(j\frac{2\pi m}{M}\right). \tag{6.9}$$

Substituting P_m into Eq.(6.8) and with some normal manipulations, the likelihood function can be given by

$$\Lambda(\vec{\boldsymbol{r}}|\tilde{\varphi}) = \frac{1}{4E_s}\prod_{k=1}^{L}\left(\frac{1}{M}\sum_{m=1}^{M}\exp\left(\frac{2E_s}{N_0}\mathrm{Re}\left\{v_k\cdot\exp\left(j\left(\frac{2\pi m}{M}-\tilde{\varphi}\right)\right)\right\}\right)\right). \tag{6.10}$$

For the simplification, instead of $\Lambda(\vec{\boldsymbol{r}}|\tilde{\varphi})$, we can maximize its logarithm

$$\Lambda^{log}(\vec{\boldsymbol{r}}|\tilde{\varphi}) = \sum_{k=1}^{L}\ln\left(\frac{1}{M}\sum_{m=1}^{M}\exp\left(\frac{2E_s}{N_0}\mathrm{Re}\left\{v_k\cdot\exp\left(j\left(\frac{2\pi m}{M}-\tilde{\varphi}\right)\right)\right\}\right)\right), \tag{6.11}$$

where additive term $\ln\left(\frac{1}{4E_s}\right)$ has been dropped. With the relation

$$\begin{aligned}2\mathrm{Re}\left\{v_k\cdot\exp\left(j\left(\frac{2\pi m}{M}-\tilde{\varphi}\right)\right)\right\} \quad &= \quad v_k\cdot\exp\left(j\left(\frac{2\pi m}{M}-\tilde{\varphi}\right)\right)+\\ &\quad\ v_k^*\cdot\exp\left(j\left(\tilde{\varphi}\ -\frac{2\pi m}{M}\right)\right)\end{aligned} \tag{6.12}$$

and

$$\begin{aligned}\left[\frac{2E_s}{N_0}\mathrm{Re}\left\{v_k\cdot\exp\left(j\left(\frac{2\pi m}{M}-\tilde{\varphi}\right)\right)\right\}\right]^p \quad &= \quad \left(\frac{2E_s}{N_0}\right)^p\sum_{q=0}^{p}\binom{p}{q}\cdot v_k^q\cdot(v_k^*)^{p-q}\cdot\\ &\quad\ \exp\left(j(p-2q)\left(\tilde{\varphi}\ -\frac{2\pi m}{M}\right)\right)\end{aligned} \tag{6.13}$$

and expanding the exponential in Eq.(6.11) into power series yields

$$\begin{aligned}&\exp\left(\frac{2E_s}{N_0}\mathrm{Re}\left\{v_k\cdot\exp\left(j\left(\frac{2\pi m}{M}-\tilde{\varphi}\right)\right)\right\}\right)\\ &\quad=\sum_{p=0}^{\infty}\frac{1}{p!}\left(\frac{2E_s}{N_0}\right)^p\sum_{q=0}^{p}\binom{p}{q}\cdot v_k^q\cdot(v_k^*)^{p-q}\cdot\exp\left(j(p-2q)\left(\tilde{\varphi}\ -\frac{2\pi m}{M}\right)\right).\end{aligned} \tag{6.14}$$

Due to the fact that

$$\exp\left(j(p-2q)\frac{2\pi m}{M}\right) = 0 \tag{6.15}$$

for

$$p-2q = l\cdot M \text{ with } l\in\mathbb{Z} \tag{6.16}$$

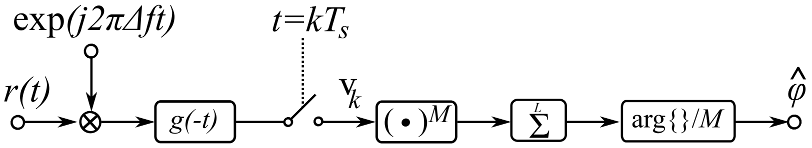

Figure 6.1.: Block diagram of M-power phase estimation

we have only a pair of $(p, q) = (0, 0)$ for $l = 0$. For $l = 1$, we have

$$(p, q) = (0, M), (1, M + 2), (2, M + 4), ... \tag{6.17}$$

and for $l = -1$

$$(p, q) = (M, M), (M + 1, M + 2), (M + 2, M + 4), ... \tag{6.18}$$

For the further derivation, we assume that E_s/N_0 is so sufficiently small that power of E_s/N_0 is greater than M and can be neglected [104]. Then, Eq.(6.11) reduces to

$$\Lambda^{log}(\vec{\boldsymbol{r}}|\tilde{\varphi}) \approx \sum_{k=1}^{L} \ln \left(1 + \frac{2}{M!} \left(\frac{E_s}{N_0} \right)^M \operatorname{Re} \left\{ v_k^M \exp(-jM\tilde{\varphi}) \right\} \right). \tag{6.19}$$

With the approximation of $\ln(1 + \varepsilon) \approx \varepsilon$, Eq.(6.19) can be rewritten as [77]

$$\Lambda^{log}(\vec{\boldsymbol{r}}|\tilde{\varphi}) \approx \operatorname{Re} \left\{ \exp(-jM\tilde{\varphi}) \sum_{k=1}^{L} v_k^M \right\}, \tag{6.20}$$

where a positive factor independent of $\tilde{\varphi}$ is neglected for simplicity.

Based on the ML estimation as shown in Eq.(4.4.3), the estimated phase $\hat{\varphi}$ that maximizes $\Lambda^{log}(\vec{\boldsymbol{r}}|\hat{\varphi})$ in Eq.(6.20), can be given by

$$\hat{\varphi} = \frac{1}{M} \arg \left\{ \sum_{k=1}^{L} v_k^M \right\}. \tag{6.21}$$

The algorithm for carrier phase estimation from Eq.(6.21) is a so-called M-power carrier phase estimation and its block diagram is illustrated in Figure 6.1. It should be emphasized that in the M-power algorithm, $\hat{\varphi} \in [-\pi/M; \pi/M]$, since $\arg\{\} \in [-\pi; \pi]$. And the M-fold ambiguity problem occurs, which can be solved by applying the differential encoding/decoding as shown in Section 3.3.2.

The M-power estimation can be interpreted as following. By the computation of v_k^M and recognizing that $b_k^M = 1$ for any PSK yields

$$v_k^M = \exp(jM\tilde{\varphi}) + N_k, \tag{6.22}$$

where N_k is a zero-mean noise term resulting from the product of *Signal·Noise* and *Noise·Noise*. As we can see that the modulation has been removed from v_k^M. Therefore taking the average of v_k^M over the observation interval can smooth out N_k and produce a vector that deviates little from the direction of $\exp(jM\tilde{\varphi})$. Hence, the argument of such a vector can be observed as an estimate of the carrier phase.

It should be noted that the summation in Eq.(6.21) can be replaced with a Wiener filter for the performance optimization [105, 106]. However, an additional implementation complexity is required and the undesigned feedback must be considered.

6.1.2. Estimation Performance

Note that the AWGN channel is assumed. The variance of the estimated phase is evaluated with Monte-Carlo simulation method and compared with the MCRB lower bound. Figure 6.2 shows the phase error variance of an M-power carrier phase estimation with an estimation length of L= 200 for various modulation formats. The phase error variance in Figure 6.2 depends on SNR, which is defined as

$$\mathrm{SNR} = 10 \cdot \log\left(\frac{E_s}{N_0}\right). \tag{6.23}$$

It should be noted that the phase estimation for 16-ASK-PSK is equal to 8-PSK. Hence, the performance of both modulation formats is comparable as shown in Figure 6.2. It can be seen that for a higher SNR, phase error variance of QPSK is close to MCRB. That is M-power carrier phase estimation is an optimal phase synchronization for QPSK with the high SNR. For higher order modulation formats like 8-PSK and 16PSK, however, the difference between phase error variance and MCRB is significant.

In high bit-rate optical transmission systems, the M-power estimation algorithm are applied to solve many problems related to the phase estimation. The laser linewidth tolerance is an important aspect for the performance evaluations of the carrier phase estimation, which was intensively studied in the last years. In [3, 107, 108], the M-power estimation is applied to compensate the phase variations caused by the laser linewidth for PolMux-QPSK modulation format. For higher order modulation formats, further investigations are shown in [109, 110].

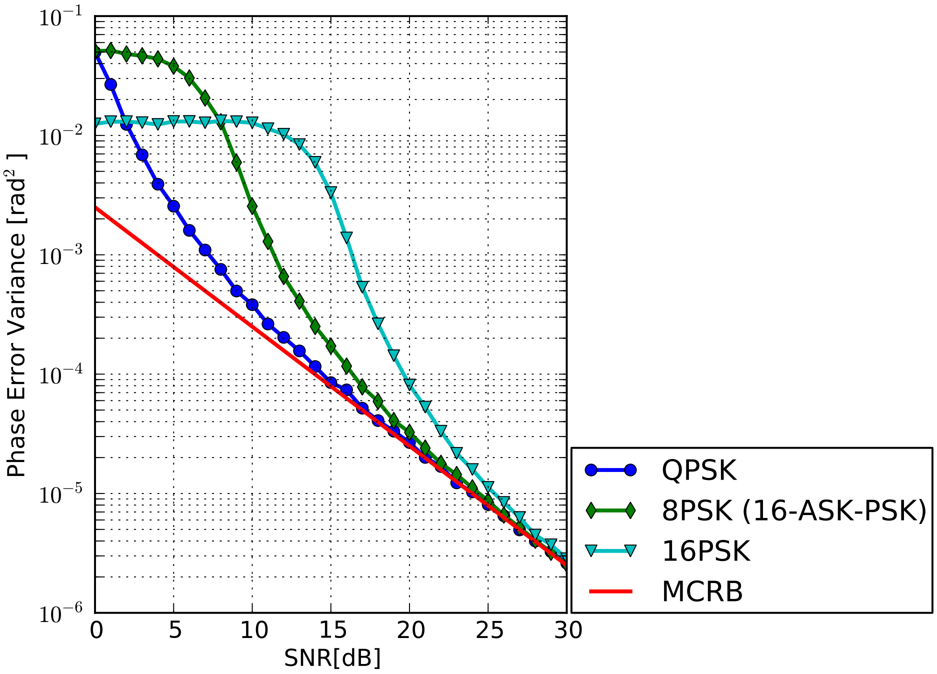

Figure 6.2.: Simulation results for performance of M-power phase estimation with L=200

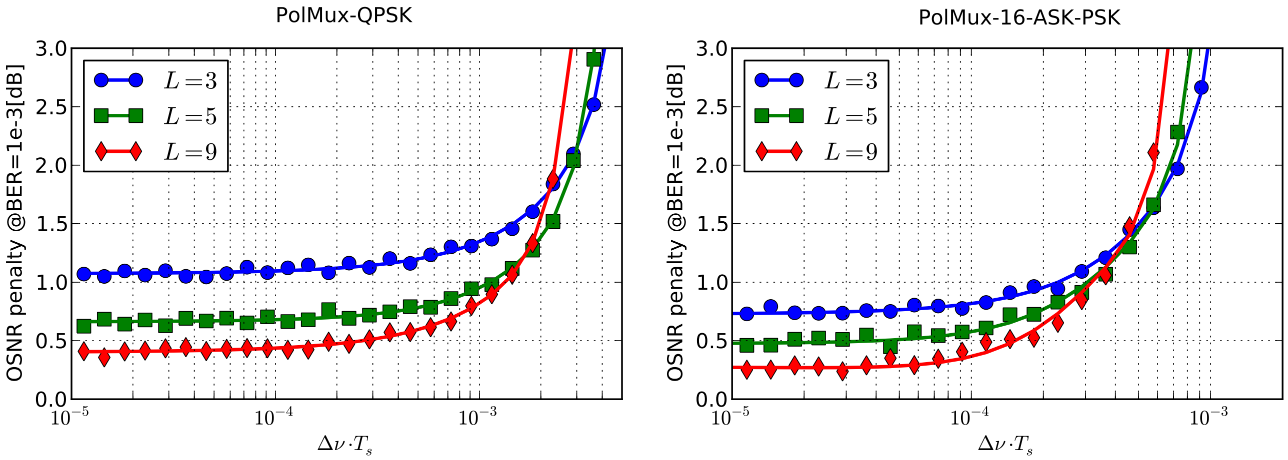

Figure 6.3.: Simulation results for laser linewidth $\Delta\nu$ vs. OSNR penalty for PolMux-QPSK and PolMux-16-ASK-PSK with M-power phase estimation

To separate the laser linewidth impacts, the back-to-back is performed with the receiver setups as shown in Section 3.5.3. Figure 6.3 shows the simulation result for the laser linewidth tolerance of the M-power estimation for PolMux-QPSK with various L. For the generalization of the simulation results, the product $\Delta\nu \cdot T_s$, which is independent of the transmission baud-rate, is defined.

Figure 6.3 depicts the laser linewidth tolerance of the M-power phase estimation for PolMux-QSPK and PolMux-16-ASK-PSK modulation formats. It can be seen that with M-power phase estimation, a very high tolerance against the laser linewidth can be achieved. However, its performance strongly depends on the estimation block length L. For a higher number of L, we have a narrow bandwidth of the averaging filter in the estimation structure, and a better noise suppression for a small laser linewidth can be performed. In contrast, for the large laser linewidth, averaging filters with a broader bandwidth are required. They can be obtained decreasing L. Hence, a lower number of L is more suitable for a larger laser linewidth.

For PolMux-16-ASK-PSK, the results show that the M-power estimation is also suitable and the performance characteristics are very similar to the PolMux-QPSK. It must be emphasized that the bandwidth of the M-power estimation for PolMux-16-ASK-PSK is basically narrower than for PolMux-QPSK due to the higher M. Hence, it can better suppress phase noise caused by amplified spontaneous emission noise (ASE-noise) (see Section A.6) and has lower tolerance against the laser linewidth.

Although an additional carrier frequency estimation at the receiver side can be assumed, in the most cases, an ideal frequency synchronization cannot be achieved. In this situation, the carrier phase estimation must be robust against the residual frequency offset, which depends on system configurations and the performance of the applied additional carrier frequency estimation. Hence, the back-to-back simulation is performed to evaluate tolerance of the M-power estimation algorithm against the residual frequency offset. The simulation results in Figure 6.4

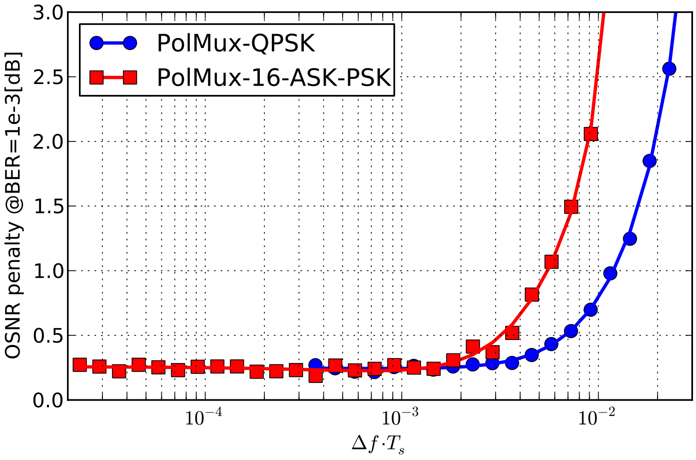

Figure 6.4.: Simulation results residual frequency offset Δf vs. OSNR penalty for PolMux-QPSK and PolMux-16-ASK-PSK with M-power phase estimation

for PolMux-QPSK and PolMux-16-ASK-PSK with the optimized estimation block length show that the M-power phase estimation is very robust against the frequency offset. Therefore, for optical transmission systems with a low frequency offset, it is feasible to apply the M-power estimation for the carrier phase as well as carrier frequency estimation. With this approach, the implementation complexity of the DSP at the receiver side can be significantly reduced. It should be noted that the relation between the estimation block length L and the frequency offset is very similar to the laser linewidth as shown in Figure 6.3.

The tolerance of the carrier phase estimation against the laser instability as shown in Section 3.1.1 is an important requirement. For the investigation, 111Gb/s PolMux-QPSK with AWGN channel is simulated. Moreover, the laser linewidth $\Delta\nu$ = 100kHz is considered. Since $\Delta\nu$ =

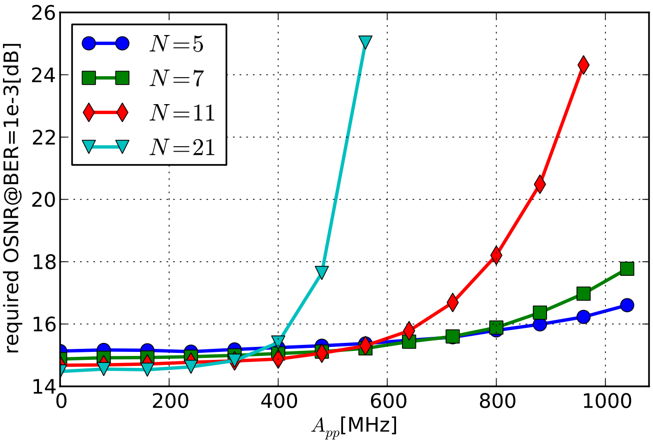

Figure 6.5.: Simulation results for required OSNR for BER=10^{-3} vs maximum peak-to-peak of frequency variations A_{pp} for 111Gb/s PolMux-QPSK

100kHz is a standard requirement for the commercially available lasers. Figure 6.5 shows the required OSNR for BER=10^{-3} depends on maximum peak-to-peak of frequency variations A_{pp}. This is shown in Section 3.1.1 with the model of the stabilized laser from Eq.(3.7) and a modulation frequency of laser stabilization f_m =35kHz. It can be seen that with $L \leq 7$, frequency variations up to 500MHz can be tolerated. For higher values of L, however, the performance of the M-power algorithm is strongly degraded without a significant performance gain for lower A_{pp}.

Not only the phase variations caused by the laser but also by the channel nonlinearities like SPM and XPM can be compensated with the M-power phase estimation. Due to the fact that the channel nonlinearities are the main limitation of the transmission distance and performance, the compensation of these nonlinear phase variations attract more and more attention. It is shown in [4] that with the M-power estimation, the the transmission distance and performance can be significantly improved.

For the investigation of the M-power phase estimation tolerance against channel nonlinearities, a loop experiment with the setups as shown in Table 6.1 is performed. In this experiment, the generated PolMux-QPSK and the OOK signal are transmitted over the optical channel with in-line CD compensation (DM) as described in Section 3.6. The detailed setups of the experiment can be found in [111]. At the receiver side, the signal is detected with the optical frontend for coherent receivers (as described in Section 3.5) followed by a digital storage oscilloscope saving blocks of 10^6 samples for off-line processing. To compensate the polarization effects and the residual chromatic dispersion, T/2 spaced FIR filters for equalization are applied.

Figure 6.6 shows the BER performance of the M-power estimation with various estimation block length L versus launch powers. For the lower launch power, ASE-noise is the dominant impairment and the performance characteristics dependent on L are similar to the simulative evaluations, where BER decreases by increasing L. Due to the fact that the impact of the

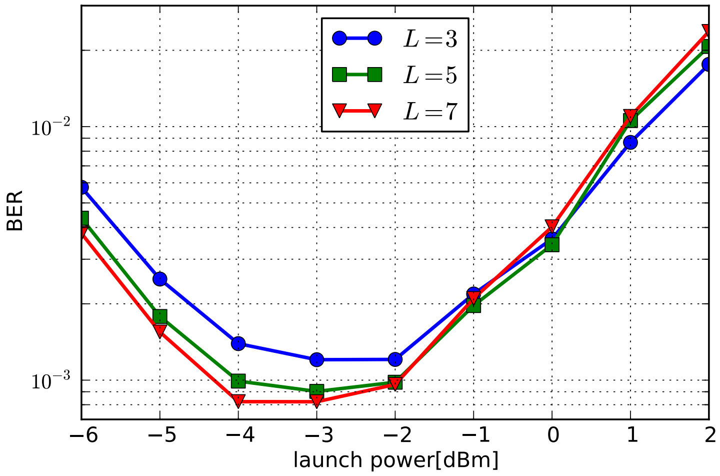

Figure 6.6.: BER vs. launch power for 111Gb/s PolMux-QPSK + 10x10.7Gb/s OOK with M-power estimation and various estimation block length L

Table 6.1.: Loop experiment setups

modulation format in central channel	PolMux-QPSK
modulation format in neighbor channels	OOK
bit-rate in central channel	111Gb/s
bit-rate in neighbor channels	10.7Gb/s
number of WDM channel	11
channel spacing	50GHz
optical filter bandwidth	44GHz
transmission distance	760km (8x95km SSMF)

channel nonlinearities is proportional to the launch power, and for a higher launch power, the nonlinearities like SPM and XPM are dominant. In this case, the BER performance for all L is approximately equal. Moreover, it can be seen from Figure 6.6 that the performance of the transmission system strongly depends on the launch power. The optimal launch power can be achieved by the balance point between the impact of ASE noise and the channel nonlinearities. In our experiment, the optimal launch power is around -4dBm.

6.2. Viterbi-Viterbi Algorithm

Viterbi-Viterbi algorithm (V&V) [112] is a generalization of the M-power estimation for a performance improvement especially at intermediate/low SNR values. In Section 6.2.1, we show that for some special case, V&V and M-power estimation are equal. In the optical transmission systems, V&V are mostly applied as this special case. Hence, V&V and M-power estimation have the same meaning in the optical transmission systems.

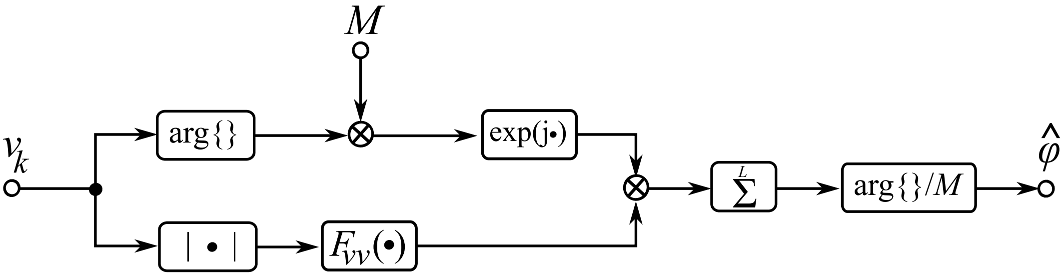

Figure 6.7.: Block diagram of Viterbi&Viterbi algorithm

6.2.1. Derivation

From Eq.(6.21), v_k can be written in the polar coordinate formula as

$$\begin{aligned} v_k &= a_{v_k} \cdot \exp(j \cdot \varphi_{v_k}), \text{ with} && (6.24)\\ a_{v_k} &= |b_k| \text{ and} && (6.25)\\ \varphi_{v_k} &= \arg\{b_k\}. && (6.26) \end{aligned}$$

Afterwards, v_k^M can be replaced by

$$w_k = F_{vv}\left(a_{v_k}\right) \cdot \exp(j \cdot M\varphi_{v_k}), \tag{6.27}$$

where $F_{vv}\left(a_{v_k}\right)$ is an appropriately chosen function of a_{v_k}. And the phase estimate can be given by [112, 77]

$$\hat{\varphi} = \frac{1}{M}\arg\left\{\sum_{k=1}^{L} F_{vv}\left(a_{v_k}\right) \cdot \exp(j \cdot M\varphi_{v_k})\right\}. \tag{6.28}$$

Block diagram of V&V algorithm is shown in Figure 6.7. Clearly, with $F_{vv}\left(a_{v_k}\right) = a_{v_k}^M$, the V&V algorithm is identical to the M-power estimation, which is the mostly used special case in the optical transmission systems.

In comparison to the M-power phase estimation, the implementation complexity can be reduced by V&V due to the separated computation of the phases and the amplitudes of the signal. Hence, the elimination of the complex number multiplications. Especially by setting $F_{vv}(a_{v_k})$ to a constant, only a real number multiplication is required for the phase estimation. Not only the implementation complexity can be reduced but also the estimation performance can be improved using the V&V algorithm as shown in the next section.

6.2.2. Estimation Performance

For the evaluation of the phase error variance, an AWGN channel is assumed. Figure 6.8 shows the phase error variance of the V&V algorithm for QPSK and 8-PSK modulation formats with $L = 200$ and various $F_{vv}\left(a_{v_k}\right)$ in comparison to MCRB. The evaluations show that $F_{vv}\left(a_{v_k}\right)$ has a minimal influence on the estimation especially for a higher SNR value. For a lower SNR value, the estimation can be improved by decreasing the order of $F_{vv}\left(a_{v_k}\right)$. This characteristic of V&V algorithm has the particular positive effect that the performance can be slightly improved and the implementation complexity can be reduced at the same time. Moreover, it can be seen that the performance characteristics of the V&V algorithm and the M-power phase estimation are very similar. Hence, a further performance investigation for V&V algorithm is not necessary.

Although V&V algorithm and the M-power phase estimation are similar in many aspects, V&V algorithm is more attractive for the hardware implementation. On the one hand, a complex multiplication requires four real number multiplications, the phase estimate with M-power power requires eight real number multiplications for QPSK and twelve for 8-PSK. On the other hand, the V&V algorithm with $F_{vv}\left(a_{v_k}\right) = $ constant requires just one real number

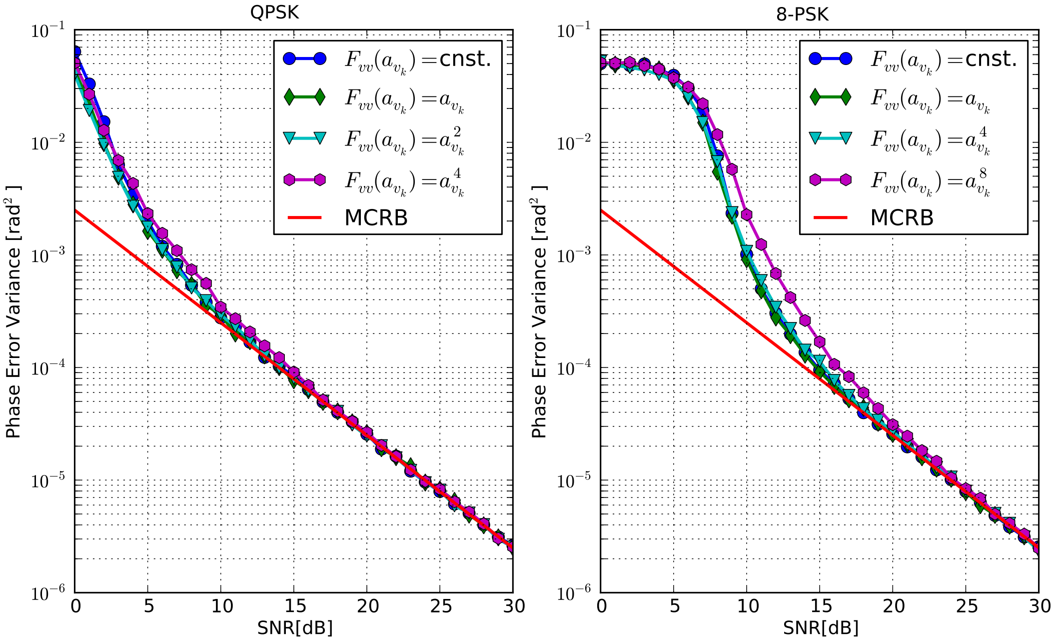

Figure 6.8.: Performance of V&V algorithm with L=200 and various F_{VV} for QPSK and 8-PSK

multiplication. Due to the fact that the required multiplication in V&V algorithm is performed between a real number and an integer in the form of 2^n, the multiplication can be further simplified to the binary bit shifting. It means that V&V algorithm can be implemented without any real number multiplication.

6.3. Polarization Coupled Carrier Phase Estimation

In [113, 114], the author has proposed polarization coupled carrier phase estimation (PCC), which based on the M-power algorithm and provide a significant performance improvement in comparison to M-power algorithm. In this section, the PCC is briefly described.

6.3.1. Algorithm Structure

Since the same LO is used for both polarizations, the frequency offset and the phase variations caused by the laser linewidth are very similar in x- and y-polarization. Moreover, it is shown in Section 2.4.1 and 2.4.1 that phase variations caused by the channel nonlinearities are correlated in both polarizations. In order to show the correlation between the phase variation in both polarizations, the phase variations of two polarizations from measured data are extracted by training symbols and are cross correlated. The cross correlation between the phase variation in

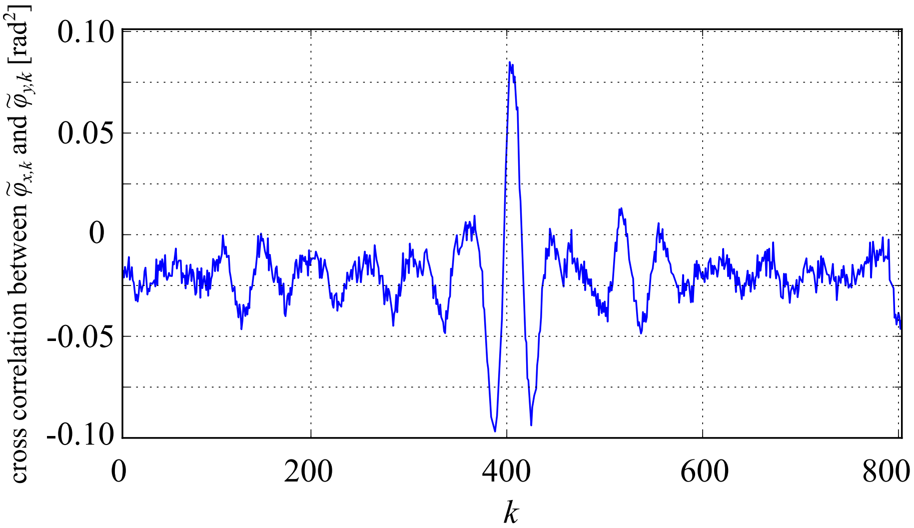

Figure 6.9.: Discrete cross correlation between phase variations of two polarizations

both polarizations $\varphi_{x,y}(t)$ can be given by

$$\varphi_{x,y}(\tau) = \lim_{T\to\infty} \frac{1}{2\cdot T} \int_{-T}^{+T} \tilde{\varphi}_x(t)\cdot\tilde{\varphi}_y(t+\tau)dt, \tag{6.29}$$

where $\tilde{\varphi}_x(t)$ and $\tilde{\varphi}_y(t)$ are phase variations in x- and y-polarization respectively. For the discrete phase variations $\tilde{\varphi}_{x,k}$ and $\tilde{\varphi}_{y,k}$ the discrete cross correlation $\varphi_{x,y,k}$ can be given by

$$\varphi_{x,y,k} = \lim_{N\to\infty} \frac{1}{2\cdot N} \sum_{i=-N}^{N} \tilde{\varphi}_{x,k}\cdot\tilde{\varphi}_{y,k+i}. \tag{6.30}$$

The discrete cross correlation is shown in Figure 6.9. It can be clearly seen that the phase variations of two polarizations are correlated. Hence, the information coupling in the phase variations of the polarizations can be applied to improve the performance of the carrier phase estimation as shown in [113, 115, 114].

Basically, the PCC as proposed by the author in [113, 114] is based on the M-Power estimation. Figure 6.10 shows the block diagram of the PCC algorithm. After the M^{th} power operation and

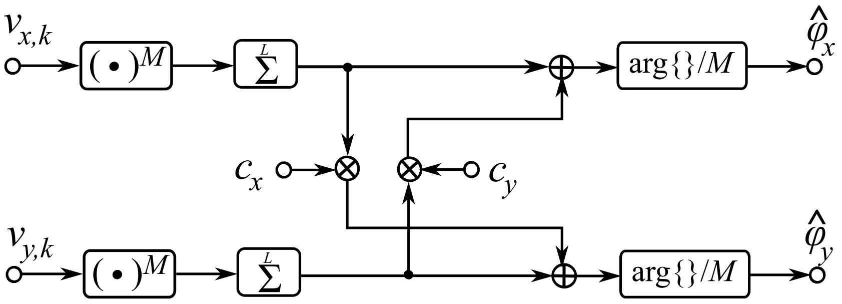

Figure 6.10.: Block diagram of polarization coupled carrier phase estimation

the summation, the computed signal between two polarizations is coupled. For the regulation of the coupled information, the coupling factors c_x and c_y with $0 \leq c_x, c_y \leq 1$ can be adjusted. In the case of an AWGN channel and/or the phase variations caused by local oscillator, c_x and c_y should be set to 1. With this setup, it can be seen that the duplication of the estimation block length L and the estimation accuracy can be improved. In contrast, in the presence of channel nonlinearities, c_x and c_y should be optimized considering the characteristics of the particular nonlinearities. It should be noted that the M^{th} power part of PCC can be replaced with V&V algorithm without any performance degradation to reduce the implementation complexity by avoiding multiplication as described in Section 6.2.2.

6.3.2. Estimation Performance

Figure 6.11 shows the phase error variance for PCC algorithm with $L = 200$ and various c_x, c_y for PolMux-QPSK and PolMux-8-PSK modulation formats in AWGN channel in comparison to the MCRB. Since the PCC algorithm is based on the M-power estimation, the characteristics of the phase error variance for both algorithms are similar. As we can see that for both modulation formats, the difference of the phase error variance to MCRB is significant for lower SNR, and is decreased by increasing SNR. It should be emphasized that the phase error variance for $c_x, c_y > 0$ can pass over the theoretical lower bound like MCRB. Since PCC uses the coupled information from two polarizations, the number of the signal samples for the summation must be considered. As we can see from Figure 6.11, with $c_x = c_y = 1.0$, the phase error variance is close to MCRB with $L = 400$ instead of $L = 200$. It means that, the estimation block length

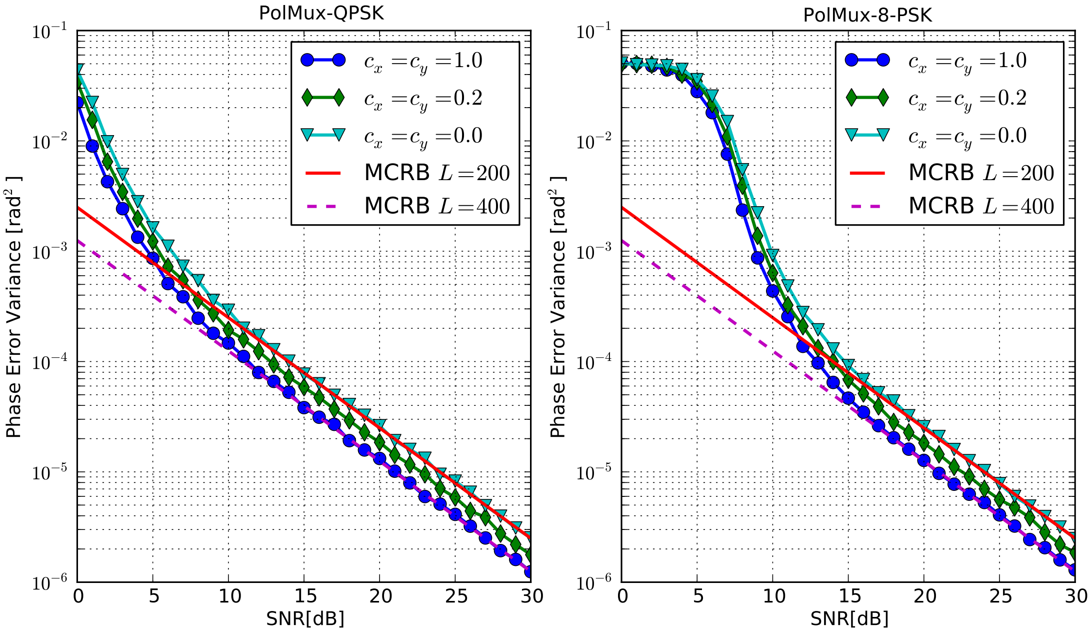

Figure 6.11.: Simulation results for performance of PCC algorithm with L=200 for QPSK and 8-PSK (16-ASK-PSK) in AWGN channel

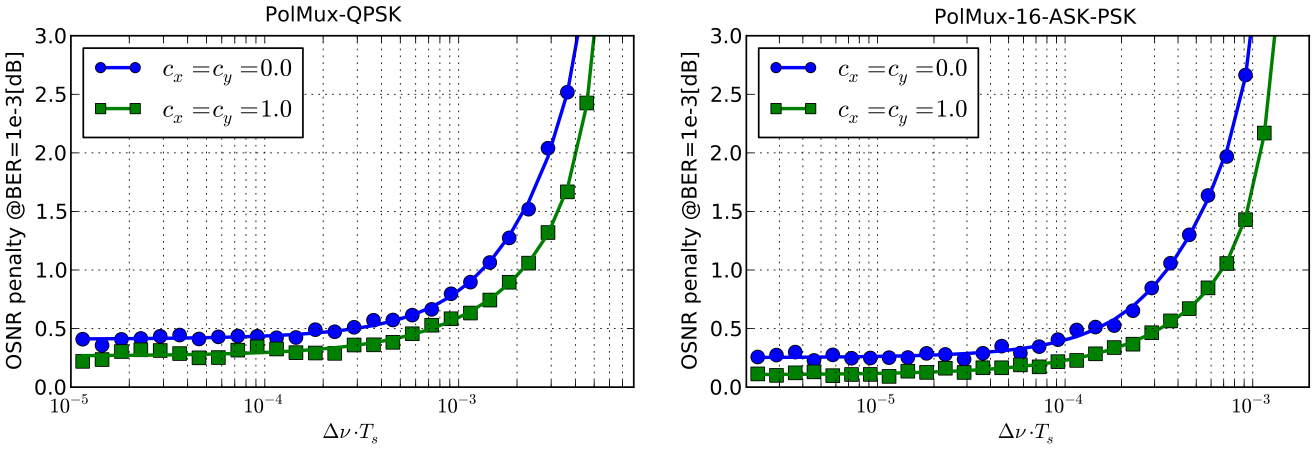

Figure 6.12.: Simulation results for laser linewidth vs. OSNR penalty for PolMux-QPSK and PolMux-16-ASK-PSK with PCC algorithm

L can be duplicated without additional complexity.

The tolerance of the PCC algorithm against the laser linewidth and the LO frequency offset is basically similar to the the M-power phase estimation as shown in Section 6.1.2. On the one hand, with a higher number of L, the bandwidth of the averaging filter is narrower and the noise can be better suppressed. On the other hand, with a lower number of L, we have the broadband averaging filter, and the tolerance against the laser linewidth and the LO frequency offset can be improved. Figure 6.12 shows the ONSR penalty dependent on the laser linewidth of PCC algorithm with optimized L for PolMux-QPSK and PolMux-16-ASK-PSK. It should be noted that, with $c_x = c_y = 0$, the PCC algorithm is equivalent to the M-power estimation. As we can see that with the phase coupling between the polarizations, the tolerance against the laser

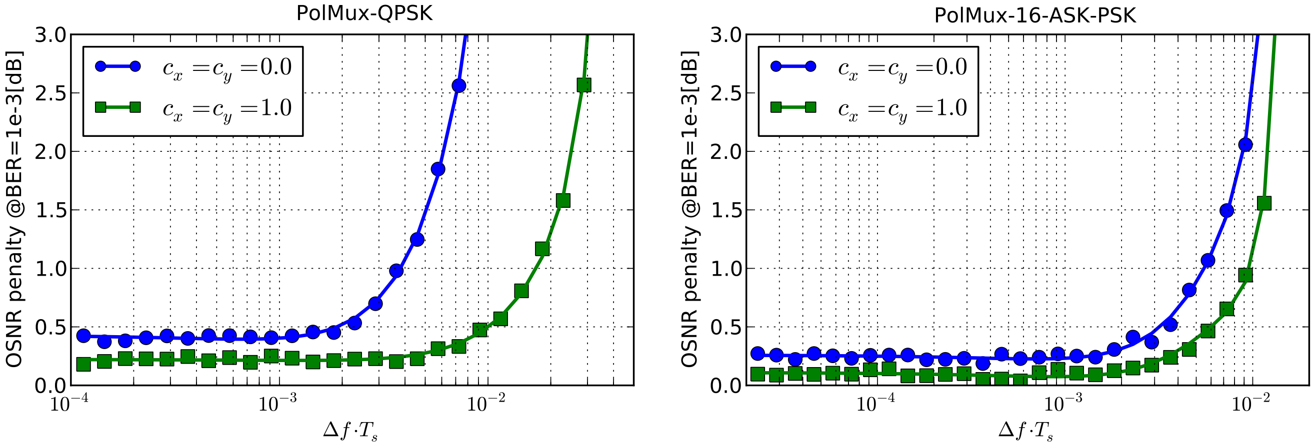

Figure 6.13.: Simulation results for residual frequency offset vs. OSNR penalty for PolMux-QPSK and PolMux-16-ASK-PSK with PCC algorithm

linewidth can be significantly improved because PCC can suppress the noise without increasing L and decreasing the filter bandwidth. For the tolerance against the residual frequency offset, the same characteristics as for the tolerance against the laser linewidth can be observed and are depicted in Figure 6.13.

Not only the tolerance against the laser linewidth and the LO frequency offset but also the tolerance against channel nonlinearities can be improved. For the demonstration, a loop experiment with the setups as shown in Table 6.2 is performed. The detailed description of the loop experiment can be found in [116]. It should be emphasized that in the experiment, the *LEAF fiber* is used in order to reduce the effect of CD. However, the channel nonlinearities in the LEAF fiber are higher in comparison to the SSMF. For the reduction of the channel nonlinearities especially XPM, the channel spacing is set to 200GHz. In this case, SPM is the dominant effect for channel nonlinearities.

Table 6.2.: Loop experiment setups

modulation format	PolMux-QPSK
baud-rate	27.75GBaud
bit-rate	111Gb/s
number of WDM channel	7
channel spacing	200GHz
optical filter bandwidth	44GHz
transmission distance	405km (5x81km *LEAF*)

The BER performance of the PCC algorithm with various coupling factors c_x, c_y dependent on the launch power for 111Gb/s PolMux-QPSK is depicted in Figure 6.14. The experimental results show that the optimal launch power is around -3dB, where the ASE-noise and the nonlinearity effects are on the balance point. The estimation block length is optimized and set to $L = 5$. As we can see from the coupled information between the polarizations, the tolerance to

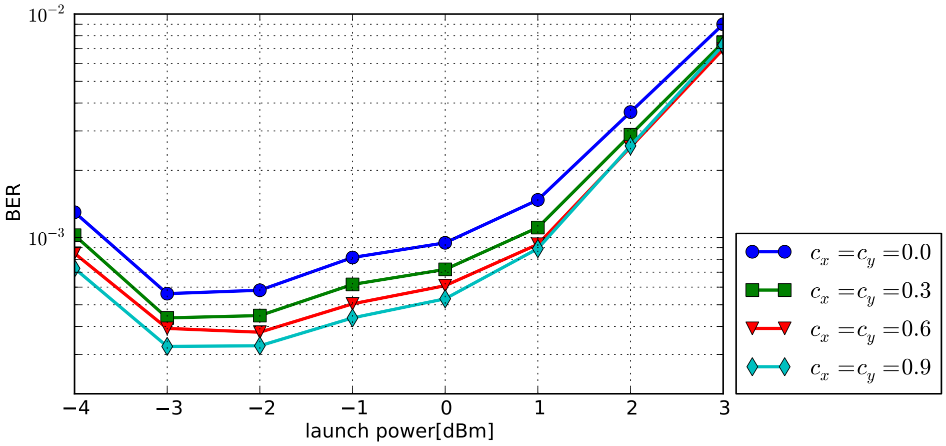

Figure 6.14.: Measured BER vs. launch power for 111Gb/s PolMux-QPSK with PCC algorithm $L = 5$ and various coupling factors c_x, c_y

nonlinearities can be significantly improved. In this case, the best performance can be achieved with $c_x = c_y = 0.9$, where the BER performance can be improved up to 200%. Unlike in the AWGN channel, $c_x = c_y = 1.0$, PCC becomes unstable, and the BER performance cannot be evaluated. In [113], it is shown that the optimal coupling factors depend on the characteristics of the channel nonlinearities.

6.4. Differential Phase Frequency Estimation

Although with algorithms based on the M-power estimation LO frequency offsets can be tolerated, at the start-up of an optical link with coherent demodulation the frequency offset can be in the range of GHz [117]. Thus the LO frequency offset can exceed the limitation of the algorithms. In these situations, an additional frequency offset estimation must be used. For the PSK based modulation format like PolMux-QPSK and PolMux-16-ASK-PSK, differential phase frequency estimation (DPFE) can be applied in combination with the M-power estimation and its derivatives to improve the LO frequency offset tolerance. In this section, DPFE is briefly described with performance evaluations.

6.4.1. Derivation and Structure

In the following, the derivation of DPFE proposed by the author is described. Basically, DPFE is based on the same principle as the *frequency estimation via phase incremental estimation* [48, 77]. It can be classified as a non-data-aided and non-timing-aided carrier frequency estimator. With an assumption of high SNR and negligible phase noise, the frequency offset $\Delta\hat{f}_k$ can be estimated by

$$\Delta\hat{f}_k = \frac{(\hat{\varphi}_k - \hat{\varphi}_{k-1})}{T_s}. \tag{6.31}$$

With

$$\Delta\hat{\varphi}_k = \hat{\varphi}_k - \hat{\varphi}_{k-1}, \tag{6.32}$$

Eq.(6.31) can be rewritten as

$$\Delta\hat{f}_k = \frac{\Delta\hat{\varphi}_k}{T_s}. \tag{6.33}$$

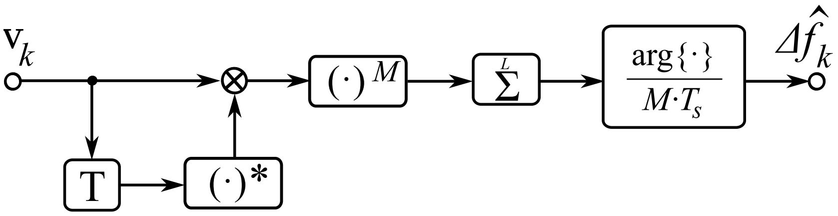

Figure 6.15.: Block diagram of differential phase frequency estimation

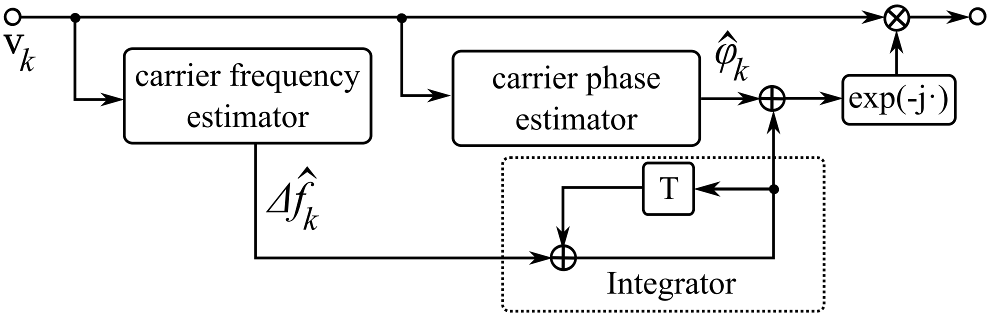

Figure 6.16.: Carrier phase and frequency correction in one step

Note that $\Delta\hat{\varphi}_k$ can be observed as the estimated phase of the differential demodulated signal as shown in Section 3.4. In the next step, we define $v_{d,k}$ as the digital differential demodulated signal which can be given by

$$v_{d,k} = v_k \cdot v_{k-1}^*, \tag{6.34}$$

where v_k is the sampled signal from the matched filter. With Eq.(6.34) and the M-power estimation, $\Delta\hat{\varphi}_k$ can be estimated by

$$\Delta\hat{\varphi}_k = \frac{1}{M} \cdot \arg\left\{\sum_{k=1}^{L}(v_k \cdot v_{k-1}^*)^M\right\}. \tag{6.35}$$

Finally, substituting Eq.(6.35) into Eq.(6.31) yields

$$\Delta\hat{f}_k = \frac{1}{M \cdot T_s} \cdot \arg\left\{\sum_{k=1}^{L}(v_k \cdot v_{k-1}^*)^M\right\}. \tag{6.36}$$

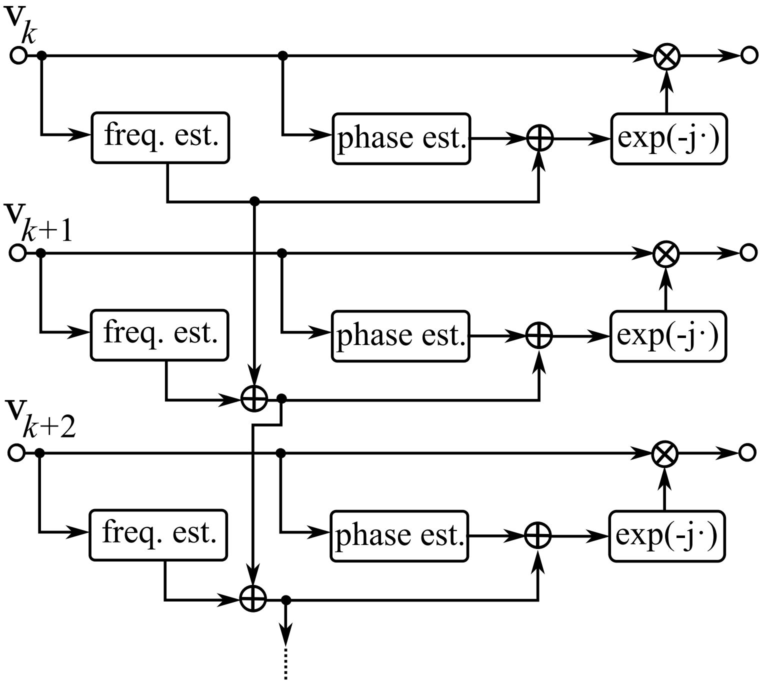

Figure 6.17.: Integrator replacement with summation for carrier phase and frequency correction

Figure 6.15 shows the block diagram of DPFE based on Eq.(6.36). Since DPFE is based on the M-power estimation, we can also apply V&V and PCC algorithms on the phase estimation part of DPFE.

For the reduction of the implementation complexity, we can correct the carrier phase and frequency in one step as shown in Figure 6.16. As we can see from Figure 6.16 the correction of the frequency offset requires an integrator that contains a feedback and breaks the feed forward structure. To avoid the feedback, the author has proposed the transformation of the integration into the summation in the interleaving parallelization as shown in Figure 6.17. With the feedback avoiding, the *prefix- and suffix-guard-interval* of the length L must be considered to achieve the correct estimation. Due to the fact that DPFE requires a large L as indicated in Section 6.4.2, the implementation of DPFE can be very complex.

6.4.2. Estimation Performance

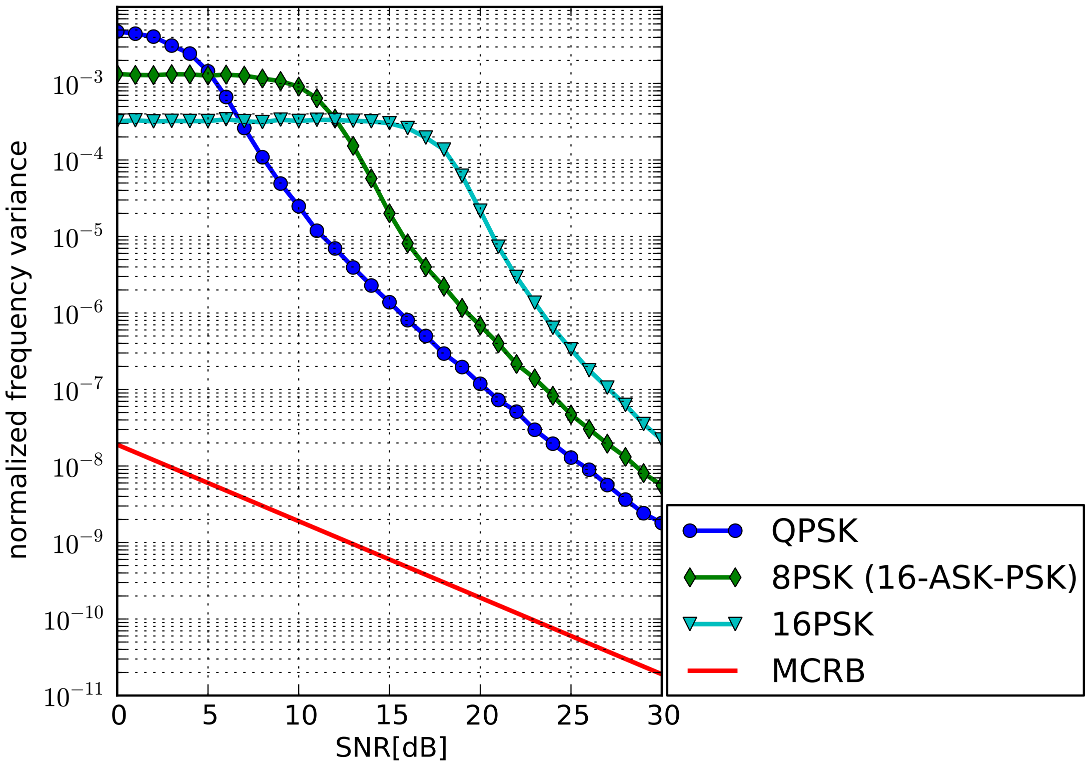

Figure 6.18.: Simulation results for performance of differential phase frequency estimation with L=200

Figure 6.18 shows the normalized frequency variance for DPFE with $L = 200$ for QPSK, 8-PSK and 16-PSK modulation formats in AWGN channel in comparison to MCRB. In contrast to the M-power carrier phase estimation, which provides the basic principle for DPFE, the performance of DPFE strongly depends on the modulation formats. Moreover, the distance

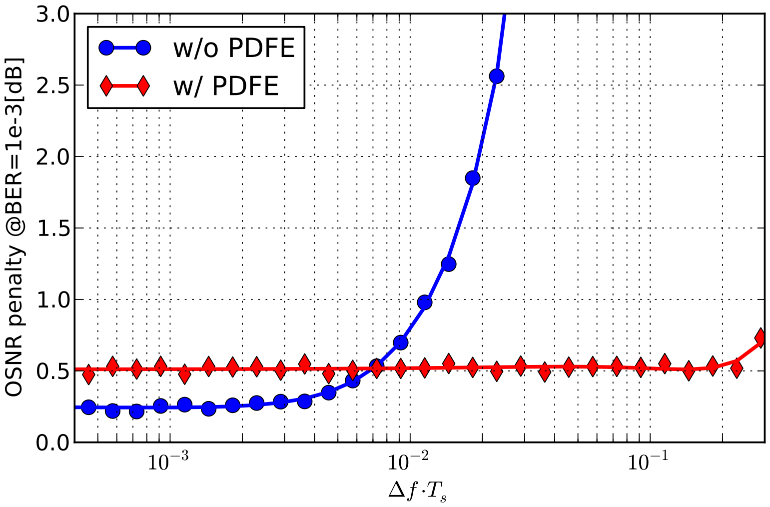

Figure 6.19.: Simulation results for frequency offset Δf vs. OSNR penalty for PolMux-QPSK with M-power phase estimation

between normalized frequency variance for DPFE and MCRB is more than two decades. It should be noted that the performance of DPFE in comparison to various frequency estimators as shown in [77] is relative good for a non-data-aided and non-timing-aided carrier frequency estimator.

For the evaluation indicated in Figure 6.19, the DPFE is used in combination with the M-power carrier phase estimation to improve the frequency offset tolerance. It should be noted that L in the range of $[100; 300]$ for DPFE and $[3; 13]$ for the M-power carrier phase estimation is optimized. The results show that with DPFE the frequency offset tolerance can be significantly improved. However, the application of DPFE has the drawback of the additional OSNR penalty about 0.3dB at lower frequency offsets. Hence, DPFE should not be used in the receiver with LO frequency offset in this range.

6.5. Minimum Distance Estimation

Although the M-power estimation and its derivatives are powerful and can simply be implemented due to the feed forward structure, the algorithms are limited to PSK-based modulation formats e.g., QPSK, 16-ASK-PSK. For QAM-based modulation formats, the feed forward carrier phase estimation algorithms, which are modifications of the M-power estimation, are proposed in [118, 119, 120]. However, the algorithms either have very limited performance especially in respect to the laser linewidth or can be applied only for 16-QAM modulation format. In contrast to the other algorithm, minimum distance estimation (MDE) [121, 74] can be applied to arbitrary modulation formats and is very robust against laser linewidth. In this Section, MDE is briefly described with performance evaluations.

6.5.1. Derivation and Structure

Unlike the M-power estimation and its derivatives, which is based on the maximum likelihood estimation criteria, the estimation principle for MDE is a modification of the MMSE estimation principle as shown in Section 4.4.5. In the first step, we define the estimation error as a distance d_k between the sampled signal from the matched filter v_k and the estimated symbol $\hat{b}_k$:

$$d_k = \hat{b}_k - v_k. \tag{6.37}$$

With MMSE, the estimated phase $\hat{\varphi}$ can be achieved by finding the phase that minimizes the mean-square error $|d_k|^2$. Unfortunately, $\hat{\varphi}$ cannot be directly calculated. Alternatively, the *trial and error* principle [122] can be applied to achieve $\hat{\varphi}$. Since the estimated phase can be only in the interval $[0, \pi/2]$, the test phase φ_i can be given by

$$\varphi_i = \frac{i}{N_q} \cdot \frac{\pi}{2}, \tag{6.38}$$

with $i \in \{0, 1, 2, 3, ...m, N_q - 1\}$ and N_q the number of test phases. It should be noted that N_q and hence the implementation complexity can be reduced by applying two-stage algorithm as shown in [123]. For each φ_i, v_k is rotated and the error distance can be calculated as

$$\begin{aligned} d_{i,k} &= v_k \cdot \exp(j \cdot \varphi_i) - \lfloor v_k \cdot \exp j \cdot \varphi_i \rfloor \\ &= v_k \cdot \exp(j \cdot \varphi_i) - \hat{b}_{i,k}, \end{aligned} \tag{6.39}$$

where $\lfloor x \rfloor$ is a so-called *floor function* as shown in Eq.(4.4).

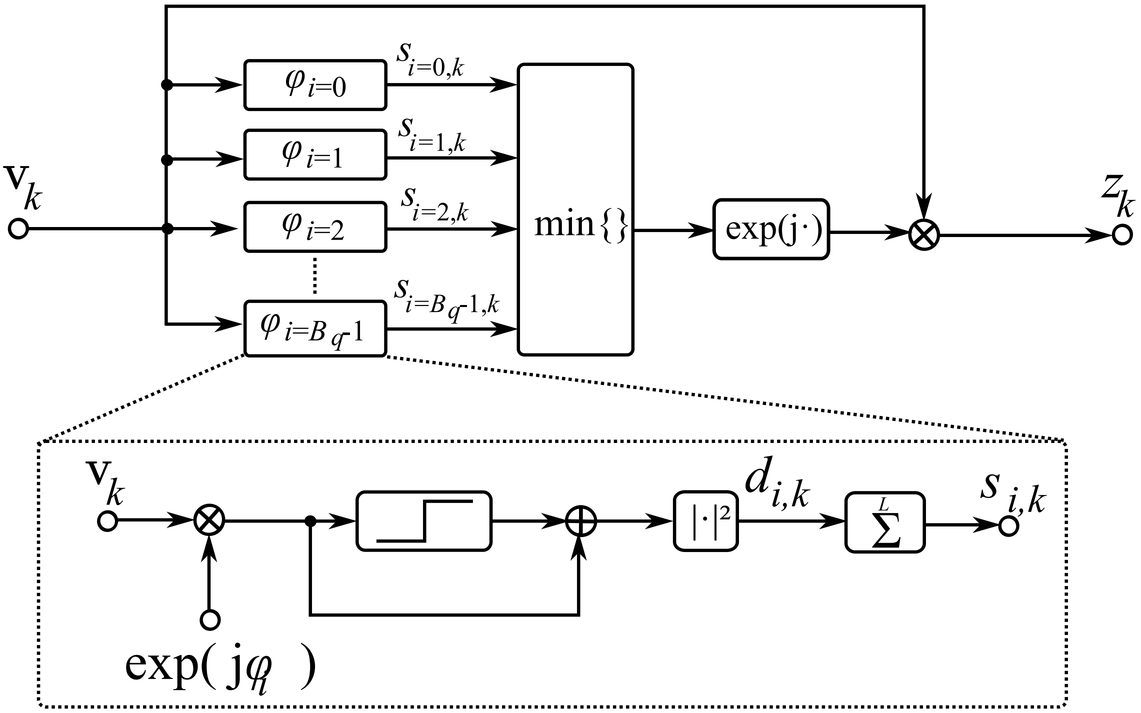

Figure 6.20.: Block diagram of Minimum Distance Estimation (MDE)

In order to reduce the estimation noise, the averaging filter with the memory length of $L = 2N + 1$ can be applied on $|d_{i,k}|^2$ for each test phase φ_i. It should be noted that the memory length of the averaging filter can be seen as the estimation block length for the comparison with the other algorithms. The averaged and filtered distance $s_{i,k}$ can be given by

$$s_{i,k} = \frac{1}{L} \cdot \sum_{n=-N}^{n=N} |d_{i,k-n}|^2. \tag{6.40}$$

Finally, the estimated $\hat{\varphi}$ can be expressed as

$$\hat{\varphi} = \text{value of } \ \varphi_i \ \text{ that minimizes } \quad s_{i,k}. \tag{6.41}$$

Since the term $1/L$ in Eq.(6.40) is constant for all φ_i, it can be neglected for Eq.(6.41). And Eq.(6.40) can be rewritten as

$$s_{i,k} = \sum_{n=-N}^{n=N} |d_{i,k-n}|^2. \tag{6.42}$$

The block diagram of MDE is illustrated in Figure 6.20.

To avoid the 4-fold ambiguity problem, the differential encoding/decoding as shown in Section 3.3.2 can be used. However, with the differential encoding/decoding, the *unwrapping problem* described in Section 6.6 cannot be solved. With the conventional phase unwrapping as shown in Section 6.6, the feed forward structure of the algorithm is broken. In [74], a modification of the differential decoding is proposed to solve this problem. However, a soft information cannot be achieved. Hence, MDE in combination with the feed forward phase unwrapping as shown in Section 6.7 is recommended.

6.5.2. Estimation Performance

For the evaluation of MDE, AWGN simulations of 16-QAM and 64-QAM modulation formats are performed. Figure 6.21 shows the phase error variance of MDE with $L = 20$ in comparison to the MCRB lower bound. Due to the quantization of the trial phases, the minimum phase error of MDE $\tilde{\varphi}_{min}$ can be written as

$$\tilde{\varphi}_{min} = \frac{\pi}{N_q}. \tag{6.43}$$

Hence, the error floor of the phase error variance always occurs for MDE dependent on N_q. This effect can be observed as the quantization noise, which is considered for the application of analog-to-digital convertor (ADC). Since the minimum phase distance decreases increasing the order of the modulation format, the higher order modulation formats require larger N_q. The comparison between 16-QAM and 64-QAM shows that with $N_q = 8$, MDE can estimate the carrier phase for 16-QAM but not for 64-QAM. It means that although MDE can be used for arbitrary modulation formats, the implementation complexity of MDE increases with the order of modulation formats.

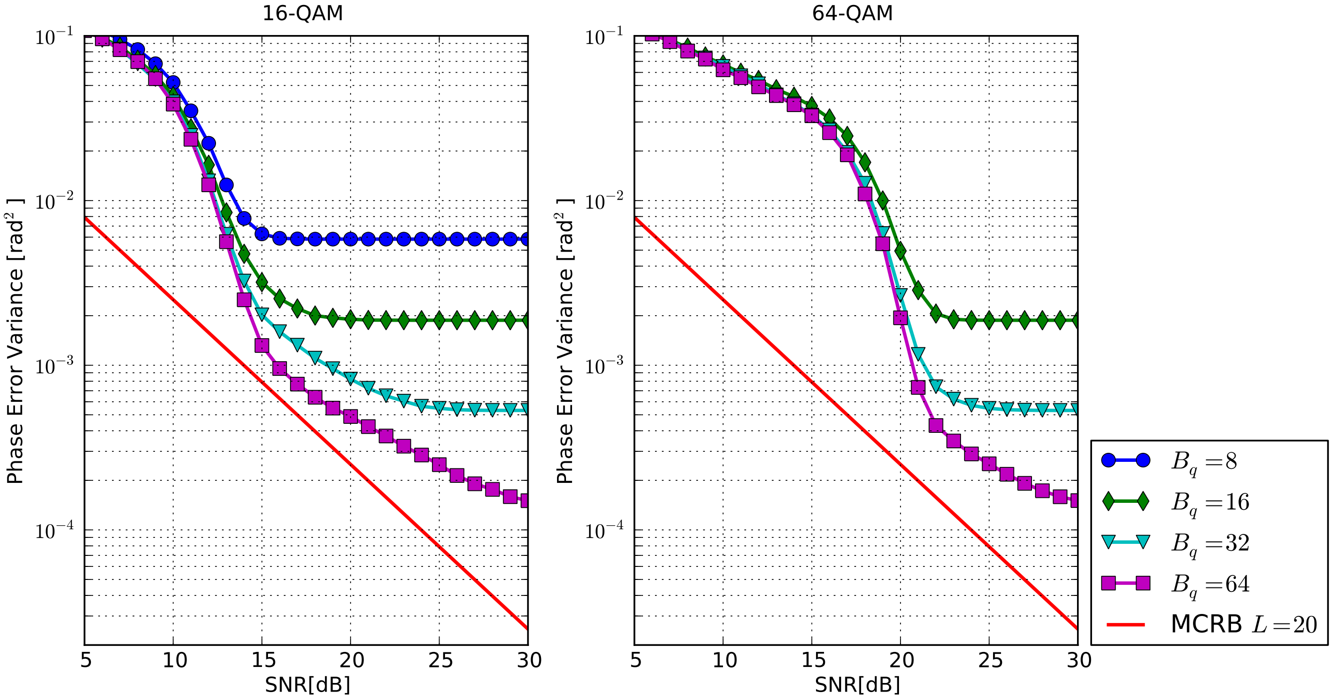

Figure 6.21.: Simulation results for performance of MDE algorithm with L=20 for 16-QAM and 64-QAM

Figure 6.22 shows the tolerance of MDE with $N_q = 32$ against the laser linewidth dependent on L for PolMux-16-QAM and PolMux-64-QAM. Although the performance of MDE in respect to the phase error variance in AWGN channel is very limited, the tolerance against laser linewidth for MDE is very high. Like the algorithms based on M-power estimation, with higher L, MDE

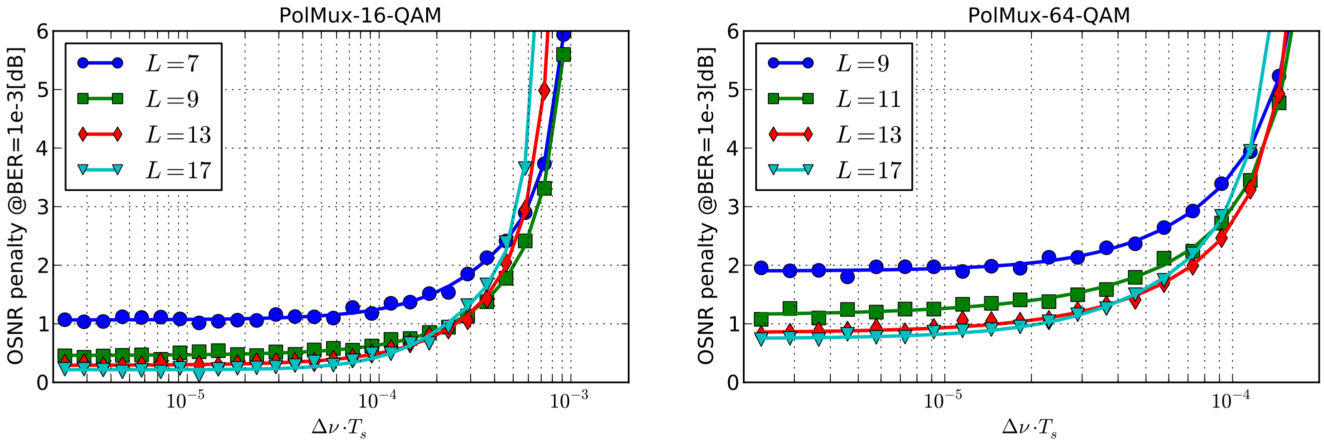

Figure 6.22.: Simulation results for laser linewidth $\Delta\nu$ vs. OSNR penalty for PolMux-16-QAM and PolMux-64-QAM with MDE and $N_q =$ 32.

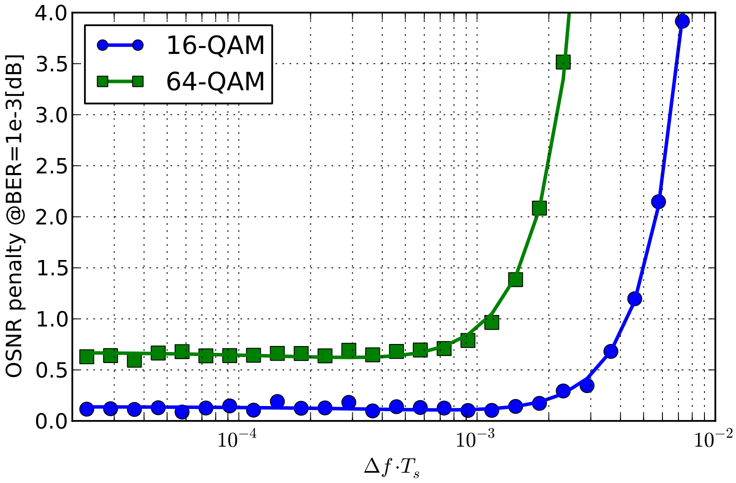

Figure 6.23.: Simulation results for residual frequency offset Δf vs. OSNR penalty for PolMux-16-QAM and PolMux-64-QAM with MDE

has a better noise suppression due to the narrow bandwidth of the estimation. In contrast, with lower L, the laser linewidth tolerance can be improved. It should be emphasized that the OSNR penalty for a lower laser linewidth is proportional to the order of the modulation format due to the minimum phase distance, which is related to the evaluations as shown in Figure 6.21. Figure 6.23 shows the tolerance of MDE with optimized L and $N_q = 32$ against the LO frequency offset for PolMux-16-QAM and PolMux-64-QAM. The same characteristics as for the tolerance against the laser linewidth can be observed.

For the investigation of the tolerance against frequency variations due to the laser instability as

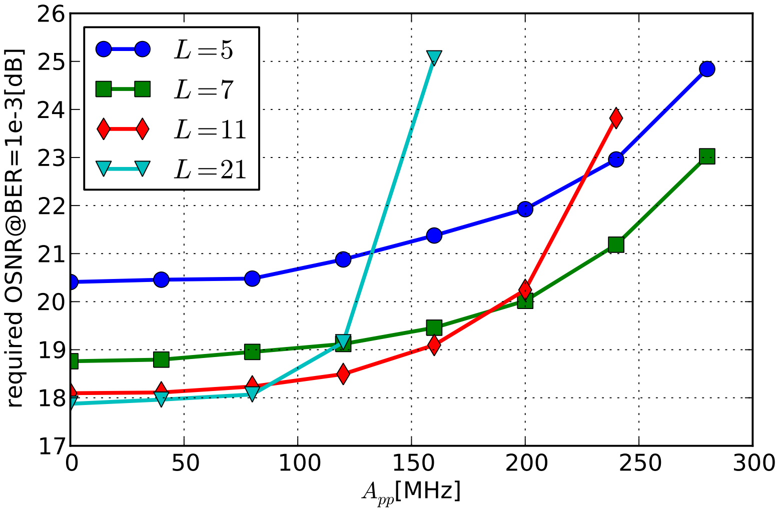

Figure 6.24.: Evaluations from measured data for required OSNR for BER=10^{-3} vs A_{pp} for 111Gb/s PolMux-16-QAM with MDE and $N_q = 32$

Table 6.3.: Loop experiment setups

modulation format	PolMux-16-QAM
baud-rate	28.0GBaud
bit-rate	224Gb/s
number of WDM channel	11
channel spacing	50GHz
optical filter bandwidth	44GHz
transmission distance	1520km (16x95km SSMF)

shown in Section 3.1.1, the simulation of 111Gb/s PolMux-16-QAM for an AWGN channel with the laser linewidth $\Delta\nu = 100$kHz is performed. Figure 6.24 shows that the required OSNR for BER=10^{-3} depends on maximum peak-to-peak of frequency variations A_{pp} and the estimation block length L and $N_q = 32$ for modulation frequency of laser stabilization f_m =35kHz. As we can see that the tolerance of MDE against LO instability strongly depends on L. It should be emphasized that the range of A_{pp} tolerance for MDE for an OSNR penalty equal to 1dB is lower than 200MHz, which can simply occur as shown in the experiment in Section 3.1.1. Hence, in the transmission system with mechanical disturbances at the transmitter or receiver side, MDE should be applied with an additional carrier frequency estimation. For the purpose, the *automatic frequency control* with the feed forward structure (see Chapter 8) is a suitable solution.

In the following, the performance of MDE for measured data from a loop experiment with the setup as shown in Table 6.3 is investigated. After generating the PolMux-16-QAM signal, the signal is transmitted over 1520km of SSMF without in-line CD-compensation. The detailed description of the loop experiment can be found in [124]. It should be emphasized that in this experiment, the carrier frequency offset Δf was manually controlled so that $\Delta f \leq 10$MHz

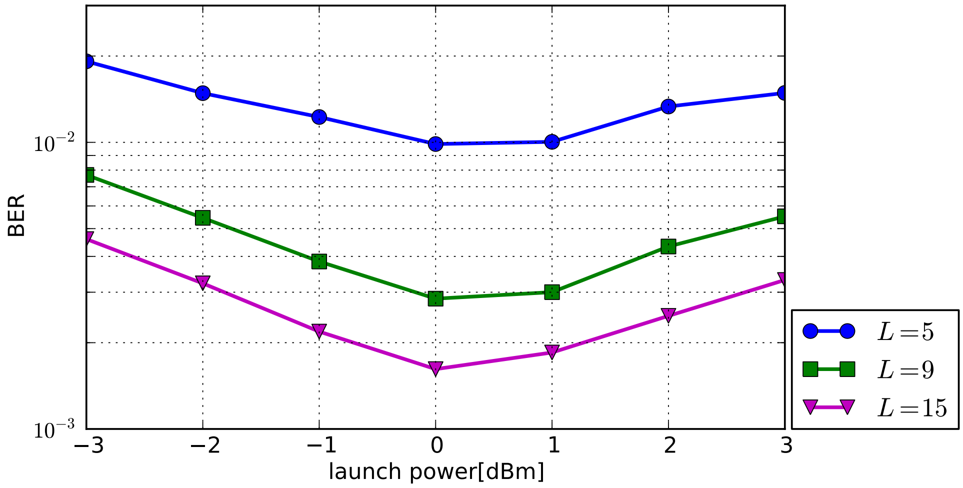

Figure 6.25.: BER vs. launch power for measured 224Gb/s PolMux-16-QAM with MDE and various estimation block length L

and a carrier frequency variation can be excluded. It can be seen from Figure 6.23 that in this range of Δf, the penalty due to Δf is negligible. Hence, it can be assumed that the impairments related to the carrier phase estimation is limited to the laser linewidth and the channel nonlinearities like SPM and XPM. Figure 6.25 depicts the BER performance of MDE dependent on the launch power and L. Like the simulation results shown in Figure 6.22, the performance of MDE strongly depends on L. In this case, the optimal performance can be achieved with $L = 17$ and a launch power around 0dBm, where the trade-off between ASE-noise and the channel nonlinearities is balanced.

6.6. Phase Unwrapping

In feed forward estimation algorithms, input signals are generally segmented into blocks, and the estimation is processed block by block. Without the corresponding between blocks, values of estimates are limited to a basic interval [65]. In carrier synchronization algorithms based on the M-power algorithm, estimated values are limited to the interval $[-\frac{\pi}{M}; \frac{\pi}{M}]$. As a consequence, feed forward algorithms cannot follow the dynamics of the synchronization parameters, and the phase ambiguity can occur.

Figure 6.26 illustrates a problem with the phase ambiguity for carrier synchronization algorithms based on the M-power algorithm, where the estimated phase $\hat{\varphi}$ are represented on the continuous-time scale and the actual phase on dotted-time scale. Due to the limited values of estimated parameters in the interval $[-\frac{\pi}{M}; \frac{\pi}{M}]$, $\hat{\varphi}$ exhibits a jump every time that the actual carrier phase φ crosses an odd multiple of π/M. Hence, the problems can be described as [77]:

1. solve the ambiguity in the first phase estimation
2. stitch together the various segments of $\hat{\varphi}$

These problems are the so-called *unwrapping problem* [48, 125, 126].

In [48, 65, 77], the signal post-processing for feed forward estimation algorithms is proposed to *unwrap* the estimated phase. We define $\hat{\varphi}_k$ with $k = 1, 2, 3, ...$ as the still wrapped estimated phase from feed forward algorithms and $2\pi m/M$ the ambiguity phase. Furthermore, $\hat{\varphi}_{u,k}$ is defined as the *final unwrapped* phase trajectory and $\hat{\varphi}_{p,k} = \hat{\varphi}_{u,k} - \frac{2\pi m}{M}$ as a *provisional* trajectory. Provisional and final trajectories can be *recursively* calculated as [77]

$$\hat{\varphi}_{p,k} = \hat{\varphi}_{p,k-1} + g_u \cdot \mathrm{saw}\left(\hat{\varphi}_k - \hat{\varphi}_{p,k-1}\right) \tag{6.44}$$

$$\hat{\varphi}_{u,k} = \hat{\varphi}_{p,k} + \frac{2\pi m}{M} \tag{6.45}$$

where

$$\mathrm{saw}(x) = [x]_{-\pi/M}^{\pi/M} \tag{6.46}$$

is a sawtooth nonlinearity that reduces x to the interval $[-\pi/M; \pi/M)$ and g_u a parameter in the range $0 < g_u \leq 1$. The block digram for Eq.(6.45) and Eq.(6.45) is illustrated in Figure 6.27.

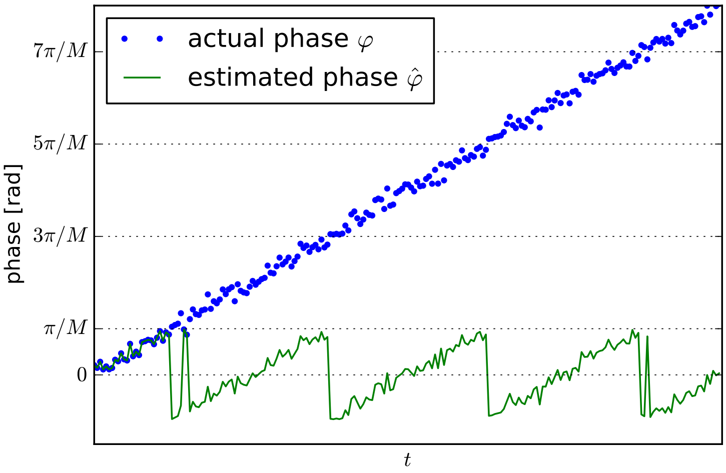

Figure 6.26.: Phase ambiguity problem for the feed forward phase estimations

The performance of the phase unwrapping can be optimized with g_u. A small g_u provides a good performance in the steady state. Nevertheless, for the carrier phase with high dynamics, a small g_u may result in a too slow updating of $\hat{\varphi}_{p,k}$. In many applications, the phase unwrapping is configured with $g_u = 1$ as shown in [48, 65].

A so-called *cycle-slip* problem is usually associated with the unwrapping method. During normal operation $\hat{\varphi}_{u,k}$ occurs small fluctuations a round the true phase φ_k. Due to the feedback mechanism, however, noise disturbance can make $\hat{\varphi}_{u,k}$ slip away from this operating condition and move toward another stable point $\varphi_k \pm 2\pi/M$. Therefore, the detrimental effect of the cycle slip on the symbol error probability is limited to the slip duration when differential encoding/decoding is applied [77]. The detailed analysis of the cycle-slip in feed forward carrier synchronization can be found in [126]

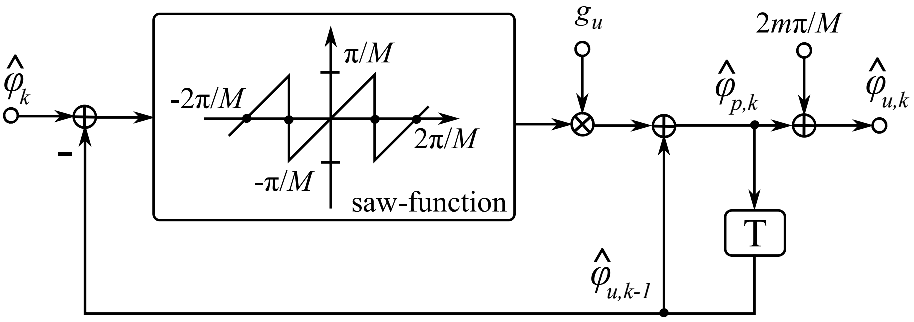

Figure 6.27.: Block diagram of phase unwrapping

6.7. Feed Forward Phase Unwrapping

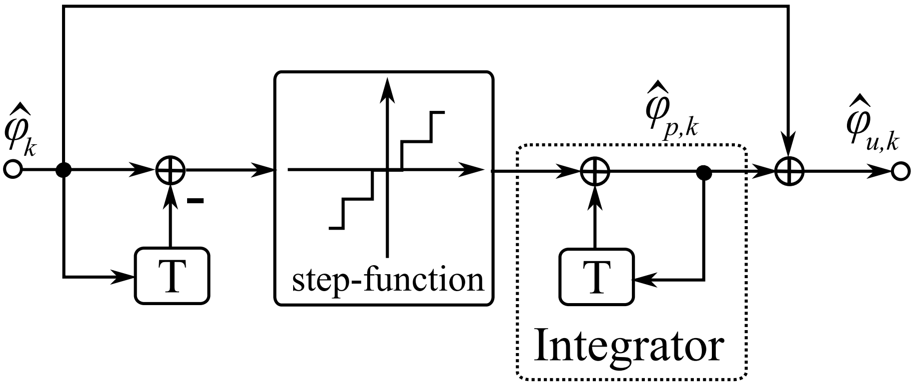

Figure 6.28.: Block diagram of redesigned phase unwrapping

An important advantage of the feed forward phase estimation, in comparison to feedback structure, is the simple hardware implementation using the interleaving parallelization architecture as shown in Section 4.2.1. However, the phase unwrapping as shown in Section 6.6 clearly contains a feedback structure, which complicates the hardware implementation. To solve the feedback problem of the phase unwrapping, the feed forward phase unwrapping proposed from the author is derived and analyzed in this section.

The key component of the phase unwrapping is the sawtooth function and the recursive computation of $\hat{\varphi}_{p,k}$. Since the sawtooth function is a nonlinear function and the recursive computation covers the input and the output of the sawtooth function, the feedback structure of the phase unwrapping as shown in Figure 6.27 can be difficultly replaced with a feed forward structure. Hence, the structure as shown in Figure 6.27 should be firstly redesigned.

Figure 6.28 shows the block diagram of the redesigned phase unwrapping. It must be emphasized that with this structure, g_u cannot be configured and the unwrapped phase is equivalent to the phase unwrapping in Section 6.6 with $g_u = 1$.

The key component of the redesigned phase unwrapping is the step function, which has the relation to the sawtooth function :

$$\mathrm{saw}(x) = x - \mathrm{step}(x), \tag{6.47}$$

and can be written as

$$\mathrm{step}(x) = x - [x]_{-\pi/M}^{\pi/M}. \tag{6.48}$$

The final trajectory can be computed by

$$\hat{\varphi}_{u,k} = \hat{\varphi}_k + \mathrm{step}\left(\hat{\varphi}_k - \hat{\varphi}_{k-1}\right) + \hat{\varphi}_{p,k-1}. \tag{6.49}$$

From Figure 6.28 and Eq.(6.49), it can be seen that the redesigned phase unwrapping clearly contains a feedback structure. However, the feedback structure can be simply replaced with

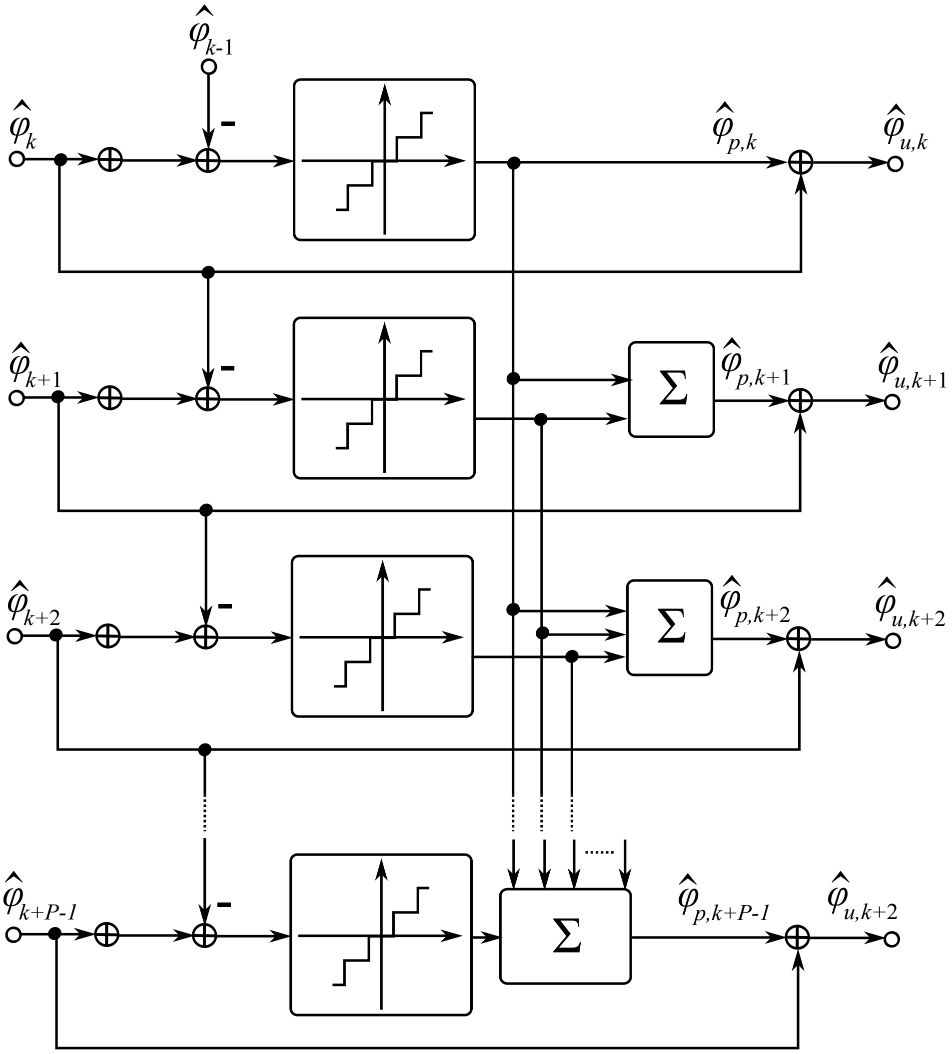

Figure 6.29.: Block diagram of redesigned phase unwrapping in interleaving parallelization architecture with a parallelization path of P

the summation :

$$\hat{\varphi}_{u,k} = \hat{\varphi}_k + \sum_{\nu=0}^{k} \text{step}\left(\hat{\varphi}_\nu - \hat{\varphi}_{\nu-1}\right). \tag{6.50}$$

The computation of the final trajectory as shown in Eq.(6.50) does not contain any feedback structure and can be implemented with the interleaving parallelization architecture. Figure 6.29 illustrates the phase unwrapping from Eq.(6.50) in the interleaving architecture with a parallelization paths of P. It should be emphasized that the redesigned phase unwrapping as shown in Figure 6.28 has a memory length of ∞ due to the integrator. Note that in the current parallelized data-block, phases $\hat{\varphi}_k, \hat{\varphi}_{k+1}, ..., \hat{\varphi}_{k+P-1}$ should be unwrapped. To keep this memory length, a *data-overlap* of a length 1 between parallelized data-blocks is required. As shown in Figure 6.29, $\hat{\varphi}_{k-1}$ is the data-overlap from the previous parallelized data-block.

6.8. Conclusions

In this Chapter, various algorithms for the feed forward carrier synchronization are described and analyzed with the performance investigations. The M-power estimation and its derivatives (V&V, PCC and DPFE) are efficient and powerful algorithms. The most problems related to the carrier synchronization in optical transmission systems can be solved by applying these algorithms. Hence, these algorithms are widely used. However, they are limited to PSK based modulation formats. Using V&V, we have more flexibility for the implementation with approximately equal performance as with the M-power carrier phase estimation. In some special cases, V&V can be implemented without any real number multiplication. Due to the fact that the phase information in two polarizations is correlated, with PCC proposed from the author, these phase information of two polarization are coupled by coupling factors c_x, c_y. As a result, the performance in all aspects is significantly improved in comparison to the M-power or the V&V the algorithm. For transmission systems with high LO frequency offset and frequency variation, an additional frequency recovery like DPFE is recommended. The LO frequency offset up to $0.25/T_s$ can be compensated with DPFE. However, an OSNR penalty of 0.25dB for lower LO frequency offset occurs.

In contrast to the M-power carrier phase estimation and its derivatives, MDE can be used for arbitrary modulation formats. Moreover, MDE is a powerful carrier phase estimation with high tolerance against phase noise and laser linewidth. The trade-off of the MDE is the high implementation complexity and the low tolerance against the LO frequency offsets. In his point of view, there is so far no suitable feed forward algorithm for the QAM based modulation formats.

The phase unwrapping is a crucial component for the feed forward carrier synchronization. However, the conventional phase unwrapping contains a feedback. As a consequence, the implementation of the feed forward algorithm can be limited by the phase unwrapping. Hence, the feed forward phase unwrapping has been proposed from the author. Since the feed forward phase unwrapping is equivalent to the conventional phase unwrapping with $g_u = 1$, in this case, the feed forward approach has the same capability as the conventional phase unwrapping.

7. Feedback Carrier Recovery

Although, feedback carrier recovery is very robust against laser-linewidth and LO frequency offsets, with the interleaving hardware parallelization architecture the performance of feedback carrier recoveries is strongly impaired [74]. However, the interleaving scheme is not mandatory for the hardware implementation. It has been proposed by the author in [73] that with a Superscalar architecture, the feedback carrier recovery can be parallelized with low complexity and almost optimal performance. In this Chapter, algorithms for the feedback carrier estimation will be briefly described and reviewed with performance evaluations.

7.1. Maximum Likelihood Loop

7.1.1. Derivation and Structure

For the the ML carrier phase estimation, the starting point is the likelihood function $\Lambda(\vec{\boldsymbol{r}}|\tilde{\varphi})$ based on the derivation in Section 4.5, which can be given by

$$\Lambda(\vec{\boldsymbol{r}}|\tilde{\varphi}) = \exp\left(\frac{1}{N_0}\sum_{k=1}^{L}\mathrm{Re}\left\{r_k \cdot \tilde{s}_k^*\right\} - \frac{1}{2N_0}\sum_{k=1}^{L}|\tilde{s}_k|^2\right), \tag{7.1}$$

where L is the observation or estimation block length and $\tilde{s}_k$ the trial signal. From Eq.(4.49), $\tilde{s}_k$ can be given by

$$\tilde{s}_k = \exp\left(j \cdot (2\pi t \Delta f + \tilde{\varphi})\right) \cdot \sum_k b_k \cdot g(\tau), \tag{7.2}$$

where $g(t)$ is signaling pulse and τ the time point at the maximum of $g(t)$. Due to the fact that $|\tilde{s}_k|^2$ is independent of $\tilde{\varphi}$, taking logarithm of Eq.(7.1) within some constants yields [77]

$$\ln \Lambda(\vec{\boldsymbol{r}}|\tilde{\varphi}) = \mathrm{Re}\left\{\sum_{k=1}^{L} r_k \cdot \tilde{s}_k^*\right\}. \tag{7.3}$$

Assuming that the frequency offset Δf is known and applied in Eq.(7.2), Eq.(7.3) can be rewritten as

$$\ln \Lambda(\vec{\boldsymbol{r}}|\tilde{\varphi}) = \mathrm{Re}\left\{\exp(-j\tilde{\varphi}) \cdot \sum_{k=1}^{L} b_k^* v_k\right\}, \tag{7.4}$$

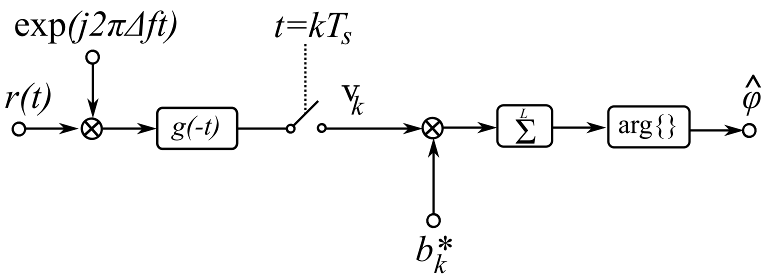

Figure 7.1.: Block diagram of ML carrier phase estimation

where v_k is the sampling of the matched filtered signal with frequency offset compensation $v(t)$ as shown in Eq.(6.2). Hence, with

$$\hat{\varphi} = \arg\left\{\sum_{k=1}^{L} b_k^* v_k\right\}, \tag{7.5}$$

the maximum of $\ln\Lambda(\vec{\boldsymbol{r}}|\tilde{\varphi})$ can be achieved [77].

The block diagram of the phase estimate in Eq.(7.5) is illustrated in Figure 7.1. It should be emphasized that b_k^* in Eq.(7.5) must be obtained by applying training symbols.

With the assumption of the ideal carrier frequency and the ideal timing, it seems to be sufficient to replace the known symbols by their estimates $\hat{b}_k$ in Eq.(7.5) to get an estimate of φ. And Eq.(7.5) becomes

$$\hat{\varphi} = \arg\left\{\sum_{k=1}^{L} \hat{b}_k^* v_k\right\}, \tag{7.6}$$

where $\hat{b}_k^*$ is the estimate of b_k^*.

However, without any additional component, the estimator as shown in Eq.(7.6) cannot estimate the carrier phase. Since the signal constellation at the detector input is rotated by the angle φ from the correct position, the quality of the detector decisions strongly depends on the amount of rotation. For example, a transmission system with QPSK modulation format with $\varphi = \pi/4$ and Nyquist pulse is assumed. Hence, the sampled signal at the receiver side can be given by

$$v_k = b_k \cdot \exp(j\frac{\pi}{4}) + n_k. \tag{7.7}$$

In this condition, we have 50% of the probability for the wrong decisions. Since $b_k \cdot \exp(j\frac{\pi}{4})$ is arranged on the borderline between the decision zones for b_k and $b_k \cdot \exp(j\frac{\pi}{4})$, the decision $\hat{b}_k$ will be either b_k or $b_k \cdot \exp(j\frac{\pi}{4})$ with the same probability. Mathematically, $\hat{b}_k$ can be formulated as

$$\hat{b}_k = b_k \cdot u_k + b_k \cdot \exp(j\frac{\pi}{4}) \cdot (1 - u_k), \tag{7.8}$$

where u_k is a realization of a Bernoulli distributed random variable $\boldsymbol{u}$ with

$$f_{\boldsymbol{u}}(u) = \begin{cases} 0.5 \text{ for } u = 0 \\ 0.5 \text{ for } u = 1 \\ 0 \text{ otherwise} \end{cases} . \tag{7.9}$$

Substituting into the sum in Eq.(7.6) with $|b_k|^2 = 1$ yields [77]

$$\sum_{k=1}^{L} \hat{b}_k^* v_k = \exp(j\frac{\pi}{4}) \sum_{k=1}^{L} u_k + \exp(-j\frac{\pi}{4}) \sum_{k=1}^{L} (1 - u_k). \tag{7.10}$$

For simplicity, the noise term n_k in Eq.(7.7) is neglected. Since the expected value of Eq.(7.10) can be computed by

$$L(0.5 \cdot \exp(j\frac{\pi}{4}) + 0.5 \cdot \exp(j\frac{\pi}{4})) = L/\sqrt{2}, \tag{7.11}$$

the mean value of the argument of Eq.(7.10) is zero and not $\pi/4$, as it should be.

Since the data recovery block as shown in Figure 7.1 detects the phase information without any correction at the input, the phase estimation can be interrupted. Hence, the phase rotation must be applied before entering the detector, which can be realized with the feedback structure. Thereby, the estimation of $\hat{b}_k$ can be performed after the phase correction and the probability for wrong decisions can be reduced. We call the carrier phase estimation with feedback structure based on Eq.(7.6) the maximum likelihood loop (MLL).

For the purpose and the estimate of $\hat{b}_k$ with the phase correction, a phase estimate $\hat{\varphi}_k$ is computed at the time $k \cdot T_s + \tau$ on the basic of the last L symbols as follows :

$$\hat{\varphi}_k = \arg \left\{ \sum_{l=k-L}^{k-1} \hat{b}_l^* v_l \right\} . \tag{7.12}$$

In the next step, v_k is rotated by $\hat{\varphi}_k$ before feeding phase rotated signal z_k into the detector, as shown in Figure 7.2. With this structure, the residual rotation at the detector input is reduced to $\varphi - \hat{\varphi}_k$, which should be less than φ. Since $\hat{b}_k$ depends on the feedback mechanism, the steady state of the system, which can be found in the following description, can be achieved.

Assume that at the beginning of the estimation, $\hat{\varphi}_k$ and φ are far from each other, the decided data $\hat{b}_k$ contains errors with high probabilities and $\hat{\varphi}_k$ fluctuates due to its random property. With a large value of L, the bandwidth of the averaging filter becomes narrow and $\hat{\varphi}_k$ is slowly varying in time. Consequently $\hat{\varphi}_k$ will be almost constant via several signaling intervals. After some corrections over the feedback loop, the difference between $\hat{\varphi}_k$ and φ becomes small and the detector decisions can be improved. At this state, the phase estimation can also be improved, which induces a further improvement for the detector decisions and so on. If the steady state is obtained, $\hat{\varphi}_k$ becomes similar to φ with small variations.

However, the steady state of MLL is not unique. In the steady state, $\hat{\varphi}_k$ can fluctuate around φ plus the multiples of symmetry of the signal constellation e.g., $2\pi/M$ for M-PSK and π/M for QAM modulation format. For any NDA or DD estimation, this phase ambiguity should be

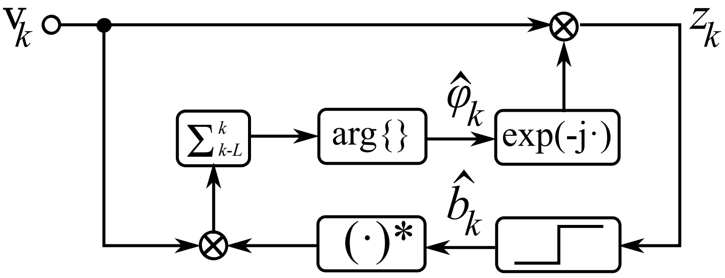

Figure 7.2.: Block diagram of MLL

anticipated due to the rotational symmetry of the signaling scheme. The detailed description about phase ambiguity problem in MLL can be found in [77].

To solve the phase ambiguity problem, the differential encoding/decoding as shown in Section 3.3.2 must be applied. Note that the algorithm is based on DD. Hence, it can be performed for arbitrary modulation formats.

7.1.2. Estimation Performance

Note that the AWGN channel is assumed. The variance of the estimated phase from the MLL with $L = 200$ for QPSK, 16-ASK-PSK and 16-QAM modulation formats in comparison to the MCRB lower bound is depicted in Figure 7.3. The evaluations show that for high SNR for all modulation formats, the variance of the estimated phase is close to the MCRB lower bound, which is the theoretical limit for the phase estimation. Hence, we can indicate MLL as an optimal carrier phase estimation for the proposed modulation formats. Like the other algorithms for the carrier synchronization, the phase error variance of MLL for low SNR is clearly higher than the MCRB lower bound. It should be noted that in this range of SNR, MCRB is lower than CRB and can cause a pessimistic misunderstanding as mentioned in Section 4.6. In comparison to the carrier synchronization with feed forward structure as shown in Chapter 6, the phase error variance of the MLL for the lower SNR is significantly lower.

For the investigation of the MLL tolerance against the laser linewidth dependent on the estimation block length L, the back-to-back PolMux-QPSK is simulated. Figure 7.4 depicts the OSNR penalty against the product $\Delta\nu \cdot T_s$ and the estimation block length L. The results show that the characteristics of MLL for the laser linewidth tolerance are similar to the feed forward algorithms. For higher L, the phase noise can be better suppressed, and for lower L the laser linewidth can be better tolerated due to the broader bandwidth of the averaging filter.

The laser linewidth tolerance of MLL with optimized L for the further modulation formats like PolMux-16-ASK-PSK and PolMux-16QAM is depicted in Figure 7.5. It is not surprising that PolMux-QPSK has the better tolerance against the laser linewidth in comparison to the higher order modulation formats. However, for the equal order modulation format, the tolerance of PolMux-16-ASK-PSK is clearly better than PolMux-16-QAM due to the higher minimum phase distance (22.5° for PolMux-16ASK-PSK and 18.43° for PolMux-16-QAM).

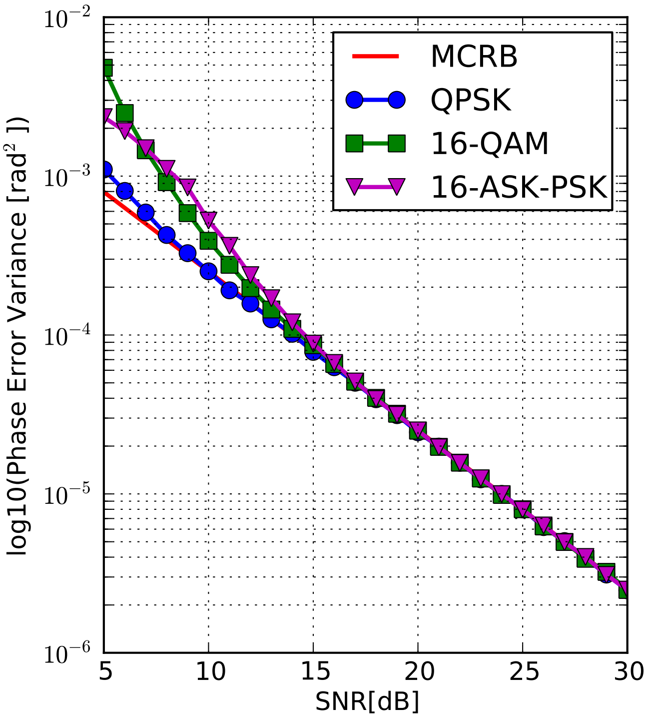

Figure 7.3.: Simulation results for performance of MLL phase estimation with L=200

For the tolerance against the residual frequency offset, the simulation results are shown in Figure 7.6. As we can see, the characteristics of the tolerance against the residual frequency offset is very similar to the laser linewidth. Although the performance of MLL for PolMux-QPSK and

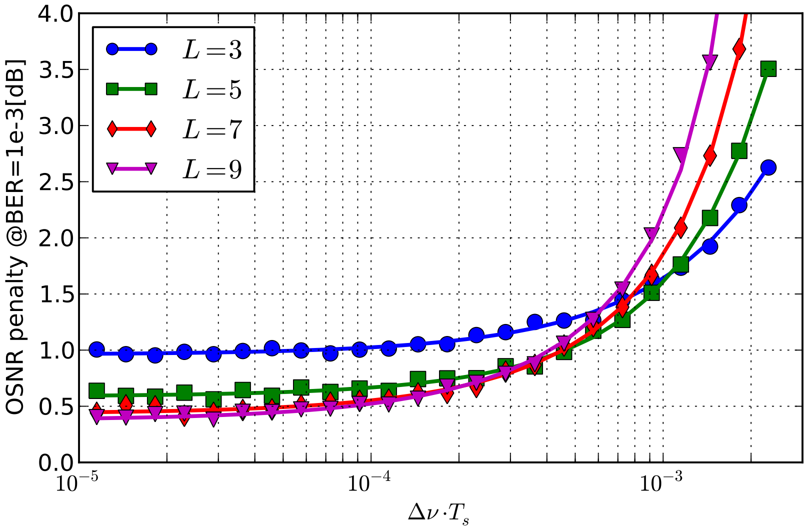

Figure 7.4.: Simulation results for laser linewidth vs. OSNR penalty for PolMux-QPSK with MLL

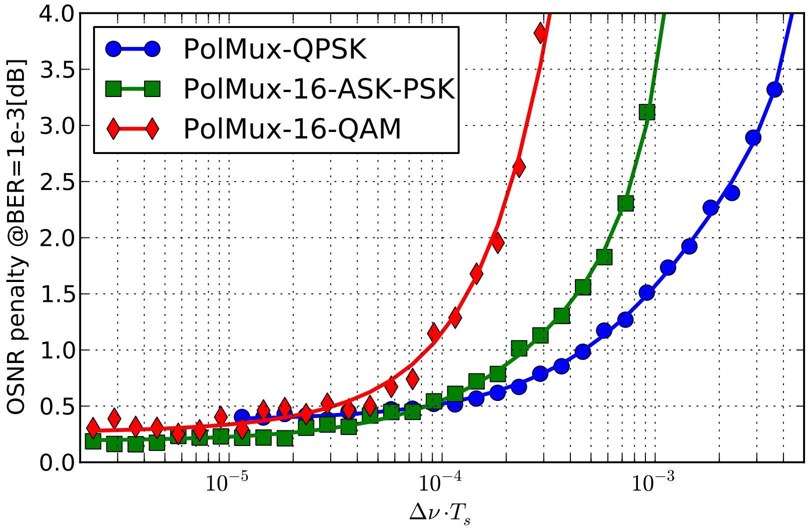

Figure 7.5.: Simulation results for laser linewidth vs. OSNR penalty for PolMux-QPSK, PolMux-16-ASK-PSK and PolMux-16-QAM with MLL and optimized L.

PolMux-16-ASK-PSK is approximately equal to the feed forward algorithms, the error propagation can occur in the feedback algorithm like MLL. Without any additional frequency offset compensation, the error propagation can totally corrupt the performance of MLL. Hence, the MLL is not a suitable stand-alone carrier synchronization for high bit-rate optical transmission systems with respect to frequency offsets. However, the basic principle of MLL can be further developed to the Costas loop, which will be described in the next section.

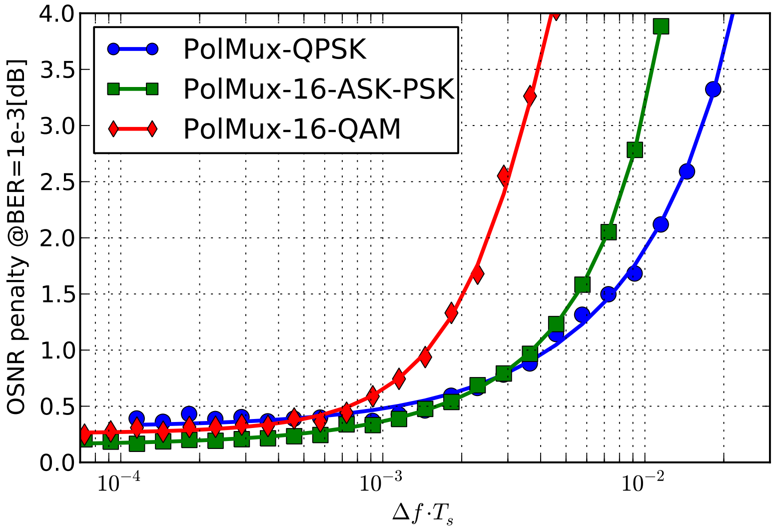

Figure 7.6.: Simulation results for residual frequency offset vs. OSNR penalty for PolMux-QPSK, PolMux-16-ASK-PSK and PolMux-16-QAM with MLL and optimized L.

7.2. Costas Loop

7.2.1. Derivation and Structure

From Eq.(7.4), the recursive structure can be applied by maximizing the log-likelihood function. One of the well-known structure is the Costas loop. The derivative of Eq.(7.4) with respect to $\tilde{\varphi}$ gives us

$$\frac{\mathrm{d}}{\mathrm{d}\tilde{\varphi}} \ln \Lambda(\vec{\boldsymbol{r}}|\tilde{\varphi}) = \sum_{k=1}^{L} \operatorname{Im}\left\{b_k^* x_k \cdot \exp(-j\tilde{\varphi})\right\}. \tag{7.13}$$

The following procedure describes the transformation of the summation in Eq.(7.13) into the feedback structure [77]:

1. We replace b_k with the decision $\hat{b}_k$ from the detector.
2. The variable $\tilde{\varphi}$ in the summation is replaced with the current estimate $\hat{\varphi}_k$.
3. The error signal is generated to improve the phase estimate in the next step.

Mathematically, the replacement of the summation with the recursion can be described as

$$\hat{\varphi}_{k+1} = \hat{\varphi}_k + g_r \cdot e_k, \tag{7.14}$$

where error signal e_k can be written as

$$e_k = \operatorname{Im}\left\{\hat{b}_k^* \cdot v_k \cdot \exp(-j\hat{\varphi}_k)\right\}, \tag{7.15}$$

and g_r is a recursion gain parameter.

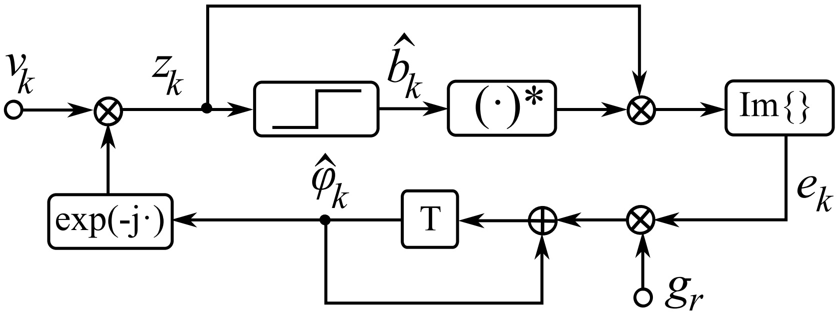

Figure 7.7.: Block diagram of a Costas loop

Figure 7.7 illustrates the block diagram of the algorithm, where e_k is the generated error signal from Eq.(7.15). Afterwards the loop filter as described in Eq.(7.14) is performed to reduce the noise from e_k. The Costas loop as shown in Figure 7.7 is a very popular recursive algorithm for the carrier phase and frequency estimation due to its performance and simple implementation.

7.2.2. Second Order Costas Loop

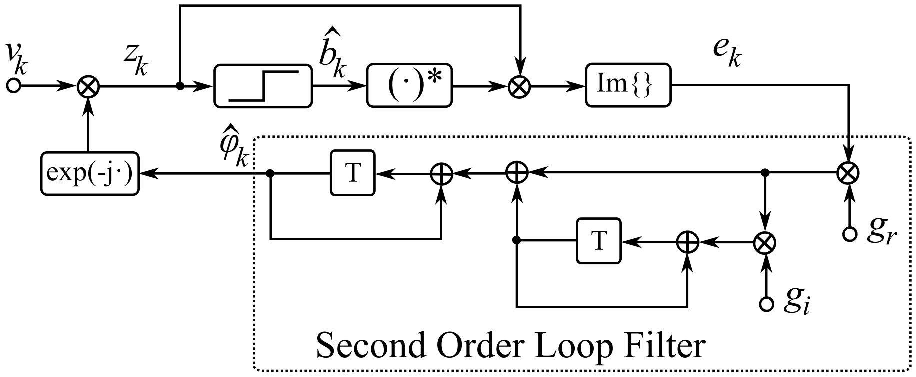

Figure 7.8.: Block diagram of a Costas loop with a second order loop filter

The first order loop filter as shown in Section 7.2.1 is designed for the phase estimation with the assumption of the ideal frequency compensation before feeding the signal into the loop. Although the Costas loop of the first order is very robust against the frequency offset, the frequency offset tolerance can be improved by applying the second order loop filter. In fact, the second order loop filter is an enhancement of the first order loop filter with an additional integrator as shown in Figure 7.8. Formally, the Costas loop with the second order loop filter can be described with the following equations [77] :

$$\hat{\varphi}_{k+1} = \hat{\varphi}_k + e'_k \tag{7.16}$$

$$e'_k = e'_{k-1} + g_r \cdot (g_i) \cdot e_k - g_r \cdot e_{k-1}. \tag{7.17}$$

Note that g_i is a positive constant defined as integration gain. Clearly, the filter becomes first order for $g_i = 0$.

We can also apply the higher order loop filter e.g., third or forth order loop filter in the Costas loop as shown [66]. However, an additional complexity must be considered and for carrier synchronizations, the improvement of the higher order loop filter in comparison to the second order loop filter is not significant [66]. Hence, the application of such a higher order loop filter is very seldom.

7.2.3. Tracking Characteristics

For the investigation of the phase acquisition in a feedback phase estimation, the S-curve of the phase error generator is a well-known powerful tool. The S-curve $S(\tilde{\varphi})$ is defined as the expectation of the of the error signal e_k, conditioned on a fixed value difference $\tilde{\varphi} = \varphi - \hat{\varphi}$ and can be given by [77]

$$S(\tilde{\varphi}) = \mathrm{E}\left\{e_k|\tilde{\varphi}\right\}. \tag{7.18}$$

For simplifying the investigation, the open loop of $S(\tilde{\varphi})$ computation can be performed as shown in Figure 7.9.

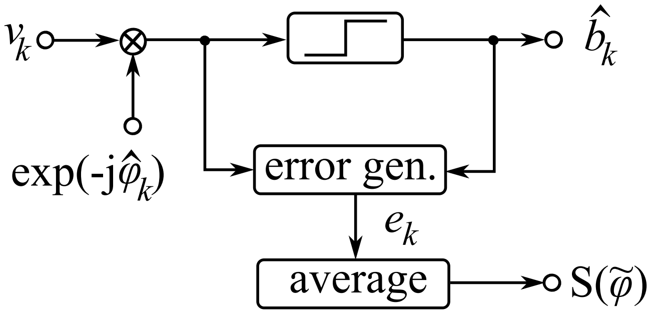

Figure 7.9.: Measuring the S-Curve of the detector

For the convenience, we firstly look at the Costas loop with the first order filter. As mentioned in Section 7.1.1 that $\hat{\varphi}_k$ varies slowly in time for the feedback phase estimation, the error signal can be observed as the sum of the local average $S(\varphi - \hat{\varphi}_k)$ with a noise term of n_k and can be written as

$$e_k = S(\varphi - \hat{\varphi}_k) + n_k. \tag{7.19}$$

Substituting into Eq.(7.14) yields

$$\hat{\varphi}_{k+1} = \hat{\varphi}_k + g_r \cdot S(\varphi - \hat{\varphi}_k) + g_r \cdot n_k. \tag{7.20}$$

The described equivalent model of the feedback phase estimation is shown in Figure 7.10.

One of the interesting properties for the S-curve is the equilibrium points, which can describe the stability characteristic of the loop. For the investigation of the equilibrium points, we begin with the following equation

$$\hat{\varphi}_{k+1} = \hat{\varphi}_k + g_r \cdot S(\varphi - \hat{\varphi}_k). \tag{7.21}$$

Afterwards, the noise-induced fluctuations around the operating point are computed. The equilibrium points $\hat{\varphi}_{eq}$ are defined as the points, where

$$\hat{\varphi}_k = \hat{\varphi}_{eq} = \text{constant} \tag{7.22}$$

or for the S-curve model

$$S(\varphi - \hat{\varphi}_{eq}) = 0. \tag{7.23}$$

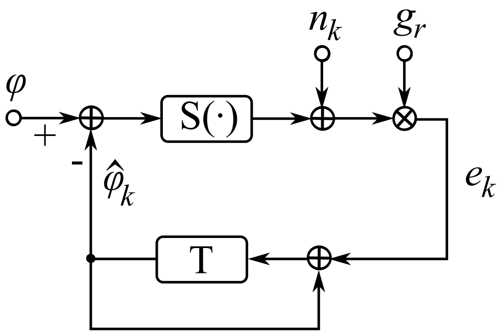

Figure 7.10.: Equivalent model for the tracking loop

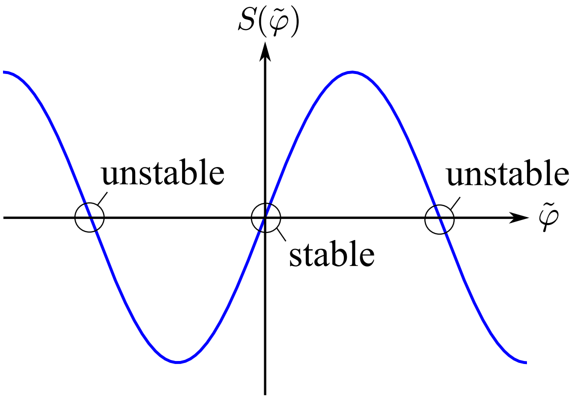

Figure 7.11.: Stable and unstable equilibrium points

From Eq.(7.21) and Figure 7.11, we can see that at the equilibrium points with positive slope of $S(\tilde{\varphi})$, the feedback loop is categorized as a *negative feedback loop*. In this case, the loop becomes stable. In contrast, with the negative slope of $S(\tilde{\varphi})$, we have a *positive feedback loop*. And the stability of the loop is impaired. The detailed analysis of the stability for the Costas loop can be found in [127, 128]. Other problems caused by the zero equilibrium points are the so called *hang-up* problem, which can complicate the acquisition of loop filter based algorithm like the Costas loop. The further studys and solution of the hang-up are proposed in [129, 130, 131].

The performance of the detector strongly depends on the SNR, especially when z_k is close to the decision boundaries. For instance, $\tilde{\varphi}$ is about multiple times of $\pi/4$ for QPSK modulation format. Practically, the noise rounds off the discontinuities at these multiples. In [77], it has been shown that the S-curve of the Costas loop for QPSK in AWGN channel with low SNR can be simply given by

$$S(\tilde{\varphi}) = \sin\left(\tilde{\varphi} - m(\tilde{\varphi}) \cdot \frac{\pi}{2}\right). \tag{7.24}$$

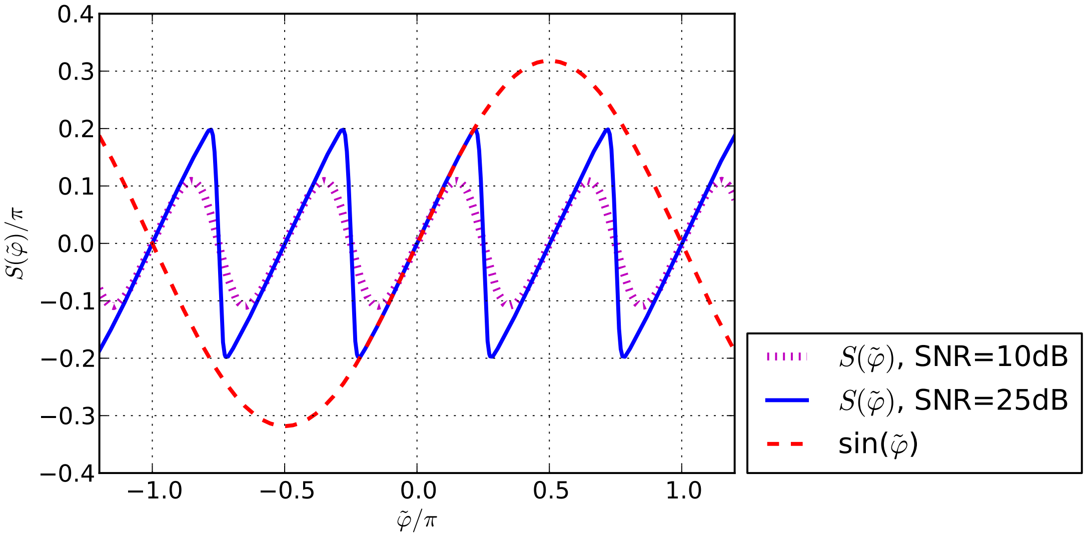

Figure 7.12.: S-curve for Costas loop for QPSK

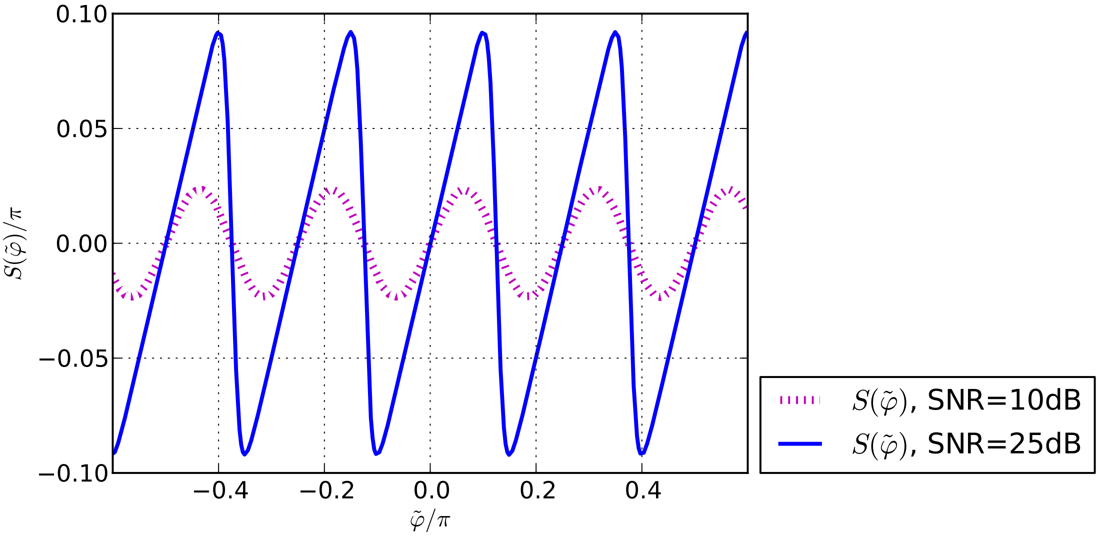

Figure 7.13.: S-curve for Costas loop for 16-ASK-PSK

The further S-curves of the Costas loop dependent on the SNR, are shown in Figure 7.12, 7.13 and 7.14 for QPSK, 16-ASK-PSK and 16-QAM modulation formats respectively. On the one hand, for the PSK based modulation like QPSK and 16-ASK-PSK with high SNR, the S-Curve has the similar form as described in Eq.(7.24). And the form of the S-curve deviates from Eq.(7.24) with decreasing SNR.

On the other hand, for the 16-QAM modulation format, the S-curve is totally different from Eq.(7.24). Due to the fact that Eq.(7.24) is derived with the assumption of the constant phase distance between the constellation points, which is not reasonable for 16-QAM modulation format, we can compare Eq.(7.24) with the S-curve of 16-QAM modulation format as shown

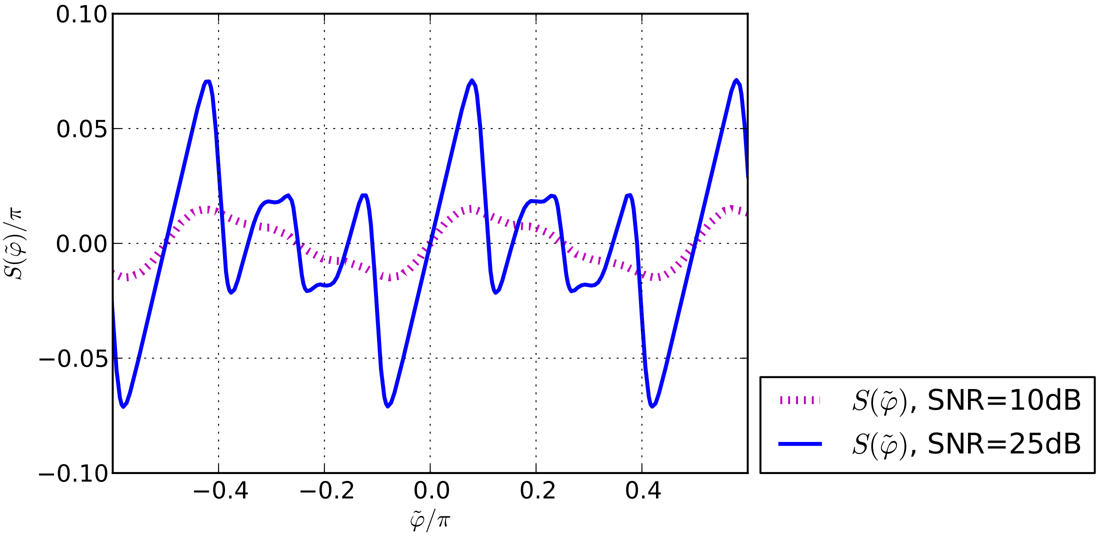

Figure 7.14.: S-curve for Costas loop for 16-QAM

Figure 7.14. An interesting point for S-curve for 16-QAM is that the number of equilibrium point is decreased with the decreasing the SNR. Moreover, the range of $\tilde{\varphi}$ for the stable acquisition is significantly reduced in comparison to the same SNR for PSK based modulation formats like 16-ASK-PSK, due to the lower tolerance against the phase noise for 16-QAM.

7.2.4. Equivalent Estimation Length

In Section 4.6, the MCRB as the performance limit for the carrier synchronization is described. Comparing the phase noise variance of an estimator to the MCRB provides a reasonable performance evaluation. However, there are different concepts between the MCRB and the Costas loop, which complicates the comparison. On the one hand, the estimated phase from the Costas loop is computed over the infinite observation length with a weighting procedure to emphasize recent data against the previous data. On the other hand, the calculation of the MCRB is limited to the finite observation length. For the reasonable comparison between the variance of the estimated phase from the Costas loop with the MCRB, the closed-loop scheme must be transformed into an equivalent open-loop scheme with the same estimation error and the estimation length. The transformed estimation length is defined as the *equivalent estimation length* L_{eq} and can be given by [77]

$$L_{eq} = \frac{1}{2 \cdot T_S \cdot B_L}, \tag{7.25}$$

where T_S is the transmission symbol interval and B_L is the loop noise bandwidth. For the first order Costas loop, B_L can be given by [77]

$$B_L = \frac{g_r \cdot A}{T_S \cdot 2 \cdot (2 - g_r \cdot A)}, \tag{7.26}$$

where A is the slope of the S-curve at the origin. From Eq.(7.24), derivative of $S(\tilde{\varphi})$ with respect to $\tilde{\varphi}$ give us $A = 1$. Substituting Eq.(7.26) into Eq.(7.25) with $A = 1$ yields [77]

$$L_{eq} = \frac{2 - g_r}{g_r}, \tag{7.27}$$

which is the equivalent estimation length for the first order Costas loop. For the second order Costas loop, we begin with the noise bandwidth of the second order loop filter [132, 66]:

$$B_L = \frac{2 \cdot g_i + g_r \cdot A \cdot (2 + g_i)}{T_S \cdot 2 \cdot (4 - g_r \cdot A \cdot (2 + g_i))} \tag{7.28}$$

and hence the equivalent estimation length for the second order Costas loop can be given by [66]

$$L_{eq} = \frac{4 - g_r \cdot A \cdot (2 + g_i)}{2 \cdot g_i + g_r \cdot A \cdot (2 + g_i)}. \tag{7.29}$$

In the most cases, we set $g_r \gg g_i$. As a consequence, L_{eq} in Eq.(7.27) and Eq.(7.29) is approximately equal.

7.2.5. Estimation Performance

With the assumption of an AWGN channel, the phase error variances of the first order Costas loop with g_r=0.05 (L_{eq} = 200) for QPSK, 16-ASK-PSK and 16-QAM modulation formats in comparison to the MCRB are depicted in Figure 7.15. The simulation results show that the performance of the first order Costas loop in AWGN channel is very similar to the MLL. Namely, the variance of the estimated phase is close to the theoretical limit especially for higher SNR. Since the second order loop filter is designed for the frequency offsets suppression and its impacts on phase error variance are insignificant, the simulation results in Figure 7.15 are also valid for the second order Costas loop.

Figure 7.16 indicates the laser linewidth tolerance of the first order Costas loop with optimized $g_r \in [0.1; 1.0]$ for PolMux-QPSK, PolMux-16-ASK-PSK and PolMux-16-QAM in the AWGN channel. Not only the phase error variance as shown in Figure 7.15 but also the tolerance against the laser linewidth of the first order Costas loop is very similar to the MLL. As we can see that Costas loops are very robust against the laser linewidth and can be used for arbitrary modulation formats due to the decision-directed scheme. The only comparable feed forward carrier phase estimation for the Costas loop is the MDE with respect to the modulation formats and the performance. For the laser tolerance, the comparison between Costas loop from Figure 7.16 and MDE from Figure 6.22 shows that for higher laser linewidths, the OSNR penalty for MDE is significantly lower than for Costas loop. However, since the laser linewidth $\Delta\nu$ = 100kHz

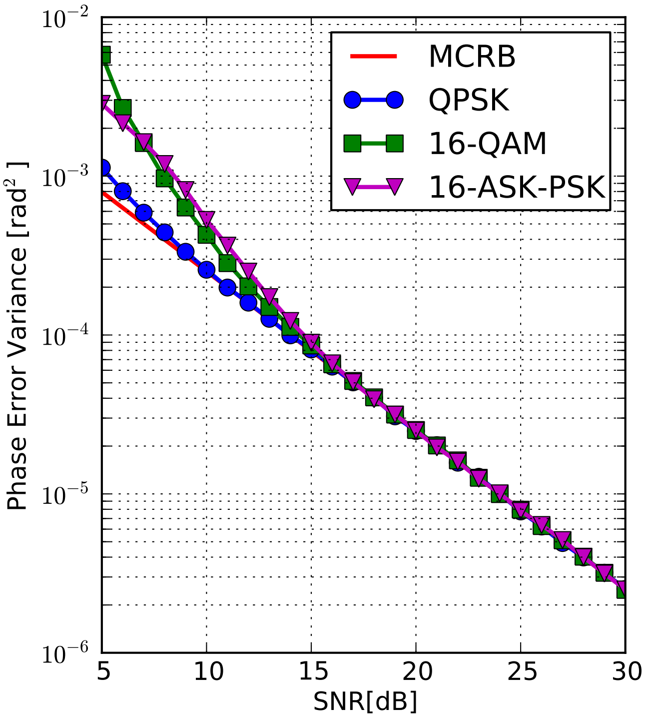

Figure 7.15.: Performance of the first order Costas loop with g_r=0.01 (L_{eq} = 200)

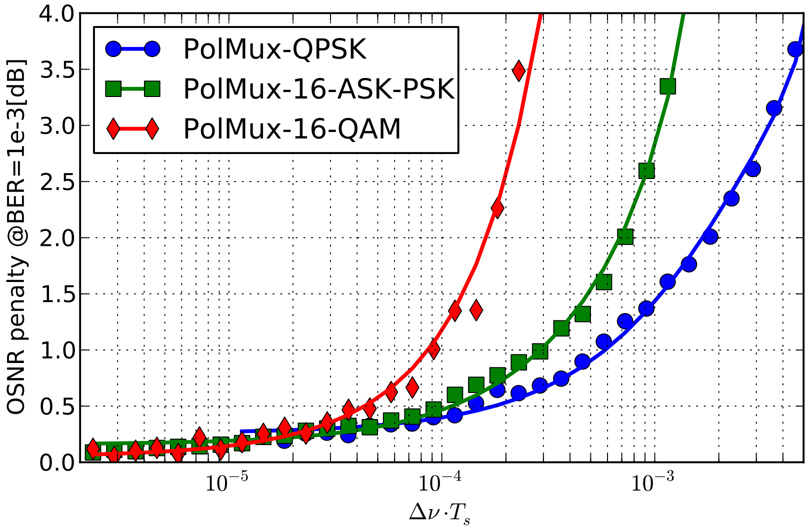

Figure 7.16.: Simulation results for laser linewidth vs. OSNR penalty for PolMux-QPSK, PolMux-16-ASK-PSK and PolMux-16-QAM with first order Costas loop and optimized $g_r \in [0.05; 1.0]$

is considered to be standard for the LO, the Costas loop and the MDE have a comparable performance for e.g., 224Gb/s PolMux-16-QAM ($\Delta\nu \cdot T_s = 3.64 \cdot 10^{-6}$).

Although the Superscalar parallelization architecture allows us to reduce the feedback delays, the feedback delay cannot be completely avoided. Therefore, the feedback degradations for the Costas loop is investigated as followed. Figure 7.17 depicts the required OSNR for BER=10^{-3} depending on the laser linewidth and the processing feedback delay D_P (see Section 4.2). The modulation format is set to QPSK. The residual evaluation parameters are identical to the

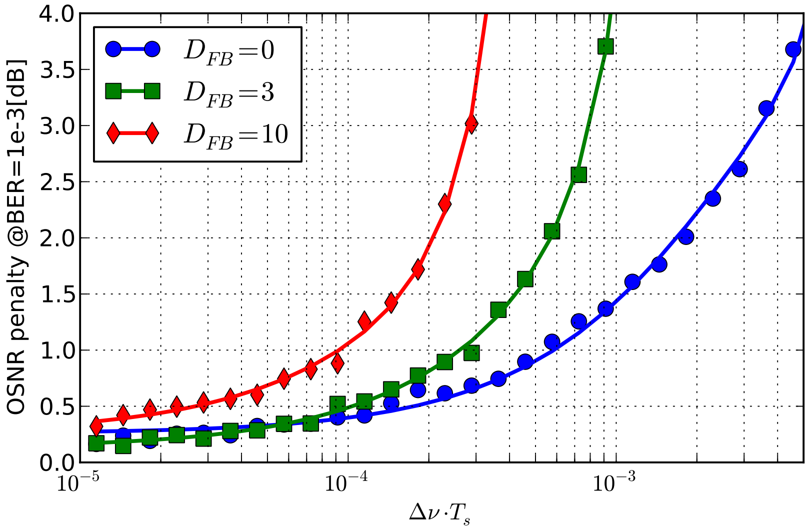

Figure 7.17.: Simulation results for performance degradation of QPSK due to feedback delay for the Costas loop

evaluation for the laser linewidth tolerance. The results show that with the feedback delay, the performance of the Costas loop is clearly degraded.

As we showed in Section 3.1.1 that the laser linewidth can be characterized as a random variable with Wiener process. Hence, the analysis for the performance degradations due to the feedback delay is complex. In the following, a simple method for the approximation of these performance degradations is proposed from the author. According to Eq.(3.3), the phase noise caused by laser linewidth $\varphi_{n_s,k}$ can be written as

$$\varphi_{n_s,k} = \varphi_{n_s,k-1} + \Delta\varphi_{n_s,k} \tag{7.30}$$

with

$$\text{Var}\left\{\Delta\varphi_{n_s,k}\right\} = 2\pi\Delta\nu_s \cdot T_s. \tag{7.31}$$

Assume that the Costas loop can perfectly prevent $\varphi_{n_s,k}$ before the feedback delay occurs. In the time interval in the presence of the feedback delay, $\varphi_{n_s,k}$ cannot be tracked from the Costas loop and is accumulated to

$$\varphi_{n_s,k} = \sum_{i=D_P-1}^{0} \Delta\varphi_{n_s,k-i} \tag{7.32}$$

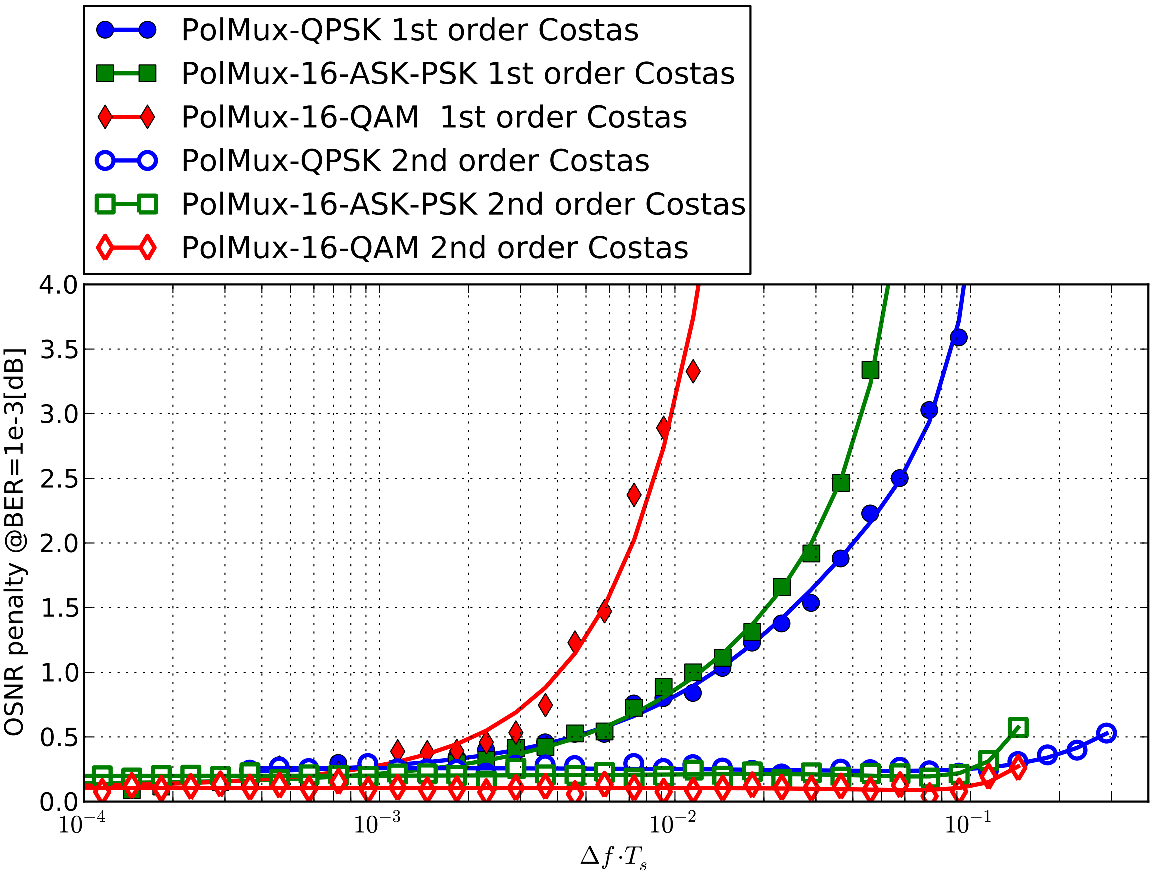

Figure 7.18.: Simulation results for residual frequency offset vs. OSNR penalty for PolMux-QPSK, PolMux-16-ASK-PSK and PolMux-16-QAM with Costas loop and optimized parameters

As a consequence, variance of $\varphi_{n_s,k}$ can be given by

$$\begin{aligned} \mathrm{Var}\left\{\varphi_{n_s,k}\right\} &= \sqrt{D_P} \cdot \mathrm{Var}\left\{\Delta\varphi_{n_s,k}\right\} && (7.33) \\ &= \sqrt{D_P} \cdot 2\pi\Delta\nu_s \cdot T_s. && (7.34) \end{aligned}$$

In other words, with a feedback delay of D_P, the variance of the phase noise caused by laser linewidth at the input of the Costas loop is about $\sqrt{D_P}$ times larger without a feedback delay. This simply approximated performance degradation conforms with the evaluation as shown in Figure 7.17 for ONSR penalty around 1dB.

In the following, the LO frequency offset tolerance of the first order and the second order Costas loop is investigated. For the simulation, the AWGN channel is assumed. Figure 7.18 shows the OSNR penalty against the LO frequency offset for PolMux-QPSK, PolMux-16-ASK-PSK and PolMux-16-QAM. The parameters g_r for the the first order and g_i for the second order Costas loop are optimized with $g_r \in [0.05; 1.0]$ and $g_r \in [0.005; 0.02]$. The simulation results show that for the first order Costas loop, the tolerance against the LO frequency offset is not significantly improved in comparison to the other algorithms for the carrier phase recovery. In contrast, for the second oder Costas loop, very large LO frequency offsets can be tolerated without significant performance loss. This is due to the fact that the second order Costas loop is designed also for frequency offset compensation. It should be noted that the limitation of the second order Costas loop from Figure 7.18 is the theoretical limit for the algorithms based on the decision-directed scheme and for each modulation format ($T_s/4$ for PolMux-QPSK, $T_s/8$ for PolMux-16-ASK-PSK and PolMux-16-QAM). In comparison to the feed forward MDE from Figure 6.23, the LO frequency offset can clearly be more tolerated by applying the second order Costas loop.

In the next step, the tolerance against frequency variations due to the laser instability as shown

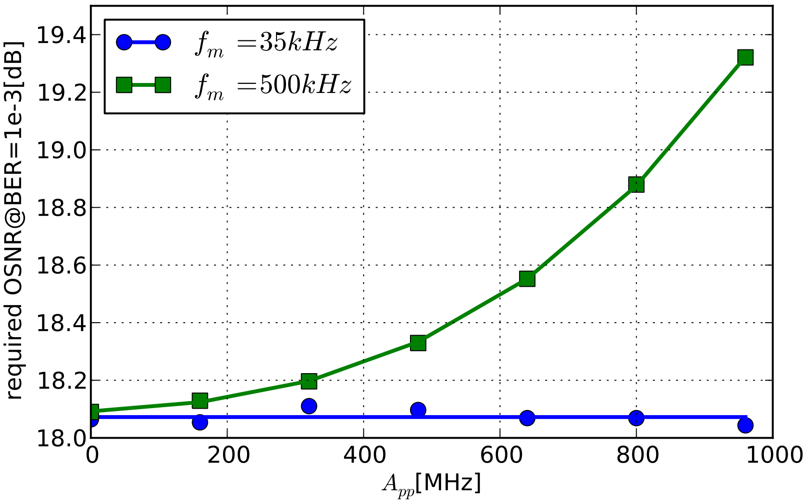

Figure 7.19.: Simulation results for required OSNR for BER=10^{-3} vs A_{pp} for 111Gb/s PolMux-16-QAM with second order Costas loop and optimized parameters

Table 7.1.: Loop experiment setups

modulation format	PolMux-16-QAM
baud-rate	28.0GBaud
bit-rate	224Gb/s
number of WDM channel	11
channel spacing	50GHz
optical filter bandwidth	44GHz
transmission distance	1000km (10x100km ultra low loss fiber)

in Section 3.1.1 with the model of the stabilized laser from Eq.(3.7) is investigated. For this purpose, the simulation of 111Gb/s PolMux-16-QAM in AWGN channel with the laser linewidth $\Delta\nu$ = 100kHz is performed. Figure 7.19 shows the required OSNR for BER=10^{-3} against A_{pp}. It should be noted that g_r and g_i in the simulation are optimized. As we can see from Figure 7.19 that the second order Costas loop is extremely tolerant against the maximum peak-to-peak of frequency variations A_{pp}. For modulation frequency of laser stabilization f_m =35kHz, the OSNR penalty is not observable. Hence, we increase f_m to the hypothetical value of 500kHz. In this case, we have the OSNR penalty of 1dB around A_{pp} =800MHz. It means that for the system with the frequency variations due to the laser instability, a second order Costas loop is a very suitable algorithm for carrier synchronization.

For the investigation of the Costas loop tolerance against the channel nonlinearities, the loop experiment with the setups as shown in Table. 7.1 was performed. After generating the PolMux-16-QAM signal, the signal is transmitted over 1000km of an ultra low loss fiber without the in-line CD-compensation. At the receiver side, the signal is detected with the optical frontend for coherent receiver as described in Section 3.5 followed by a digital storage oscilloscope saving blocks of 10^6 samples for off-line processing. To compensate for polarization effects and the residual chromatic dispersion, T/2 spaced FIR filters for equalization are applied. The detailed

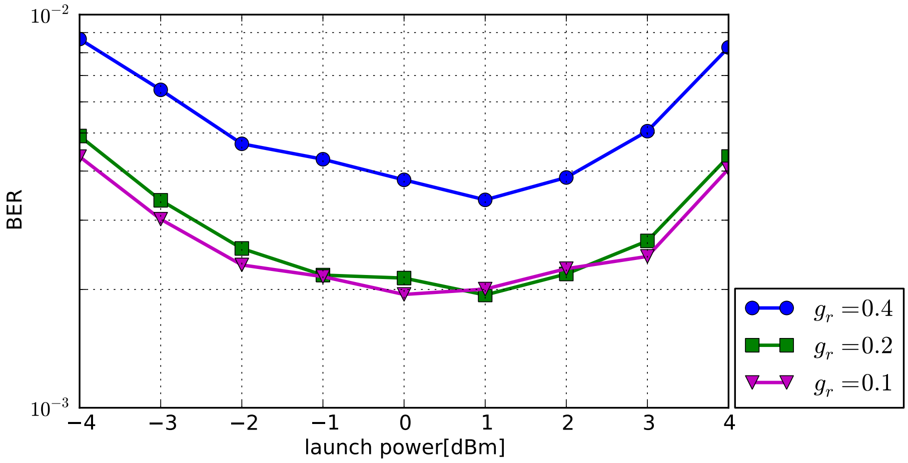

Figure 7.20.: Measurement evaluations for BER vs. launch power for 224Gb/s PolMux-16-QAM with second order Costas loop

description of the loop experiment can be found in [124].

The evaluation in Figure 7.20 shows the BER performance against launch power and g_r for the second order Costas loop. For all evaluations, g_i is set to 0.004. Since the LO frequency offset in the loop experiments is manually controlled so that $\Delta f \leq 10$MHz and the carrier frequency variation can be excluded, g_i is quite irrelevant for the performance of the Costas loop. Moreover, it can be assumed that the impairments related to the carrier phase estimation is limited to the laser linewidth and the channel nonlinearities like SPM and XPM.

For the parameter optimization, with $g_r = 0.1$ and $g_r = 0.2$ and the launch power around 1dBm due to the balanced trade-off between ASE-noise and the channel nonlinearities, the optimal BER performance can be achieved.

7.2.6. Implementation Complexity

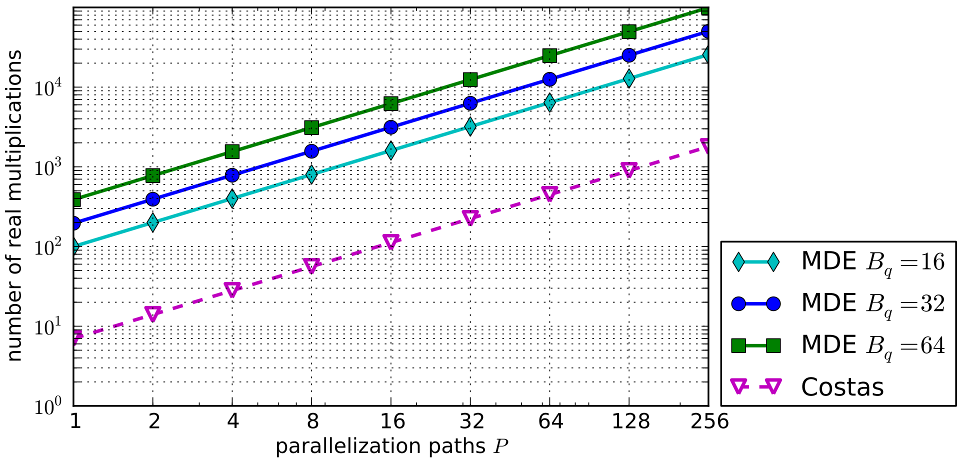

Figure 7.21.: Number of real multiplications vs. parallelization degree P for second order Costas loop and MDE

One of the key criteria for choosing the algorithm for carrier synchronization is the implementation complexity. With a low implementation complexity, the cost and the power consumption of the transceiver can be clearly reduced. In this section the implementation complexity between the second order Costas loop and MDE is compared because the both carrier synchronization algorithms can be applied for arbitrary modulation formats and have comparable performance. For the implementation complexity comparison the number of parallelization paths P as shown in Section 4.2 must be considered. Moreover, it should be emphasized that the MDE should be implemented with the interleaving parallelization architecture due to the simplification. Likewise the second order Costas loop should be implemented with the Superscalar architecture due to the reduction of the parallelization delay.

One of the criteria against MDE is the hardware implementation complexity. Due to the fact that each trial phase rotation and the calculation of its distance to the decided symbol must

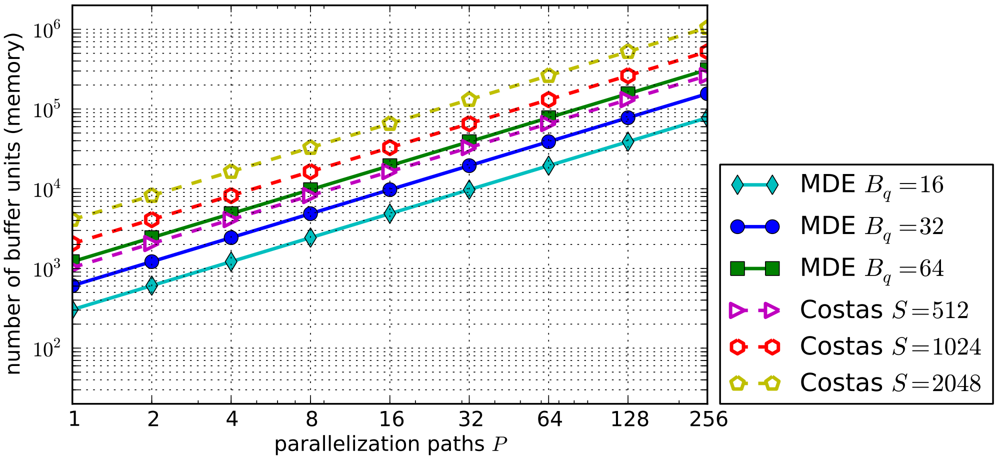

Figure 7.22.: Number of buffer units vs. parallelization degree P for the second order Costas loop and MDE

be applied in each parallelization path, the number of the overall real number multipliers for MDE is $6 \cdot B_q \cdot P$. For the second order Costas loop, 7 multipliers for each parallelization path are required. Figure 7.21 depicts the number of the overall real number multipliers depending on the number of parallelization paths P. It can be clearly observed that the implementation complexity of MDE is much higher than the second order Costas loop with Superscalar parallelization.

The other criterion for the complexity evaluation is the number of buffer units. Although, the Costas loop requires a small number of the buffer units, the application of the Superscalar parallelization requires 2 SxP matrices of buffer units for data structure transformation, where S is the number of samples per processing block as shown in Section 4.2. On the other hand, MDE requires the buffer units for the distance averaging that is equal to $L \cdot B_q \cdot P$. From the comparison of the number of buffer units in Figure 7.22, it can be seen that the number of the buffer units between the Costas loop and MDE is dependent on the parameters and higher for Superscalar parallelization. However, memory should come at a lower cost of chip design than multipliers.

7.3. Adaptive Bandwidth Algorithm

Although the Costas loop is a very powerful algorithm for carrier synchronization, for some special cases, the Costas loop requires long time for the acquisition. To reduce the acquisition time, the parameters g_r and g_i can be increased with the trade-off of the tracking performance loss. Hence, the adaptive bandwidth algorithm (ABA) is proposed by the author to solve the acquisition problem without the trade-off of the tracking performance loss.

As we can see from Eq.(7.26) and Eq.(7.28), the noise bandwidth strongly depends on g_r and

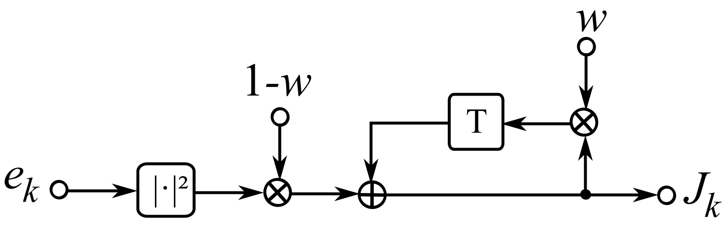

Figure 7.23.: Block diagram for leap indicator

g_i. In the acquisition mode, the loop filter with a wide noise bandwidth is desirable for the short acquisition time. Nevertheless, in the steady state, the loop filter with a narrow noise bandwidth is desirable for the tracking performance. For the convenience, we firstly consider the first order loop filter. To provide these features, we can replace g_r with the adaptive filter gain $g_{r,ABA}$, which can be given by

$$g_{r,ABA} = \frac{g_r}{\kappa} \tag{7.35}$$

with

$$\kappa = \begin{cases} 1 & \text{for } k < 1 \\ k & \text{for } 1 \le k \le l_{ABA} \\ l_{ABA} & \text{else} \end{cases}, \tag{7.36}$$

where k is the index of signal samples and adaptation length $l_{ABA} \in \mathbb{N}^+$ is design parameter for the algorithm.

The functionality of ABA can be described as following. To speed up the acquisition time, g_r in Eq.(7.35) is much greater than g_r in the Costas loop without ABA. From Eq.(7.35) and Eq.(7.36), we can see that for $k \le l_{ABA}$, $g_{r,ABA}$ is inversely proportional to the time index k. As a consequence, the loop filter bandwidth decreases with the time and the tracking performance can be improved.

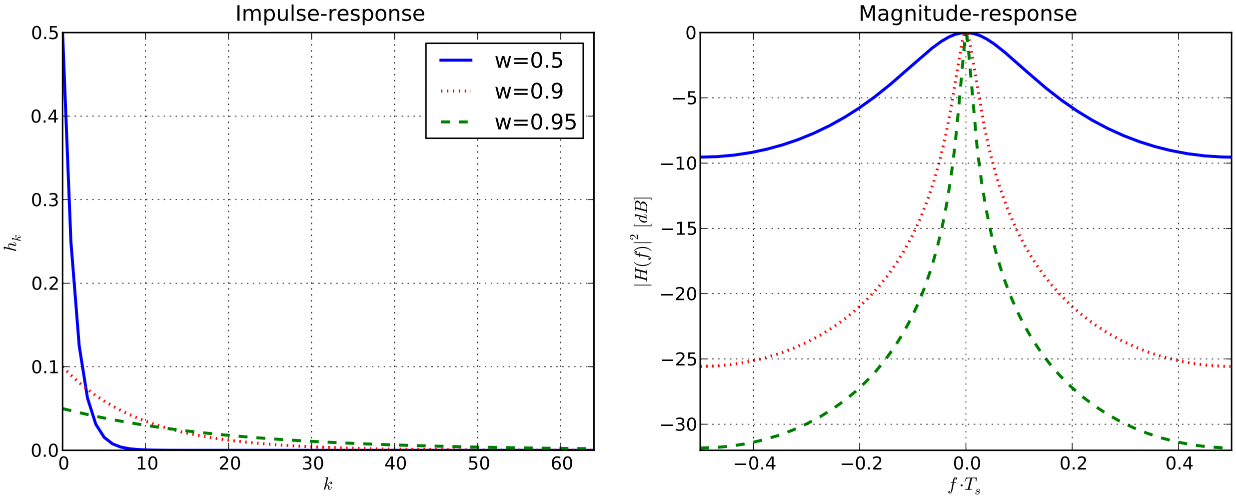

Figure 7.24.: Impulse-response and magnitude-response of the filter for jumb indicator

However, the following problem should be addressed. Assume that a phase or frequency jump occurs in the steady state. If κ is very large or $g_{r,ABA}$ is very small, the acquisition time can be very long dependening on l_{ABA}. In this case, the acquisition must be restarted by setting $\kappa = 1$.

As mentioned in Section 7.2.3, in the steady state, e_k approximately tends to be zero and elsewhere $|e_k|^2 > 0$. Therefore, we can use $|e_k|^2$ as an indicator for restarting the acquisition. However, $|e_k|^2$ is typically very noisy. As a consequence, the decision threshold for restarting the acquisition based on $|e_k|^2$ is inaccurate. For the noise suppression with low implementation complexity, a two-tap recursive feedback filter is proposed. We define J_k as the *jump indicator*, which is the filtered signal of $|e_k|^2$ with the proposed filter and can be given by

$$J_k = w \cdot J_{k-1} + (1 - w) \cdot |e_k|^2, \tag{7.37}$$

with $w \in [0.5; 1.0)$. The impulse-response of the filter h_k can be given by

$$h_k = (1 - w) \cdot w^k. \tag{7.38}$$

Figure 7.24 shows the impulse-response and the magnitude-response of the filter with various w.

In the next step, for restarting the acquisition mode, we define κ_{min} as the minimal number of samples waiting for the decision and J_{max} as the tolerable upper bound for J_k. In other words, we wait until $\kappa > \kappa_{min}$. If $J_k > J_{max}$, the acquisition is renewed. Choosing κ_{min} should be the point where the impulse-response tends to zero. Since the filter has a infinite impulse response, the state of the zero impulse-response cannot be theoretically obtained. However, the approximation of κ_{min} can be calculated by

$$\kappa_{min} \approx \frac{\log(h_{k\to\infty}) - \log(1 - w)}{\log(w)}, \tag{7.39}$$

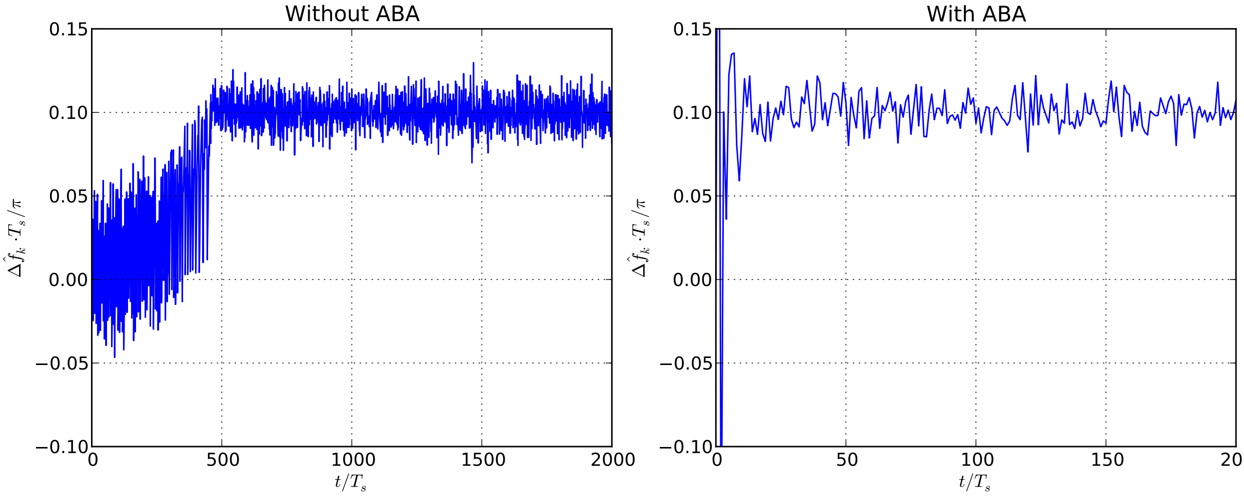

Figure 7.25.: Acquisition of the estimated frequency offset $\Delta\hat{f}_k \cdot T_s$ with and without ABA

where $h_{k\to\infty}$ is the desirable value of h_k by $k \to \infty$. Nevertheless, setting J_{max}, depends on many parameters. In our evaluations, we use the approximation

$$J_{max} \approx S(\pi/16)^2, \tag{7.40}$$

to achieve J_{max}. With the jump indicator mechanism, κ in Eq.(7.36) can be rewritten as

$$\kappa = \begin{cases} 1 & \text{for } k < 1 \text{ or } \ (\kappa > \kappa_{min} \text{ and } J_k > J_{max}) \\ k & \text{for } 1 \leq k \leq l_{ABA} \\ l_{ABA} & \text{else} \end{cases} . \tag{7.41}$$

For the second order loop filter, the adaptive filter gain $g_{r,ABA}$ can be written as

$$g_{i,ABA} = \frac{g_i}{\kappa}, \tag{7.42}$$

where κ is the joint variable with Eq.(7.35).

It should be noted that for small g_r, g_i and l_{ABA}, we can apply ABA without the jumb indicator mechanism. With Eq.(7.35) and Eq.(7.36), the requirements of the fast acquisition and the accurate estimation can also be fulfilled.

For the demonstration of the ABA, the acquisition of a frequency jump $\Delta\hat{f}_k \cdot T_s$ with and without ABA is depicted in Figure 7.25. Since $\Delta\hat{f}_k$ cannot directly be estimated with the Costas loop, it can be calculated by

$$\Delta\hat{f}_k \cdot T_s = \frac{\hat{\varphi}_k}{dt}. \tag{7.43}$$

In the evaluations, a signal with QSPK modulation format is generated and transmitted over an AWGN channel with 15dB SNR. For the second order Costas loop without ABA, a loop filter with $g_r = 0.2$ and $g_i = 0.025$ is used. In contrast, with ABA, the parameters are configured as followed $g_r = 4.0, g_i = 0.5, l_{ABA} = 20, w = 0.99, \kappa_{min} = 458$ and $J_{max} = 0.04$. The parameters are configured like this so that the loop filter in the tracking mode with and without ABA have the same noise bandwidth. The evaluations in Figure 7.25 show that the Costas loop without ABA reaches the steady state within about $480 \cdot T_s$. While with ABA, within about $20 \cdot T_s$. In this case, the improvement of the acquisition time about 2400% can be achieved without the trade-off of the tracking performance loss.

7.4. Conclusions

In this Chapter, two feedback algorithms for carrier phase recovery, namely the MLL and the Costas loop are described and analyzed. Due to the fact that both algorithms are based on decision-directed schemes, they can be applied for all modulation formats. Although the MLL is very robust against the laser linewidth, its tolerance against the LO frequency offset is relatively low. Moreover, error propagations can be induced. Hence, the MLL is not suitable as a stand-alone carrier synchronization for the high bit-rate optical transmission systems. In contrast, the Costas loop, can tolerate a wider range of the LO frequency offset and has an approximately equal tolerance against the laser linewidth as MLL. It means that the Costas loop can fulfill the requirements as a stand-alone carrier synchronization in the system, where Δf is smaller than the theoretical limit of the decision directed scheme.

For the implementation, the Superscalar parallelization architecture must be applied for the feedback carrier synchronization due to the delay reduction. However, the performance degradation caused by the feedback delay must be considered for the deployment of the Costas loop. In comparison to the MDE (see Section 6.5) the implementation complexity can significantly reduced and the tolerance against the LO frequency offset can be significantly improved by a Costas loop.

Moreover, the ABA algorithm, which can greatly reduce the acquisition time for the Costas loop without the trade-off of the tracking performance loss, is described and analyzed.

8. Automatic Frequency Control

At the start-up of an optical link with coherent demodulation, the frequency offset can be in the range of GHz [117]. However, conventional digital signal processing algorithms in digital receivers like the timing recovery and the time domain equalization cannot tolerate huge frequency offsets [48]. The typical carrier synchronization bandwidth shown in Chapter 6 and 7 is usually even smaller, in order to minimize ASE-noise influence. Hence, a coarse carrier frequency recovery prior to other DSP algorithms is required. An automatic frequency control (AFC) is necessary in order to solve this problem, because a wide range of frequency offsets can be estimated. In this Chapter, algorithms based on AFC are briefly described and reviewed with performance evaluations.

8.1. Application of Automatic Frequency Control

With the AFC, the structure of DSP as shown in Section 3.5.3 must be modified. After the signal detection with the optical frontend and the digitization with ADC, a coarse LO frequency offset in the range of GHz can be estimated an compensated with a AFC to relax the other parts of DSP. It should be emphasized that the time domain carrier is also required for the accurate estimation of the carrier phase and frequency. Figure. 8.1 illustrates DSP with AFC in coherent receiver.

In general, only *the spectrum asymmetry detectors* are different in the various algorithms for the AFC. The residual parts of the estimator, however, are based on the same structure. In

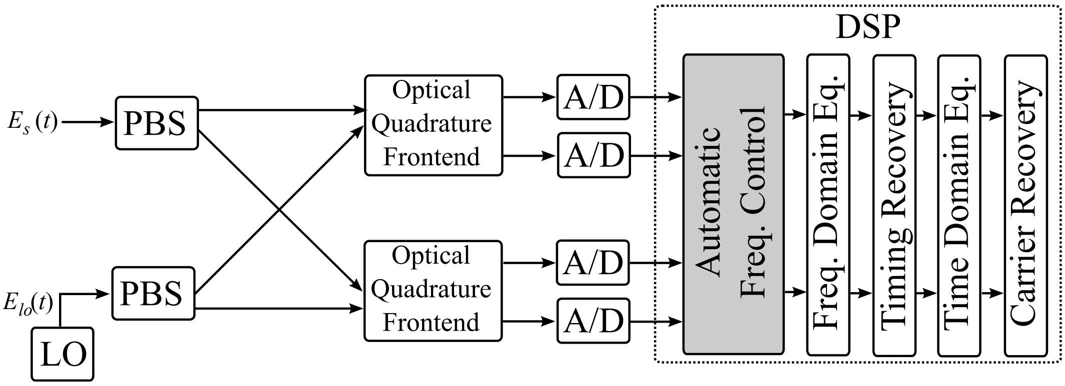

Figure 8.1.: DSP with automatic frequency control in coherent receiver

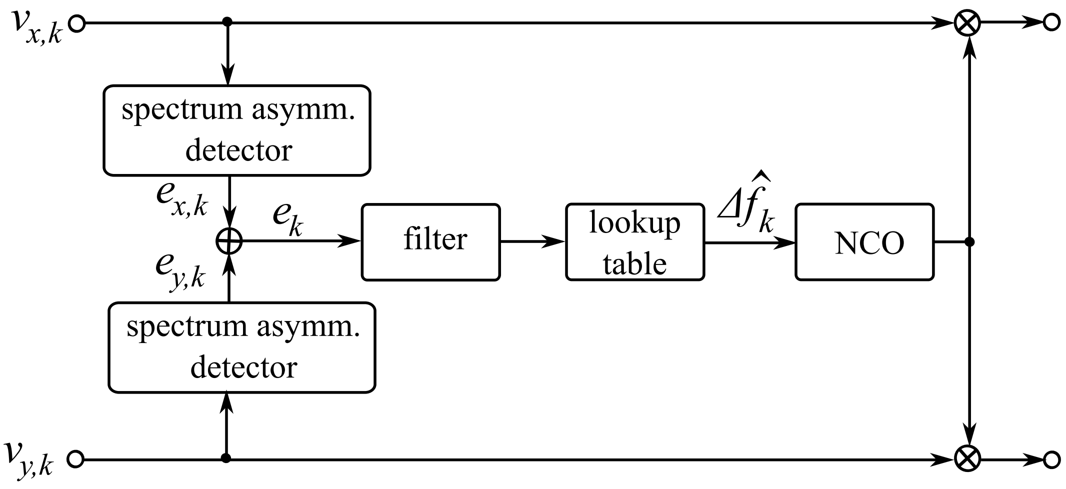

Figure 8.2.: Feed forward estimator for AFC

the following, two alternative schemes for the AFC are briefly described.

The first scheme is the feed forward estimator as illustrated in Figure 8.2.

In this scheme, the sampled signals $v_{x,k}, v_{y,k}$ from x- and y-polarization respectively are fed into spectrum asymmetry detectors to calculate the error signals $e_{x,k}, e_{y,k}$

Due to the equalization for PMD, the LO frequency offset compensation must be identical in both polarizations. Hence, $e_{x,k}, e_{y,k}$ are summed to e_k before feeding into the filter for the noise suppression. Although we can use any arbitrary filter in this scheme, for the convenience and the reduction of the implementation complexity an averaging filter is preferred. Since the amplitude of the error signal can depend on many parameters e.g., bandwidth of the optical filters, bandwidth of the electrical filters, and averaged signal power, the frequency offset Δf cannot be directly estimated from the filtered error signal. To solve this problem, we apply a lookup table, which converts the filtered error signal into the estimated frequency offset $\Delta\hat{f}$. Afterwards, numerically-controlled oscillator (NCO) can be applied by using $\Delta\hat{f}$ to compensate for the LO frequency offset.

Figure 8.3 depicts a second scheme with a feedback structure. It must be emphasized that this scheme should be implemented with the Superscalar parallelization architecture as shown in Section 4.2.2 to reduce the performance loss caused by the feedback delay. Basically, the error calculation and summation of the feedback scheme is identical to the feed forward scheme. The key difference to the feed forward scheme is the LO frequency offset correction before the error calculation and the application of the loop filter. In the feedback scheme, $e_{x,k}, e_{y,k}$ tend to be zero, if the final frequency offset $\Delta\hat{f}$ is achieved. Hence, the lookup table is not required. Since the loop filter applied in this scheme is the same as the loop filter for the first order Costas loop as shown in Section 7.2, the characteristics of the loop filter are not analyzed here. Moreover, for an improvement of the acquisition, ABA can be used for the adaptation of g_r. Due to the simple implementation without the lookup table, the feedback scheme is preferred for further investigations in this Chapter.

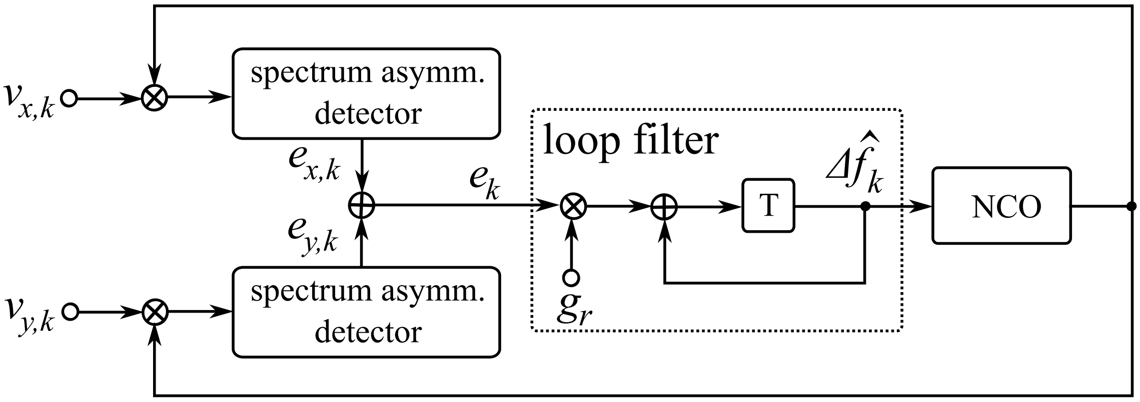

Figure 8.3.: Feedback estimator for AFC

8.2. Double Power Measurement

Since the spectrum of the signal with a carrier frequency offset is asymmetric, we can use this characteristic for frequency offset estimation. For double power measurement (DPM) [133, 134, 135], two digital single side band bandpass filters BP1 and BP2 with transfer-functions of $H_{BP1}(f)$ and $H_{BP2}(f)$ are used respectively to detect the asymmetry of the signal spectrum as illustrated in Figure 8.4. It should be emphasized that the center frequency of the bandpass filters should be the Nyquist frequencies f_{Nq} for BP1 and -f_{Nq} for BP2 with

$$f_{Nq} = \frac{1}{2 \cdot T_s}. \tag{8.1}$$

The signals $e_{x,k}$ and $e_{y,k}$ for the digitized signals in x- and y-polarization can be given by

$$e_{x,k} = |v_{x,k} * h_{BP1,k}|^2 - |v_{x,k} * h_{BP2,k}|^2 \tag{8.2}$$

$$e_{y,k} = |v_{y,k} * h_{BP1,k}|^2 - |v_{y,k} * h_{BP2,k}|^2, \tag{8.3}$$

where $h_{BP1,k}$ and $h_{BP2,k}$ are the impulse-response for BP1 and BP2 respectively. Figure 8.5 shows the block diagram of the error signal generator for the DPM in x-polarization. For accurate estimation, a sampling rate of $2f_s = 2/T_s$ for $v_{x,k}$ and $v_{y,k}$ is recommended.

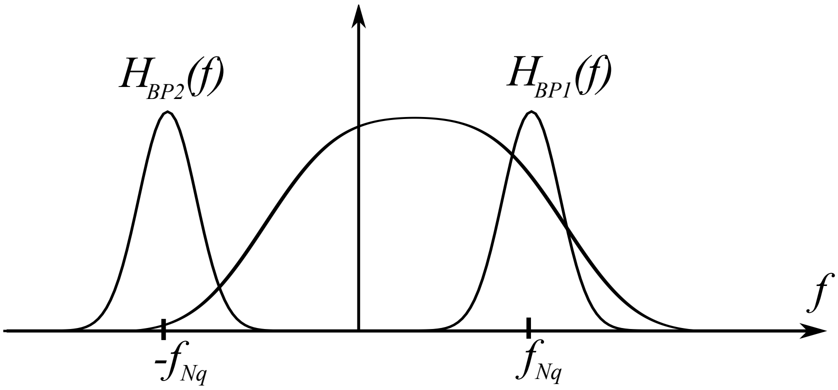

Figure 8.4.: Signal spectrum and transfer function of the single side bandpass filters

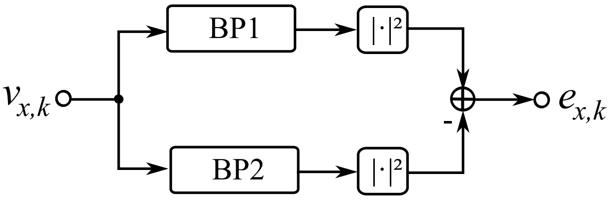

Figure 8.5.: Block diagram of error signal generator with DPM for x-polarization

The filters BP1 and BP2 are the key components for the implementation complexity and performance optimization of DPM. Note that $G(f)$ is the transfer-function of the filter for the pulse-shaping. In [134], it has been shown that with the condition

$$G(f+f_{Nq})\cdot H_{BP1}(f+f_{Nq}) = G(f-f_{Nq})\cdot H_{BP2}(f-f_{Nq}), \tag{8.4}$$

the optimal performance for DPM can be achieved. However, the implementation of BP1 and BP2 from Eq.(8.4) is complex due to the asymmetry of $H_{BP1}(f)$ and $H_{BP2}(f)$. Moreover, for this filter optimization, the characteristics of all filters in the whole transmission system must be known, because the signal pulse-shape can be changed by each filtering. Hence, the filter optimization from Eq.(8.4) is not suitable for the DSP in the high bit-rate optical transmission systems.

Due to the fact that BP1 and BP1 are the single side band bandpass filters, the filter coefficients of the digital implementation via FIR or IIR are complex numbers. For the complexity reduction of the implementation, the following modification of DPM proposed by the author [135] can be applied. In the first step, the center frequency of the signal spectrum can be relocated to f_{Nq} and $-f_{Nq}$. In the next step, the bandpass filters BP1 and BP2 can be replaced by a lowpass filter with the impulse response $h_{TP,k}$, which can be realized with real number filter coefficients.

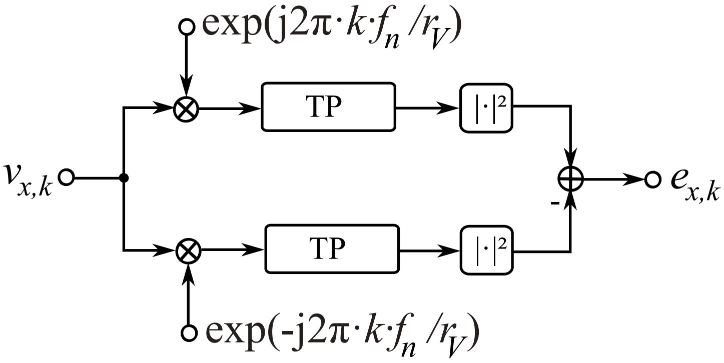

Figure 8.6.: Block diagram of simplified error signal generator with DPM for x-polarization

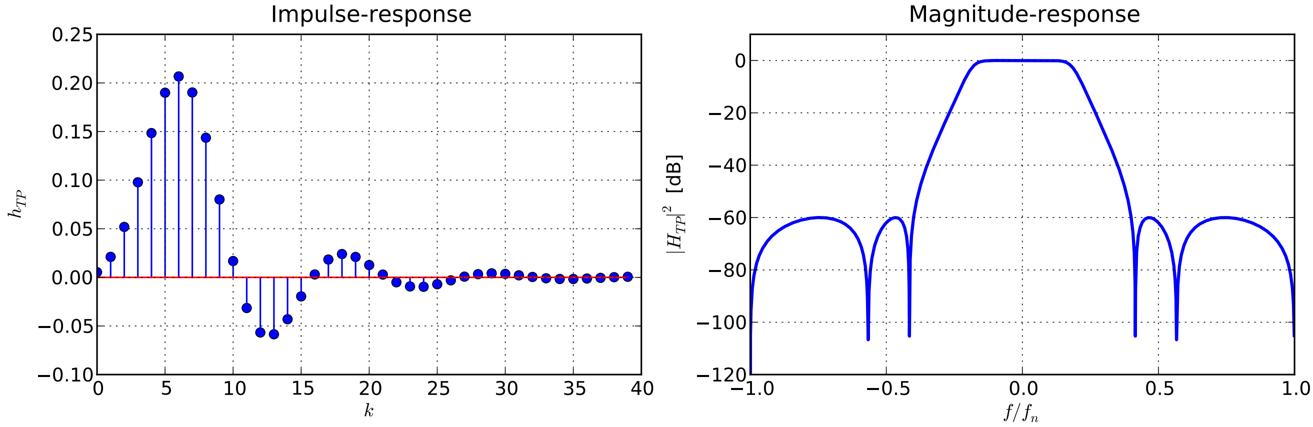

Figure 8.7.: Impulse-response and magnitude-response of a IIR Chebyshev lowpass filter for the DPM

Finally, the signal $e_{x,k}$ and $e_{y,k}$ in Eq.(8.3) and Eq.(8.3) can be rewritten as

$$e_{x,k} = \left| v_{x,k} \cdot \exp\left(j2\pi k \frac{f_{Nq}}{r_V} \right) * h_{TP,k} \right|^2 - \left| v_{x,k} \cdot \exp\left(j2\pi k \frac{-f_{Nq}}{r_V} \right) * h_{TP,k} \right|^2 \tag{8.5}$$

$$e_{y,k} = \left| v_{y,k} \cdot \exp\left(j2\pi k \frac{f_{Nq}}{r_V} \right) * h_{TP,k} \right|^2 - \left| v_{y,k} \cdot \exp\left(j2\pi k \frac{-f_{Nq}}{r_V} \right) * h_{TP,k} \right|^2 , \tag{8.6}$$

where r_V is the sample rate. Figure 8.6 shows the block diagram of the error signal generator for DPM in x-polarization.

For the performance evaluation, a *IIR-Chebyshev* lowpass filter with the passband of $0.2 \cdot f_{Nq}$ and 12 taps is used. Figure 8.7 depicts the impulse-response and the magnitude-response of the filter. It should be noted, that the S-curve of DPM strongly depends on the characteristics of the lowpass filter. With the filter from Figure 8.7, the S-curve for DPM as shown in Figure 8.8 can be achieved. As we can see from the S-curve that with DPM, the LO frequency offset of $\pm f_{Nq}$ can be estimated. The slope of S-curve $A \approx 1$ can influence the loop filter noise bandwidth

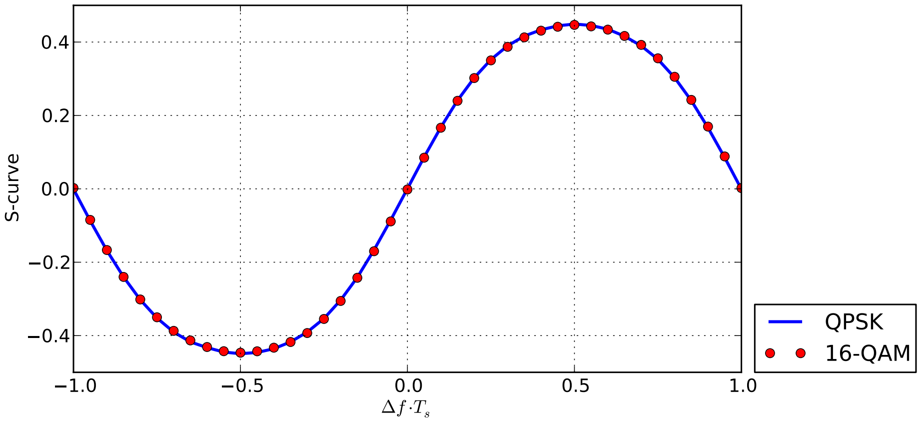

Figure 8.8.: S-curve of DMP for QPSK and 16-QAM

as shown in Section 7.2.4. Moreover, there is no difference between S-curve for QPSK and 16-QAM modulation formats. It means that DPM is independent of the modulation format. This characteristic is very desirable.

8.3. Balanced Quadricorrelator

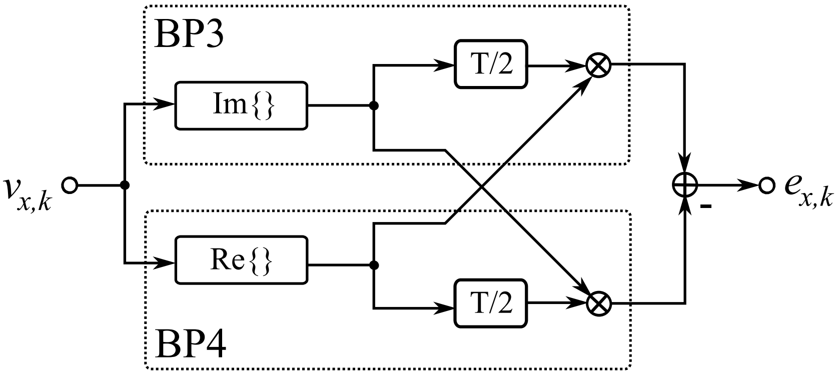

Figure 8.9.: Block diagram of error signal generator with balanced Quadricorrelator for x-polarization

The balanced Quadricorrelator (BQ) algorithm [136, 137, 135] is a well-known and powerful algorithm for AFC. Basically, DPM and BQ are based on the same principle [134, 138]. The difference between DPM and BQ is the implementation form and the transfer-function of the bandpass filters. Fig. 8.9 depicts the block diagram of the error signal generator in the x-polarization for the BQ algorithm, which can be written as [134]

$$e_{x,k} = \underbrace{\mathrm{Re}\{v_{x,k}\}\cdot\mathrm{Im}\{v_{x,k-1}\}}_{\mathrm{BP3}} - \underbrace{\mathrm{Re}\{v_{x,k-1}\}\cdot\mathrm{Im}\{v_{x,k}\}}_{\mathrm{BP4}} \tag{8.7}$$

$$e_{y,k} = \mathrm{Re}\{v_{y,k}\}\cdot\mathrm{Im}\{v_{y,k-1}\} - \mathrm{Re}\{v_{y,k-1}\}\cdot\mathrm{Im}\{v_{y,k}\}. \tag{8.8}$$

The transfer function $H_{BP3}(f)$ and $H_{BP4}(f)$ of BP3 and BP4 respectively in Eq.(8.8) can be rewritten to [138]

$$H_{BP3}(f) = -j + \exp\left(-j2\pi f\frac{T_s}{2}\right) \tag{8.9}$$

$$H_{BP4}(f) = j + \exp\left(-j2\pi f\frac{T_s}{2}\right). \tag{8.10}$$

With this form of bandpass, the implementation complexity of BQ is much lower than DPM, which requires two additional digital filters. Figure 8.10 illustrates the magnitude-responses of BP3 and BP4 and shows that the bandpass filters have a wide range passband, which impairs the estimation accuracy. It should be noted that a $\frac{T}{2}$-spaced sampling is required for the BQ.

For a performance improvement, we can filter the sampled signals $v_{x,k}$ and $v_{y,k}$ with a bandpass pre-filter before the calculation of the error signal. The pre-filter can suppress the pattern-jitter noise or the so called self-noise, which occurs due to the data information. In [138], the

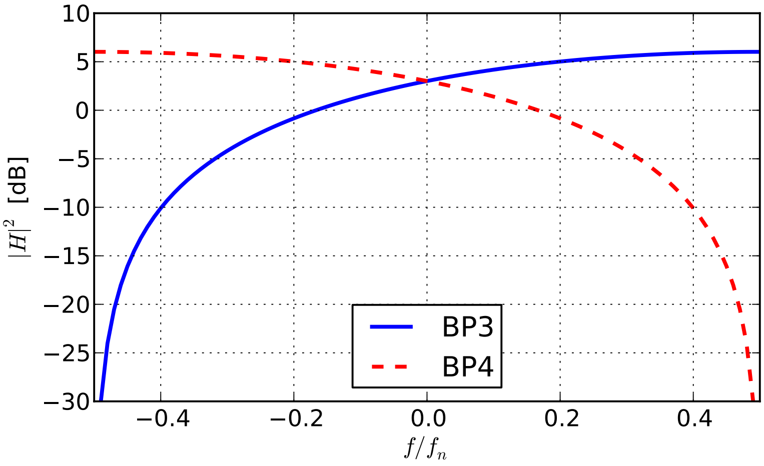

Figure 8.10.: Magnitude-response of the bandpass filters for the balanced Quadricorrelator

transfer-function of the pre-filter is proposed. Note that $H_{pre}(f)$ is the transfer-function of the pre-filter and $G_0(f)$ the normalized transfer-function of the pulse-shaping filter $G(f)$ with

$$G_0(f) = \frac{G(f)}{G(0)}. \tag{8.11}$$

With the followed condition, the optimal pre-filter can be achieved [138] :

$$|H_{pre}(f)| = \frac{1}{T_s \cdot \sin(\pi f T_s)} \cdot \frac{|G_0(f)|^{-2} \cdot \left[|G_0(f)|^{-2} \frac{d}{df} |G_0(f)|^2\right]_{\text{even}}}{\left[|G_0(f)|^{-2} + |G_0(f)|^{-4}\right]_{\text{even}}}, \tag{8.12}$$

where

$$[X(f)]_{\text{even}} = \frac{X(f) + X(f_{Nq} - f)}{2} \tag{8.13}$$

and

$$\arg\left\{H_{pre}(0.5 f_{Nq} + f) \cdot G(0.5 f_{Nq} - f)\right\} = \arg\left\{H_{pre}(0.5 f_{Nq} - f) \cdot G(0.5 f_{Nq} - f)\right\}. \tag{8.14}$$

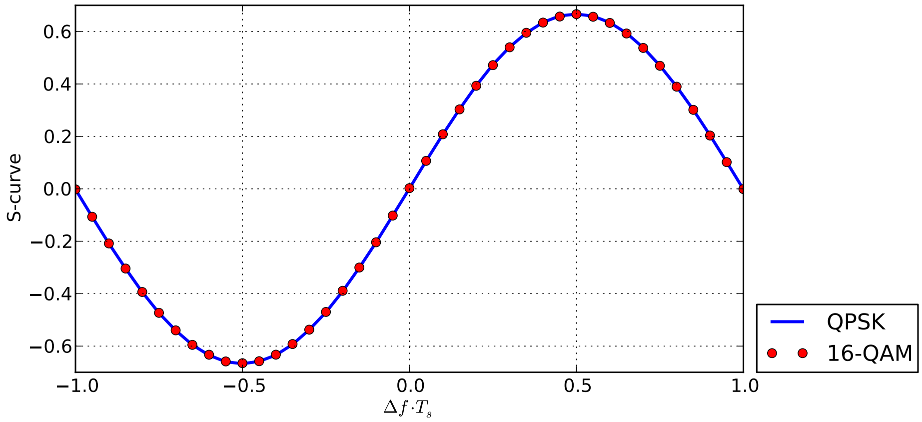

Figure 8.11.: S-curve of balanced Quadricorrelator for QPSK and 16-QAM

As we can see from Eq.(8.12) and Eq.(8.14) that the pre-filter strongly depends on $G(f)$ and has an asymmetrical transfer-function. Like the optimal bandpass filters for DPM, the implementation of the pre-filter for the optimal BP is not suitable for high bit-rate optical transmission systems.

Figure 8.11 depicts the S-curve of the BQ for QPSK and 16-QAM modulation formats. Like DPM, from the S-curve, we can see that the BQ can estimate the LO frequency offset up to f_{Nq} and is independent of the modulation format. Due to the bandpass filters BP3 and BP4, which have an amplifying characteristic in the passband frequency range, BQ provide an S-curve slope for $\Delta f = 0$ of $A = 2$.

8.4. Frequency Domain Automatic Frequency Control

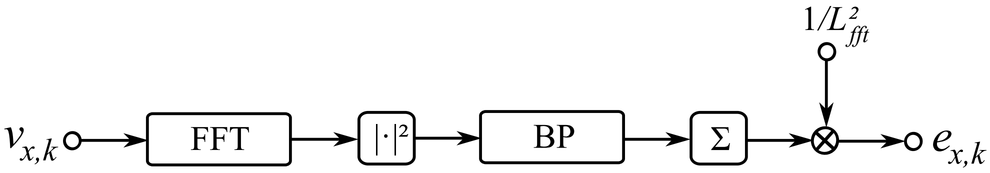

Figure 8.12.: Block diagram of error signal generator with frequency domain automatic frequency control for x-polarization

Due to the complexity, the implementation of the bandpass filter for DPM and BQ is limited and the optimal performance cannot be achieved. However, in a receiver with a frequency domain equalization, the signal spectrum can be directly accessed from the fast Fourier transformation (FFT). Hence, the author has proposed an algorithm for AFC using signal spectrum from FFT to simplify and optimize $e_{x,k}$ and $e_{y,k}$ [139]. Due to the direct access of the signal spectrum, the algorithm is called frequency domain automatic frequency control (FD-AFC) [139].

Figure 8.12 depicts the block diagram of the error calculation with the FD-AFC for x-polarization. Note that $V_{x,k}$ is the *discrete Fourier transform* for $v_{x,k}$ and $V_{y,k}$ for $v_{y,k}$ via FFT with a length of L_{fft}. The error signal can be calculated by

$$e_{x,k} = \frac{1}{L_{fft}^2} \sum_{n=k-L_{fft}}^{k} |V_{x,n}|^2 \cdot H_{BP,n} \tag{8.15}$$

$$e_{y,k} = \frac{1}{L_{fft}^2} \sum_{n=k-L_{fft}}^{k} |V_{y,n}|^2 \cdot H_{BP,n}, \tag{8.16}$$

where $H_{BP,k}$ is the sampling of the transfer-function $H_{BP}(f)$ for bandpass filter with

$$H_{BP,k} = H_{BP}\left(f - k \cdot r_V\right). \tag{8.17}$$

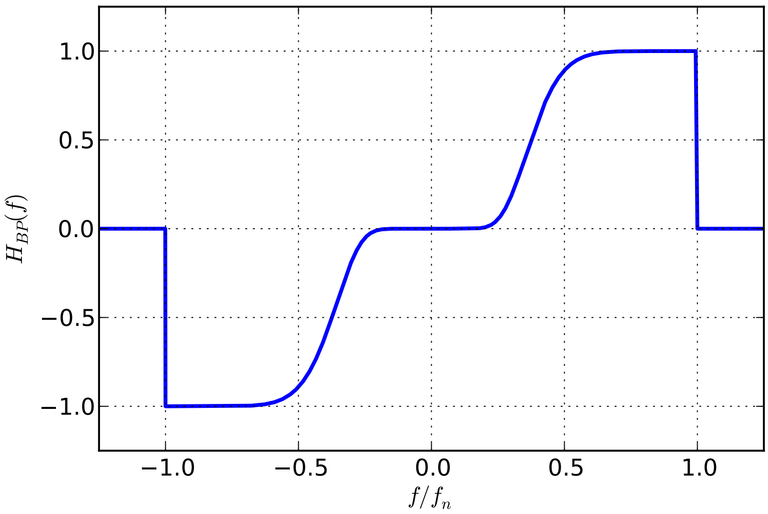

Figure 8.13.: Transfer-function of bandpass filter for FC-AFC

Basically, $H_{BP}(f)$ is a modification of the bandpass filter optimization for DPM according to Eq.(8.4) with

$$H_{BP}(f) = \begin{cases} |H_{BP1}(f)| & \text{for } f \geq 0 \\ -|H_{BP2}(f)| & \text{for } f < 0. \end{cases} \tag{8.18}$$

For a Gaussian pulse-shaping, $H_{BP}(f)$ is illustrated in Figure 8.13.

The S-curve of the FD-AFC for QSPK and 16-QAM is illustrated in Figure 8.14. The modulation format, independent of the FD-AFC and the estimation range of $\pm f_{Nq}$ like DPM and BQ, can be read from the S-curve. With the FD-AFC, we have an S-curve slope for $\Delta f = 0$ of $A = 1.1$.

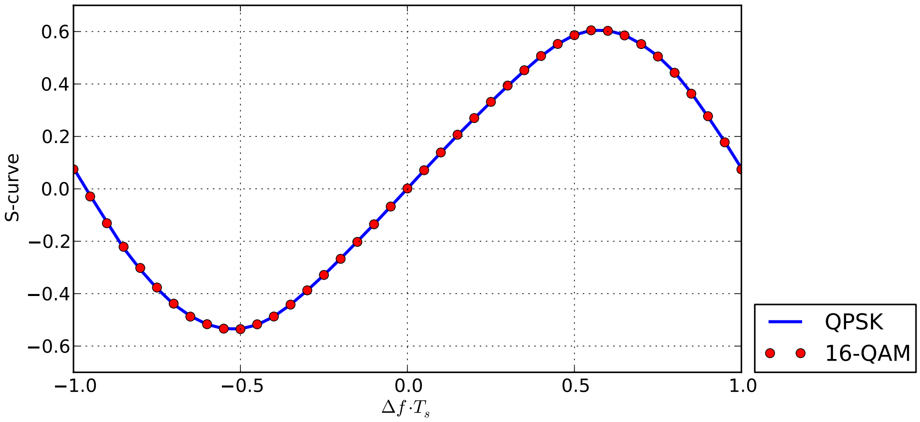

Figure 8.14.: S-curve of the FD-AFC for QPSK and 16-QAM

8.5. Estimation Bias

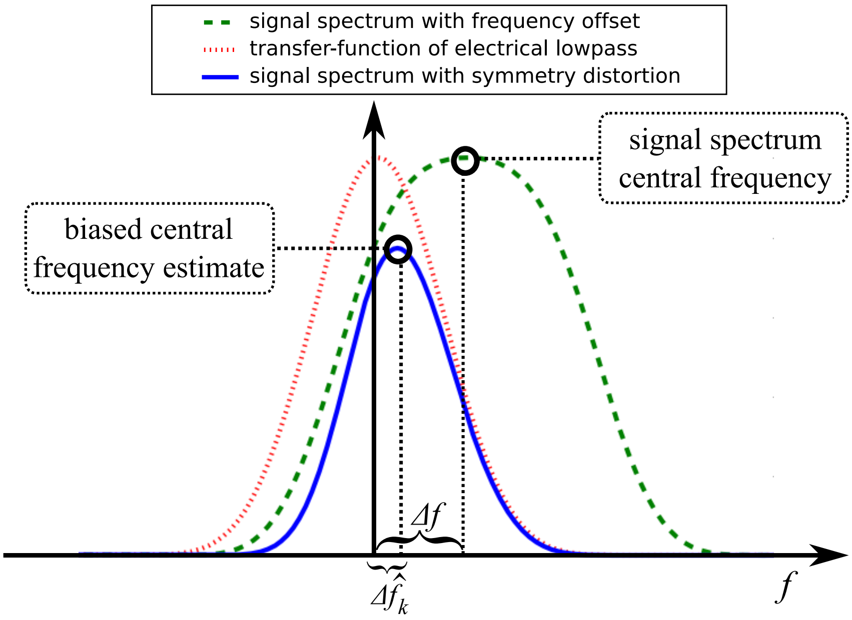

Figure 8.15.: Spectrum symmetry distortion by electrical lowpass filtering

In a digital implementation of AFC and a digital frequency offset correction, an analog feedback to the LO is not required for reducing implementation complexity. However, the symmetry characteristic of the signal spectrum with a frequency offset is distorted by the electrical lowpass filtering after down conversion of the signal with the free running LO. Figure 8.15 illustrates the cause for the spectrum symmetry distortion, which induces an estimation bias in the AFC. Due to the acquisition characteristics of the feedback AFC, the frequency estimation remains,

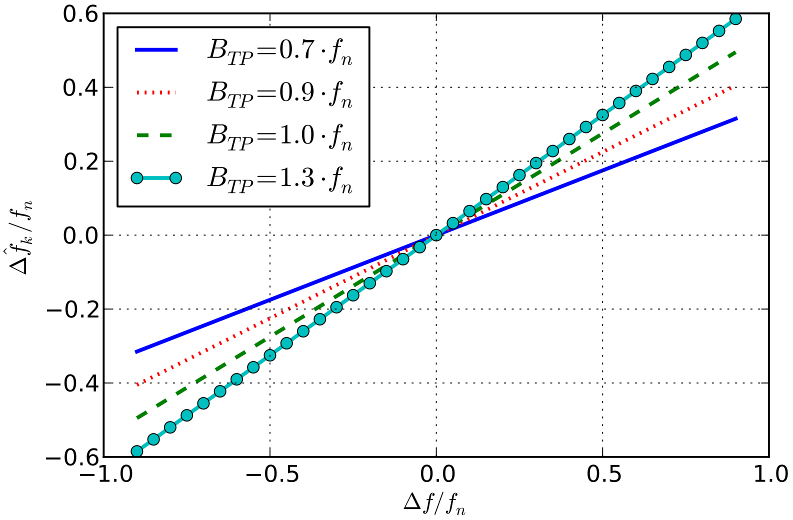

Figure 8.16.: Estimation bias of AFC vs. electrical lowpass bandwidth B_{TP}

when the signal spectrum central is relocated to f=0Hz. With electrical lowpass filtering, the signal spectrum central frequency and Δf are not identical. Hence, the estimation is biased.

In contrast, with analog feedback to the LO, the estimation bias due to electrical lowpass filtering does not occur. However, additional implementation complexity must be considered.

Since the estimation bias is caused by the electrical lowpass filtering, the dimension of the estimation bias depends on the bandwidth of the electrical lowpass filter as shown in Figure 8.16. Although the estimation with AFC is biased, $\Delta\hat{f}_k$ is linearly dependent on Δf and can be given by

$$\Delta\hat{f}_k = m_{bias} \cdot \Delta f \tag{8.19}$$

where m_{bias} is defined as the estimation bias gradient. Hence, we can correct the estimation bias by finding m_{bias} and simply divide m from $\Delta\hat{f}_k$. From Figure 8.16, we find out that m_{bias} can be simply computed by

$$m_{bias} = \frac{B_{TP}}{2 \cdot f_{Nq}} \tag{8.20}$$

with B_{TP} being the bandwidth of the electrical lowpass filter.

On the one hand, for the feed forward approach, the bias correction can be directly applied in the the look-up table. On the other hand, for the feedback approach, the structure of AFC must be modified as illustrated in Figure 8.17. After estimating $\Delta\hat{f}_k$ from the loop filter, $\Delta\hat{f}_k$ must be corrected according to Eq.(8.19). As the consequence, the S-curve of the error signal generator is relocated with

$$S\left(\Delta f + m_{bias} \cdot \Delta\hat{f}_k\right) = 0. \tag{8.21}$$

Hence, the error signal e_k must be corrected to

$$e_{corr,k} = e_k - S\left(m_{bias} \cdot \Delta\hat{f}_k\right) \tag{8.22}$$

as indicated in Figure 8.17.

It should be noted that the correction of the estimation bias depends on system configurations. For the application of AFC, we recommend that the estimation bias must be investigated by a

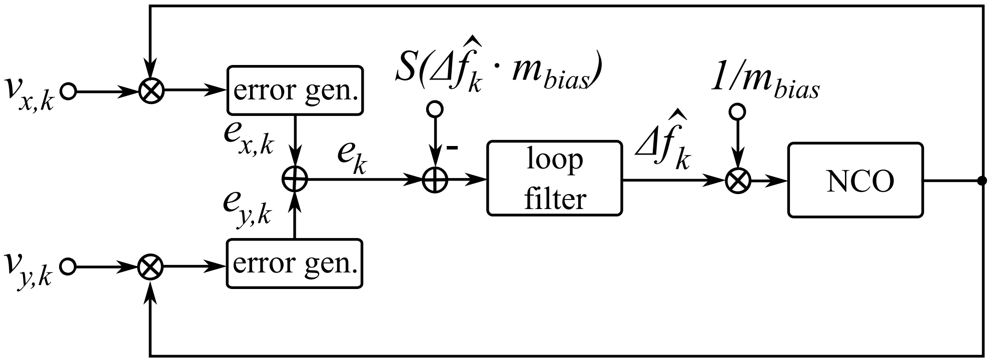

Figure 8.17.: Modified feedback estimator for AFC considered estimation bias

system design. Moreover, not only the electrical lowpass filtering induces the estimation bias of AFC, but also all effects, which can influence on the symmetry of the signal spectrum. In the scope of this dissertation, these and further effects are not investigated.

8.6. Estimation Performance

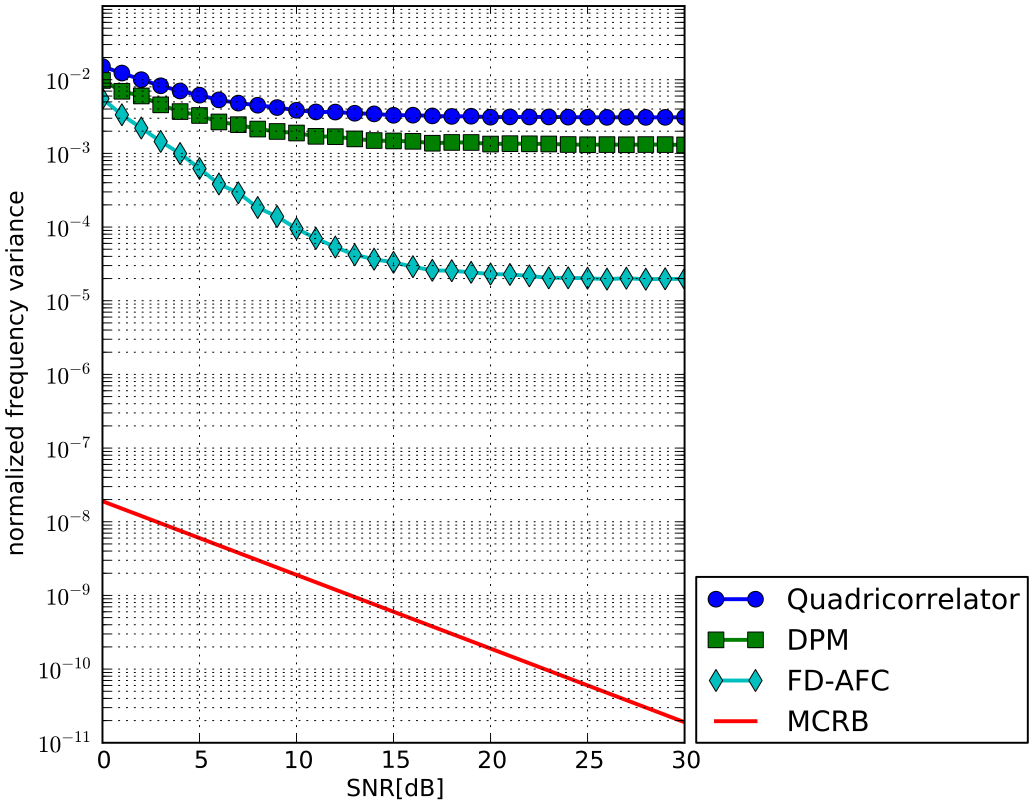

Figure 8.18.: Simulative performance evaluation of feedback AFC with $L_{eq} = 200$ for various algorithms

Figure 8.18 shows the performance of the feedback AFC with $L_{eq} = 200$ for the algorithms DPM, BQ and FD-AFC in the AWGN channel. For $L_{eq} = 200$, the parameter g_r in the loop filter must be adjusted for each algorithm considering the S-curve slope A. Although the evaluations are performed for QPSK, the performance of the AFC for other modulation formats is identical to QPSK due to the modulation format independence of the AFC.

For the DPM, the lowpass filter as shown in Figure 8.7 is used and for the BQ, pre-filter according to Eq.(8.12) and Eq.(8.14) is not applied. As we can see, all algorithms have the variance floor caused by the self-noise. In comparison to BQ, DPM has a better performance because the filter used in DPM can suppress more self-noise. Due to the optimal bandpass filter, the performance of FD-AFC is significantly better than the other algorithms. The estimated frequency variance of FD-AFC is about two decades lower than DPM and BQ. However, the variance floor indicates that with FD-AFC and the optimized bandpass filter, the self-noise cannot be completely suppressed. This is due to the fact that for the filter optimization, only the pulse-shaping filter is considered and not the optical bandpass and electrical lowpass filters.

It should be emphasized that the optical channel has the characteristics of an all-pass filter as described in Chapter 2 and the symmetry of the signal spectrum cannot be changed by the optical channel. Hence, the performance evaluations as shown in Figure 8.18 are also valid for the signal with distortions from the optical channel like CD and PMD. As a consequence, we can use the AFC before the channel equalization. This is a useful feature for the AFC.

In the following, the auhor shows the acquisition of the AFC. The acquisition is one of the key requirements, which must be satisfied for a feedback estimator. For a carrier frequency estimator like AFC, it is notably important in cases of LO frequency jumps and LO frequency variations as shown in Section 3.1.1. In [77], it is shown that for a carrier frequency with a loop filter according to Figure 8.3, the acquisition time T_{acq} can be approximately given by

$$T_{acq} \approx \frac{1.15}{B_L}, \tag{8.23}$$

where B_L is the noise bandwidth of the loop filter and can be calculated according to Eq.(7.26). Substituting Eq.(7.26) into Eq.(8.23) yields

$$T_{acq} \approx \frac{T_S \cdot 2.3 \cdot (2 - g_r \cdot A)}{g_r \cdot A}. \tag{8.24}$$

As an example, Figure 8.19 shows the acquisition of the FD-AFC without ABA setting $g_r = 0.02$. With this setup, the loop filter has the bandwidth of $B_L \approx 5.6e - 3/T_s$, and hence, $T_{acq} \approx 207 \cdot T_s$, which approximately equal to the simulation.

To improve the acquisition time, ABA can be used. Figure 8.19 shows that with ABA, the acquisition time of the AFC can be reduced significantly. For the derivation of the acquisition for ABA, Eq.(8.24) can be rewritten as

$$T_{acq} = C_{acq} \cdot T_s, \tag{8.25}$$

where C_{acq} is defined as acquisition constant and can be given by

$$C_{acq} = \frac{2.3 \cdot (2 - g_r \cdot A)}{g_r \cdot A}. \tag{8.26}$$

With ABA, for each step of the acquisition, the bandwidth of the loop filter is reduced. Hence, the acquisition time is increased. We define N_{ABA} as the number of signal samples, where the steady state for ABA can be achieved. According to Eq.(8.25), N_{ABA} can be calculated solving the following equation :

$$\sum_{i=1}^{N_{ABA}} \frac{T_{acq}}{i \cdot C_{acq}} = T_{acq}, \tag{8.27}$$

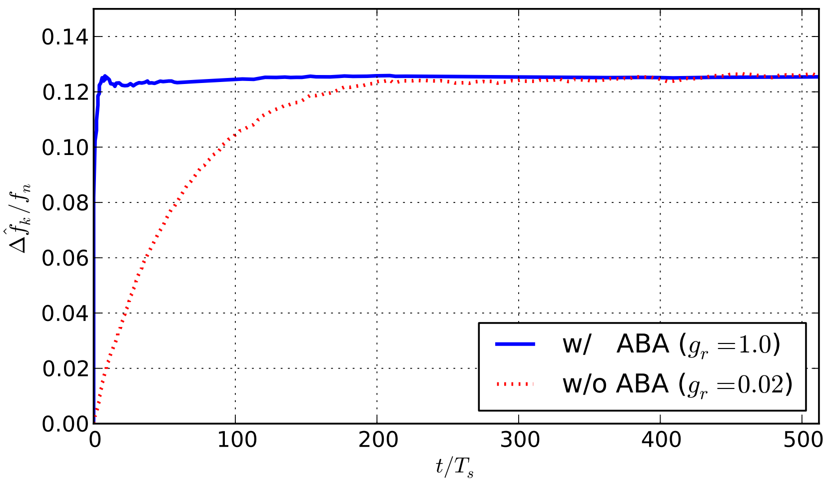

Figure 8.19.: Acquisition of FD-AFC with and without ABA

which can be simplified to

$$\sum_{i=1}^{N_{ABA}} \frac{1}{i} = C_{acq}. \tag{8.28}$$

Unfortunately, Eq.(8.28) cannot directly solved. However, the summation in Eq.(8.28) can be approximately calculated by

$$\sum_{i=1}^{N_{ABA}} \frac{1}{i} \approx 0.6 + \log(N_{ABA}), \tag{8.29}$$

for $N_{ABA} > 10$ And N_{ABA} can be approximately given by

$$N_{ABA} \approx 10^{((2.3\cdot(2-g_r\cdot A))/(g_r\cdot A)-0.6)} \tag{8.30}$$

As we can see from Eq.(8.30), ABA can reduce the acquisition time only with sufficient g_r. In other case, the steady state cannot be achieved. We recommended to set $g_r \cdot A \geq 1.0$. As an example, Figure 8.19 shows the acquisition of FD-AFC with ABA setting $g_r = 1.0$ and $g_r \cdot A = 1.1$, where we have the steady state within 20 signal samples.

8.7. Conclusions

With an AFC, a wide range of LO frequency offset can be estimated and corrected. Since AFC operates with the asymmetry of the signal spectrum and the distortions in the optical channel have all-pass characteristics, the AFC is very robust against the channel distortions. Hence, AFC can be used prior to the other DSP algorithms like timing recovery and equalization, and it can relax their operations.

Three algorithms for the AFC, namely DPM, BQ and FD-AFC have been described in this chapter. The optimization of DPM and BQ against the self-noise impairment can be applied with the trade-off of the implementation complexity and is not suitable for high bit-rate optical transmission systems. In contrast, with FD-AFC, the bandpass filter can be optimized without addition implementation complexity. However, the self-noise impairment cannot be completely avoided due to filters with unknown transfer function in optical links, which change the pulse-shaping of the signal. In contrast, for the optimization of the AFC, the exact function of pulse-shaping is required to avoid the self-noise impairment.

Since the FD-AFC has the best performance among three error generators and its implementation complexity is relative low, the FD-AFC is our preferred algorithm for the AFC.

One of the problems for the applying of AFC is the distortion of the spectrum symmetry due to the electrical lowpass filter, which induces the estimation bias for AFC. The problem has been analyzed and its solution has been proposed. However, the spectrum symmetry can be distorted also from other effects, which have not been investigated in the scope of this dissertation.

The acquisition of the AFC with the feedback structure can be significantly improved with the ABA (see Section 7.3). Especially, it is recommended for systems with LO frequency variation and frequency jumps.

9. Conclusions and Outlook

9.1. Algorithms Discussions

In this dissertation, various algorithms for the digital carrier synchronization for high bit-rate optical transmission systems are described and analyzed. However, there is no perfect algorithm, which can be used for all purposes. Instead of finding the *holy grail* for the carrier synchronization, it is more reasonable to design a suitable carrier synchronization for the transmission system. The following criteria should be considered before choosing and designing the carrier synchronization :

- detection technique (direct detection/coherent)
- modulation formats
- implementation complexity
- impairments in the transmission system
  - channel nonlinearities
  - laser linewidth
  - LO frequency offset
  - frequency variations caused by laser instability

For the direct detection technique, applying DSP is not a common task because the linear channel distortions like CD and PMD cannot be equalized with DSP due to the nonlinearity of the detection technique. However, it has been shown that for differential phase detection, the performance can be significantly improved by using DSP. With MSDD, the phase information is estimated over multiple symbols based on a likelihood function of the phase differential detection. Despite the performance improvement, MSDD is not a suitable algorithm due to the implementation complexity, which grows exponentially with the estimation block length. In contrast to MSDD, with MSPE the implementation complexity can be strongly reduced due to its recursive structure. Moreover, a performance can be further improved. The further enhancement of the phase estimation for the differential phase detection is IMSPE proposed by the author. It replaces the recursion by an the iterative approach and feedback can be completely avoided. The performance of IMSPE is approximately equal to MSPE. On the one hand, it should be noted that with MSPE and IMSPE, the performance of the differential phase detection is very close to coherent detection with differential encoding/decoding.

On the other hand, for coherent detection techniques, the carrier synchronization is one of the crucial components in the DSP. The most well-known and widely used carrier phase estimation algorithm in the coherent detection is the M-power estimation due to the low implementation complexity and high estimation performance. In the AWGN channel, the phase error variance of the M-power estimation is close to the MCRB lower bound dependent on SNR and modulation formats. Moreover, with the high tolerance against the laser linewidth, the LO frequency offset and the frequency variations can be achieved. Using V&V, we have a more flexibility for the implementation with approximately equal performance to the M-power estimation. In some special cases, V&V can be implemented without real number multiplication. Due to the fact that in optical transmission systems with PolMux, the informations in both polarizations are coupled. Hence the author has proposed PCC, which is based on the M-power estimation and can significantly improve estimation performance by using the coupling information between polarizations. In order to reduce the LO frequency offset, we can use DPFE in combination with the M-power carrier phase estimation and its derivatives. In this case, an LO frequency offset up to $0.25/T_s$ can be tolerated with the trade-off of the OSNR penalty of 0.25dB in the rage of low LO frequency offsets.

A key drawback of the algorithms based on the M-power estimation is the limitation to PSK based modulation formats. Nevertheless, MDE is the only carrier phase estimation, which can be used for the arbitrary modulation formats. Although MDE is a very powerful algorithm and can tolerate very large laser linewidths, the implementation complexity of MDE is very high. Moreover, the tolerance against LO frequency offsets and frequency variations of MDE is limited. However, we can apply AFC with a feed forward structure to solve these problems.

The phase unwrapping is an important component for feed forward carrier synchronization and contains a feedback. As a consequence, the implementation of feed forward algorithms can be limited by this phase unwrapping. Hence, the author has proposed the feed forward approach for the phase unwrapping with the same capability as the conventional phase unwrapping.

In contrast, for the feedback approach, the phase unwrapping is not necessary. In this dissertation, two feedback algorithms for carrier synchronization, namely MLL and the Costas loop are described and analyzed. The phase error variances form both algorithms are very close to the MCRB lower bound for all modulation formats. Due to the tolerance against LO frequency offset and frequency variations, the Costas loop is preferred. However, the implementation of feedback algorithms with the conventional hardware parallelization induces a huge feedback delay, which can degrade the performance of the feedback algorithms. Therefore, the author has proposed the application of the Superscalar parallelization architecture for feedback carrier synchronization to reduce the feedback delay. Moreover, the trade-off between the acquisition time and tracking performance must be considered before applying feedback algorithms. To reduce this trade-off, we can use ABA, which has been proposed from the author, to improve the acquisition of the Costas loop without the trade-off of the tracking performance. In some special cases, the improvement of acquisition of about 2400% can be achieved.

The addressed algorithms can be only used afte equalization and have the limitations due to the LO frequency offsets. Nevertheless, the other parts of DSP like timing recovery and equalization cannot be operated in the presence of the LO frequency offsets in a range of GHz. To solve these problems, we can use an AFC prior to the timing recovery and the equalization. Moreover, an AFC can be applied independent of the modulation formats and is very robust against the channel distortions. Although AFC can be implemented with a feed forward as well as a feedback approach, the feedback approach is preferred due to the simple implementation without a lookup table. Three algorithms for error generators for AFC are demonstrated and discussed namely DPM, BQ and FD-AFC. Since FD-AFC, which has been proposed from the author, has the best performance among three algorithms and its implementation complexity is relative low, FD-AFC is our recommendation for the error generator for AFC. Like the Costas loop, we can apply ABA to improve the acquisition of the AFC.

9.2. Feed Forward vs. Feedback

With the Superscalar parallelization architecture, the feedback carrier synchronization can compete against the feed forward algorithms. However, we cannot generally predict which approach is better than the other. Basically, for the feed forward algorithms the following problems must be considered :

- phase unwrapping
- implementation complexity due to the estimation block length
- undesired feedback e.g. the frequency offset correction in DPFE

For the feedback algorithms, the following problems must be considered :

- hang-up
- stability due to the feedback delay

Moreover, the phase ambiguity problems cannot be solved with both approaches. Hence, the differential encoding/decoding for NDA or the framing synchronization for DA must be applied.

In comparison to the feed forward algorithms, the second order Costas loop can basically tolerate more LO frequency offset and frequency variations. For PSK based modulation formats, DPFE can be used to enhance the tolerance with the trade-off of a small OSNR penalty. However, an AFC can solve the problem of LO frequency offsets and the frequency variations, since a very wide range of LO frequency offsets can be estimated and compensated with an AFC independent of modulation formats.

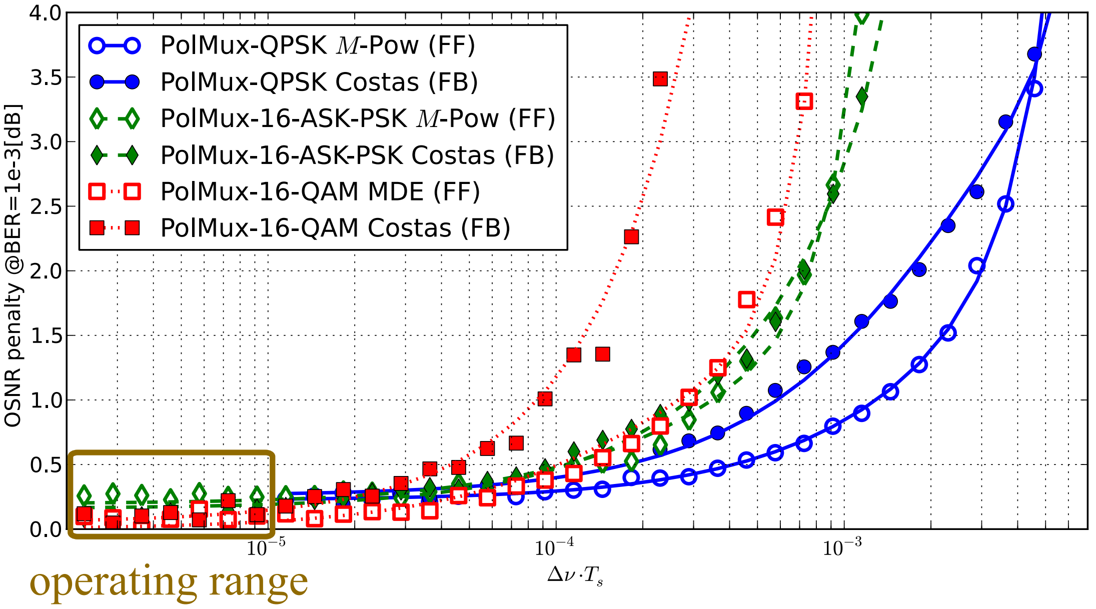

Figure 9.1.: Laser linewidth tolerance feed forward(FF) vs. feedback(FB) algorithms

Assume that an AFC is used. The key impairment for the carrier synchronization is the laser linewidth. Figure. 9.1 shows the laser linewidth tolerance of feed forward algorithms in comparison to feedback algorithm like the Costas loop. Generally, the feed forward algorithms can tolerate more laser linewidth. Due to the fact that a typical linewidth of 100kHz can be assumed by the commercially standard lasers, the typical operating range of the carrier synchronization in the high bit-rate optical transmission systems is approximately in the interval $[10^{-6} \cdot T_s; 10^{-5} \cdot T_s]$ where the performance of the feed forward and feedback algorithms is approximately equal. This is dependent on the baud-rate and the modulation format. However, the performance degradation due to the feedback delay for the feedback algorithm must be considered. With the Superscalar parallelization architecture, a feedback delay in the range of $[3; 6]$ can be achieved. The performance of the Costas loop is also approximately equal to the feed forward algorithms.

With respect to the implementation complexity, the difference between the M-power estimation and the Costas loop is low. As a consequence for PSK based modulation formats, it is regardless thar the M-power estimation or the Costas loop is used. In contrast, for QAM based modulation formats, the implementation of MDE is very complex. Therefore, the Costas loop is our preferred algorithm.

9.3. Outlook

Due to the usually considered interleaving parallelization architecture, the research on the carrier synchronization and the other components of DSP in optical transmission systems has concentrated on feed forward algorithms. Although feedback algorithms are very powerful, they were not appropriated for optical transmission systems. A solution for those problems e.g., the suppression of the phase noise caused by the laser linewidth and the channel nonlinearities is the proposed enhanced algorithms using Superscalar.

So far, the carrier synchronization has been mainly investigated independent of the other components of the DSP. Hence, the collaboration of the carrier synchronization with the other components of DSP like equalization, timing recovery and feed forward error correction (FEC) should be investigated in more detail. With the approach as such, a performance improvement and/or a complexity reduction may be achieved.

Alternatively to the *signal carrier* and orthogonal frequency devision multiplexing (OFDM) systems, the multi-subcarrier system [140, 141] can combine the advantages of the both existing systems. In the multi-subcarrier systems, a signal laser can be used for multiple subcarriers. Hence, we can use the joint information between the subcarriers to improve the estimation performance.

Due to the growth of the bandwidth requirement even in optical transmission system, the spectral efficiency must be increased via the modulation format. Two approaches are so far proposed, namely QAM and ASK-PSK. Although the ASK-PSK modulation formats have lower tolerance against the amplitude noise like ASE-noise, in this dissertation and in [109], it is shown that the ASK-PSK modulation format can tolerate more laser linewidth independent of the algorithm for the carrier synchronization. Furthermore, with respect to the channel nonlinearities [142] and channel coding [143], the ASK-PSK modulation formats are more suitable. Hence, for more bandwidth efficiency, the ASK-PSK approach should be preferred.

In the future, lasers with improved linewidth [144] can be used in optical transmission systems. The technology of this new type of laser can relax the requirements for the carrier synchronization. However, applying a powerful carrier synchronization with such narrow linewidth lasers allows us to increase the order of the modulation formats and thus increase the spectral efficiency. As a consequence, instead of the laser linewidth tolerance, the other requirements for the carrier synchronization have to be fulfilled.

A. Appendix

A.1. Lorentzian Function

The Lorentzian function [145] is the singly peaked function given by

$$L(x) = \frac{1}{\pi}\frac{\frac{\Gamma}{2}}{(x-x_0)^2+\frac{\Gamma}{2}^2}, \tag{A.1}$$

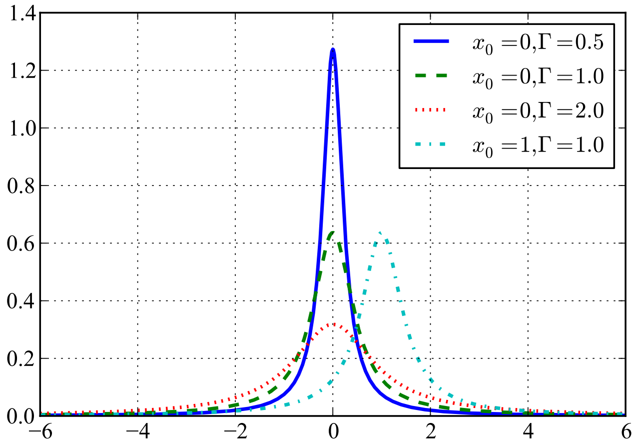

Figure A.1.: Example values of Lorentzian function

where x_0 is the center and Gamma is a parameter specifying the width. The Lorentzian function is normalized so that

$$\int_{-\infty}^{\infty} L(x) = 1. \tag{A.2}$$

It has a maximum at $x = x_0$, where

$$L'(x) = -\frac{16(x-x_0)\Gamma}{\pi|4(x-x_0)^2+\Gamma^2|^2} = 0. \tag{A.3}$$

Its value at the maximum is

$$L(x_0) = \frac{2}{(\pi\Gamma)}. \tag{A.4}$$

It is equal to half its maximum at

$$x = x_0 \pm \frac{\Gamma}{2} \tag{A.5}$$

and so has full width at half maximum Γ. The function has inflection points at

$$\acute{L}(x) = 16\Gamma \frac{12(x-x_0)^2 - \Gamma^2}{\pi|4(x-x_0)^2 + \Gamma^2|^3} = 0, \tag{A.6}$$

giving

$$x_1 = x_0 - \frac{\sqrt{3}\Gamma}{6}, \tag{A.7}$$

where

$$L(x_1) = \frac{3}{2\pi\Gamma} \tag{A.8}$$

A.2. Derivation of Degradation due to Phase Errors for QPSK

In [77], it has been shown that degradation due to phase errors for QPSK can be derived as following. In the first step, b_k is defined as transmitted complex symbol for QPSK modulated signal and can be given by

$$b_k = \cos(\varphi_k) + j \cdot \cos(\varphi_k), \tag{A.9}$$

with

$$\varphi_k \in \left\{ \frac{\pi}{4}, \frac{3\cdot\pi}{4}, \frac{-\pi}{4}, \frac{-3\cdot\pi}{4} \right\} \tag{A.10}$$

For the simplification, the ideal equalization, timing and frequency synchronization are assumed. The digitalized received signal with phase errors as described in Eq.(4.24) can be written as

$$r_k = b_k \cdot \exp(j \cdot \tilde{\boldsymbol{\varphi}}) + n_k^i + j \cdot n_k^q, \tag{A.11}$$

where n_k^i, n_k^q are zero mean additive white noise with the variance of σ_n^2, with

$$\sigma_n = \frac{1}{\sqrt{SNR}}. \tag{A.12}$$

In Eq.(A.11), we assume that $b_k = \exp(j \cdot \pi/4)$ is constant transmitted symbol. The probability that r_k is in the first quadrant and can be correctly detected can be given by

$$\begin{aligned} F_{\boldsymbol{c}}(c|\tilde{\boldsymbol{\varphi}} = \tilde{\varphi}) &= 1 - F_{\boldsymbol{e}}(e|\tilde{\varphi}) && \text{(A.13)} \\ &= \mathrm{P}\left\{ \mathrm{Re}\left\{r_k\right\} \geq 0; \mathrm{Im}\left\{r_k\right\} \geq 0 \right\} && \text{(A.14)} \\ &= \mathrm{P}\left\{ \cos\left(\frac{\pi}{4} + \tilde{\varphi}\right) + n_k^i \geq 0; \sin\left(\frac{\pi}{4} + \tilde{\varphi}\right) + n_k^q \geq 0 \right\}, && \text{(A.15)} \end{aligned}$$

where $\boldsymbol{c}$ represents the random variable of correct detection and $\boldsymbol{e}$ the random variable of incorrect detection.

In the next step, we rewrite the probability in Eq.(A.15) to

$$F_{\boldsymbol{c}}(c|\tilde{\boldsymbol{\varphi}}=\tilde{\varphi}) = \left[1-Q\left(\frac{\cos\left(\frac{\pi}{4}+\tilde{\varphi}\right)}{\sigma_n}\right)\right]\left[1-Q\left(\frac{\sin\left(\frac{\pi}{4}+\tilde{\varphi}\right)}{\sigma_n}\right)\right], \tag{A.16}$$

with

$$Q(x) = \int_{x}^{\infty} \exp\left(\frac{-x^2}{2}\right) dx. \tag{A.17}$$

Substituting Eq.(A.12) and Eq.(A.16) into Eq.(A.13) yields

$$\begin{aligned} F_{\boldsymbol{e}}(e|\tilde{\boldsymbol{\varphi}}=\tilde{\varphi}) = \quad & Q\left(\sqrt{2\cdot\mathrm{SNR}}\cdot\cos\left(\frac{\pi}{4}+\tilde{\varphi}\right)\right)+Q\left(\sqrt{2\cdot\mathrm{SNR}}\cdot\sin\left(\frac{\pi}{4}+\tilde{\varphi}\right)\right) \\ - \quad & Q\left(\sqrt{2\cdot\mathrm{SNR}}\cdot\cos\left(\frac{\pi}{4}+\tilde{\varphi}\right)\right)\cdot Q\left(\sqrt{2\cdot\mathrm{SNR}}\cdot\sin\left(\frac{\pi}{4}+\tilde{\varphi}\right)\right) \end{aligned} \tag{A.18}$$

In the next step, we compute $F_{\boldsymbol{e}}(e|\tilde{\boldsymbol{\varphi}}=\tilde{\varphi})$, with fixed value of $\tilde{\varphi}$. Applying the integration over the unwanted random variable, the average error probability can be given by

$$F_{\boldsymbol{e}}(e) = \int_{-\infty}^{\infty} F_{\boldsymbol{e}}(e|\tilde{\boldsymbol{\varphi}}=\tilde{\varphi})\cdot f_{\tilde{\boldsymbol{\varphi}}}(\tilde{\varphi})d\tilde{\varphi}. \tag{A.19}$$

We can now substitute Eq.(4.25) and Eq.(A.18) into Eq.(A.19) to achieve $F_{\boldsymbol{e}}(e)$. However, the integral is mathematically not resolvable. Hence, Eq.(A.19) is numerically evaluated and verified with simulation results, which is shown in Figure 4.16.

A.3. Derivation of Degradation due to Phase Errors for 16-ASK-PSK

For the investigation of performance degradation due to the phase errors for 16-ASK-PSK, the following equations are derived by the author. Due to the fact that 16-ASK-PSK signal is modulated and detected by separating signal into amplitude and phase part. Hence, it is convenient to express the transmitted symbol b_k in polar coordination as

$$b_k = a_{b_k}\cdot\exp\left(j\varphi_{b_k}\right), \tag{A.20}$$

where

$$a_{b_k} \in \{r_1, r_2\}, \tag{A.21}$$

and

$$\varphi_{b_k} \in \left\{0, \frac{\pi}{4}, \frac{\pi}{2}, \frac{3\pi}{4}, \pi, \frac{-\pi}{4}, \frac{-\pi}{2}, \frac{-3\pi}{4}\right\}. \tag{A.22}$$

For 16-ASK-PSK, the ratio between r_1 and r_2 can be freely chosen, which can be defined as

$$\rho = \frac{r_2}{r_1}. \tag{A.23}$$

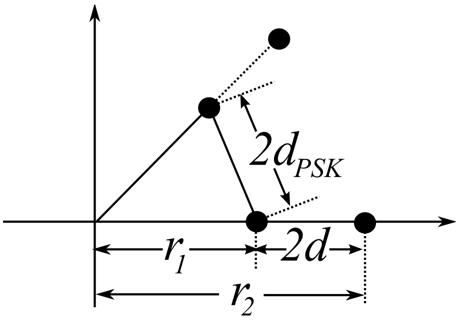

Figure A.2.: Constellation with euclidean distance between signal points for 16-ASK-PSK in the first quadrant.

However, the performance of 16-ASK-PSK depends on the value of ρ. For higher ρ, the performance is limited by the euclidean distance of PSK detection. For lower ρ, on the other hand, the performance is limited by the euclidean distance of ASK detection. Therefore ρ should be optimized to obtain the balance point between PSK and ASK detection. Figure. A.2 shows the constellation of 16-ASK-PSK with euclidean distance between signal points in the first quadrant, where $2d$ is the euclidean distance for ASK detection and $2d_{PSK}$ for PSK. For optimization d and d_{PSK} should be equal :

$$\begin{aligned} d &= d_{PSK} \\ \frac{r_2 - r_1}{2} &= r_1 \cdot \sin\left(\frac{\pi}{8}\right) \\ \frac{r_2}{r_1} &= 1 + 2 \cdot \sin\left(\frac{\pi}{8}\right) \end{aligned} \tag{A.24}$$

Substituting Eq.(A.23) into Eq.(A.24), we obtain the optimized ρ, which can be written as

$$\rho = 1 + 2 \cdot \sin\left(\frac{\pi}{8}\right). \tag{A.25}$$

The optimized value of ρ in Eq.(A.25) will be used for the further derivations in this section. Figure. A.3 shows the symbol error probability of 16-ASK-PSK, which depends on ρ.

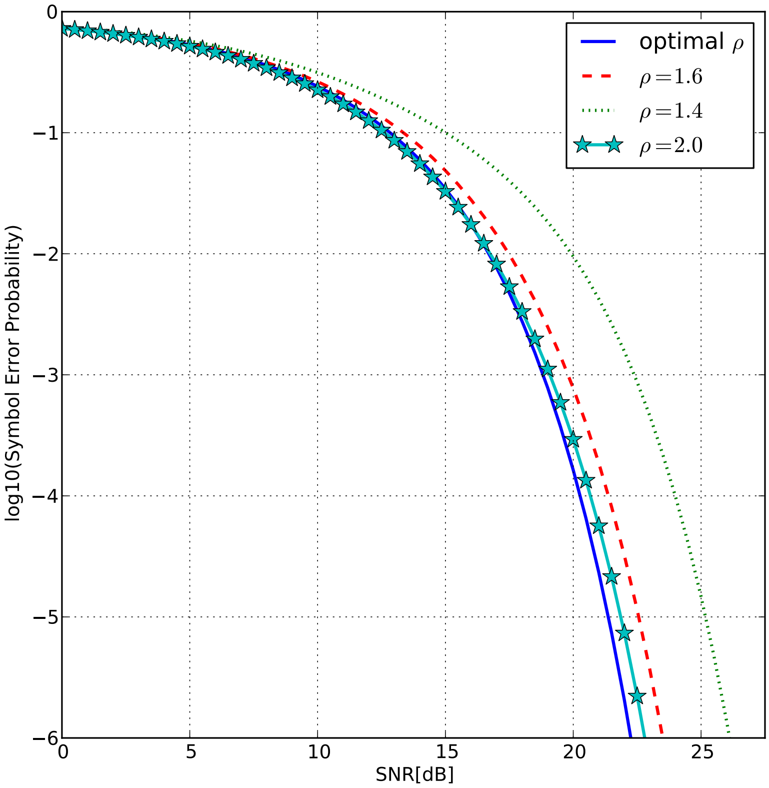

Figure A.3.: Symbol error probability of 16-ASK-PSK against ρ

In the next step, the symbol error probability for 16-ASK-PSK dependent on SNR is calculated. For this purpose, the equalization, timing and frequency synchronization at the receiver side are assumed, and the digitalized received signal can be written as

$$r_k = b_k + n_k^i + j \cdot n_k^q, \tag{A.26}$$

where n_k^i, n_k^q are zero mean additive white noise with the variance of σ_n^2. The joint PDF between n_k^i and n_k^q can be given by

$$f_n(n_k^i, n_k^q) = \frac{1}{\sigma_n^2 2\pi} \cdot \exp\left(-\frac{(n_k^i - \mu^i)^2 + (n_k^q - \mu^q)^2}{2\sigma_n^2}\right), \tag{A.27}$$

where μ^i is the expectation value of n_k^i and μ^q of n_k^q. In the case of zero mean white noise, μ^i and μ^q are set to 0.

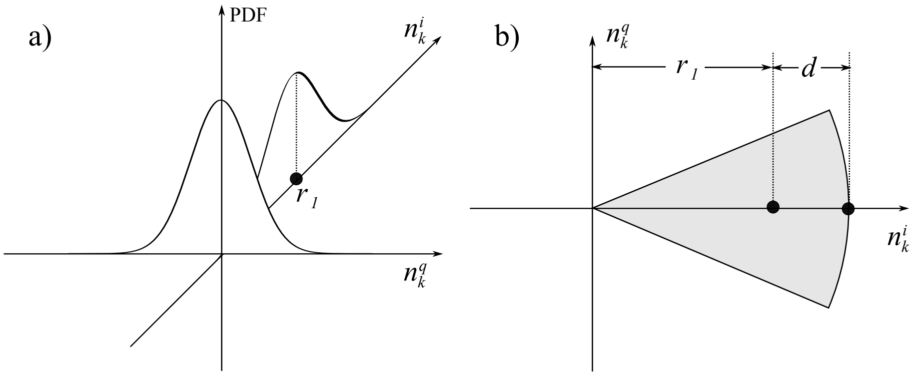

Figure A.4.: Illustration of correct detection probability for inner ring of 16-ASK-PSK a) jointly probability density function of n_k^i and n_k^q b) area for correct detection

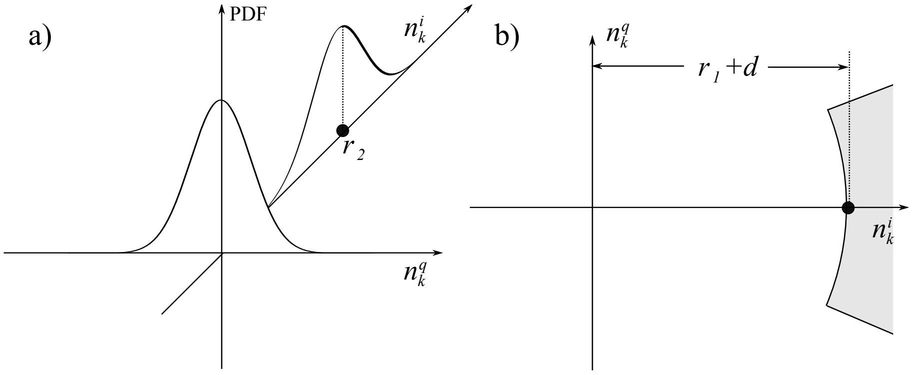

Figure A.5.: Illustration of correct detection probability for outer ring of 16-ASK-PSK a) jointly probability density function of n_k^i and n_k^q b) area for correct detection

For the probability of correct detection, the volume of the joint PDF under the area as shown in Figure. A.4 b) for the inner ring and Figure. A.5 b) for the outer ring must be calculated. However, the joint PDF $f_n(n_k^i, n_k^q)$ in Eq.(A.27) is based on the Cartesian coordination system, which is only convenient for the volume calculation under the rectangle area. Hence, $f_n(n_k^i, n_k^q)$ should be transformed into polar coordination system as shown in [27]. For this purpose, we define V and θ as magnitude and phase of $n_k^i + j \cdot n_k^q$ respectively, which can be given by [27]

$$\begin{aligned} V &= \sqrt{(n_k^i)^2 + (n_k^q)^2} && \text{(A.28)} \\ \theta &= \arctan\left(\frac{n_k^q}{n_k^i}\right), && \text{(A.29)} \end{aligned}$$

n_k^i and n_k^q can be rewritten as

$$\begin{aligned} n_k^i &= V\cos(\theta) && \text{(A.30)} \\ n_k^q &= V\sin(\theta). && \text{(A.31)} \end{aligned}$$

Substituting Eq.(A.30) and Eq.(A.31) into Eq.(A.27) yields the joint PDF

$$f_n(\theta, V) = \frac{1}{\sigma_n^2 2\pi} \cdot \exp\left(-\frac{(V\cos(\theta) - \mu^i)^2 + (V\sin(\theta)\mu^q)^2}{2\sigma_n^2}\right). \tag{A.32}$$

By setting μ^i and μ^q in Eq.(A.32) to the arbitrary given signal point, the polar coordinated joint PDF of n_k^i and n_k^q around this signal point can be achieved. Hence, the joint PDF for $a_{b_k} = r_1$ and $\varphi_{b_k} = 0$ can be given by

$$f_{n,r_1,0}(\theta, V) = \frac{1}{\sigma_n^2 2\pi} \cdot \exp\left(-\frac{V^2 - 2r_1 V\cos(\theta) + r_1^2}{2\sigma_n^2}\right) \tag{A.33}$$

and for $a_{b_k} = r_2, \varphi_{b_k} = 0$

$$f_{n,r_2,0}(\theta, V) = \frac{1}{\sigma_n^2 2\pi} \cdot \exp\left(-\frac{V^2 - 2r_2 V\cos(\theta) + r_2^2}{2\sigma_n^2}\right). \tag{A.34}$$

The illuatrations of $f_{n,r_1,0}(\theta, V)$ and $f_{n,r_1,0}(\theta, V)$ are shown in Figure. A.4 and A.5 respectively.

For the simplification, the probability for the correct symbol detection $F_{\boldsymbol{c}}(c)$ with $\varphi_{b_k} = 0$ is firstly calculated using case differentiations for inner ring and outer ring :

$$F_{\boldsymbol{c}}(c) = \begin{cases} \int\limits_{-\pi/8}^{\pi/8} \int\limits_{0}^{r_1+d} f_{n,r_1,0}(\theta, V) dV d\theta, & \text{for } a_{b_k} = r_1 \\ \int\limits_{-\pi/8}^{\pi/8} \int\limits_{r_1+d}^{\infty} f_{n,r_2,0}(\theta, V) dV d\theta, & \text{for } a_{b_k} = r_2 \end{cases}. \tag{A.35}$$

Assuming that all symbols have the same occurrence probability, $F_{\boldsymbol{c}}(c)$ can be given by

$$F_{\boldsymbol{c}}(c) = \frac{1}{2}\left(\int\limits_{-\pi/8}^{\pi/8} \int\limits_{0}^{r_1+d} f_{n,r_1,0}(\theta, V) dV d\theta + \int\limits_{-\pi/8}^{\pi/8} \int\limits_{r_1+d}^{\infty} f_{n,r_2,0}(\theta, V) dV d\theta\right). \tag{A.36}$$

Since the characteristics of the joint PDF are identical for each value of $\varphi_{b_k} = 0$, with assuming of the same occurrence probability for all symbols, $F_{\boldsymbol{c}}(c)$ in Eq.(A.36) is also the overall probability for the correct symbol detection for 16-ASK-PSK. Finally, the symbol error probability for 16-ASK-PSK can be given by

$$\begin{aligned} F_{\boldsymbol{e}}(e) &= 1 - F_{\boldsymbol{c}}(c) \\ &= 1 - \frac{1}{2}\left(\int\limits_{-\pi/8}^{\pi/8} \int\limits_{0}^{r_1+d} f_{n,r_1,0}(\theta, V) dV d\theta + \int\limits_{-\pi/8}^{\pi/8} \int\limits_{r_1+d}^{\infty} f_{n,r_2,0}(\theta, V) dV d\theta\right). \end{aligned} \tag{A.37}$$

Unfortunately, there is no simple expression for $F_{\boldsymbol{c}}(c)$ in Eq.(A.37), which can be only achieved with nummerical evaluations.

For the convenience, r_1, r_2, d and σ_n should be given in relation to the SNR. Hence, the averaged energy per symbol E_s of 1 is assumed, and the relation between r_1, r_2 and E_s can be given by

$$E_s = 16\left(8 \cdot r_1^2 + 8 \cdot r_2^2\right). \tag{A.38}$$

Substituting Eq.(A.23) into Eq.(A.38), r_1 and r_2 can be written as

$$r_1 = \sqrt{\frac{1}{2 \cdot (\rho^2 + 1)}} \tag{A.39}$$

$$r_2 = \sqrt{\frac{\rho^2}{2 \cdot (\rho^2 + 1)}} \tag{A.40}$$

and σ_n can be given by

$$\sigma_n = \frac{1}{\sqrt{2\text{SNR}}}. \tag{A.41}$$

In the next step, the the symbol error probability for 16-ASK-PSK with constant phase rotation of $\tilde{\varphi}$ is derived. Due to the fact that $F_{\boldsymbol{c}}(c)$ in Eq.(A.36) is based on the polar coordination of joint PDF, $F_{\boldsymbol{c}}(c|\tilde{\boldsymbol{\varphi}} = \tilde{\varphi})$ can be simply given by shifting the limit of $\tilde{\varphi}$ for the integral of θ and $F_{\boldsymbol{c}}(c|\tilde{\boldsymbol{\varphi}} = \tilde{\varphi})$ can be written as

$$F_{\boldsymbol{c}}(c|\tilde{\boldsymbol{\varphi}} = \tilde{\varphi}) = \frac{1}{2}\left(\int\limits_{-\pi/8+\tilde{\varphi}}^{\pi/8+\tilde{\varphi}} \int\limits_{0}^{r_1+d} f_{n,r_1,0}(\theta, V) dV d\theta + \int\limits_{-\pi/8+\tilde{\varphi}}^{\pi/8+\tilde{\varphi}} \int\limits_{r_1+d}^{\infty} f_{n,r_2,0}(\theta, V) dV d\theta \right). \tag{A.42}$$

Assuming $\tilde{\boldsymbol{\varphi}}$ as a zero mean gaussian distributed random variable with a variance of $\sigma_{\tilde{\varphi}}$, the symbol error probability for 16-ASK-PSK considering the phase errors can be given by

$$F_{\boldsymbol{e}}(e) = \int\limits_{-\infty}^{\infty} (1 - F_{\boldsymbol{c}}(c|\tilde{\boldsymbol{\varphi}} = \tilde{\varphi})) \cdot \frac{1}{\sigma_{\tilde{\varphi}}\sqrt{2\pi}} \cdot \exp\left(-\frac{\tilde{\varphi}^2}{2\sigma_{\tilde{\varphi}}^2}\right) d\tilde{\varphi}. \tag{A.43}$$

The numerical and simulative evaluations of Eq.(A.43) are shown in Figure. 4.16.

A.4. Derivation of Degradation due to Phase Errors for 16-QAM

For the investigation of performance degradation due to the phase errors for 16-ASK-PSK, the following equations are derived by the author. Let b_k be transmitted complex symbol of 16-QAM modulated signal with

$$b_k = b_k^i + j \cdot b_k^q, \tag{A.44}$$

and

$$b_k^i, b_k^q \in \{-3 \cdot d, -d, d, 3 \cdot d\}, \tag{A.45}$$

where $2 \cdot d$ is the euclidean distance between the symbols. For the simplification, the ideal equalization, timing and frequency synchronization are assumed, and the digitalized received signal can be written as

$$r_k = b_k + n_k^i + j \cdot n_k^q, \tag{A.46}$$

where n_k^i, n_k^q are zero mean additive white noise with the variance of σ_n^2.

In the first step, the probability for the correct symbol detection in the first quadrant $F_{\boldsymbol{c}}(c)$ is calculated. For $F_{\boldsymbol{c}}(c)$ calculation, we have four case differentiations for each symbol in the first quadrant:

$$F_{\boldsymbol{c}}(c) = \begin{cases} \mathrm{P}\left\{|n_k^i| \leq d; |n_k^q| \leq d\right\} & \text{, for } \; b_k = d + j \cdot d \\ \mathrm{P}\left\{|n_k^i| \leq d; n_k^q > -d\right\} & \text{, for } \; b_k = d + j \cdot 3 \cdot d \\ \mathrm{P}\left\{n_k^i > -d; |n_k^q| \leq d\right\} & \text{, for } \; b_k = 3 \cdot d + j \cdot d \\ \mathrm{P}\left\{n_k^i > -d; n_k^q > -d\right\} & \text{, for } \; b_k = 3 \cdot d + j \cdot 3 \cdot d \end{cases} \tag{A.47}$$

Assuming, all symbols have the same occurrence probability, $F_{\boldsymbol{c}}(c)$ can be given by

$$\begin{aligned} F_{\boldsymbol{c}}(c) = \quad & \frac{1}{4} \cdot \mathrm{P}\left\{|n_k^i| \leq d; |n_k^q| \leq d\right\} \\ + \quad & \frac{1}{4} \cdot \mathrm{P}\left\{|n_k^i| \leq d; n_k^q > -d\right\} \\ + \quad & \frac{1}{4} \cdot \mathrm{P}\left\{n_k^i > -d; |n_k^q| \leq d\right\} \\ + \quad & \frac{1}{4} \cdot \mathrm{P}\left\{n_k^i > -d; n_k^q > -d\right\}. \end{aligned} \tag{A.48}$$

Due to the fact that the QAM constellation is symmetrical to the real and imaginary axis, the probability in Eq.(A.48) is valid in all four quadrants. Furthermore with the assuming for the symbols occurrence probability, the probability in Eq.(A.48) is also the overall probability for the correct symbol detection for 16-QAM. For given n_k^i, n_k^q as normal distributed random variables with the variance of σ_n^2, Eq.(A.48) can be rewritten as

$$\begin{aligned} F_{\boldsymbol{c}}(c) &= \frac{1}{4} \cdot \left[2 \cdot Q\left(\frac{d}{\sigma_n}\right) - 1\right]^2 + \frac{1}{2} \cdot \left[2 \cdot Q\left(\frac{d}{\sigma_n}\right) - 1\right] \cdot Q\left(\frac{d}{\sigma_n}\right) + \frac{1}{4} \cdot Q\left(\frac{d}{\sigma_n}\right)^2 \\ &= 2.25 \cdot Q\left(\frac{d}{\sigma_n}\right)^2 - 1.5 \cdot Q\left(\frac{d}{\sigma_n}\right) - 0.25, \end{aligned} \tag{A.49}$$

with

$$Q(x) = \int_x^\infty \exp\left(\frac{-x^2}{2}\right) dx. \tag{A.50}$$

Hence, the symbol error probability for 16-QAM can be calculated by

$$\begin{aligned} F_{\boldsymbol{e}}(e) &= 1 - F_{\boldsymbol{e}}(e) \\ &= 1.25 - 2.25 \cdot Q\left(\frac{d}{\sigma_n}\right)^2 + 1.5 \cdot Q\left(\frac{d}{\sigma_n}\right). \end{aligned} \tag{A.51}$$

In the next step, the symbol error probability for 16-QAM with constant phase rotation of $\tilde{\varphi}$ is derived based on the previous approach. With the constant phase rotation, the digitalized received signal in Eq.(A.46) can be rewritten as

$$r_k = \left(b_k + n_k^i + j \cdot n_k^q\right) \cdot \exp\left(j\tilde{\varphi}\right). \tag{A.52}$$

For symbol detection, r_k in Eq.(A.52) is separated in the real and imaginary part:

$$\begin{aligned}
\mathrm{Re}\left\{r_k\right\} &= \mathrm{Re}\left\{\left(b_k + n_k^i + j \cdot n_k^q\right) \cdot \exp\left(j\tilde{\varphi}\right)\right\} \\
&= \mathrm{Re}\left\{\left(b_k^i + n_k^i + j \cdot (b_k^q + n_k^q)\right) \cdot (\cos(\tilde{\varphi}) + j \cdot \sin(\tilde{\varphi}))\right\} \\
&= \cos(\tilde{\varphi}) \cdot \left(b_k^i + n_k^i\right) - \sin(\tilde{\varphi}) \cdot (b_k^q + n_k^q) \\
&= b_k^i \cos(\tilde{\varphi}) - b_k^q \sin(\tilde{\varphi}) + n_k^i \cos(\tilde{\varphi}) - n_k^q \sin(\tilde{\varphi}) \qquad \text{(A.53)} \\
\mathrm{Im}\left\{r_k\right\} &= \mathrm{Im}\left\{\left(b_k + n_k^i + j \cdot n_k^q\right) \cdot \exp\left(j\tilde{\varphi}\right)\right\} \\
&= b_k^q \cos(\tilde{\varphi}) + b_k^i \sin(\tilde{\varphi}) + n_k^q \cos(\tilde{\varphi}) + n_k^i \sin(\tilde{\varphi}). \qquad \text{(A.54)}
\end{aligned}$$

One of the important part for the analysis of the symbol error probability is the characteristics of the noise e.g., the noise PDF. Due to the phase rotation, the noise characteristics in Eq.(A.53) and Eq.(A.54) should be proven. Hence, we define

$$n_k^{\varphi} = n_k^i \cdot \cos(\tilde{\varphi}) - n_k^q \cdot \sin(\tilde{\varphi}) \qquad \text{(A.55)}$$

as the noise in the real part of the rotated received signal. Since $\tilde{\varphi}$ is a constant phase, $\cos(\tilde{\varphi})$ and $\sin(\tilde{\varphi})$ are also constant. Therefore, PDF of $n_k^i \cdot \cos(\tilde{\varphi})$ and $n_k^q \cdot \sin(\tilde{\varphi})$ are also Gaussian with zero mean and the variance of $\cos^2(\tilde{\varphi}) \cdot \sigma_n^2$ and $\sin^2(\tilde{\varphi}) \cdot \sigma_n^2$ respectively. Due to the fact that n_k^i and n_k^q are stochastic independent, the PDF of n_k^{φ} is the convolution between PDF of $n_k^i \cdot \cos(\tilde{\varphi})$ and $n_k^i \cdot \cos(\tilde{\varphi})$, which can be given by

$$\begin{aligned}
f_{\boldsymbol{n}^{\varphi}}(n_k^{\varphi}) &= \mathcal{N}\left(0, \cos^2(\tilde{\varphi}) \cdot \sigma_n^2\right) * \mathcal{N}\left(0, \sin^2(\tilde{\varphi}) \cdot \sigma_n^2\right) \\
&= \mathcal{N}\left(0, \sigma_n^2 \cdot \left(\cos^2(\tilde{\varphi}) + \sin^2(\tilde{\varphi})\right)\right) \\
&= \mathcal{N}\left(0, \sigma_n^2\right). \qquad \text{(A.56)}
\end{aligned}$$

From Eq.(A.56), it can be seen that the PDF of n_k^{φ} is identical to the PDF of n_k^i and the approach can be applied for the noise in the imaginary part. Hence, with the replacement of $n_k^i \cdot \cos(\tilde{\varphi}) - n_k^q \cdot \sin(\tilde{\varphi})$ with n_k^i in Eq.(A.53) and $n_k^q \cos(\tilde{\varphi}) + n_k^i \sin(\tilde{\varphi})$ with n_k^q in Eq.(A.54), the equations can be rewritten as

$$\begin{aligned}
\mathrm{Re}\left\{r_k\right\} &= b_k^i \cos(\tilde{\varphi}) - b_k^q \sin(\tilde{\varphi}) + n_k^i \qquad \text{(A.57)} \\
\mathrm{Im}\left\{r_k\right\} &= b_k^q \cos(\tilde{\varphi}) + b_k^i \sin(\tilde{\varphi}) + n_k^q. \qquad \text{(A.58)}
\end{aligned}$$

From Eq.(A.57) and Eq.(A.58), the probability for the correct detection of the symbol with a constant phase rotation of $\tilde{\varphi}$ can be calculated by using four case differentiations like the previous approach and can be written as

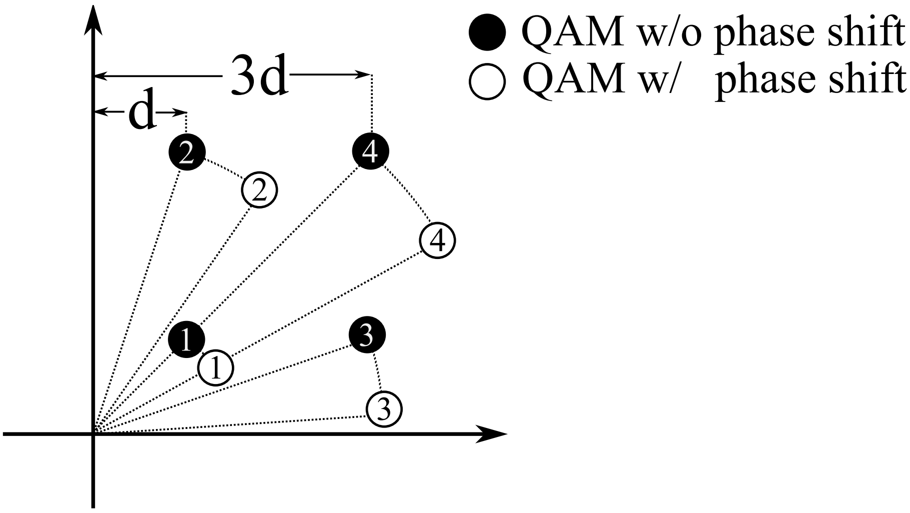

Figure A.6.: Constellation 16-QAM in the first quadrant with and without a constant phase shift

$$F_{\boldsymbol{c}}(c|\tilde{\boldsymbol{\varphi}}=\tilde{\varphi}) = \begin{cases} \mathrm{P}\left\{0<\mathrm{Re}\left\{r_k\right\}\leq 2d; 0<\mathrm{Im}\left\{r_k\right\}\leq 2d\right\}, \\ \text{for}\ \ b_k = d + j\cdot d \\ \\ \mathrm{P}\left\{0<\mathrm{Re}\left\{r_k\right\}\leq 2d; 2d<\mathrm{Im}\left\{r_k\right\}\right\}, \\ \text{for}\ \ b_k = d + j\cdot 3\cdot d \\ \\ \mathrm{P}\left\{2d<\mathrm{Re}\left\{r_k\right\}; 0<\mathrm{Im}\left\{r_k\right\}\leq 2d\right\}, \\ \text{for}\ \ b_k = 3\cdot d + j\cdot d \\ \\ \mathrm{P}\left\{2d<\mathrm{Re}\left\{r_k\right\}; 2d<\mathrm{Im}\left\{r_k\right\}\right\}, \\ \text{for}\ \ b_k = 3\cdot d + j\cdot 3\cdot d \end{cases} \tag{A.59}$$

Assuming that all symbols have the same occurrence probability, $F_{\boldsymbol{c}}(c|\tilde{\boldsymbol{\varphi}}=\tilde{\varphi})$ can be given by

$$\begin{aligned} F_{\boldsymbol{c}}(c|\tilde{\boldsymbol{\varphi}}=\tilde{\varphi}) = \quad & \frac{1}{4}\cdot\underbrace{\mathrm{P}\left\{0<\mathrm{Re}\left\{r_k\right\}\leq 2d; 0<\mathrm{Im}\left\{r_k\right\}\leq 2d\right\}}_{P_1} \\ + \quad & \frac{1}{4}\cdot\underbrace{\mathrm{P}\left\{0<\mathrm{Re}\left\{r_k\right\}\leq 2d; 2d<\mathrm{Im}\left\{r_k\right\}\right\}}_{P_2} \\ + \quad & \frac{1}{4}\cdot\underbrace{\mathrm{P}\left\{2d<\mathrm{Re}\left\{r_k\right\}; 0<\mathrm{Im}\left\{r_k\right\}\leq 2d\right\}}_{P_3} \\ + \quad & \frac{1}{4}\cdot\underbrace{\mathrm{P}\left\{2d<\mathrm{Re}\left\{r_k\right\}; 2d<\mathrm{Im}\left\{r_k\right\}\right\}}_{P_4} \qquad (A.60) \\ = \quad & \frac{1}{4}\cdot P_1 + \frac{1}{4}\cdot P_2 + \frac{1}{4}\cdot P_3 + \frac{1}{4}\cdot P_4 \qquad (A.61) \end{aligned}$$

For calculating P_1, P_2, P_3 and P_4 in Eq.(A.61), $\mathrm{Re}\{r_k\}$ and $\mathrm{Im}\{r_k\}$ in Eq.(A.60) are replaced with the terms as shown in Eq.(A.57) and Eq.(A.58) :

$$
\begin{aligned}
P_1 &= \mathrm{P}\left\{0 < b_k^i \cos(\tilde{\varphi}) - b_k^q \sin(\tilde{\varphi}) + n_k^i \leq 2d; 0 < b_k^q \cos(\tilde{\varphi}) + b_k^i \sin(\tilde{\varphi}) + n_k^q \leq 2d\right\} \\
&= \mathrm{P}\left\{0 < d\cos(\tilde{\varphi}) - d\sin(\tilde{\varphi}) + n_k^i \leq 2d; 0 < d\cos(\tilde{\varphi}) + d\sin(\tilde{\varphi}) + n_k^q \leq 2d\right\} \\
&= \mathrm{P}\left\{0 < d\cos(\tilde{\varphi}) - d\sin(\tilde{\varphi}) + n_k^i \leq 2d\right\} \cdot \mathrm{P}\left\{0 < d\cos(\tilde{\varphi}) + d\sin(\tilde{\varphi}) + n_k^q \leq 2d\right\} \\
&= \mathrm{P}\left\{0 < d\cos(\tilde{\varphi}) - d\sin(\tilde{\varphi}) + n_k^i\right\} \cdot \mathrm{P}\left\{d\cos(\tilde{\varphi}) - d\sin(\tilde{\varphi}) + n_k^i \leq 2d\right\} \cdot \\
&\quad \mathrm{P}\left\{0 < d\cos(\tilde{\varphi}) + d\sin(\tilde{\varphi}) + n_k^q\right\} \cdot \mathrm{P}\left\{d\cos(\tilde{\varphi}) + d\sin(\tilde{\varphi}) + n_k^q \leq 2d\right\} \\
&= \mathrm{P}\left\{d\sin(\tilde{\varphi}) - d\cos(\tilde{\varphi}) < n_k^i\right\} \cdot \mathrm{P}\left\{n_k^i \leq 2d - d\cos(\tilde{\varphi}) + d\sin(\tilde{\varphi})\right\} \cdot \\
&\quad \mathrm{P}\left\{-d\cos(\tilde{\varphi}) - d\sin(\tilde{\varphi}) < n_k^q\right\} \cdot \mathrm{P}\left\{n_k^q \leq 2d - d\cos(\tilde{\varphi}) - d\sin(\tilde{\varphi})\right\} \\
&= \left[1 - Q\left(\frac{d\sin(\tilde{\varphi}) - d\cos(\tilde{\varphi})}{\sigma_n}\right)\right] \cdot Q\left(\frac{2d - d\cos(\tilde{\varphi}) + d\sin(\tilde{\varphi})}{\sigma_n}\right) \cdot \\
&\quad \left[1 - Q\left(\frac{-d\cos(\tilde{\varphi}) - d\sin(\tilde{\varphi})}{\sigma_n}\right)\right] \cdot Q\left(\frac{2d - d\cos(\tilde{\varphi}) - d\sin(\tilde{\varphi})}{\sigma_n}\right) \qquad \text{(A.62)}
\end{aligned}
$$

$$
\begin{aligned}
P_2 &= \mathrm{P}\left\{0 < b_k^i \cos(\tilde{\varphi}) - b_k^q \sin(\tilde{\varphi}) + n_k^i \leq 2d; 2d < b_k^q \cos(\tilde{\varphi}) + b_k^i \sin(\tilde{\varphi}) + n_k^q\right\} \\
&= \mathrm{P}\left\{0 < d\cos(\tilde{\varphi}) - 3d\sin(\tilde{\varphi}) + n_k^i \leq 2d; 2d < d\cos(\tilde{\varphi}) + 3d\sin(\tilde{\varphi}) + n_k^q\right\} \\
&= \mathrm{P}\left\{3d\sin(\tilde{\varphi}) - d\cos(\tilde{\varphi}) < n_k^i; \right\} \cdot \mathrm{P}\left\{n_k^i \leq 2d - d\cos(\tilde{\varphi}) + 3d\sin(\tilde{\varphi})\right\} \cdot \\
&\quad \mathrm{P}\left\{2d - d\cos(\tilde{\varphi}) - 3d\sin(\tilde{\varphi}) < n_k^q\right\} \\
&= \left[1 - Q\left(\frac{3d\sin(\tilde{\varphi}) - d\cos(\tilde{\varphi})}{\sigma_n}\right)\right] \cdot Q\left(\frac{2d - d\cos(\tilde{\varphi}) + 3d\sin(\tilde{\varphi})}{\sigma_n}\right) \cdot \\
&\quad \left[1 - Q\left(\frac{2d - d\cos(\tilde{\varphi}) - 3d\sin(\tilde{\varphi})}{\sigma_n}\right)\right] \qquad \text{(A.63)} \\
& \qquad \text{(A.64)}
\end{aligned}
$$

$$
\begin{aligned}
P_3 &= \mathrm{P}\left\{2d < b_k^i \cos(\tilde{\varphi}) - b_k^q \sin(\tilde{\varphi}) + n_k^i; 0 < b_k^q \cos(\tilde{\varphi}) + b_k^i \sin(\tilde{\varphi}) + n_k^q \leq 2d\right\} \\
&= \mathrm{P}\left\{2d < 3d\cos(\tilde{\varphi}) - d\sin(\tilde{\varphi}) + n_k^i; 0 < 3d\cos(\tilde{\varphi}) + d\sin(\tilde{\varphi}) + n_k^q \leq 2d\right\} \\
&= \mathrm{P}\left\{2d - 3d\cos(\tilde{\varphi}) + d\sin(\tilde{\varphi}) < n_k^i\right\} \cdot \mathrm{P}\left\{-3d\cos(\tilde{\varphi}) - d\sin(\tilde{\varphi}) < n_k^q\right\} \cdot \\
&\quad \mathrm{P}\left\{n_k^q \leq 2d - 3d\cos(\tilde{\varphi}) - d\sin(\tilde{\varphi})\right\} \\
&= \left[1 - Q\left(\frac{2d - 3d\cos(\tilde{\varphi}) + d\sin(\tilde{\varphi})}{\sigma_n}\right)\right] \cdot \left[1 - Q\left(\frac{-3d\cos(\tilde{\varphi}) - d\sin(\tilde{\varphi})}{\sigma_n}\right)\right] \cdot \\
&\quad Q\left(\frac{2d - 3d\cos(\tilde{\varphi}) - d\sin(\tilde{\varphi})}{\sigma_n}\right) \qquad \text{(A.65)} \\
& \qquad \text{(A.66)}
\end{aligned}
$$

$$
\begin{aligned}
P_4 &= \mathrm{P}\left\{2d < b_k^i \cos(\tilde{\varphi}) - b_k^q \sin(\tilde{\varphi}) + n_k^i; 2d < b_k^q \cos(\tilde{\varphi}) + b_k^i \sin(\tilde{\varphi}) + n_k^q; \right\} \\
&= \mathrm{P}\left\{2d < 3d\cos(\tilde{\varphi}) - 3d\sin(\tilde{\varphi}) + n_k^i; 2d < 3d\cos(\tilde{\varphi}) + 3d\sin(\tilde{\varphi}) + n_k^q; \right\} \\
&= \left[1 - Q\left(\frac{2d - 3d\cos(\tilde{\varphi}) + 3d\sin(\tilde{\varphi})}{\sigma_n}\right)\right] \cdot \\
&\quad \left[1 - Q\left(\frac{2d - 3d\cos(\tilde{\varphi}) - 3d\sin(\tilde{\varphi})}{\sigma_n}\right)\right]. \qquad (A.67)
\end{aligned}
$$

Finally, Eq.(A.62), Eq.(A.63), Eq.(A.65) and Eq.(A.67) can be substituted into Eq.(A.61) to achieve $F_{\boldsymbol{c}}(c|\tilde{\boldsymbol{\varphi}} = \tilde{\varphi})$, which is not explicitly written here. For the convenience, d and σ_n in Eq.(A.62), Eq.(A.63), Eq.(A.65) and Eq.(A.67) should be expressed as a function of SNR. For the purpose, the relation between d and the averaged energy per symbol E_s can be written as

$$E_s = \frac{1}{16}\left(4 \cdot d^2 + 8 \cdot \left(d^2 + 3^2 \cdot d^2\right) + 4 \cdot 3^2 \cdot d^2\right). \qquad (A.68)$$

Assuming a constant $E_s = 1$, d can be given by

$$d = \frac{2}{\sqrt{39}}, \qquad (A.69)$$

and σ_n can be given by

$$\sigma_n = \frac{1}{\sqrt{2\mathrm{SNR}}}. \qquad (A.70)$$

The degradation due to phase errors can be calculated by assuming the phase noise as zero mean normal distributed random variable with the variance of $\sigma_{\tilde{\varphi}}$ and the average symbol error probability can be given by

$$F_{\boldsymbol{e}}(e) = \int_{-\infty}^{\infty} \left(1 - F_{\boldsymbol{c}}(c|\tilde{\boldsymbol{\varphi}} = \tilde{\varphi})\right) \cdot \frac{1}{\sigma_{\tilde{\varphi}}\sqrt{2\pi}} \cdot \exp\left(-\frac{\tilde{\varphi}^2}{2\sigma_{\tilde{\varphi}}^2}\right) d\tilde{\varphi}. \qquad (A.71)$$

The numerical and simulative evaluations of Eq.(A.71) are shown in Figure. 4.16.

A.5. Optical Signal to Noise Power Ratio

Since carrier frequency in optical transmission systems is much higher than the modulation frequency, the noise bandwidth is much wider than the signal bandwidth. Consequently, the resulting SNR can be strongly influenced by signal filtering. In order to provide the description of signal quality independent of receivers, optical signal-to-noise ratio (OSNR) is used, which gives us the ratio between the signal power and the noise power in a given bandwidth. In [42], it has been shown that OSNR can be given by

$$\mathrm{OSNR} = \frac{P_r}{2 \cdot N_0 \cdot B_n}, \qquad (A.72)$$

where P_r is the power of received signal, N_0 the noise power spectrum in each polarization and B_n the given noise bandwidth. The mostly used B_n in optical transmission systems is the noise bandwidth corresponding to 0.1nm. For the carrier signal with a wavelength of 1550.0nm, B_n corresponding to 0.1nm can be calculated as

$$B_n = \frac{c}{1549.05\text{nm}} - \frac{c}{1550.05\text{nm}} = 12.5\text{GHz}, \tag{A.73}$$

where c=$3 \cdot 10^8$m/s is the speed of light. From the definition of OSNR, the noise bandwidth is constant and independent of system configurations. In contrast, the signal bandwidth, depends on system configurations e.g., symbol rate and number of samples per symbol. Consequently, the performance comparison of systems with different system configurations using OSNR can become misleading. In [141], the author has shown that E_s/N_0 is more suitable for this performance comparison.

A.6. Amplified Spontaneous Emission

In [146], amplified spontaneous emission noise (ASE-noise) is described as followed:

"Amplifiers inside the transmission link will not only show stimulated emission, but a part of the amplified intensity comes from the spontaneous emission of the amplifier. This part will increase with the amplification and is called amplified spontaneous emission (ASE)."

In other words, ASE-noise is noise induced by optical amplification.

List of Abbreviations

A/D	analog digital converters 34, 68
ABA	adaptive bandwidth algorithm 129, 136, 147, 149, 152
ADC	analog-to-digital convertor 101, 135
AFC	automatic frequency control 135, 152, 153
ASE-noise	amplified spontaneous emission noise 86, 88, 95, 105, 128, 135, 155
ASIC	application-specific integrated circuits 81
ASK	amplitude shift keying 25, 27, 160
ASK-DPSK	amplitude shift keying with differential phase shift keying 28
ASK-PSK	amplitude-phase shift keying 22, 25, 27, 81, 155
AWGN	additive white Gaussian noise 63, 64, 85, 114, 123

BD	balanced detectors 29
BER	bit error rate 68, 71
BPSK	binary phase shift keying 26
BQ	balanced Quadricorrelator 140, 153

CD	chromatic dispersion 5–7, 9, 10, 34–36, 73, 95, 147, 151
CMA	constant modulus algorithm 34
CRB	Cramér-Rao-Bounds 58
CW	continuous wave 12, 31

DA	data-aided 39, 153
DCF	dispersion-compensation fiber 7, 35, 73
DD	decision-directed 39, 113, 114
DFB	single-mode distributed feedback lasers 11
DGD	differential group delay 8
DLI	delay line interferometer 21, 22, 28–30, 63
DM	dispersion-managed links 7, 88
DPFE	differential phase frequency estimation 96, 109, 152
DPM	double power measurement 137, 153
DPSK	differential phase shift keying 28, 30, 35
DSP	digital signal processing 33, 34, 36, 37, 40, 41, 63, 68, 73, 74, 81, 135, 151

ECL	external cavity lasers 11, 13

FB	feedback 37–40
FD-AFC	frequency domain automatic frequency control 142, 153
FEC	feed forward error correction 155
FF	feed-forward 37, 39, 40
FFT	fast Fourier transformation 142
FIR	finite impulse response 34, 37, 41, 138
FPGA	field-programmable gate arrays 81
FWM	four wave mixing 9, 10
GVD	group-velocity dispersion 6, 7
IIR	infinite impulse response 38, 41, 138
IMSPE	iterative multiple symbol phase estimation 75–77, 80, 151
IQM	IQ modulators 11, 17, 28
IS	electrical impulse shapers 18, 27
LED	light emitting diodes 11
LMS	least mean square 34
LO	local oscillator 31–34, 91, 96, 111, 124, 135
MAP	maximum a posteriori 55, 56
MCRB	modified Cramér-Rao-Bounds 37, 58, 59, 114, 122, 123, 152
MDE	minimum distance estimation 99, 109, 152
ML	maximum likelihood 55, 56, 82, 111
MLL	maximum likelihood loop 113, 114, 152
MMSE	minimum mean square error 34, 56, 100
MSDD	multiple symbol differential detection 63, 68, 70–75, 77, 80, 151
MSE	mean square error 54, 56
MSPE	multiple symbol phase estimation 70–75, 77, 80, 151
MZM	Mach-Zehnder modulators 11, 16, 17, 27
NCO	numerically-controlled oscillator 136
NDA	non-data-aided 39, 113, 153
NDM	none dispersion managed links 36
NRZ	non-return to zero 18
NTA	none-timing-aided 40
OFDM	orthogonal frequency devision multiplexing 155
OOK	on off keying 35, 63, 88, 89
OSNR	optical signal to noise ratio 23, 68, 72
OTDM	optical time-division multiplexing 34

P/S	parallel to serial converter 41
PAPR	peak-to-average power ratio 36
PBS	polarization beam splitters 33
PCC	polarization coupled carrier phase estimation 91, 92, 98, 109, 152
PDF	probability density function 37, 54, 56, 57, 59, 161–164, 166
PLL	phase locked loop 38
PM	phase modulators 11, 15, 17, 26
PMD	polarization mode dispersion 5, 8, 34, 36, 73, 136, 147, 151
PolMux	polarization-multiplex 8, 30, 33, 71, 73, 77, 152
PSK	phase shift keying 22, 25, 27, 81, 82, 84, 113, 160
QAM	quadrature amplitude modulation 22, 25, 113, 155, 165
QPSK	quadrature phase shift keying 26
RZ	return to zero 18
S/P	serial to parallel converter 41
SI	save interval 76, 77
SNR	signal to noise ratio 39, 40, 51, 61, 68, 82, 85, 114, 120–123, 161, 163, 169
SPM	self phase modulation 5, 9, 10, 35, 88, 89, 105, 128
SSMF	standard single mode fiber 6, 7, 9, 35, 73, 95, 104
TA	timing-aided 40
V&V	Viterbi-Viterbi algorithm 89, 90, 98, 109, 152
WDM	wavelenght division multiplexing 10, 19, 30, 34–36, 89, 95, 104, 127
XPM	cross phase modulation 5, 9, 10, 35, 88, 89, 95, 105, 128

Symbols List

A	Slope of the S-curve 122
a	Ratio of impulse rising time 9
A_{1_k}	QAM alphabet for quadrant representation 25
A_{2_k}	QAM alphabet for second sub-constellation 25, 26
A_{d_k}	Differntial Alphabet 24, 25
$a_{IQM}(t)$	Amplitude modulation for optical IQ modulator 17
A_k	Integer representation of a complex symbol 23
A_{pp}	Maximum peak-to-peak of frequency variations 14, 104
α	Attenuation constant 6, 9
α_{IR}	Infrared-absorption attenuation 6
α_{OH}	OH-absorption attenuation 6
α_S	Rayleigh-scattering attenuation 6
ΔB_{SPM}	SPM frequency range 9
ΔB_{XPM}	XPM frequency range 10
B_j	Strength of the jth resonance frequency 6
b_k	Digital complex symbol 22, 23, 81
b_k^i	In-phase component of digital complex symbol 22
b_k^q	quadrature component of digital complex symbol 22
B_L	Loop noise bandwidth 122
B_m	Modal birefringence 7, 8
$B_\nu(S)$	Bessle polynomial 20
$\beta(\omega)$	Mode-propagation constant 6, 7
c	The speed of light 170
C_{acq}	Acquisition constant 147
C_{MP}	Constant for calculation of likelihood function 82
D	Dispersion parameter 6, 7, 10
D_{FB}	Entire feedback delay 45, 49
d_k	Distance between sampled signal and estimated symbol 100
D_P	Processing feedback delay 45, 124
D_p	PMD parameter 8
e	Charge per electron 29
$\vec{E}_{CW}(t)$	Normalized electrical filed of ideal carrier signal 12
$\vec{E}_{CWn}(t)$	Normalized electrical filed of noisy carrier signal 12
$E_I(t)$	In-phase output filed from 3dB coupler 29
$E_{in}(t)$	Incoming optical carrier for optical modulator 16

e_k	Error signal 117
$E_{out}(t)$	Outgoing optical field from optical modulator 16
$E_{out_1}(t)$	Output filed from 2 x 4 90° hybrid 33
$E_{out_2}(t)$	Output filed from 2 x 4 90° hybrid 33
$E_{out_3}(t)$	Output filed from 2 x 4 90° hybrid 33
$E_{out_4}(t)$	Output filed from 2 x 4 90° hybrid 33
$E_Q(t)$	Quadrature output filed from 3dB coupler 29
E_s	Energy per symbol 61
$E(t)$	Normalized electrical single field 29
ε	Realization of random variable for parameter estimation 58
$\boldsymbol{\varepsilon}$	Random variable for parameter estimation 58
$\hat{\boldsymbol{\varepsilon}}$	Random variable for estimated parameter 58
$\tilde{\boldsymbol{\varepsilon}}$	Random variable for unwanted parameter in an estimator 60
$\vec{\tilde{\varepsilon}}$	Vector of unwanted parameter in an estimator 59
η	Quantum efficiency of the photodiode 29
η_D	Decision metric for multiple symbol differential detection algorithm 65
f_0	Center frequency of band-pass filter 19
f_c	3dB bandwidth of filter 19
Δf	Frequency offset 31
Δf_{SPM}	SPM frequency deviation 9
$\Delta \hat{f}_k$	Estimated frequency offset in digital domain 96
$f_{md}(t)$	output signal of the laser with mechanical disturbances 14
f_{lo}	Frequency of local oscillator 31
f_m	Modulation frequency for laser stabilization 15
$f_n(t)$	General function of frequency variations over the time 14
f_{Nq}	Nyquist frequency 137
f_s	Frequency of carrier signal 12, 14, 31
$G_0(f)$	Normalized transfer-function of the pulse-shaping filter 141
$G(f)$	Transfer-function of the filter for the pulse-shaping 138
g_i	Integrate parameter for loop filter 118
$g_{r,ABA}$	Adaptive loop filter recursive gain 132
g_r	Recursive parameter for loop filter 117
$g_{r,ABA}$	Adaptive loop filter recursive gain 130
g_{sn}	Degradation function of transmitted signal 53
g_u	Gain parameter for phase unwrapping 105
γ	Nonlinear propagation coefficient 9
h	Planck constant 29
$H_{BP}(f)$	Transferfunction of band-pass filter 19

$H_{BP1}(f)$	Transfer function of bandpass filter for double power measurement 138
$h_{BP1,k}$	Impulse response of bandpass filter for double power measurement 137
$h_{TP,k}$	Impulse response of a lowpass filter 138
$H_{BP2}(f)$	Transfer function of bandpass filter for double power measurement 138
$h_{BP2,k}$	Impulse response of bandpass filter for double power measurement 137
$H_{BP3}(f)$	Transfer function of bandpass filter for balanced Quadricorrelator 140
$H_{BP4}(f)$	Transfer function of bandpass filter for balanced Quadricorrelator 140
h_k	Impulse response of digital filter 54
$h_{k,i}$	Time variance impulse response of digital filter 54
$H_{pre}(f)$	Transfer function of pre-filter for balanced Quadricorrelator 141
$I_0(x)$	Zeroth order modified Bessel function 65
$I_I(t)$	Output signal from coherent balaced detection 32
i_{sh}	Shot-noise photocurrent after balanced detection 32
i_{sh_1}	Shot-noise photocurrents of photodiodes 31
i_{sh_2}	Shot-noise photocurrents of photodiodes 31
i_{sh_i}	shot-noise photocurrents in in-phase arm 33
i_{sh_q}	shot-noise photocurrents in quadrature arm 33
J_k	Jump indicator 131
L	Estimation block length 65, 85
l_{ABA}	Adaptation length of adaptive bandwidth algorithm 130
L_B	Beat length 7
$l_{b,k}$	Burst error length 76
l_c	Polarization correlation length 8
L_{eff}	Fiber effective length. 9
$L_{eff,XPM}$	Walk-off fiber length 10
l_{PM}	Length of electrode 16
L_{eq}	Equivalent estimation length 122
L_f	Length of fiber optics 5, 8, 9
L_{fft}	Block length of fast Fourier transformation 142
L_m	Memory length of digital signal processing 42
Λ^{log}	Log-likelihood function 58
Λ	Likelihood function 57
λ	Optical wavelength 6, 16
λ_D	Zero-dispersion wavelength 7
$\Delta\lambda$	Wavelength difference 10
m	Number of bits per symbol 23, 26
m_{bias}	Estimation bias gradient 145
$\mu_{\tilde{\varphi}}$	Mean of random variable for phase error 51

N	Number of iterations in iterative multiple symbols phase estimation 77
N_0	Spectral density of noise 57
N_{ABA}	Number of samples for acquisition with adaptive bandwidth algorithm 147
N_{buff}	Number of required buffer units 44, 49
$n_{eff}(t)$	Effective refractive index 16
$\Delta n_{eff}(t)$	Change of the effective refractive index 16
N_{FWM}	Total number of generated FWM mixing products 10
n_g	Group refractive index 6
N_k	General noise term in digital domain 84
n_k	Noise in digital domain 54
$n(\omega)$	Frequency dependent refractive index 6
N_q	Number of test phases for minimum distance estimation 100
$n(t)$	Noise 53
N_{WDM}	Number of WDM channels 10
n_x	Modal refractive index for x-polarizytion 7
n_y	Modal refractive index for y-polarizytion 7
ν	Filter order 19
$\Delta\nu$	Accumulated laser linewidth 86
$F_{vv}\left(a_{v_k}\right)$	Chosen function of amplitude of signal for Viterbi & Viterbi algorithm 90
$\Delta\nu_{eff}$	Beat-linewidth 32
$\Delta\nu_s$	Carrier signal laser linewidth at transmitter side 13
ω_j	jth resonance frequency in fiber optics 6
P	Number of parallelization paths 41
P_0	Power launched at the input of a fiber 5
$P_{cp}(t)$	Momentary co-propagate power of wavelength 10
$\delta P(t)$	Intensity fluctuations of carrier signal 12
P_{lo}	Power of local oscillator signal 31
P_m	Constellation point 82
P_{max}	Maximal impulse power 9
P_r	Power of received signal 170
P_s	Power of carrier signal, power of transmitted signal 5, 12, 31, 61
$P(t)$	Momentary power of the pulse 9
c_x	Coupling factor from x-polarization to y-polarization 93
c_y	Coupling factor from y-polarization to x-polarization 93
$\varphi_{d,k}$	Sample of differential encoded phase 65
$\varphi_{d,k,c}$	Estimated phase from feed forward multiple symbol estimation in the current iteration 76
$\varphi_{d,k,c}$	Estimated phase from feed forward multiple symbol estimation in the previous iteration 76

$\Delta\varphi_n(t)$	Overall laser phase noise 32
φ_{DPI}	Arbitrary phase shift for DLI 21
$\varphi_{DLI,I}$	Phase shift of DLI in in-phase branch 29, 30
$\varphi_{DLI,Q}$	Phase shift of DLI in quadrature branch 30
$\hat{\varphi}_{eq}$	Equilibrium point 119
$\hat{\varphi}$	Estimated phase 84
$\hat{\boldsymbol{\varphi}}$	Random variable for estimated phase 51
$\vec{\hat{\varphi}}_k$	Vector of estimated phase in digital domain 65
$\varphi_{IQM}(t)$	Phase modulation for optical IQ modulator 17
$\Delta\hat{\varphi}_k$	Estimated phase of differential demodulated signal in digital domain 97
$\tilde{\varphi}_{min}$	Minimum phase error of minimum distance estimation 101
$\varphi_n(t)$	Overall laser phase noise 31
$\varphi_{n_{lo}}(t)$	Signal laser phase noise of local oscillator 31
$\varphi_{n_s}(t)$	Signal laser phase noise 12, 31
$\dot{\varphi}_{n_s}(t)$	Signal laser frequency noise 13
$\Delta\varphi_{n_s}(t)$	Phase change due to laser phase noise 12, 13, 30
$\hat{\varphi}_{p,k}$	Provisional phase trajectory 105
$\varphi_{PM}(t)$	Phase modulation of a phase modulator 16
$\boldsymbol{\varphi}$	Random variable for actual phase 51
$\tilde{\boldsymbol{\varphi}}$	Random variable for phase error 51
φ_{lo}	Initial phase of local oscillator 31
φ_s	Initial phase of carrier signal 12, 31
$\varphi_{SI,k}$	Estimated phase from save interval 76
φ_{SPM}	SPM Phase rotation 9
$\Delta\varphi(t)$	Difference of modulation phase of two consecutive symbols 30
$\tilde{\varphi}$	Phase error 81
$\hat{\varphi}_{u,k}$	Final unwrapped phase 105
$\varphi_{x,y}(t)$	Cross correlation between phase variation in two polarizations 92
$\varphi_{x,y,k}$	Discrete cross correlation between phase variation in two polarizations 92
φ_{XPM}	XPM Phase rotation 9
ψ	Arbitrary phase shift for 2x4 90° Hybird 20, 21, 32
q_k	Phase reference for recursive multiple symbol differential detection algorithm 70
R	Responsivity of the photodiode 29
r_b	Data rate 22
r_k	Sample of received signal 41, 54
r_S	Symbol rate 23
$r(t)$	Received signal 53, 81
r_V	Sample rate 139
S	Sample block length for each parallelization path in the Superscalar parallelization architecture 47

$s_{i,k}$	Averaged distance between sampled signal and estimated symbol 101
s_k	Transmitted signal in digital domain 54
$\hat{s}_k$	Estimate of transmitted signal in digital domain 54
$\hat{s}_{\mathrm{MAP}}$	Maximum a Posteriori estimate 55
$\hat{s}_{\mathrm{ML}}$	Maximum Likelihood estimate 55
$\hat{s}_{\mathrm{MMSE}}$	Minimum Mean Square Error estimate 56
$S(\tilde{\varphi})$	S-curve of a feedback carrier phase estimation 118
$s(t)$	Transmitted signal 53
$\hat{s}(t)$	Estimate of transmitted signal 53
$\tilde{s}(t)$	Estimation error of transmitted signal 53
$\sigma^2_{\tilde{\varphi}}$	Variance of random variable for phase error 51
T_{acq}	Acquisition time 147
t_{add}	Processing time for addition 43
T_b	Bit duration 22
ΔT	Time delay between two polarizations 8
Δt	Electrical rise time 18
t_{mul}	Processing time for multiplication 43
T_p	Processing time in a processing iteration 42
$T_{p,min}$	Minimum processing time in a processing iteration 43
T_r	Sampling time duration 42
T_s	Symbol interval 9, 18, 21, 22, 61, 86
$\Delta\tau$	Differential Group delay 8
τ_{gr0}	Group delay for $f = 0$ 20
T_e	Filter time constant 18
θ_k	Phase introduced by channel 63
$u_{ext}(t)$	External voltage for optical modulator 16
u_k	Simple of output signal from differential phase optical detector 70
$u_{PM}(t)$	External voltage for optical phase modulator 17
Υ	Estimation function 53
$v_{d,k}$	Digital differential demodulated signal 97
v_g	Group velocity 6
v_k	Sampled output signal from matched filter 82
V_π	Voltage for π phase shift 16
$V_{\pi 1}$	V_π for upper MZM branch 16
$V_{\pi 2}$	V_π for lower MZM branch 16
$v(t)$	Output signal from matched filter 81
w	Forgetting factor 70, 131
$W_E(f)$	Power spectral density of the carrier signal 13
ξ	XPM weighting factor 10
z_k	Output signal from digital signal processing 70

Bibliography

[1] Payne D., "FTTP Deployment Options and Economic Challenges," in *Proc. Eur. Conf. Optical Commun. (ECOC)*, Vienna, Austria, Sep. 2009, paper 3.4.1.

[2] Bülow H., "Optoelectronic synchronisation scheme for ultrahigh-speed optical demultiplexer," *Electronics Letters*, vol. 31, pp. 1355 – 1364, 1995.

[3] Noé R., "PLL-Free Synchronous QPSK Polarization Multiplex/Diversity Receiver Concept With Digital I&Q Baseband Processing," *Photonics Technology Letters*, vol. 17, pp. 887–889, 2005.

[4] van den Borne D., et al., "Carrier phase estimation for coherent equalization of 43-Gb/s POLMUX-NRZ-DQPSK transmission with 10.7-Gb/s NRZ neighbours," in *Proc. Eur. Conf. Optical Commun. (ECOC)*, Berlin, Germany, Sep. 2007, paper We7.2.3.

[5] Brinkmeyer E., "Optische Kommunikationstechnik," Voges E., Petermann K., Ed. Berlin: Springer, 2002, ch. 3.4.1.

[6] Agrawal G. P., *Nonlinear Fiber Optics*, 4th ed. Academic Press, 2007.

[7] Marcuse D., *Light Transmission Optics.* New York: Van Nostrand Reinhold, 1982.

[8] Ainslie B. J., Day C. R., "A review of single-mode fibers with modified dispersion characteristics," *Journal of Lightwave Technology*, vol. 4, p. 967–979, 1986.

[9] Kaminow I.P., "Performance of an improved InGaAsP ridge waveguide laser at 1.3 μm," *Journal of Quantum Electron*, vol. QE-17, p. 15, 1981.

[10] Hakki B.W., "Polarization mode dispersion compensation by phase diversity detection," *Photonics Technology Letters*, vol. 9, pp. 121 – 123, 1997.

[11] Bülow H., "Limitation of Optical First-Order PMD Compensation," in *Proc. Optical Fiber Commun. Conf. (OFC)*, U.S.A., 1999, paper WE1.

[12] Poole C. D., Nagel J., *Optical Fiber Telecommunications III.* Boston: Academic Press, 1997, ch. 6.

[13] Bülow H., "Analysis of system outage induced by second order PMD in the presence of

chromatic dispersion," in *Proc. Eur. Conf. Optical Commun. (ECOC)*, Madrid, Spain, 1998, paper WdC5.

[14] Kogelnik H., Jopson R. M., Nelson L. E., *Optical Fiber Telecommunications.* Boston: Academic Press, 2002, ch. 15.

[15] Renner H., "Optische Kommukationstechnik," Voges E., Petermann K., Ed. Berlin: Springer, 2002, ch. 4.15.

[16] Damask J. N., *Polarization Optics in Telecommunications.* New York: Springer, 2005.

[17] Seimetz M., *High-Order Modulation for Optical Fiber Transmission*, 1st ed. Berlin: Spinger, 2009.

[18] Hooijmans P. W., *Coherent Optical System Design.* John Wiley and Sons, 1994.

[19] Kazovsky L. G., *Optical Fiber Communication Systems.* Artech House, 1996.

[20] Petermann K., *Laser diode modulation and noise.* Dordrecht/Boston/London: Kluwer Academic, 1988.

[21] Kuschnerov M., et al., "Impact of Mechanical Vibrations on Laser Stability and Carrier Phase Estimation in Coherent Receivers," *Photonics Technology Letters*, vol. PP, pp. 1–1, 2010.

[22] Piyawanno K., et al., "Effects of Mechanical Disturbance on Local Oscillators and Carrier Synchronization," in *Proc. OptoElectronics and Communications Conference (OECC)*, Sapporo, Japan, Jul. 2010, paper 13P-13.

[23] Driscoll M. M., Donovan J. B., "Vibration-Induced Phase Noise: It Isn't Just About The Oscillator," *Frequency Control Symposium 2007 Joint with the 21st European Frequency and Time Forum.*, pp. 535–540, 2007.

[24] Hoffmann D., "Optische Kommunikationstechnik," Voges E., Petermann K., Ed. Berlin: Springer, 2002, ch. 15.5.

[25] Covega, http://www.covega.com/.

[26] Haykin S., *Communication Systems.* John Wiley and Sons, 1994.

[27] Proakis J. G., *Digital Communications.* McGraw-Hill, 2001.

[28] von Wangenheim L., *Aktive Filter in RC- und SC-Technik.* Heidelberg: Hüthig Buch Verlag, 1991.

[29] Kazovsky L. G. et al., "Wide-linewidth phase diversity homodyne receivers," *IEEE Jour-*

nal of Lightwave Technology, vol. 6, no. 10, pp. 1527–1536, 1988.

[30] Jorgensen B.F. et al., “Analysis of amplifier noise in coherent optical communication systems with optical image rejection receivers,” *IEEE Journal of Lightwave Technology*, vol. 10, no. 5, pp. 660–671, 1992.

[31] Djordjevic I. B., “Performance optimization and exact laser linewidth requirements evaluation for optical PSK homodyne communication systems with Costas loop or DDL,” *Journal of Optical Communications*, vol. 20, no. 5, pp. 178–182, 1999.

[32] Kazovsky L. G. et al., “Decision-driven phase-locked loop for optical homodyne receivers : Performance analysis and laser linewidth requirements,” *IEEE Journal of Lightwave Technology*, vol. LT-3, no. 6, pp. 1238–1247, 1985.

[33] Seimetz M., Weinert C.M., “Options, feasibility and available of 2 x 4 90° hybrid for coherent optical systems,” *IEEE Journal of Lightwave Technology*, vol. 24, no. 3, pp. 1317–1322, 2006.

[34] Hoffmann D. et al., “Integrated optics eight-port 90°-hybrid on $LiNbO_3$,” *IEEE Journal of Lightwave Technology*, vol. 7, no. 5, pp. 794–798, 1989.

[35] Yamazaki S., Emura K., “Feasibility Study on QPSK Optical-Heterodyne Detection System,” *Journal of Lightwave Technology*, vol. 8, pp. 1646–1653, 1990.

[36] Seimetz M., Noelle M., Patzak E., “Optical Systems With High-Order DPSK and Star QAM Modulation Based on Interferometric Direct Detection,” *Journal of Lightwave Technology*, vol. 25, pp. 1515–1529, 2007.

[37] Gnauck A. H., et al., “10 × 112-Gb/s PDM 16-QAM transmission over 630 km of fiber with 6.2-b/s/Hz spectral efficiency,” in *Proc. Optical Fiber Commun. Conf. (OFC)*, San Diego, CA, U.S.A., Mar. 2009, paper PDPB8.

[38] De Jonghe G., Moeneclaey M., “Cycle slip analysis of the M-th power NDA feedforward carrier synchronizer for M-PSK using narrowband postfiltering,” in *3rd European Conference on Satellite Communications - ECSC-3, 1993.*

[39] Hwang J. K., Chiu Y. L., “Performance Analysis of an Angle Differential-QAM Scheme for Resolving Phase Ambiguity,” in *Advanced Communication Technology 2008.*

[40] Weber W. J., “Differential Encoding for Multiple Amplitude and Phase Shift Keying Systems,” *IEEE Trans. on Commun.*, vol. COM-26, pp. 385–391, 1978.

[41] Seimetz M., “Multi-format transmitter for coherent optical M-PSK and M-QAM transmission,” in *ICTON, Th.B1.5*, Barcelona, 2005.

[42] Ho K. P., *Phase-Modulated Optical Communication Systems.* Springer, 2005.

[43] Spinnler B., Hauske F.N., Kuschnerov M., "Adaptive Equalizer Complexity in Coherent Optical Receivers," in *Proc. Eur. Conf. Optical Commun. (ECOC)*, Brussel, Belgium, Sep. 2008, paper We.2.E.4.

[44] Ishihara K. et al., "Coherent Optical Transmission with Frequency-domain Equalization," in *Proc. Eur. Conf. Optical Commun. (ECOC)*, Brussel, Belgium, Sep. 2008, paper We.2.E.3.

[45] Kuschnerov M. et al., "Adaptive Chromatic Dispersion Equalization for Non-Dispersion Managed Coherent Systems," in *Proc. Optical Fiber Commun. Conf. (OFC)*, San Diego, CA, U.S.A., Mar. 2009, paper OMT1.

[46] Hauske F.N. et al., "Frequency Domain Chromatic Dispersion Estimation," in *Proc. Optical Fiber Commun. Conf. (OFC)*, San Diego, CA, U.S.A., Mar. 2010, paper JThA11.

[47] Gardner F. M., "A BPSK/QPSK Timing-Error Detector for Sampled Receivers," *IEEE Trans. on Commun.*, vol. COM-34, pp. 423–429, 1986.

[48] Oerder M., Meyr H., "Digital Filter and Square Timing Recovery," *IEEE Trans. on Commun.*, vol. COM-36, pp. 605–612, 1988.

[49] Mueller K. H., Mueller M., "Timing Recovery in Digital Synchronous Data Receivers," *IEEE Trans. on Commun.*, vol. COM-24, pp. 516–531, 1976.

[50] Kuschnerov M., et al., "Digital Timing Recovery for Coherent Fiber Optic Systems," in *Proc. Optical Fiber Commun. Conf. (OFC)*, San Diego, CA, U.S.A., Mar. 2008, paper JThA63.

[51] ——, "Joint Equalization and Timing Recovery for Coherent Fiber Optic Receivers," in *Proc. Eur. Conf. Optical Commun. (ECOC)*, Brussel, Belgium, Sep. 2008, paper Mo.3.D.3.

[52] Godard D. N., "Self-recovering equalization and carrier tracking in two-dimensional data communication systems," *IEEE Trans. on Commun.*, vol. COM-28, p. 1867–1875, 1980.

[53] Widrow B., Hoff M. E. Jr., "Adaptive switching circuits," *IRE WESCON Conv. Rec.*, vol. 4, p. 96–104, 1960.

[54] Godard D. N., "Synthesis of a nonlinear Bayes detector for Gaussian signal and noise fields using Wiener filters," *IEEE Trans. Inform. Theory*, vol. IT-13, pp. 116–118, 1967.

[55] Metropolis N., Ulam S., "The Monte Carlo Method," *Journal of the American Statistical Association*, vol. 44, p. 335–341, 1949.

[56] Taha T. R., Ablowitz M. I., "Analytical and numerical aspects of certain nonlinear evolution equations. II. Numerical, nonlinear Schrödinger equation," *Journal of Computational*

Physics, vol. 55, pp. 203–230, 1982.

[57] Miki T., Ishio S., “Viabilities of the Wavelength-Division-Multiplexing Transmission System Over an Optical Fiber Cable,” *IEEE Trans. on Commun.*, vol. COM-26, pp. 1082 – 1087, 1978.

[58] Tucker R. S., Eisenstein G., Korotky S. K., “Optical time-division multiplexing for very high bit-rate transmission,” *Journal of Lightwave Technology*, vol. 6, pp. 1737 – 1749, 1988.

[59] Haunstein H., Urbansky R., “Application of Electronic Equalization and Error Correction on Lightwave Systems,” in *Proc. Eur. Conf. Optical Commun. (ECOC)*, Stockholm, Sweden, Sep. 2004, paper Th1.5.1.

[60] Cavallari M., Fludger C. R. S., Anslow P. J., “Electronic Signal Processing for Differential Phase Modulation Formats,” in *Proc. Optical Fiber Commun. Conf. (OFC)*, U.S.A., Mar. 2004, paper TuG2.

[61] Hauske F. N., et al., “Iterative Electronic Equalization Utilizing Low Complexity MLSEs for 40 Gbit/s DQPSK Modulation,” in *Proc. Optical Fiber Commun. Conf. (OFC)*, U.S.A., Mar. 2005, paper OMG2.

[62] Killey R. I., et al., “Reduction of Intrachannel Nonlinear Distortion in 40-Gb/s-Based WDM Transmission over Standard Fiber,” *Photonics Technology Letters*, vol. 12, pp. 1624–1626, 2000.

[63] Coelho L.D. et al., “Global Optimization of RZ-DPSK and RZ-DQPSK Systems at Various Data Rates,” in *Proc. Optical Fiber Commun. Conf. (OFC)*, San Diego, CA, U.S.A., Mar. 2009, paper OMT6.

[64] van den Borne D. et al., “POLMUX-QPSK modulation and coherent detection: the challenge of long-haul 100G transmission,” in *Proc. Eur. Conf. Optical Commun. (ECOC)*, Vienna, Austria, Sep. 2009, paper 3.4.1.

[65] Meyr H., Moeneclaey M., Fechtel S. A., *Digital Communication Receivers.* John Wiley and Sons, 1998.

[66] Gardner F. M., *Phaselock Techniques*, 3rd ed. John Wiley and Sons, 2005.

[67] Cacciamani E., Wolejsza C., “Phase-ambiguity resolution in a four-phase psk communications system,” *IEEE Trans. on Commun.*, vol. COM-19, p. 1200–1210, 1971.

[68] Kuschnerov M., et al., “Joint Equalization and Timing Recovery for Coherent Fiber Optic Receivers,” in *Proc. Eur. Conf. Optical Commun. (ECOC)*, Brussel, Belgium, Sep. 2008, paper We.2.E.3.

[69] Meyrs M. H., Franks L. E., “Joint Carrier Phase and Timing Recovery for PAM Systems,” *IEEE Trans. on Commun.*, vol. COM-28, pp. 1121–1129, 1980.

[70] Morelli M., Vitetta G. M., “Joint Phase and Timing Recovery for MSK-type Signals,” *IEEE Trans. on Commun.*, vol. COM-48, pp. 1997–1999, 2000.

[71] Chang C. M., Cheng K. C., “Joint Linear Timing and Carrier Phase Estimation of DS-CDMA Multiuser Communications,” *IEEE Journal on Sel. Areas in Commun.*, vol. 1, pp. 87–98, 2000.

[72] Mengali U., “Joint Phase and Timing Acquisition in Data Transmission,” *IEEE Trans. on Commun.*, vol. 25, pp. 1174 – 1185, 1983.

[73] Piyawanno K., et al., “Low Complexity Carrier Recovery for Coherent QAM using Superscalar Parallelizatio,” in *Proc. Eur. Conf. Optical Commun. (ECOC)*, Torino, Italy, Sep. 2010, paper We.7.A.3.

[74] Pfau T., Hoffmann S., Noé R., “Hardware-Efficient Coherent Digital Receiver Concept With Feedforward Carrier Recovery for M-QAM Constellations,” *Journal of Lightwave Technology*, vol. 27, pp. 989–999, 2009.

[75] Jouppi N. P., “The nonuniform distribution of instruction-level and machine parallelism and its effect on performance,” *IEEE Transactions on Computers*, vol. 18, pp. 1645 – 1658, 1989.

[76] Kamen E. W. , Su J. K., *Introduction to Optimal Estimation.* Springer, 1999.

[77] Mengali U., D’Andrea A. N., *Synchronization Techniques for Digital Receivers*, 1st ed. Plenum Press, 1997.

[78] Van Trees H. L., *Detection, Estimation, and Modulation Part I.* Wiley, 1968.

[79] Kroschel K., *Statistische Informationstechnik.* Springer, 2003.

[80] Sage A. P., *Estimation Theory with Applications to Communications and Control.* McGraw-Hill, 1974.

[81] K. S. M., *Fundamentals of Statistical Signal Processing : Estimation Theory.* Prentice-Hall, 1993.

[82] Barankin E. W., “Locally best unbiased estimates,” *Ann. Math. Statist.*, vol. 20, pp. 477–501, 1949.

[83] Ziv J., Zakai M., “Some Lower Bounds on Signal Parameter Estimation,” *IEEE Transactions on Information Theory*, vol. IT-15, pp. 386–391, 1969.

[84] Bellini S., Tartara G., “Bounds on Error in Signal Parameter Estimation,” *IEEE Transactions on Information Theory*, vol. Com-22, pp. 340–342, 1974.

[85] Seidman L. P., “Performance Limitations and Error Calculations for Parameter Estimation,” *Proc.IEEE*, vol. 5, pp. 644–652, 1970.

[86] Cowley W. G., “Phase and Frequency Estimation for PSK Packets : Bounds and Algorithms,” *IEEE Transactions on Information Theory*, vol. COM-44, pp. 26–28, 1996.

[87] Moeneclaey M., Bruyland I., “The Joint Carrier and Symbol Synchronizability of Continuous Phase Modulated Waveforms,” in *Conf. Rec. ICC’86*, 1986.

[88] Moeneclaey M., “A Simple Lower Bound on Linearized Performance of Practical Symbol Synchronizers,” *IEEE Transactions on Information Theory*, vol. COM-31, pp. 1029–1032, 1983.

[89] ——, “A Fundamental Lower Bound to the Performance pf Practical Joint Carrier and Bit Synchronizers,” *IEEE Transactions on Information Theory*, vol. COM-32, pp. 1007–1012, 1984.

[90] Solomentsev E. D., *Encyclopaedia of Mathematics*, Hazewinkel M., Ed. Springer, 2001.

[91] Rao C. R., *Breakthroughs in Statistics: Foundations and basic theory*, Kotz S., Johnson N. L., Ed. Springer, 1945.

[92] D’Andrea A. N., Mengali U., “The Modified Cramer-Rao Bound and Its Applications to Synchronization Problems,” *IEEE Transactions on Information Theory*, vol. COM-42, pp. 1391–1399, 1994.

[93] Jensen J. L. W. V., *Acta Mathematica.* Springer, 1906.

[94] Divsalar D., Simon M. K., “Multiple-Symbol Differential Detection of MPSK,” *IEEE Trans. on Commun.*, vol. COM-38, pp. 300 – 308, 1990.

[95] Wilson S. G., Freebersyser J., Marshall C., “Multi-Symbol Detection of M-DPSK,” in *IEEE, Global Telecommunications Conference, 1989, and Exhibition. Communications Technology for the 1990s and Beyond.*, GLOBECOM 89.

[96] Leib H., “Data-aided noncoherent demodulation of DPSK,” *IEEE Trans. on Commun.*, vol. COM-43, pp. 722 – 725, 1995.

[97] Edbauer F., “Bit error rate of binary and quaternary DPSK signals with multiple differential feedback detection,” *IEEE Trans. on Commun.*, vol. COM-40, pp. 457 – 460, 1992.

[98] Calabro S., et al., “Improved Detection of Differential Phase Shift Keying through Multi-

Symbol Phase Estimation," in *Proc. Eur. Conf. Optical Commun. (ECOC)*, Glasgow, Scotland, Sep. 2005, paper We4.P.118.

[99] van den Borne D., "Differential quadrature phase shift keying with close to homodyne performance based on multi-symbol phase estimation," *Optical Fibre Communications and Electronic Signal*, 2005.

[100] Liu X., "Receiver Sensitivity Improvement in Optical DQPSK and DQPSK/ASK through Data-Aided Multi-Symbol Phase Estimation," in *Proc. Eur. Conf. Optical Commun. (ECOC)*, Cannes, France, Sep. 2006, paper We4.P.118.

[101] Liu X., et al., "DSP-Enabled Compensation of Demodulator Phase Error and Sensitivity Improvement in Direct-Detection 40-Gb/s DQPSK," in *Proc. Eur. Conf. Optical Commun. (ECOC)*, Cannes, France, Sep. 2006, paper Th4.4.5.

[102] Liu X., "Generalized data-aided multi-symbol phase estimation for improving receiver sensitivity in direct-detection optical m-ary DPSK," *Optics Express*, vol. 15, 2007.

[103] K. Piyawanno, F. N. Hauske, M. Kuschnerov et al., "Complexity Reduction of MSPE by an Iterative Algorithm for Optical D(Q)PSK," in *Proc. OptoElectronics and Communications Conference (OECC)*, Yokohama, Japan, Jul. 2007, paper 13P-13.

[104] Moeneclaey M., De Jonghe G., "ML-Oriented NDA Carrier Synchronization for General Rotationally Symmetric Constellation," *IEEE Trans. on Commun.*, vol. COM-42, pp. 2531–2533, 1994.

[105] Taylor M., "Phase Estimation Methods for Optical Coherent Detection Using Digital Signal Processing," *Journal of Lightwave Technology*, vol. 27, pp. 901–914, 2009.

[106] Ip I., Kahn J. M., "Feedforward Carrier Recovery for Coherent Optical Communications," *Journal of Lightwave Technology*, vol. 25, pp. 2675–2692, 2007.

[107] Noé R., "Phase Noise-Tolerant Synchronous QPSK/BPSK Baseband-Type Intradyne Receiver Concept With Feedforward Carrier Recovery," *Journal of Lightwave Technology*, vol. 23, pp. 802–808, 2005.

[108] Kikuchi K., "Phase-Diversity Homodyne Detection of Multilevel Optical Modulation With Digital Carrier Phase Estimation," *Journal of Selected Topics in Quantum Electronics*, vol. 12, pp. 563–570, 2006.

[109] Seimetz M., "Laser Linewidth Limitations for Optical Systems with High-Order Modulation Employing Feed Forward Digital Carrier Phase Estimation," in *Proc. Optical Fiber Commun. Conf. (OFC)*, San Diego, CA, U.S.A., Mar. 2008, paper OTuM2.

[110] Kikuchi K., "Coherent Detection of Phase-Shift Keying Signals Using Digital Carrier-Phase Estimation," in *Proc. Optical Fiber Commun. Conf. (OFC)*, CA, U.S.A., Mar.

2006, paper OTuT4.

[111] Alfiad M. S., et al., “111-Gb/s POLMUX-RZ-DQPSK Transmission over 1140 km of SSMF with 10.7-Gb/s NRZ-OOK Neighbours,” in *Proc. Eur. Conf. Optical Commun. (ECOC)*, Brussel, Belgium, Sep. 2008, paper Mo.4.E.2.

[112] Viterbi A. J., Viterbi A. M., “Nonlinear Estimation of PSK-Modulated Carrier Phase with Application to Burst Digital T ransmission,” *IEEE Transactions on Information Theory*, vol. IT-29, no. 4, pp. 543–551, 1983.

[113] Kuschnerov M., et al., “Joint-Polarization Carrier Phase Estimation for XPM-Limited Coherent Polarization-Multiplexed QPSK transmission with OOK-neighbors,” in *Proc. Eur. Conf. Optical Commun. (ECOC)*, Brussel, Belgium, Sep. 2008, paper Mo.4.D.2.

[114] Piyawanno K., et.al, “Polarization Coupled Carrier Phase Estimation for Coherent Polarization Multiplexed QPSK with OOK-neighbours,” in *Proc. Optical Fiber Commun. Conf. (OFC)*, San Diego, CA, U.S.A., Mar. 2009, paper OMT6.

[115] Piyawanno K., et al., “Correlation Based Carrier Phase Estimation for WDM DP-QPSK Transmission,” *Photonics Technology Letters*, vol. 20, pp. 2090–2092, 2008.

[116] Alfiad M. S., et al., “111-Gb/s POLMUX-RZ-DQPSK Transmission over LEAF: Optical versus Electrical Dispersion Compensation,” in *Proc. Optical Fiber Commun. Conf. (OFC)*, San Diego, CA, U.S.A., Mar. 2009, paper OThR4.

[117] Nakashima H., et al., “Novel Wide-range Frequency Offset Compensator Demonstrated with Real-time Digital Coherent Receiver,” in *Proc. Eur. Conf. Optical Commun. (ECOC)*, Brussel, Belgium, Sep. 2008, paper Mo.3.D.4.

[118] Seimetz M., “Performance of coherent optical square-16-QAM-systems based on IQ-transmitters and homodyne receivers with digital phase estimation,” in *Proc. Optical Fiber Commun. Conf. (OFC)*, San Diego, CA, U.S.A., Mar. 2006, paper NWA4.

[119] Louchet H., Kuzmin K., Richter A., “Improved DSP algorithms for coheerent 16-QAM transmission,” in *Proc. Eur. Conf. Optical Commun. (ECOC)*, Brussel, Belgium, Sep. 2008, paper Tu.1.E.6.

[120] Fatadin I., Ives D., Savory D. J., “Laser Linewidth Tolerance for 16-QAM Coherent Optical Systems Using QPSK Partitioning,” *Photonics Technology Letters*, vol. 22, pp. 631–633, 2010.

[121] Rice F., Cowley B., Moran B., “Cramer-Rao Lower Bounds for QAM Phase and Frequency Estimation,” *IEEE Transactions on Information Theory*, vol. COM-49, pp. 1582–1591, 2001.

[122] Ashby W. R., *Design for a Brain*, 2nd ed. John Wiley and Sons, 1960.

[123] Zhou X., Yu J., "Two-stage feed-forward carrier phase recovery algorithm for high-order coherent modulation formats," in *Proc. Eur. Conf. Optical Commun. (ECOC)*, Torino, Italy, Sep. 2010, paper We.7.A.6.

[124] Alfiad M. S., et al., "Transmission of 11x224 Gb/s POLMUX-RZ-16QAM over 1500 km of LongLine and pure-silica SMF," in *Proc. Eur. Conf. Optical Commun. (ECOC)*, Torino, Italy, Sep. 2010, paper We.8.C.2.

[125] Fitz M. P., "Equivocation in Nonlinear Digital Carrier Synchronizers," *IEEE Trans. on Commun.*, vol. COM-39, pp. 1672–1682, 1991.

[126] De Jonghe G., Moeneclaey M., "Cycle Slip Analysis of the NDA-FF Carrier Synchronizers Based on the Viterbi & Viterbi Algorithm," in *Proc. IEEE ICC'94*, New Orleans, Louisiana, U.S.A, May. 1994.

[127] Osborne H., "Stability analysis of an nth power digital phase-locked loop–part i: First-order dpll," *IEEE Trans. on Commun.*, vol. COM-28, pp. 1343 – 1354, 1980.

[128] ——, "Stability analysis of an nth power digital phase-locked loop–part ii: Second- and third-order dpll's," *IEEE Trans. on Commun.*, vol. COM-28, pp. 1355 – 1364, 1980.

[129] Gardner F. M., "Hangup in phase-lock loops," *IEEE Trans. on Commun.*, vol. COM-25, p. 1210–1214, 1977.

[130] Meyr H., Popken L., "Phase acquisition statistics for phase-locked loops," *IEEE Trans. on Commun.*, vol. COM-27, p. 1365–1372, 1980.

[131] Gardner F. M., "Equivocation as a cause of pll hangup," *IEEE Trans. on Commun.*, vol. COM-30, p. 2242–2243, 1982.

[132] Jury E. I., *Theory and Application of the z-Transform Method.* R.E.Kriger Publishing Co, 1964.

[133] Messerschmit D. G., "Frequency detectors for pll acquisition in timing and carrier recovery," *IEEE Trans. on Commun.*, vol. COM-27, pp. 1288–1295, 1979.

[134] Alberty T., Hespelt V., "A New Pattern Jitter Free Frequency Error Detector," *IEEE Trans. on Commun.*, vol. COM-37, pp. 159–163, 1989.

[135] Piyawanno K., et al., "Spectrum-based Frequency Offset Estimation for Coherent Receivers," in *ITG Fachtagung*, Leipzig Germany, 2009.

[136] Natali F. D., "AFC tracking algorithms," *IEEE Trans. on Commun.*, vol. COM-32, pp. 935–947, 1984.

[137] Gardner F. M., "Properties of Frequency Difference Detectors," *IEEE Trans. on Com-*

mun., vol. COM-33, pp. 131–138, 1985.

[138] D'Andrea A. N., Mengali U., "Performance of a Quadricorrelator Driven by Modulated Signal," *IEEE Trans. on Commun.*, vol. COM-38, pp. 1952–1957, 1990.

[139] Piyawanno K., et al., "Fast and Accurate Automatic Frequency Control for Coherent Receivers," in *Proc. Eur. Conf. Optical Commun. (ECOC)*, Vienna, Austria, Sep. 2009, paper 7.3.1.

[140] Xia T. J., et al., "92-Gb/s Field Trial with Ultra-High PMD Tolerance of 107-ps DGD," in *The National Fiber Optic Engineers Conference (NFOEC)*, San Diego, CA, U.S.A., Mar. 2008, paper NThB3.

[141] Piyawanno K. et al., "Optimal Symbol Rate for Optical Transmission Systems with Coherent Receivers," in *Signal Processing in Photonic Communications (SPPCom)*, Karlsruhe, Germany, June. 2010, SPWA2.

[142] Piyawanno K., et al., "Nonlinearity mitigation with carrier phase estimation for coherent receivers with higher-order modulation formats," in *LEOS Annual Meeting Conference Proceedings*, Antalya, Turkey, Sep. 2009, pp 426-427.

[143] Djordjevic I. B., et al., "Coded Polarization-Multiplexed Iterative Polar Modulation (PM-IPM) for Beyond 400 Gb/s Serial Optical Transmission," in *Proc. Optical Fiber Commun. Conf. (OFC)*, San Diego, CA, U.S.A., Mar. 2010, paper NWA4.

[144] Dai Z., Zhang X., "Stable High Power Narrow Linewidth Single Frequency Fiber Laser Using a FBG F-P Etalon and a Fiber Saturable Absorber," *Photonics and Optoelectronic (SOPO)*, vol. 2010 Symposium on, pp. 1–1, 2010.

[145] Weisstein E. W., "Lorentzian Function," MathWorld - A Wolfram Web Resource http://mathworld.wolfram.com/LorentzianFunction.html.

[146] Schneider T., *Nonlinear Optics in Telecommunications.* Springer, 2004.

Index